UNIVERSITÀ DEGLI STUDI DI PADOVA

UNIVERSITY OF PADOVA

Department of Physics and Astronomy "G.Galilei"

PhD COURSE IN ASTRONOMY

CYCLE XXXIV

SEARCHING FOR EXOPLANETS IN STELLAR ASSOCIATIONS USING TESS

PhD Candidate: ELENI EVANGELIA MANTHOPOULOU

Coordinator: Prof. GIOVANNI CARARRO
Supervisor: Prof. GIAMPAOLO PIOTTO
Co-Supervisors: Dr. DOMENICO NARDIELLO
Dr. MARCO MONTALTO

2018 – 2021

UNIVERSITÀ DEGLI STUDI DI PADOVA

Dipartimento di Fisica e Astronomia "G.Galilei"

CORSO DI DOTTORATO DI RICERCA IN ASTRONOMIA

CICLO XXXIV

SEARCHING FOR EXOPLANETS IN STELLAR ASSOCIATIONS USING TESS

Dottoranda: ELENI EVANGELIA MANTHOPOULOU

Coordinatore: Prof. GIOVANNI CARARRO
Supervisore: Prof. GIAMPAOLO PIOTTO
Co-Supervisori: Dr. DOMENICO NARDIELLO
Dr. MARCO MONTALTO

2018 – 2021

Abstract

PhD Thesis

Searching for exoplanets in stellar associations using TESS

Eleni-Evangelia Manthopoulou

For the predominant part of exoplanet's hosts the age is not well constrained and consequently planet properties, demographics, and occurrence rates have been widely unmapped as a function of time. Discovering exoplanets in stellar associations can shed light on these topics as they provide the opportunity to investigate planet formation and evolution in environments with well-defined age. Moreover, for the members of stellar associations we can define with high accuracy their stellar properties and consequently characterize a potential exoplanet around them more efficiently in comparison with field stars. The Full-Frame Images (FFIs) of Transiting Exoplanet Survey Satellite (TESS) offer a huge data mining archive of millions of targets to investigate. We have analyzed the light curves of $\sim$12 000 stars belonging to 40 young associations and moving groups with ages spanning from 1 to 680 Myr. Our targets have been monitored during the primary mission of TESS (July 2018 – July 2020) from Sector 1 to 26. We have extracted the light curves of young association's members from the FFIs, corrected the systematic errors that affected them, accounted for stellar variability, performed transit simulations to probe the detection efficiency of our technique to discover different types of transiting exoplanets, and estimated their frequency. We report the detection of 24 candidate exoplanets in our sample. Eighteen of our candidates are novel discoveries. Our candidate planets belong to 10 different young stellar associations with ages between 10 and 50 Myr and have been validated through a series of vetting tests (odd/even, secondary transit depth, etc). We also measured the frequencies of candidate planets in stellar associations for different orbital periods and planetary radii, taking into consideration the detection efficiency of our technique and the false positive probabilities of our candidates. Furthermore, we exploited the

Stellar Age – Planet radius distribution of known candidates and confirmed exoplanets with well measured ages and orbital periods less than 100 days. Giant ($R_P \geq 11.2$ $R_\oplus$) and small ($R_P < 3.9$ $R_\oplus$) size planets do not show any peculiar trend on their distribution, whereas the distribution of planets in the radius regime of $4R_\oplus \leq R_P \leq 10R_\oplus$ have attracted a lot of interest within the exoplanet community. These planets are concentrated at ages less than 100 Myr and it is still unclear why there are no detections of planets with this size orbiting older stars. Various scenarios (i.e atmospheric escape, core-powered mass loss, dynamical evolution etc) have been proposed to explain this behavior but until today no secure conclusions have been made. Consequently, increasing the candidate and eventually confirmed exoplanets around young stars we can take significant steps towards the understanding of the evolution and formation mechanisms that prevail in the early stages of an exoplanet's life, which are still into debate among the exoplanet community.

Acknowledgements

I would like to thank my supervisor Prof.Giampaolo Piotto for his trust, continuous guidance and suggestions during my PhD. I have benefited greatly from your wealth of knowledge and assistance. I am extremely grateful that three years ago you gave me the opportunity to pursue my PhD at the University of Padova, took me on as a student and continued to support me over the years.

I am indebted also to my co-supervisors Dr.Domenico Nardiello and Dr.Marco Montalto without whom this thesis would not be possible. They have generously provided me with invaluable feedback and guidance on my analysis and support me 24/7, at times responding to emails late at night and early in the morning. Covid-19 hit at the second year of my PhD, but we all tried our best to continue our co-operation through zoom meetings, helping each other to get through this hard period which had an impact in many aspects in the life of people across the globe. I will never forget your encouraging messages when things where not going as planned and your patience through out my project.

I would like to recognize the assistance I received from Prof.Luca Malavolta on the modeling of my candidate exoplanets with `PyORBIT`. Thank you for patiently answering my million questions and doubts. Moreover, thanks should also go to the PhD student Giacomo Mantovan for kindly providing me with the calculation of the False Positive probabilities of my candidates with the software `VESPA`.

I am fortunate to have been a part of the Exoplanets and Stellar Populations Group (ESPG) at the University of Padova, which welcomed me in Italy and made me feel like home. Grazie Gaia, Giacomo, Marco, Mimmo, Luca I (Ranger), Luca II (Sbuffo), Lorenzo, Valerio, Tiziano, Fatime and Valentina. I wiil always remember our fantastic spritzs and nights of observations.

It is important to strike a balance with life outside the third floor where the PhD offices are in La Specola, as I love to call the Department of Astronomy in Padova. I cannot stress enough about how grateful I am for the new friends I made in Padova during the past three years and a half, that turned into family away from home. Life would not be the same without them. Special thanks my bestie Cote, and also Jose, Katerina, and Thodoris. Thanks goes also to the best housemates/buddies ever Elli, Chrysanthi and Giovanni. You will always have a special place in my heart and I will cherish our Italian (and international) adventures forever. I am also thankful to my best friends in Greece who have always supported me since childhood and listen to my worries even when I was explaining to them why my code was not working. Thank you Eleni, Katerina, Maria and, Marianna.

Thank you to my partner in crime, Achilleas, for constantly listening to my rant, for his support in the good and difficult periods and for the sacrifices he made in order for me to pursue my PhD degree.

Most importantly, I am grateful for my family's unconditional, unequivocal, and loving support. For not questioning my crazy dreams to be an Astrophysicist, even when I told them that I will have to leave Greece for an unknown period of time and go hunt exoplanets.

We made it happen!

"The cosmos is within us. We are made of star-stuff. We are a way for the universe to know itself."

"The universe is a pretty big place. If it's just us, seems like an awful waste of space."

Carl Sagan

"I will never stop looking up the starry sky."

Contents

List of Figures

List of Tables

Chapter 1

Introduction

1.1 Exoplanets

Human kind has long been interested on the mysteries of the sky and stars. There are evidences of early solar-lunar calendars from $\sim 2\,000$ B.C. in Egypt and Mesopotamia. Around 280 B.C. the Greek astronomer and mathematician Aristarchos was the first to propose a heliocentric model placing the Sun at the center of the known Universe (solar system) with the Earth and other planets on an orbit around it. The objects orbiting around the Sun were named 'planets', which has roots from the Greek word πλανήτης (planētēs) and means 'wanderer'; because astronomers at this period observed that certain bodies moved across the sky in comparison to other stars.

Nowadays, with the term exo-planet we define the planetary bodies that orbit their host star and are located outside of our solar system. The history of exoplanet discoveries dates back to 1992 with the detection of two rocky planets around the pulsar PSR B1257+12 in the constellation of Virgo (Wolszczan & Frail, 1992). A year later, Backer et al. (1993) found the first circumbinary planet orbiting the pulsar PSR B1620-26 A and the white dwarf WD B1620-26, located 1 170 light years away from Earth in the Scorpius constellation. This planet has an additional prize since it is also the first planet discovered in a globular cluster named Messier 4 or M4. The biggest breakthrough though came on November 1^{st} 1995[1] when Michel Mayor and Didier Queloz announced the first ever definitive detection of an exoplanet around a main sequence star with the name 51 Pegasi (Mayor & Queloz, 1995), 50 light-years from Earth in the northern constellation of Pegasus. The planet is a gaseous giant planet with half of the mass of Jupiter ($M_P = 0.46 M_J$), a period of 4.2 days and a semi-major axis a =0.0527 AU (Figure 1.1). For this discovery the authors were awarded the Nobel Prize in Physics on 2019 (shared with James Peebles for theoretical discoveries in physical cosmology).

[1]The publishing date of the paper: "A Jupiter-mass companion to a solar-type star"

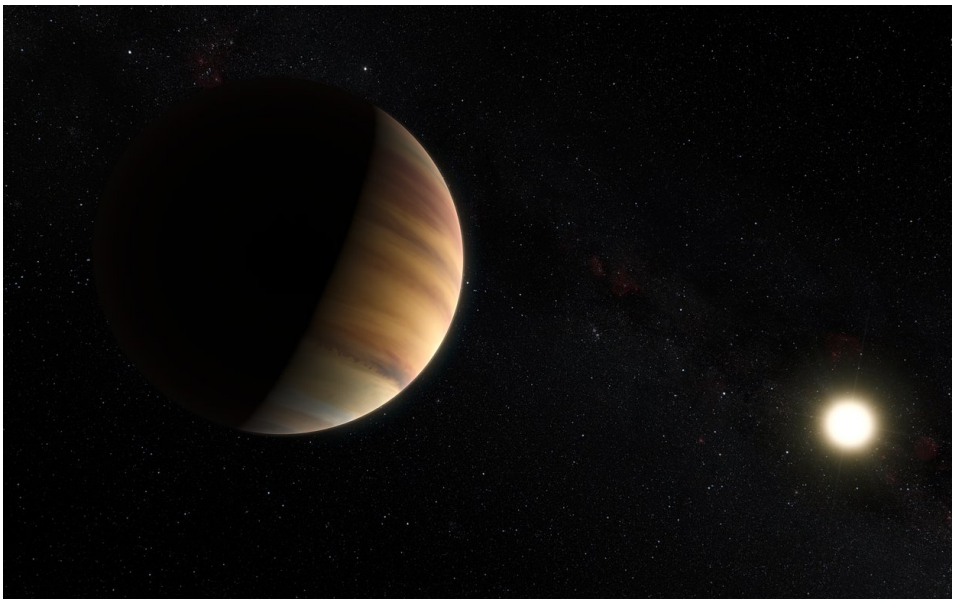

Figure 1.1: Artist impression of the first exoplanet 51 Peg b (left) discovered by Mayor & Queloz (1995) orbiting the main sequence star 51 Pegasi (right) in the constellation of Pegasus. ©ESO/M. Kornmesser/Nick Risinger/.

Since the discovery of 51 Peg b, the number of known exoplanets has rapidly increased. To date, more than 4 800 exoplanets have been confirmed[2] and 8 000 more candidate exoplanets are waiting for confirmation. Before the launch of the Kepler space mission on 2009, the most fruitful method to discover exoplanets was the Radial Velocity technique. Today this image has changed drastically as shown in Figure 1.2. The majority of exoplanet discoveries have been accomplished using the transit method with a percentage of 76.8%, followed by the radial velocity technique with 18.4%, microlensing with 2.5%, imaging with 1.1%, and the remaining methods[3] with 1.1% (Figure 1.3). Exoplanets show a wide diversity on their characteristics (i.e masses, radii, temperatures etc) from small rocky planets with a fraction of the size of Earth to gas giants with the size of Jupiter or even larger, from ice, water to lava worlds. Following the planet types: Gas Giant, Neptune-like, Super-Earth and Terrestrial as defined in the NASA website Exoplanet Exploration[4] we found that most of the confirmed exoplanets up to now are Neptune sized planets (1719 out of 4884), next are the Super Earths and Giants with similar numbers of 1516 and 1458 discoveries, re-

[2] As of 21^{st} December 2021 found in `https://exoplanets.nasa.gov/`

[3] Timing Variations: 0.45%; Eclipse Timing Variations: 0.33%; Orbital Brightness Modulation: 0.18%; Pulsar Timing: 0.14%; Pulsation Timing Variations: 0.04%; Disk Kinematics: 0.02%; and Astrometry: 0.02%.

[4] Exact definition of each planet type can be found here: `https://exoplanets.nasa.gov/what-is-an-exoplanet/planet-types/overview/`

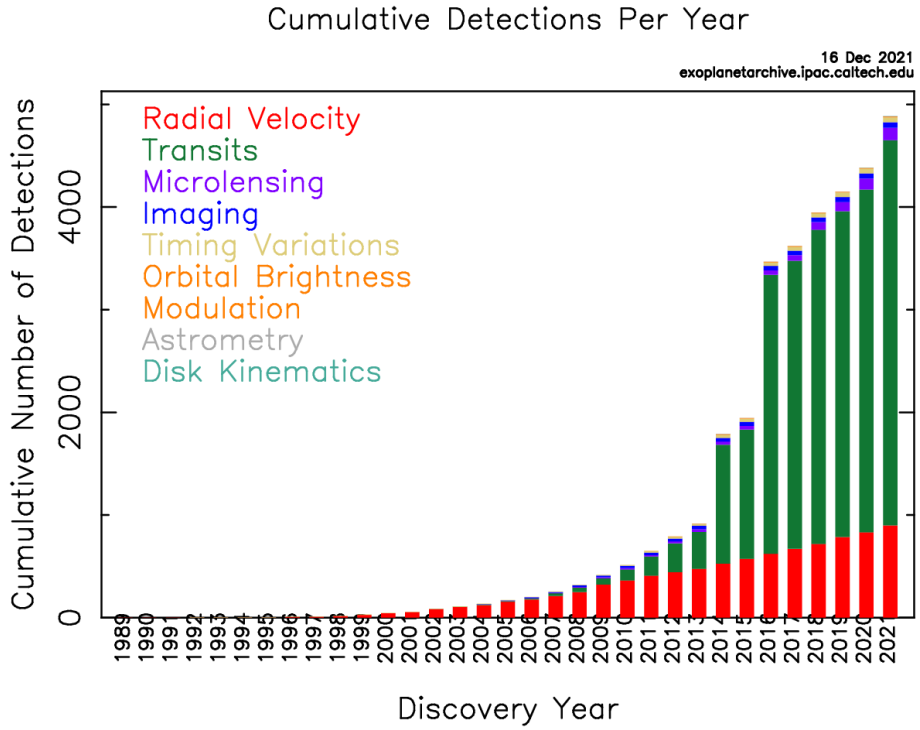

Figure 1.2: Histogram of the exoplanet discoveries per year up to 2021. © `https://exoplanetarchive.ipac.caltech.edu/exoplanetplots/`.

spectively. The least amount of planets are of terrestrial type with only 186 confirmed discoveries (Figure 1.4).

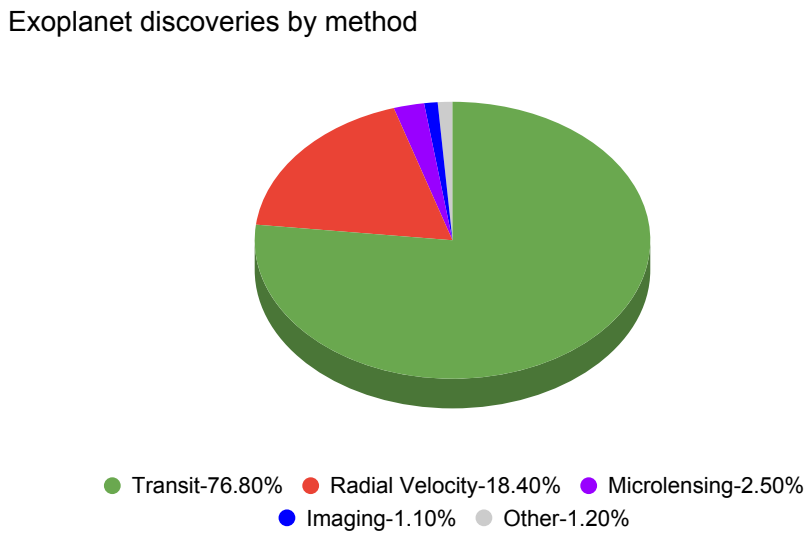

Figure 1.3: Exoplanet discoveries by method. Transit (green): 76.8%; Radial Velocity (red): 18.4%; Microlensing (purple): 2.5%; Imaging (blue): 1.10%; Other methods (grey): 1.20%.

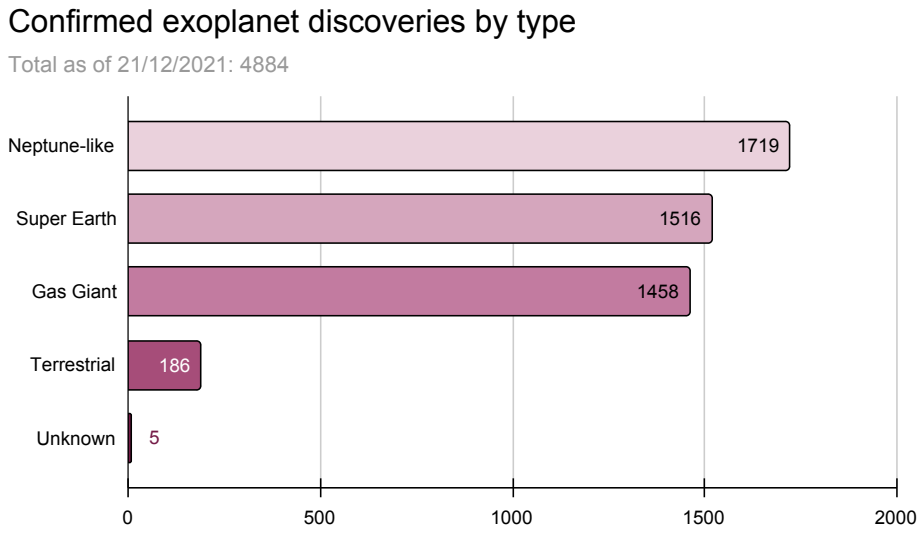

Figure 1.4: Confirmed exoplanets classified by type based on the NASA website Exoplanet Exploration[5]. Total as of 21/12/2021: 4884, from which 1719 are Neptune-size (or Neptune-like following the identification of the NASA website); 1516 Super Earths; 1458 Gas Giants; 186 Terrestrial planets; and 5 of unknown type.

1.2 Detection techniques

As mentioned in Section 1.1 there are many methods, direct or indirect, to detect an exoplanet. We will do a brief overview of the two most successful techniques to date based on their efficiency to discover extrasolar planets: the transit and radial velocities method.

1.2.1 Transit method

When an object passes in front of a star it blocks a percentage of the light that arrives to a hypothetical observer, causing (periodic) changes on the flux of the star which should be in principle approximately constant. A primary transit is occurring when the smaller object, a planet, passes in front of its host star, whereas a secondary eclipse or occultation when it passes behind it. In the case of a primary transit, we can measure the variation of the star's flux over a period of time (light curve). This can allow us to determine directly the planet radius (R_P), the inclination (i) of the orbit, and the semi-major axis (a) of the planet. Figure 1.5 shows a schematic representation of a transit event (Deeg & Alonso, 2018). When the planet passes in front of the disc of the star its observed flux is reduced by an amount δ, showing a dimming on the star's light curve (bottom panel of Figure 1.5 where δ is presented as ΔF). The parameter δ is commonly referred as the depth of the transit and considering circular orbits and negligible planet flux can be calculated by:

$$\delta \approx \left(\frac{R_P}{R_\star}\right)^2, \tag{1.1}$$

where $R_\star$ is the radius of the host star. The full duration of a transit event (t_F) is defined as the time where the entire planetary disk is in front of the stellar disc. The total transit duration (t_T) is considered as the time where any part of the planet obscures the stellar disc and its strongly dependent on the impact parameter (b). The latter is defined as the minimal projected distance to the center of the stellar disc during a transit event and for circular orbits can be approximated by:

$$b = \frac{a \cos i}{R_\star} \tag{1.2}$$

The way a planet transits its host star affects the value of b. If b=0 then the planet crosses the center of the star's disc, the transit duration is the longest possible and i=90°, whereas if $0 < b < 1$ the duration of the transit will be shorter. When b=1 or $b \geq 1+R_P/R_\star$ the transiting planet does not fully cover the stellar disc and we observe a grazing transit with a 'V-shaped' light curve. Another factor that plays a significant role on determination of the contact times of the planet with the host star and affects the shape of the

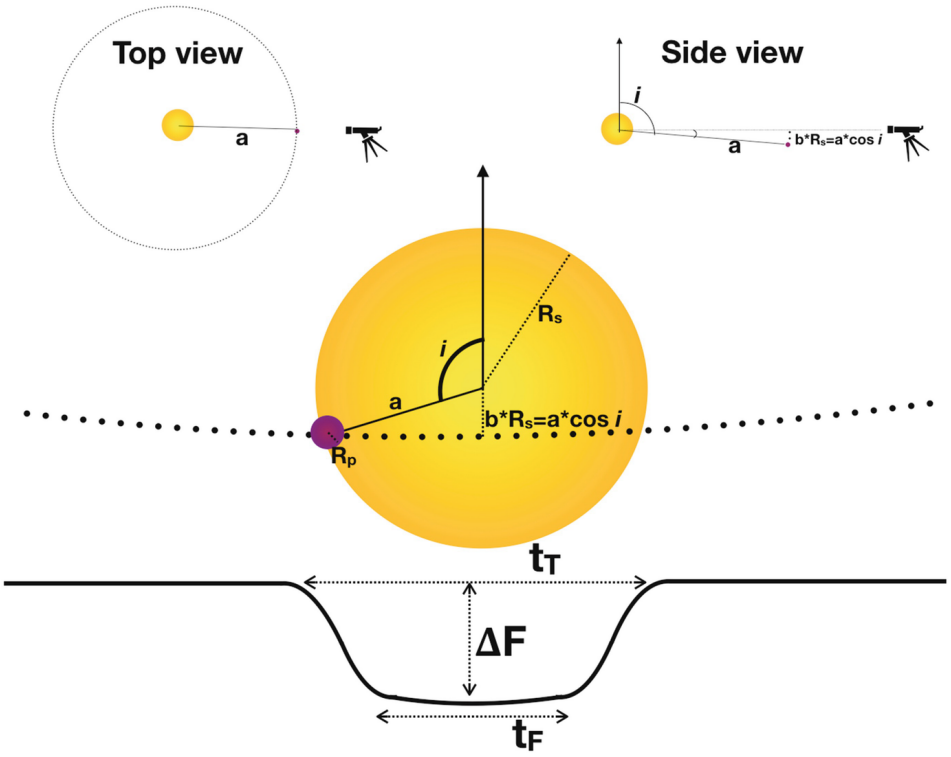

Figure 1.5: Schematic representation of a transit event. Bottom panel: observed light curve of a transiting planet; Central panel: model representation as seen from the observer's point of view; Top panel: alternative view points, top view of the transit event (left) and side view (right). Details on the main text. © see Figure 2 from Deeg & Alonso (2018).

transit light curve is the limb darkening (LD). The brightness of the parent star gradually decreases from the center to the edge of the stellar disc or limb. This phenomenon results in a smaller transit depth when the planet is at the edge of the star and a deeper one when is in the center. Consequently, in the light curve is harder to identify the exact moments where the planet disc is entirely in contact with the stellar disc (second and third contact in eclipse terminology)[6] and its shape is rounded at the center of the transit.

The transit method is currently the most successful in discovering exoplanets, with more than 3 600 new detections until now (Section 1.1), even though only observers who view the orbit of the planet nearly edge-on are able to detect the transit (Winn, 2010). This configuration is illustrated in Figure 1.6. When a planet completes a full orbit around a star leaves a 'footprint' in the celestial sphere which is shown by the shadow band in Figure 1.6. This shadow band represents the possible observing area of the transiting planet. The a-priori probability that a given planet is eligible to

[6] see details on Figure 2 from Winn (2010)

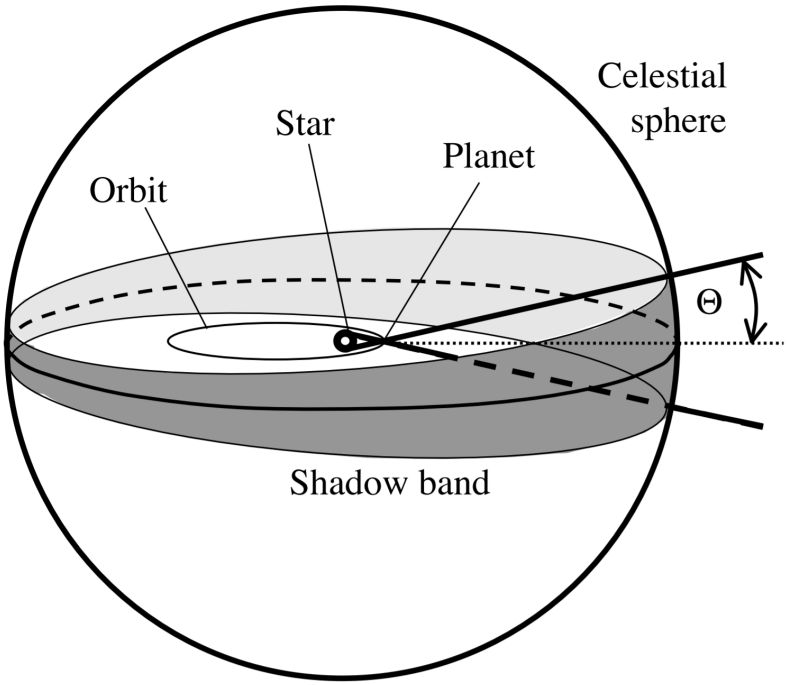

Figure 1.6: Illustration of a transit-observer configuration. Observers inside the penumbra of the planet (shadow band), defined by a cone with opening angle Θ, are eligible to observe the transit. © see Figure 3 from Winn (2010).

be observed transiting its host star is a function of the planetary orbit, the planetary and stellar radii as defined by (Winn, 2010):

$$P_p^{tr} = \left(\frac{R_\star \pm R_P}{a}\right)\left(\frac{1 + esin(\omega)}{1 - e^2}\right) \tag{1.3}$$

where the "+" sign allows grazing eclipses and the "−" sign excludes them, e is the orbital eccentricity and ω the observer's celestial longitude.

1.2.2 Radial Velocities

The Radial Velocity technique is based on the Doppler effect. In this method, astronomers measure Doppler shifts (or wavelength changes) in the observed spectrum of a star which are caused by an orbiting planet. More massive planets result in larger and more easily detected Doppler shifts, in comparison with lower mass planets. Considering a 2-body system (star-planet) the radial velocity is defined as the barycentric velocity of the star projected on the line of sight. The semi-amplitude (K) of the radial velocity of a star can

Figure 1.7: Artist impression of TESS spacecraft © NASA.

be expressed in units of ms^{-1} and with the planet mass in Jupiter masses (M_J):

$$K = \frac{28.4329\, ms^{-1}}{\sqrt{1-e^2}} \frac{M_P\, sini}{M_J} \left(\frac{M_\star + M_P}{M_\odot}\right)^{-2/3} \left(\frac{P}{yr}\right)^{-1/3} \tag{1.4}$$

If the mass of the host star ($M_\star$) is known then it is possible to calculate the minimum planetary mass ($M_P$sini), but the true mass of the planet can be defined if also the inclination (i) of the planet's orbit is acquired. If the planet transits its host star, the inclination can be calculated (Section 1.2.1), so the radial velocity and transit methods can be complementary to each other with an optimal goal to fully characterize an exoplanet.

1.3 Transiting Exoplanet Satellite Survey

The Transiting Exoplanet Satellite Survey (TESS, Ricker et al. 2014) is a NASA mission launched in April of 2018 with a main goal to discover hundreds of exoplanets around close-by bright stars that will be able to be followed up with spectroscopic facilities to measure planetary masses and atmospheric compositions. TESS spacecraft (Figure 1.7) launched on a SpaceX Falcon 9 Rocket from the Cape Canaveral Space Force Station located on Cape Canaveral in Florida, United States of America. It is equipped with four identical and highly optimized wide-field of view cameras that jointly can observe a 24° × 90° area of the sky known as sector (Figure 1.8 (a)), with a resolution of ∼ 21 arcsec/pixel. Each hemisphere is split into 13 partially overlapping sectors starting from an ecliptic latitude of 6° to the

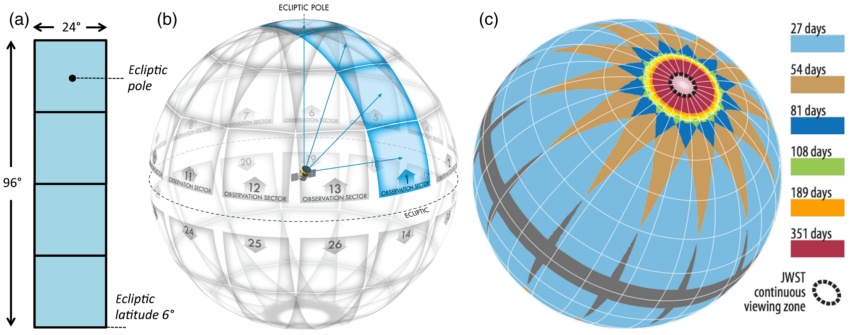

Figure 1.8: TESS field of view and coverage map. (a): Joint field of view of the four cameras of TESS (24° × 90°); (b): Illustration of the 26 sectors of TESS in the Northern and Southern ecliptic hemisphere; (c) Coverage map of TESS, color-coded by the duration of observations in each part of the sky. © Figure 7 from Ricker et al. (2014).

ecliptic pole (Figure 1.8 (b)). Each sector is imaged for approximately 27 consecutive days (27×13 = 351 days ∼ 1 year). Some areas of the sky are monitored in more than one sectors with the maximum period in the ecliptic poles defined with red color in Figure 1.8 (c). This area is named Continuous Viewing Zone (CVZ) of TESS and the stars inside it are observed approximately an entire year (13 sectors). The Southern hemisphere was observed by TESS in the first year of the survey from July 2018 to July 2019 followed by the Northern hemisphere in the second year from July 2019 to July 2020. In Figure 1.9 the complete mosaic of TESS sectors is presented. In the Northern hemisphere a part of the sky was not able to be observed which created a gap in the sky coverage of TESS. This area corresponds to sectors 14-16 and 24-26 for which the instrument boresight was shifted from its canonical pointing at +54° to +85° ecliptic latitude in order to avoid excessive contamination by stray Earth-moonlight in camera 1 and 2 of TESS.

By the end of its two year primary mission TESS observed approximately 75% of the entire sky (Figure 1.9). More than 200 000 pre-selected stars have been monitored with a 2-minute cadence and are available to the community as Target Pixel Files (TPFs) or as calibrated light curves. Almost every star outside ± 6° of the ecliptic plane has been observed with a 30-minute cadence in the primary mission and these data were released only in the form of Full-Frame Images (FFIs, Figure 1.10). The FFIs can allow us to extract light curves of every star with TESS magnitude down to 16–17 mag inside TESS sectors and create a huge data mining archive of millions of stars not only to search for possible exoplanets but also to contribute in other fields in astronomy like asteroseismology, variable stars, supernovae, Galactic and extragalactic sources etc.

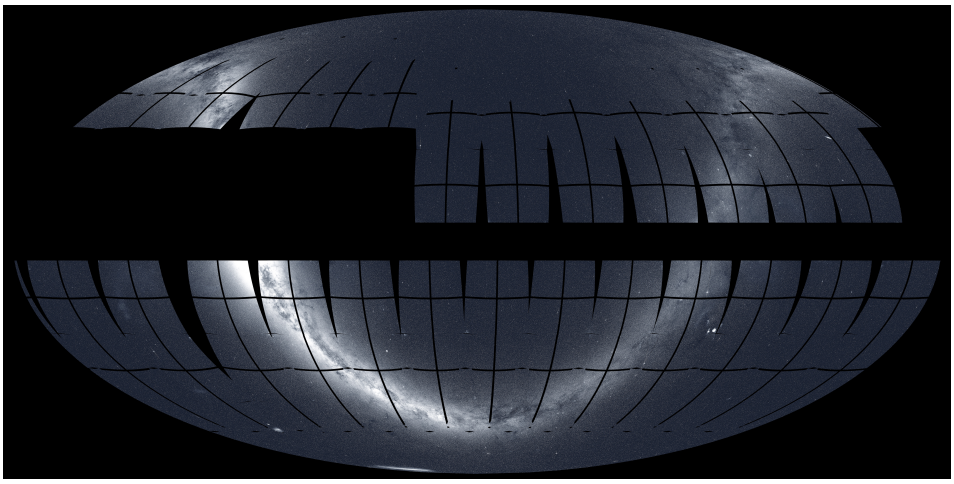

Figure 1.9: Southern and Northern mosaic of TESS observations during the primary mission. © NASA,/MIT/TESS and Ethan Kruse (USRA).

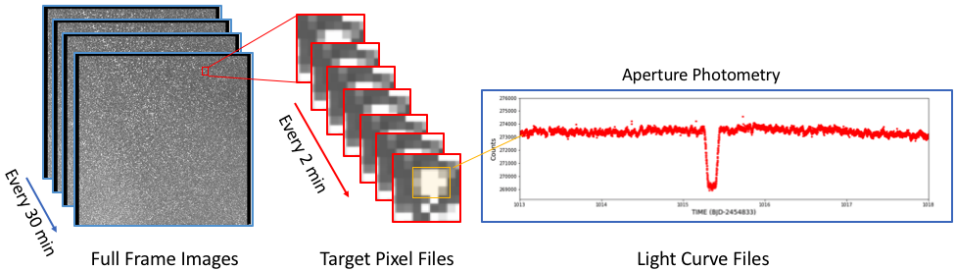

Figure 1.10: Photometric Data products of TESS. From the Full Frame Images to the extracted light curves of stars observed with a 2-min cadence in the TPFs. © NASA, `https://heasarc.gsfc.nasa.gov/docs/tess/data-products.html`

The launch and successful operation of TESS opened a new era of exoplanet discoveries. TESS has been constantly monitoring the sky for almost 4 years (at the time of writing this thesis), hunting for new worlds. From the 2-min cadence data and FFIs of TESS 175 confirmed exoplanets have been discovered until today and more than 5 000 candidates that astronomers are trying to validate and eventually confirm[7].

1.4 Stellar associations

Stellar associations are sparse groups of stars, sparser than open or globular clusters. They usually contain a relatively small number of stars, from approximately 10 to few hundreds, that share the same origin and are moving in the same direction but they are not gravitationally bound to each other. The Armenian scientist and astronomer Victor Ambartsumian was the first to introduce the term stellar associations in 1947 and he firstly divided them in two groups: OB and T associations based on the characteristics of their member stars. A moving group is the remnant of a stellar association and have been extensively studied by Olin Eggen in the 1960s. Eggen (1958) defined that moving groups are dissociated star clusters that have maintained components of their initial velocities and similarly with the members of a stellar association have the same origin.

Figure 1.11: The Scorpius-Centaurus Association © CFA Harvard Smithsonian).

Despite the plethora of exoplanet discoveries (> 4 800, Section 1.1) we only know few planets around young stars. Based on the NASA Exoplanet Archive[8] only 143 exoplanets have been confirmed orbiting stars with an

[7] As of 21/12/2021 `https://exoplanets.nasa.gov/tess/`

[8] `https://exoplanetarchive.ipac.caltech.edu/`

(measured) age less than 1 Gyr, which corresponds to 2.9% of the total amount of discovered confirmed planets up to now. Young planets though can provide us unique insights into the formation and early dynamic history of exoplanet systems, but searches of these objects have been hampered by the activity of the young host stars that makes the detection of an exoplanet around them more difficult and complicated. Using proper pipelines to search and eventually increase the number of young planets can shed light into many unanswered questions regarding the formation and evolution mechanisms on the early stages of an exoplanet's life, where the majority of their evolution is happening (i.e Spiegel & Burrows 2012; Ida et al. 2013). More specifically, phenomena like accretion (Manara et al., 2019), atmosperic escape causing mass-loss (Owen, 2019) or core-powered mass loss (Ginzburg et al., 2018), dynamical evolution such as migration due to interaction with the protoplanetary disc or planet-planet scattering (Fabrycky & Tremaine 2007; Chatterjee et al. 2008) or dynamical interactions with other planetary bodies (Schlichting et al., 2015) are occurring in the early life of an exoplanet and can have a significant impact on the distribution and architecture of the exoplanet population we observe.

Young associations and moving groups can be ideal laboratories to target and search for young planets, since they supply us with a wide sample of stars with well determined stellar parameters and ages in comparison with single field stars. The members of a young association or moving group are born from the same molecular cloud and consequently have similar chemical compositions, positions and kinematics but also age. This implies that we can determine with high accuracy their stellar properties (Torres et al., 2006) such as mass, radius, effective temperature, and age using theoretical models. Knowing the star's properties can play a significant role on the characterization of a potential exoplanet around them. Moreover, for the predominant part of exoplanet hosts up to now the age is not well constrained and consequently planet properties, demographics and occurrence rates have been widely unmapped as a function of time. This image can be shifted if more studies start to target stars in stellar associations. Until today, five young exoplanets have been discovered using TESS data. The first one is in the Tucana-Horologium (THA) association with an age of 45^{+4}_{-4} Myr (Table 2.1) around the star DS Tuc A (Benatti et al. 2019a; Newton et al. 2019) and other two have been found in the Beta Pictoris Moving Group (BPMG) with an age of 24^{+3}_{-3} Myr orbiting the star AU Microscopii (Plavchan et al. 2020a; Klein et al. 2021; Martioli et al. 2021). Mann et al. (2020a) confirmed through kinematics, lithium abundance, and rotation that HD 63433 (TIC 130181866) is actually a member of the Ursa Major moving group (UMa) and discovered two transiting planets around it using TESS data. Moreover, V1298 Tau is a young (23^{+4}_{-4} Myr) star initially observed during the K2 campaign 4. Using data form this campaign, David et al. (2019) found that V1298 Tau hosts four transiting exoplanets with radii

between 5.5 10.3 $R_{\oplus}$. Recently, TESS re-observed V1298 Tau during the extended mission. Feinstein et al. (2021) analyzed these TESS data from the 10-minutes FFIs and managed to recover the signals of the four planets discovered by David et al. (2019), updated their ephemerides but found shallower transits for V1298 Tau bcd in the redder TESS bandpass at the 1–2σ level. These discoveries are promising that more young planets can be found in stellar associations using TESS data increasing the sample of planets around stars with well determined ages ($<$ 1 Gyr) and thus help us to understand and investigate the causes of planetary evolution and the mechanisms that prevail in the early life of an exoplanet that are still questionable.

The remainder of the PhD thesis is organised as follows. Chapter 2 discusses the young star target selection observed by TESS during the primary mission, as well as the extraction and correction (systematic errors and stellar variability) of their light curves. Furthermore, in this chapter we present the color-magnitude diagrams and isochrone fit of the selected young associations and moving groups. Chapter 3 describes the planet search using the BLS algorithm, the planet simulations we carried out in order to establish the performances of our technique to discover transiting planets and the vetting tests we applied to our candidates to validate them. The discovered candidate exoplanets in our sample are discussed in detail in Chapter 4. In Chapter 5, we present the modeling and planetary properties of our candidate exoplanets and an estimation of their False Positive Probability. Chapter 6 discusses the frequency of candidate exoplanets in young associations and moving groups and the stellar age versus planetary radius distribution of candidate and confirmed exoplanets with well measured ages and orbital periods less than 100 days, before a summary and conclusion in Chapter 7.

Chapter 2

Observations and Data analysis

This chapter discusses the construction of the list of stars we will target in young associations and moving groups observed by TESS, as well as the extraction of their light curves using cutting-edge tools, the PATHOS pipeline. Furthermore, we present the color-magnitude diagrams and isochrone fit of the selected associations and describe the pre-analysis of the light curves, such as the correction of systematic effects and exclusion of the variability, steps with a significant impact on the search of exoplanet transits.

2.1 Young associations and moving groups in TESS

The first step of our analysis was to define the sample of stars we will target and search for exoplanets. Since there was not a unique catalogue of stars containing information about all the discovered young associations and moving groups in the literature, we created our list by combining results from previous individual studies. We decided to use catalogues available in the literature from 2006 to 2020 and their references within.

The first one we used was from Torres et al. (2006), in which the authors created the SACY sample, where SACY stands for Search for Associations Containing Young Stars. This sample contains 1626 members in nearby young associations, 1511 identified by the authors using high-resolution optical spectroscopy and the remaining 115 objects from the literature. The second catalogue we exploited was from Fernández et al. (2008) which included 8 young local associations[1]. Four years later, Billot et al. (2010a) studied the star formation in Vulpecula OB association, located in the Galactic plane at 2.3 kpc from the Sun, and reported 856 young stellar candidates. Bell et al. (2015) published a self-consistent, absolute isochronal age scale for 9 young

[1] closer than 100 pc

nearby moving groups in the solar neighbourhood with a total number of 526 members. Using 2MASS near infrared photometry and proper motion information Elliott et al. (2016) identified 84 wide companions in a sample of 542 previously known members of young associations. We also took into consideration the BANYAN all-sky survey catalogues (Gagné et al. 2014; Gagné et al. 2015b; Gagné et al. 2015a; Gagné et al. 2018a; Gagné et al. 2018b; Gagné & Faherty 2018) which provided us with hundreds of new members. The authors used a modified Bayesian analysis to calculate the membership probability of stars in nearby young associations. They applied their technique to already identified members, for which they redefined their membership, but they also made new discoveries using Gaia DR2 (Gaia Collaboration et al., 2018) and Tycho data. Furthermore, Gagné et al. (2018c) worked towards the characterization of the Volans-Carina (VOLCAR) association and identified 19 possible young members using Gaia DR2 data and 46 candidates which need further investigation to be confirmed. The same year, Luhman et al. (2018) studied the Upper Scorpius (USCO) association using parallaxes, proper motions, color-magnitude diagrams from various wide-field surveys as well as spectroscopy to measure or refine the spectral types and membership probabilities of possible members of the association. Their final catalogue, with already known and newly discovered members, contains 1631 objects for the USCO association. Moreover, we included in our sample the 378 members reported by Baron et al. (2019) in 13 young associations. Part of the young stars were observed by AO direct-imaging planet searches, by the seeing-limited PSYM-WIDE[2] (Naud et al., 2017) and WEIRD[3](Baron et al., 2018) surveys, focusing on young moving groups with ages of less than 300 Myr. Tang et al. (2019) worked on the membership of GROUP X, a nearby moving group in a distance of $\sim$ 101 pc (Tang et al., 2018). The authors identified 218 candidate members, taking into consideration the 27 candidates previously identified by Oh et al. (2017). Cantat-Gaudin et al. (2019) searched for young stars in the Vela-Puppis region and identified 11843 member. The authors grouped these stars in seven distinct young populations with different ages and kinematical distribution. The Cepheus association was the target of Klutsch et al. (2020) work, in which they reported 201 young star candidates divided in two populations that are spatially and kinematically separated. Additionally, the authors published a list of 99 comoving companions to their original targets in the Cepheus region that we also added to our sample. The last catalogue we took into account was about the μ Taurus (MUTAU) association. Gagné et al. (2020) reported 500 young candidate members for the MUTAU using Gaia DR2 data and the BANYAN Σ tool (Gagné et al., 2018a) to define their membership probabilities.

[2]stands for Planet Search around Young-associations M dwarfs
[3]stands for e Wide-orbit Exoplanet search with InfraRed Direct imaging

Because we combined catalogues from different studies, the identifiers of the targets were not coherent. Some of them were from the TYCHO catalogue, others from 2MASS and few of them in Gaia DR2 catalogue. The later one, can provide significant information about the stars in our catalogue that were vital for our future analysis such as updated positions, parallaxes, proper motions, magnitudes etc. So joined all the catalogues from the literature and used the SIMBAD database (Wenger et al., 2000) to assign a Gaia DR2 identification to each target by performing a cross-match using the identifier (e.g., 2MASS, TYC) provided from their initial catalogues and the Gaia DR2 cataloque. We also did a cross-match using their positions (RA,DEC) taking into consideration their proper motions to make sure that the matching was accurate.

In this way we created a catalogue with coherent identifiers from Gaia DR2 and managed to exclude any duplicated sources in our sample. Then, we did a cross match with the TIC catalog to acquire also the TIC ID, and calculated the TESS magnitude based on the equation in Stassun et al. (2019a) (Eq. 2.1).

$$\mathrm{T}= \begin{cases} G - 0.00522555(G_{BP}\text{-}\mathrm{G}_{RP})^3 + 0.0891337(G_{BP}\text{-}\mathrm{G}_{RP})^2 - 0.633923(G_{BP}\text{-}\mathrm{G}_{RP}) + 0.0324473 \\ \\ G - 0.430, \text{ for stars with no valid } G_{BP}\text{-}\mathrm{G}_{RP} \text{ colors} \end{cases} \tag{2.1}$$

Furthermore, we excluded sources with $T > 18$ *mag* as well as those outside of TESS field by doing a conservative elimination of the stars with ecliptic latitude $-4° < \beta < +4°$.

Finally, our input catalogue of stars inside the field of TESS contains 12 164 sources in 40 young associations and moving groups in the northern and southern ecliptic hemisphere. The associations in our sample cover a wide span of ages ranging from 1 to 680 Myr and their names, abbreviation, number of members, ages and their references are reported in Table 2.1.

2.2 Color-Magnitude diagrams & Isochrone fitting

In order to extract the stellar properties of the stars in our sample we fitted isochrones to the color-magnitude diagram (CMD) of each young association and moving group in Table 2.1 using the PARSEC version 1.2S models (Bressan et al., 2012).

We transformed the isochrones from the theoretical to the observational plane using the following approach. We used the distances (d) computed by Bailer-Jones et al. (2021) using the Gaia Early Data Release 3 (EDR3) of each individual star to calculate its absolute G_0 magnitude using the distance modulus (e.g., $G_0 = G + 5 - 5\times \log_{10}(d)$). Moreover, we took into consideration the interstellar reddening and extinction for each star in our

Table 2.1: Ages of the young associations and moving groups in our input catalogue

Association Name	Abbreviation	N.Members	Age (Myr)	Range (Myr)	Ref.Age
AB Doradus moving group	ABDMG	350	50.0	50^{+20}_{-5}	(1)
β Pictoris moving group	BPMG	201	24.0	24^{+3}_{-3}	(2)
Carina association	CAR	157	40.0	-	(1)
Carina-Near moving group	CARN	94	200.0	200^{+50}_{-50}	(3)
Volans-Carina	VOLCAR	59	90.0	90^{+5}_{-7}	(5)
Coma Berenices cluster	CBER	66	562.0	562^{+98}_{-52}	(6)
Columba association	COL	236	42.0	42^{+6}_{-4}	(2)
			24.11	4.0-54.5	(4)
ϵ Chamaeleontis association	EPSC	58	3.7	$3.7^{+4.6}_{-1.4}$	(7)
η Chamaeleontis association	ETAC	2	6.0	6^{+2}_{-1}	(8)
Hyades cluster	HYA	94	680.0	-	(9)
			650.0	650^{+70}_{-70}	(10)
Lower Centaurus Crux association	LCC	280	15.0	15^{+3}_{-2}	(11)
Octans association	OCT	141	35.0	35^{+5}_{-5}	(12)
Platais 8	PL8	12	60.0	-	(13)
Pleiades Cluster	PLE	5	112.0	112^{+5}_{-5}	(14)
μ Taurus	MUTAU	255	62.0	62^{+7}_{-7}	(15)
Taurus star-forming region	TAU	46	1	1-2	(16)
Tucana-Horologium	THA	346	45.0	45^{+4}_{-4}	(2)
32 Orionis association	32OR	39	22.0	22^{+4}_{-3}	(2)
TW Hya	TWA	125	10.0	10^{+3}_{-3}	(2)
Upper Centaurus Lupus	UCL	324	16.0	16^{+2}_{-2}	(11)
Ursa Major cluster	UMA	21	414.0	414^{+23}_{-23}	(17)
Upper Scorpius association	USCO	123	10.0	10^{+3}_{-3}	(11)
χ^1 For cluster	XFOR	9	500.0	-	(18)
Argus	ARG	111	40.0	-	(1)
Coronae Australis	CRA	17	5.0	4-5	(19)
Upper CrA	UCRA	3	10	-	(20) (Note I)
IC 2602 OC	IC2602	2	46.0	46^{+6}_{-5}	(21)
IC 2391 OC	IC2391	5	50.0	50^{+5}_{-5}	(22)
Cepheus association	CEPH	151	15	15^{+5}_{-5}	(23)
Cepheus moving group	CEPHCM	87	15	15^{+5}_{-5}	(23)
Vela Puppis	VLP	7732	50.0	10, 20, 50	(24)
	VLP1	182	45.0	45^{+5}_{-5}	(24)
	VLP2	1836	45.0	45^{+5}_{-5}	(24)
	VLP3	821	35.0	35^{+10}_{-5}	(24)
	VLP4	3006	35.0	35^{+10}_{-5}	(24)
	VLP5	414	25.0	25^{+10}_{-5}	(24)
	VLP6	514	20.0	20^{+5}_{-5}	(24)
	VLP7	959	10.0	10^{+5}_{-3}	(24)
Vulpecula	VOLP	228	3	3^{+1}_{-1}	(25) (Note II)
Orion Molecular Cloud	OMC	1	15	10,12-15,21	(26)
Group X	GROUPX	218	300	300^{+60}_{-60}	(27)

(1) Torres et al. (2008)[b]; (2) Bell et al. (2015)[c]; (3) Zuckerman et al. (2006)[d]; (4) Ujjwal et al. (2020)[a]; (5) Gagné et al. (2018c)[a]; (6) Silaj & Landstreet (2014)[a]; (7) Murphy et al. (2013)[a]; (8) Luhman & Steeghs (2004)[a]; (9) Gossage et al. (2018)[e]; (10) Martín et al. (2018)[f]; (11) Pecaut & Mamajek (2016)[g]; (12) Murphy & Lawson (2015)[h]; (13) Platais et al. (1998)[a]; (14) Dahm (2015)[f]; (15) Gagné et al. (2020)[i]; (16) Kenyon & Hartmann (1995)[a]; (17) Jones et al. (2015)[a]; (18) Pöhnl & Paunzen (2010)[a], (19) Gennaro et al. (2012)[j]; (20) Gagné et al. (2018a); (21) Dobbie et al. (2010)[h]; (22) Barrado y Navascués et al. (2004)[h]; (23) Klutsch et al. (2020)[b,a]; (24) Cantat-Gaudin et al. (2019)[a]; (25) Billot et al. (2010b); (26) Zari et al. (2019)[a]; (27) Messina et al. (2021)[m].

[a] isochrone fitting; [b] Li I 6707 ÅEW and color-magnitude diagram; [c] semi-empirical isochrone fitting; [d] Li I 6707 ÅEW and activity indicators ; [e] isochrone fitting taking into account rotation of the stars ; [f] Lithium Depletion Boundary (LDB) technique and evolutionary models by Baraffe et al. (2015) ; [g] isochrone fit. Its a median age derived considering the B-type main-sequence turn-off, the F-type pre-MS turn-on and the pre-MS G-type stars ; [h] Lithium Depletion Boundary (LDB) technique ; [i] empirical comparison of CMD sequence with other nearby young associations ; [j] Bayesian approach using the composite age-probability distribution ; [k] Li I 6707 ÅEW and gyrochronology ; [l] spectroscopy, estimation of the physical parameters using the Kurucz (1993) model atmospheres and isochrone fitting; [m] gyrochronology; Note I: This population likely constitutes of stars that formed along a filament between CRA and Sco-Cen 10 Myr ago.; Note II: Based on the age of NGC 6823 cluster. The 856 YSO candidates in Vul OB1, 239 are likely protostars with infalling envelops(class 0/I), 464 are disk-bearing stars (class II),and 153 are class III objects with very little circumstellar material.

catalogue based on the work of Montalto et al. (2021a) and calculated an average value of reddening and extinction for each association as presented in Table 2.2. The ages used for the isochrone fitting are reported in Table 2.1 with the corresponding references . In case there was no error provided by the authors for the estimation of the age we used a conservative error of 10% for homogeneity reasons. Regarding the metallicities of the young association and moving groups in our input list we fitted isochrones with [Fe/H]=0.0 ± 0.1 since on average their metallicities are similar to that of the Sun. We took into consideration this uncertainty on the metallicity to the final errors of the stellar parameters of the stars computed from the isochrones. The CMD with the isochrone fitted for each of the 40 young associations and moving groups in our sample are presented in Appendix A (Figure A.1 to A.10).

After fitting an isochrone to the CMD of each association and moving group, we interpolated them in respect to the G magnitude of each star and extracted information about each star's mass, radius and effective temperature which we later used for the transit search (Section 3.2.1) and in some cases as priors for the modelling of the candidate exoplanets found around them (Figure 5.1).

2.3 Light curve extraction and correction of systematic errors

The light curves of the stars in our input catalogue were extracted from the Full-Frame Images (FFIs) of TESS, using the PATHOS pipeline developed and described in detail by Nardiello et al. (2019). In summary, for each FFI the positions and magnitudes of the stars in the input catalogue are transformed into the astrometric and photometric reference system of the single FFI. For each star and for each image, the routine considers all the neighbour stars within a radius of 20 TESS pixels in the Gaia DR2 catalogue and transforms their calibrated magnitudes into instrumental fluxes. Then using the local PSF, the transformed fluxes and positions, the software constructs a model of the neighbour stars and subtracts them from the image. On the neighbour-subtracted images, the target flux of each star in our input catalog is measured using aperture photometry with four aperture sizes of 1, 2, 3 and 4 pixel radius and PSF-fitting photometry.

Due to gaps between the CCD/Camera or sectors of TESS, it was not possible to extract the light curves for $\sim$ 6.45% of stars in our input list, which minimized our catalogue of stars in young associations and moving groups to 11 598 (Figure 2.1). Our targets are observed in Sectors 1 to 26, which correspond to the first two scientific years of TESS. In the first year, 10 593 association members in our input list were observed in the southern hemisphere. These represent the 91% of our targets and are monitored by

Table 2.2: Interstellar reddening and extinction values in Gaia G and G_{RP} used for the isochrone fitting

Abreviation	mean(E(B-V))	mean(A_G)	mean($A_{G_{RP}}$)
32OR	0.0028 ± 0.0006	0.0063 ± 0.0036	0.0053 ± 0.0026
ABDMG	0.0015 ± 0.0034	0.0027 ± 0.0062	0.0022 ± 0.0044
ARG	0.0051 ± 0.0021	0.0115 ± 0.0093	0.0091 ± 0.0069
BPMG	0.0023 ± 0.0010	0.0051 ± 0.0043	0.0043 ± 0.0032
CAR	0.0034 ± 0.0009	0.0075 ± 0.0040	0.0063 ± 0.0029
CARN	0.0006 ± 0.0005	0.0013 ± 0.0031	0.0011 ± 0.0020
CBER	0.0029 ± 0.0037	0.0075 ± 0.0082	0.0059 ± 0.0061
CEPH	0.0586 ± 0.0201	0.1402 ± 0.0576	0.1103 ± 0.0435
CEPHCM	0.0278 ± 0.0163	0.0657 ± 0.0364	0.0533 ± 0.0287
COL	0.0013 ± 0.0017	0.0032 ± 0.0062	0.0026 ± 0.0046
CRA	0.0365 ± 0.0066	0.0935 ± 0.0265	0.0752 ± 0.0202
EPSC	0.0202 ± 0.0165	0.0501 ± 0.0539	0.0410 ± 0.0394
ETAC	0.0035 ± 0.0160	0.0076 ± 0.0241	0.0064 ± 0.0204
HYA	0.0006 ± 0.0002	0.0014 ± 0.0032	0.0011 ± 0.0020
IC2391	0.0053 ± 0.0002	0.0140 ± 0.0038	0.0106 ± 0.0030
IC2602	0.0127 ± 0.0179	0.0000 ± 0.0000	0.0000 ± 0.0000
LCC	0.0131 ± 0.0005	0.0315 ± 0.0063	0.0253 ± 0.0039
MUTAU	0.0620 ± 0.0020	0.1370 ± 0.0081	0.1156 ± 0.0062
OCT	0.0039 ± 0.0016	0.0103 ± 0.0060	0.0080 ± 0.0041
OMC	0.0351 ± 0.0379	0.0801 ± 0.0780	0.0668 ± 0.0648
PL8	0.0051 ± 0.0009	0.0134 ± 0.0068	0.0104 ± 0.0053
PLE	0.0489 ± 0.0012	0.1462 ± 0.0096	0.1121 ± 0.0061
TAU	0.0907 ± 0.0090	0.2173 ± 0.0283	0.1744 ± 0.0217
THA	0.0015 ± 0.0018	0.0031 ± 0.0050	0.0026 ± 0.0037
TWA	0.0037 ± 0.0009	0.0080 ± 0.0039	0.0069 ± 0.0031
UCL	0.0195 ± 0.0027	0.0506 ± 0.0118	0.0391 ± 0.0084
UCRA	0.0155 ± 0.0006	0.0385 ± 0.0018	0.0307 ± 0.0011
UMA	0.0005 ± 0.0004	0.0013 ± 0.0029	0.0010 ± 0.0017
USCO	0.0808 ± 0.0117	0.1899 ± 0.0339	0.1568 ± 0.0257
VOLCAR	0.0045 ± 0.0002	0.0100 ± 0.0032	0.0083 ± 0.0022
VOLP	2.4618 ± 0.0615	2.4877 ± 0.1785	1.9670 ± 0.1362
XFOR	0.0009 ± 0.0002	0.0020 ± 0.0026	0.0017 ± 0.0013
VLP1	0.0544 ± 0.0025	0.1367 ± 0.0107	0.1078 ± 0.0072
VLP2	0.0409 ± 0.0037	0.0994 ± 0.0124	0.0795 ± 0.0088
VLP3	0.0528 ± 0.0028	0.1240 ± 0.0103	0.1009 ± 0.0071
VLP4	0.0529 ± 0.0027	0.1217 ± 0.0106	0.1002 ± 0.0078
VLP5	0.1160 ± 0.0033	0.2776 ± 0.0130	0.2227 ± 0.0091
VLP6	0.0480 ± 0.0039	0.1113 ± 0.0131	0.0905 ± 0.0095
VLP7	0.0451 ± 0.0018	0.1020 ± 0.0100	0.0846 ± 0.0071
GROUPX	0.0000 ± 0.0000	0.0000 ± 0.0000	0.0000 ± 0.0000

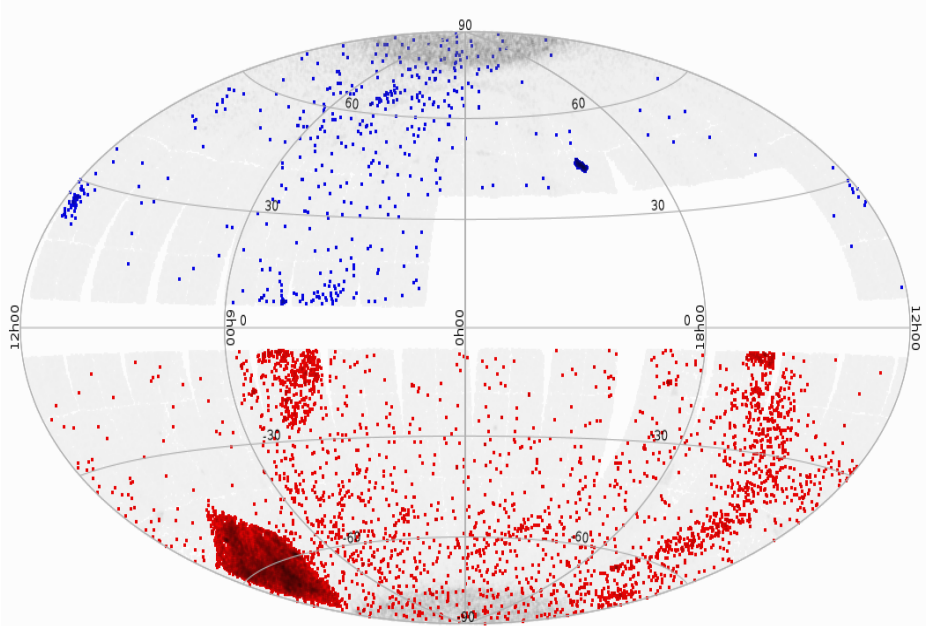

Figure 2.1: Aitoff projection in ecliptic coordinates of the fields observed by TESS during the first two years of mission and the observed young associations and moving groups. The grey points correspond to the targets observed in the 2-min candence mode of TESS in Sectors 1-26. The red and blue points are the members of the young associations and moving groups with extracted light curves from the FFIs in the southern and northern ecliptic hemisphere, respectively.

TESS from the 25^{th} of July 2018 until the 18^{th} of July 2019. On the other hand, in the second year the remaining 1 005 stars were observed in the northern hemisphere from 18^{th} of July 2019 to 4^{th} of July 2020.

TESS light curves are affected by systematic errors related to the spacecraft, detector, and environment. More specifically, light curves of stars located on the same detector and observed in the same sector of TESS share common systematic trends. This fact allows us to model these trends using co-treding basis vectors (CBVs) which can be then used to correct the light curves. The correction of TESS light curves is also implemented in the PATHOS pipeline and it is described in Nardiello et al. (2019) and Nardiello et al. (2020).

2.4 Photometric precision

To select the optimal photometry for each star in our catalogue we used the Point-to-Point Root Mean Square (P2P RMS) trends, which are not highly affected by intrinsic stellar variability. The P2P RMS is defined as the 68.27th percentile of the sorted residual from the median value of the

vector δf_i = f_i - f_{i+1}, where f is the value of flux at a given epoch i. We experimented with the fit of the P2P RMS versus T magnitude distributions by applying different polynomial functions with orders ranging from n=1 to n=7, with a goal to find which one produces a better fit. On average, the best fit was the one of a 6^{th} order polynomial for each photometric method (Figure 2.2).

Based on the star's T magnitude, we adopted the photometric method that provides the minimum mean P2P-RMS as the most suitable for each target. In principle, for bright stars with $T \leq 8$ mag we used the 4-pixel aperture photometry, whereas we found that 3-pixel and 2-pixel were more appropriate for stars with 8 $mag \leq T \leq 10.2$ mag and 10.2 $mag \leq T \leq 11.5$ mag, respectively. Moreover, sources with 11.5 $mag \leq T \leq 14$ mag were analyzed using the PSF-fitting photometry and fainter stars with $T \geq 14$ mag using the 1-pixel aperture photometry.

2.5 Variability elimination

Removing the presence of signals due to variability of the star from the light curves leads to an amplified potential transit signal that is easier to detect. For this reason, we applied a high-pass filter to the light curves, following a similar procedure with the one described by Montalto et al. (2020). Each light curve was interpolated using a cubic smoothing spline defined on N number of knots. We decided to use three different grid of knots:(i) one knot every 4-hours, (ii) one knot every 8-hours and (iii) one knot every 13-hours. Using this technique, not only we can produce a finer model and exclude short and long period variables, but also ensure that transits with a duration longer than 4 or 8 hours are not flattened out from the light curves. Using the splined normalized light curve we identified possible outliers and temporarily excluded them from the light curve for this step. To accomplish that we used boundaries defined by the interquartile range (IQR) of each light curve. The IQR is the difference of the 75^{th} and the 25^{th} percentiles of the cumulative distribution of the flux measurements, which correspond to the third quartile (Q_3) and first quartile (Q_1), respectively (IQR=Q3-Q1). More specifically, any measurement of flux (f_i) that belongs to the regions defined as $f_i < Q_1 - 1.5 \times IQR$ or $f_i > Q_3 + 1.5 \times IQR$ is identified as an outlier (Figure 2.3). The smoothing spline is therefore re-calculated from the original light curve, excluding the identified outliers. Based on the second smoothing spline model we predicted the photometric values in each photometric method, using the `predict()`[4] function in R. The final flattened light curve is computed as the ratio of the original and the predicted light curve (Figure 2.4).

[4]Functions to Accompany J. Fox and S. Weisberg, An R Companion to Applied Regression, Third Edition, Sage, 2019.

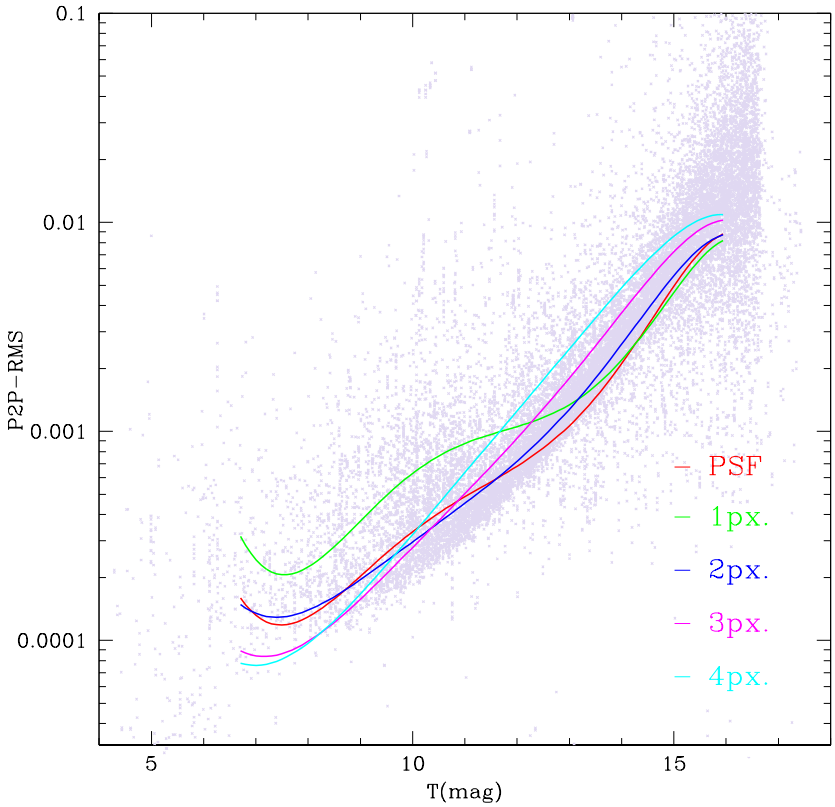

Figure 2.2: Mean trends of the P2P-RMS as a function of the TESS magnitude (T) for each photometric method. PSF: red line; 1-pixel: green line; 2-pixel: blue line; 3-pixel: magenta line; 4-pixel: cyan line. As an example, we have plotted the P2P-RMS distribution obtained with PSF-fitting photometry (grey crosses).

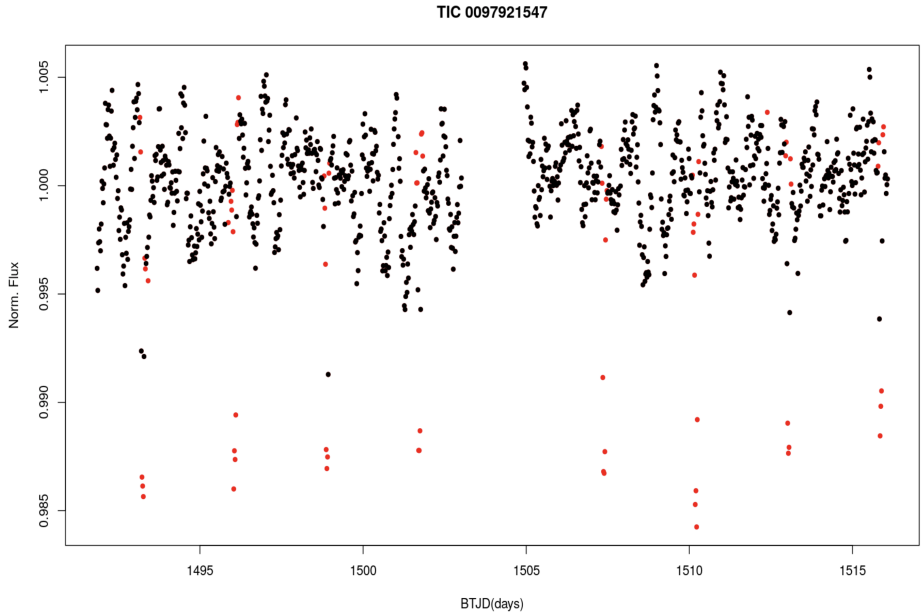

Figure 2.3: Normalized light curve of TIC 0097921547 corrected for systematic effects. The red points represent the outliers identified in this light curve using the boundaries defined by the interquartile range (IQR).

Except of the correction of systematic effects and the exclusion of the star variability, before searching for transits we performed an additional analysis. We excluded all the defective photometric points with a value of flux f=0 and DQUALITY$\neq$ 0, following the information in the TESS Science Data Products Description Document (Twicken et al. 2020)[5]. Furthermore, photometric data related with a local sky background greater than $4\sigma_{sky}$[6] of the sky median value in each sector of TESS were also removed. For each star, we determined the number of observed sectors and combined the corresponding light curves to obtain a final light curve that contained all the available photometric measurements by TESS.

[5] https://heasarc.gsfc.nasa.gov/docs/tess/documentation.html

[6] σ_{sky} defined as the standard deviation of the local sky background of the star's light curve in each sector

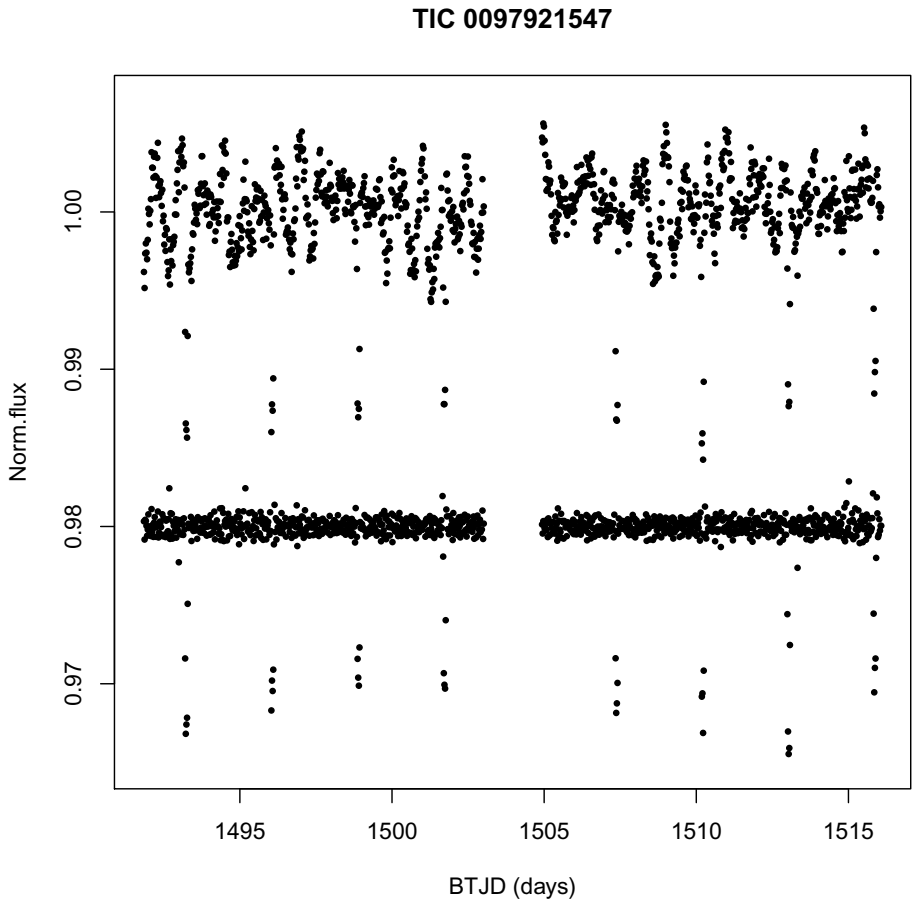

Figure 2.4: Top: Normalized light curve of TIC 0097921547 corrected for systematic effects. Bottom: the final light curve of the star normalized by a cubic smoothing spline fitted only using out-of-transit data. The flattened light curve has been shifted vertically by an arbitrary amount for clarity reasons.

Chapter 3

Searching for candidate exoplanets

3.1 Planet Search

To detect periodic dimmings of planetary origin we used the Box-Least-Squares algorithm (BLS) of Kovács et al. (2002). This is a tool widely used for exoplanet transit searches in large photometric data sets. The algorithm scans the star's light curve and searches for periodic box-shaped dimmings. This method makes the search in large data sets fairly quick in comparison to other algorithms and allows reliable detections of extrasolar planets. The algorithm works by searching through frequencies, then phases the light curve for each frequency and finally fits a model in the phased light curve with three parameters: duration of the transit , depth of the transit (δ) and reference time or central time (T_0, Figure 3.1).

The BLS algorithm produces a periodogram which helps to identify the period of a transiting body in the tested light curve. It represents the power spectrum as a function of the scanned periods and the dominant peak corresponds to the period of the transit (Figure 3.2).

Two important statistics calculated by the BLS algorithm are the effective Signal to noise ratio (S/N) and the Signal Detection Efficiency (SDE). They have been defined by Kovács et al. (2002) and are calculated as in Eq.3.1 and Eq.3.2, respectively. The S/N is defined as:

$$S/N = \frac{\delta}{\sigma_{LC}} \left(\frac{1}{N_{in}} + \frac{1}{N_{out}} \right)^{-\frac{1}{2}} , \tag{3.1}$$

where δ is calculated as the difference of the average in-transit and the out-of-transit measurements, σ_{LC} is the photometric precision of the light curve estimated as the standard deviation of the out-of-transit measurements and N_{in}, N_{out} are the number of in and out of transit measurements, respectively. The SDE is defined as:

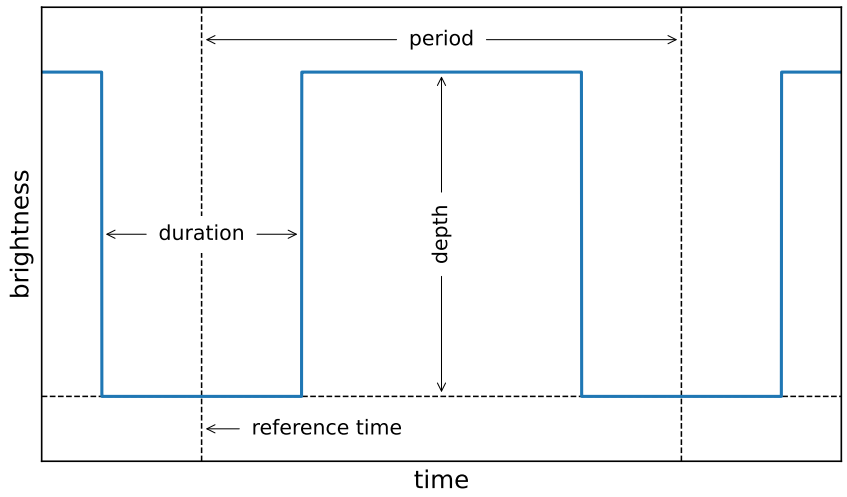

Figure 3.1: Transit modelling using the BLS algorithm. The BLS searches for box-shaped transits and fits a model using four parameters: period, duration, depth and reference time which corresponds to the mid-transit time.
©https://docs.astropy.org/en/stable/timeseries/bls.html#id5

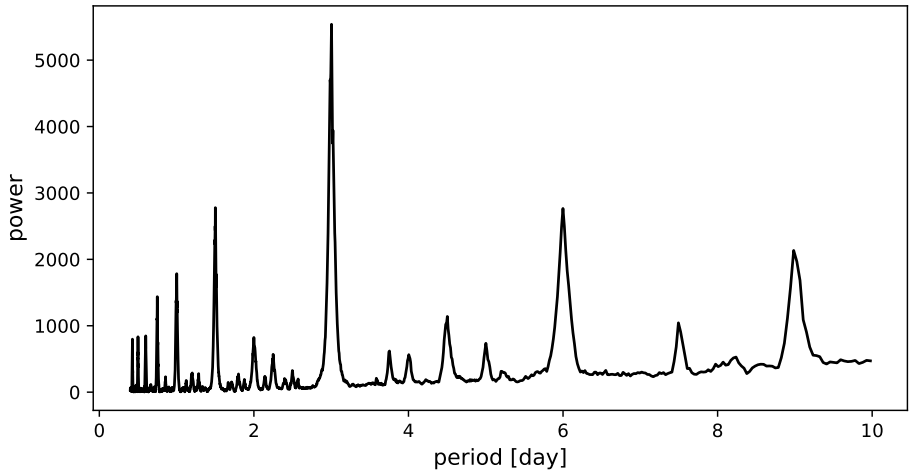

Figure 3.2: Example of a BLS periodogram for a given light curve. Its highest peak is at a period of 3 days and this is also the period of the transiting body.
©https://docs.astropy.org/en/stable/timeseries/bls.html#id5

$$SDE = \frac{SR_{peak} - <SR>}{sd(SR)} \ , \tag{3.2}$$

where SR_{peak} is the power of the BLS peak, $<SR>$ is the average power and sd(SR) is the standard deviation of the BLS power spectrum.

Using the BLS algorithm we searched for signals starting from $P_{min} = 0.25$ days to the total observed time-span of each light curve (ΔT). The period step ΔP at any period P was determined by imposing $N_{tr}\Delta P = \epsilon$ with ϵ=5 min and $N_{tr}=\Delta T/P$ expected number of transits of period P, to ensure that the first and the last transit in the observable window where folded with a precision of 5 min, for any tested period P. Considering a circular orbit and a 90° planetary orbital inclination, the maximum transit duration (τ_{max}) was computed at period P as $\tau_{max} \simeq \frac{P}{\pi} \arcsin \frac{R_\star}{a}$, where a is the orbital semi-major axis and $R_\star$ the radius of the host star. Based on this, we defined the minimum and maximum fractional transit durations equal to $q_{min} = 0.1\frac{\tau_{max}}{p}$ and $q_{max} = 1.1\frac{\tau_{max}}{p}$, respectively. Moreover, each folded light curve was divided in a number of bins (nbins) for each trial period, where $nbins = \frac{2}{q_{min}}$.

3.2 Classification

To identify signals of plausible exoplanet origin we performed a series of transit simulations of various planets (with radii between 1 Earth radius and 2.5 Jupiter radii) and used a logistic regression model to classify the recovered signals by estimating an optimal cut-off probability.

Logistic regression is a supervised classification algorithm and is used when the dependent variable is binary, which means that can take 2 distinct values (i.e 0/1 or pass/fail etc). More specifically, the logistic regression or sigmoid function is an S-shaped curve (Figure 3.3 and 3.4) that gets as an input any real number and transforms it into a value between 0 and 1. In our case, we used it because we wanted to classify a given star into 2 possible categories: i) a host of a possible candidate exoplanet and ii) not a host star. The logistic regression transforms its output using the sigmoid function to return a probability value (P_r). Using the effective Signal to Noise ratio (S/N) and the Signal Detection efficiency (SDE) of a primary transit we can calculate the corresponding detection probability and then classify it into a host of possible candidate exoplanet, if its detection probability is higher than the cut-off point, or into a "not a host star" if it is lower (more details on Section 3.2.3).

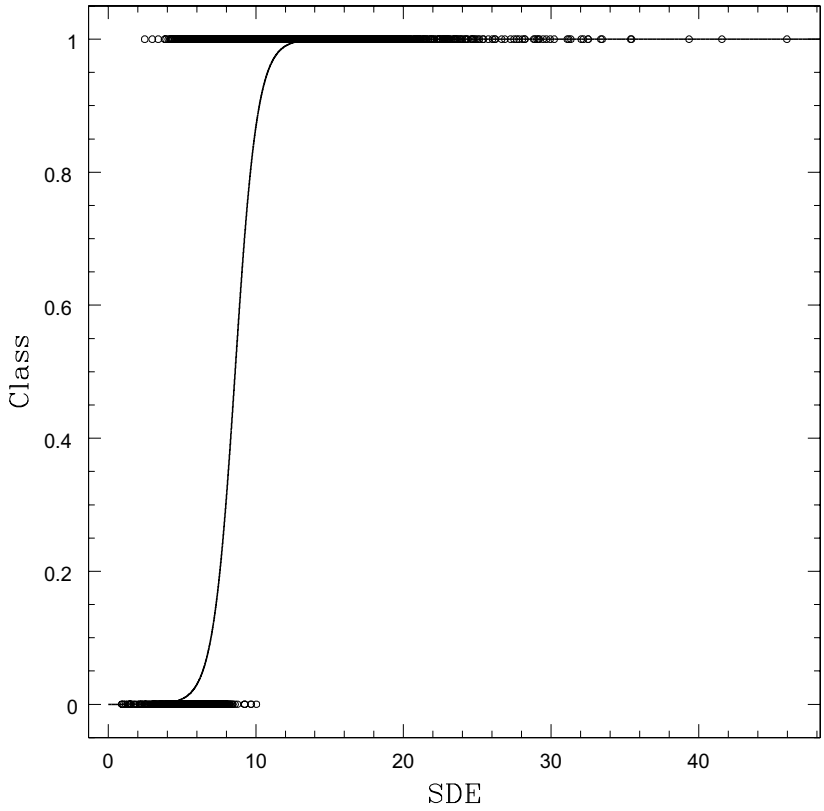

Figure 3.3: Example plot of logistic regression or sigmoid function, S-shaped curve, with one independent variable (i.e SDE), $P_r = \frac{1}{1+e^{-(x_0+x_1(SDE))}}$. In this case, the Signal Detection Efficiency (SDE) estimations are mapped into values between 0 and 1, forming two distinct classes. The class 1 represents the the "host stars" and class 0 the "not host stars".

The detection probability is given by:

$$P_r = \frac{1}{1 + e^{-(x_0+x_1(S/N)+x_2(SDE))}}, \tag{3.3}$$

where x_0, x_1 and x_2 are the coefficients of the logistic regression model.

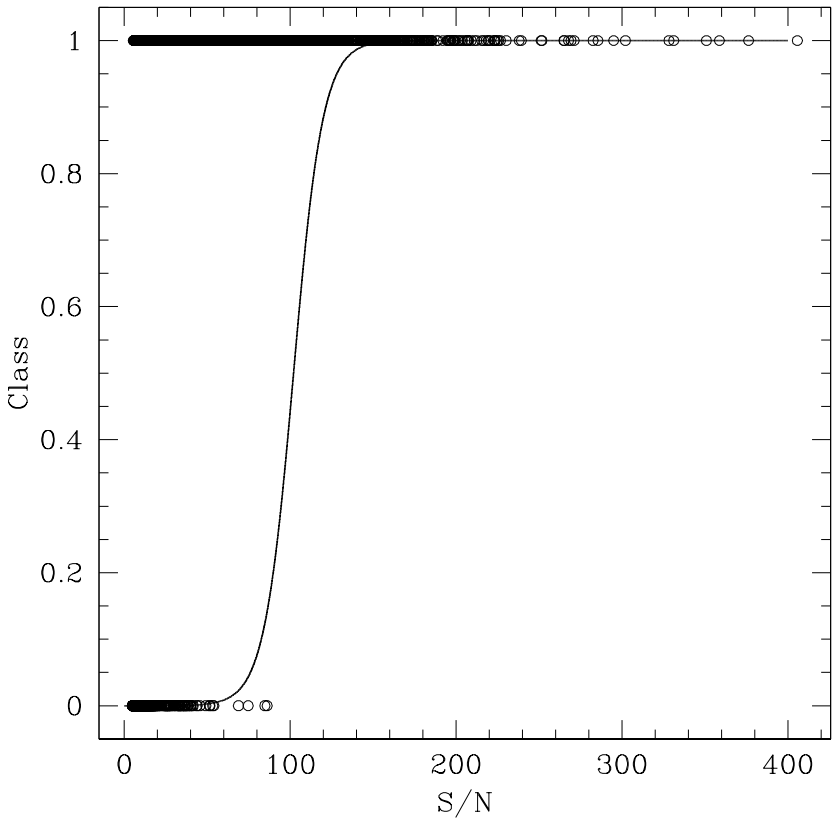

Figure 3.4: Example plot of logistic regression or sigmoid function with one independent variable (i.e S/N), $P_r = \frac{1}{1+e^{-(x_0+x_1(S/N))}}$. Same as in Figure 3.3 but for the effective signal to noise ratio (S/N).

3.2.1 Planet Simulations

To train the logistic regression model to identify plausible transiting planets, we used different sets of simulations. For this purpose, we created two samples of light curves: i) the first one contained light curves of constant stars and ii) the second light curves with artificially injected transits.

For the constant sample, we performed a quick search for variables in our input catalog of 11 598 stars using the Generalized Lomb-Scargle (GLS) algorithm (Zechmeister & Kürster, 2009). We selected stars with $S/N<120$ and we visually inspected their light curves to exclude any remaining variables or problematic cases. After the inspection, we created a sample of 1160 constant light curves from the initial catalog in which no signals where found. Moreover, we ensured that this selected sample of stars replicated the global properties, like distribution of sectors and T magnitude, of our input catalog of stars in young associations/moving groups. In order to increase this sample we bootstrapped it to obtain a final constant sample of 6780 light curves.

The injected sample was created by injecting to the constant flattened light curves transits in two period ranges. In the first set, we injected transits with periods uniformly distributed betweeen 0.2 to 5 days and in the second between 5 to 365 days; which is the maximum time span of our observations. Furthermore, in each set of periods we injected Mandel-Agol transit models (Mandel & Agol, 2002) of planets with radii uniformly distributed between 1 Earth radius and 2.5 Jupiter radii. By injecting uniformly distributed periods and planet radii we made sure that every possible scenario has an equal likelihood to happen and no biases are introduced to our analysis.

In order to compute the maximum transit duration (τ_{max}) for the BLS search we need to define the stellar parameters of the host star as mentioned in Section 3.1. We estimated the mass and radius of the stars in our sample by fitting an isochrone to the color-magnitude diagram (CMD) of each association/moving group and interpolating the results from the isochrone for each parameter (i.e M, R etc.) with respect to the G magnitude of the star as described in Section 2.2.

Then, we searched for transits (both in the constant and injected sample) using the BLS algorithm and registered the S/N and SDE that it restituted for each light curve. We also considered the period corresponding to the highest peak in the BLS periodogram as the period of the transit. For the injected sample, we calculated the recovered period accuracy in percent as $\frac{|(P_{inj}-P_{rec})|}{P_{inj}} \cdot 100\%$, where P_{inj} and P_{rec} are the injected and recovered transit period, respectively. Light curves with a recovered period accuracy less than 1% were selected. The final constant and injected samples used for the simulations of different kind of planets have 2200-2600 light curves each, depending on the photometry.

As mentioned before, we treated this problem as a binary classification

problem and we attributed the positive class (1) to the injected/simulated planets and the negative class (0) to the constant stars. Then 80% of the data were used for training the logistic regression model and the remaining 20% for testing.

3.2.2 Training

To train the logistic regression model we use the `Caret` package[1] (`train` function) in R, using a 10-fold cross validation (CV) method repeated 5 times. This method first randomly splits the training data into 10 subsets, reserves one of them and trains the model using the remaining 9 sets. Then, it tests the model on the reserved set and records a prediction error. The 10-fold CV is finished when all of the 10 subsets have been used as the test set. A cross-validation error is computed by averaging the 10 recorded errors, which corresponds to the performance metric of the model. We repeated this procedure 5 times and the final model error is computed as the mean error of the 5 repetitions. The resulted final logistic regression models and errors for short ($P = 0.2 - 5$ days) and longer ($P = 5 - 365$ days) periods for each photometric method are reported in Table 3.1 and 3.2, respectively. See also Figures 3.5 and 3.6.

Table 3.1: Best fit parameters of the logistic regression model for short period candidates, $P = 0.2 - 5$ days.

Photometry	x0	x1	x2
PSF	-11.456 ±0.462	0.102 ±0.009	1.335 ±0.065
1-px.	-11.543 ±0.468	0.113 ±0.009	1.342 ±0.065
2-px.	-11.162 ±0.437	0.083 ±0.007	1.319 ±0.062
3-px.	-11.412 ±0.444	0.076 ±0.007	1.363 ±0.064
4-px.	-11.270 ±0.425	1.345 ±0.061	0.078 ±0.006

3.2.3 Performance of the Logistic Regression

We tested the logistic regression model described in Section 3.2.2 using the 20% of light curves we reserved for testing and that were not included in the training procedure of the model.

In order to measure the diagnostic ability of the model and define the optimal cut-off probability we performed the Receiving Operating Characteristics (ROC) analysis. The ROC curve is a mapping of the true positive rate (sensitivity) versus the false positive rate (1 – specificity) for all possible

[1] `https://github.com/topepo/caret/`

Table 3.2: Best fit parameters of the logistic regression model for long period candidates, $P = 5 - 365$ days

Photometry	x0	x1	x2
PSF	-7.964 ±0.324	0.211 ±0.008	0.790 ±0.048
1-px.	-8.432 ±0.343	0.212 ±0.008	0.867 ±0.051
2-px.	-7.799 ±0.312	0.177 ±0.007	0.821 ±0.047
3-px.	-7.474 ±0.287	0.158 ±0.006	0.817 ±0.043
4-px.	-7.434 ±0.276	0.150 ±0.006	0.834 ±0.041

cut-off values (Figure 3.5, 3.6). The Area Under the Receiving Operating Characteristics curve (AUROC) is a measure of the separability between the 2 cases (host star/ not a host star) with acceptable values ranging from 0.5 (no diagnostic ability) to 1 (perfect diagnostic ability). Consequently, higher AUROC values indicate better test performance. The identification of the cut-off point value of the detection probability requires a simultaneous assessment of sensitivity and specificity. To specify the optimal cut-off point we used the Youden index (Eq.3.4).

$$Youden = Sensitivity + Specificity - 1 = TPR - FPR \tag{3.4}$$

More specifically, this index corresponds to the point where the Youden function, which is the difference between True Positive Rate (TPR) and False Positive Rate (FPR), is maximized. The colored points in the ROC curves of Figures 3.5, 3.6 correspond to the TPR and FPR of our adopted cut-off values in each photometry. The highest TPR for transit periods between 0.2 and 5 days is achieved in PSF photometry (red curve) with a value of 94.88%, while the lowest in 3-pixel aperture photometry (magenta curve) with a corresponding value of 91.29% (Table 3.3). For longer transit periods ranging from 5 to 365 days (Table 3.4), 1-pixel aperture photometry is characterized by the higher TPR (87.53%) and 3-pixel photometry by the lower (76.31%).

The TPR represents the detection efficiency of our technique in discovering exoplanet candidates, ranging from Earth-size to Giant-size planets, for each photometric method. In practice, a detection efficiency of 98.93 % in the 1-pixel aperture photometry for the short transit periods (0.2 days $<$ P $<$ 5 days) means that in a sample of 100 exoplanets we are able to detect almost 98 of them and miss the remaining 2 planets. The AUROC, cut-off value of the detection probability, FPR and TPR values corresponding to the best model of each aperture photometry are reported in Table 3.3 and Table 3.4 for the short and longer transit periods, respectively. Based

Table 3.3: Performance measures of the logistic regression for signals with periods from 0.2 to 5 days, for each photometric method. FPR=False Positive Rate; TPR=True Positive Rate, AUROC=Area Under the ROC curve.

Photometry	Cut-off (%)	FPR (%)	TPR (%)	AUROC (%)
PSF	40.0	3.32	94.88	98.67
1-pixel	55.0	1.50	93.10	98.93
2-pixel	57.0	1.92	91.43	97.73
3-pixel	45.0	1.45	91.29	97.82
4-pixel	38.0	3.27	93.06	97.32

Table 3.4: Performance measures of the logistic regression signals with periods from 5 to 365 days, for each photometric method. FPR=False Positive Rate; TPR=True Positive Rate, AUROC=Area Under the ROC curve.

Photometry	Cut-off (%)	FPR (%)	TPR (%)	AUROC (%)
PSF	38.0	11.16	84.46	93.02
1-pixel	47.0	7.35	87.53	95.88
2-pixel	40.0	9.89	87.15	94.03
3-pixel	55.0	5.52	76.31	92.23
4-pixel	49.0	9.81	76.89	91.55

on these performance measures of the logistic regression, signals are classified as transits of candidate exoplanets when their predicted probability is higher than the cut-off value in each photometry, or not as transits if their predicted probability is lower than the cut-off value. We applied the aforementioned criteria in our sample of 11 598 stars in young associations and moving groups for each set of flattened light curves, characterized by a different grid of knots as mentioned in Section 2.5. For the first set (1 knot/4 hrs) we classified as candidate exoplanets 830 stars, for the second (1 knot/8 hrs) 829, similarly with the first one, while for the third set (1 knot/13 hrs) we found 699 stars. Some stars have been classified as candidates in more than one set of knots or even in all three of them. In these cases, we flattened the light curve of the candidate exoplanet using all the available set of knots that it was recovered and selected the number of knots that produced the best results. We then used the selected light curve, with the best flattening, to apply the validation tests described in Section 3.3. Finally, we visually inspected the light curves of the stars classified as hosts of candidate planets to exclude false positives due to the presence of artifacts and we applied the validation tests mentioned in Section 3.3 to account for sources likes variables or eclipsing binaries that can show similar behavior

in the light curves as transiting exoplanets.

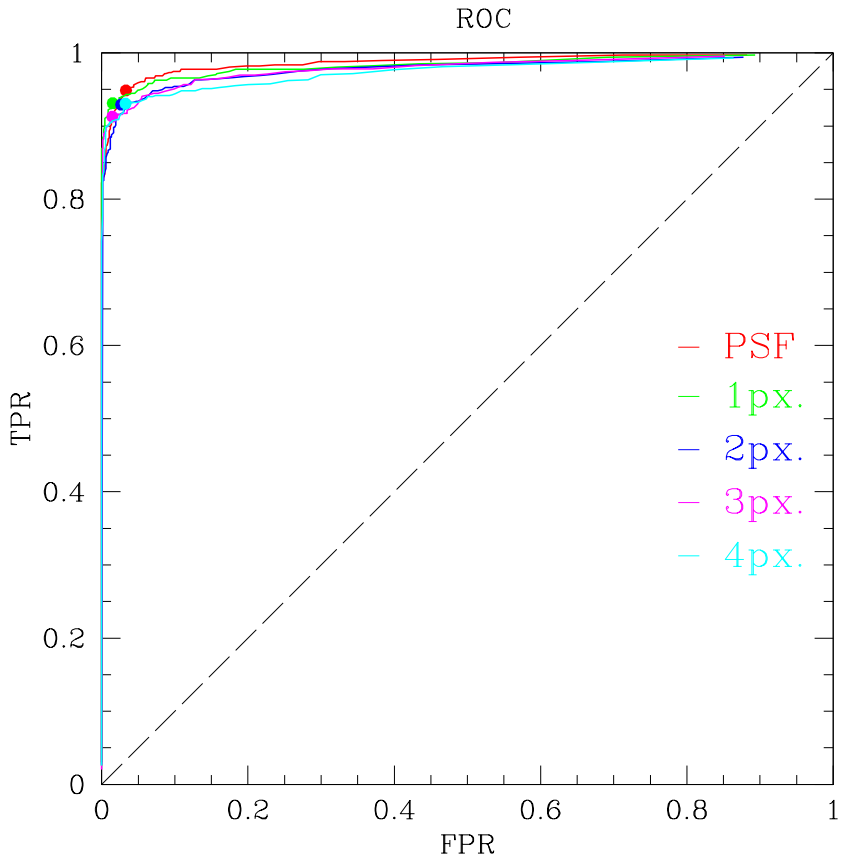

Figure 3.5: ROC curves (solid colored lines) for the best model (Table 3.1) and for candidate exoplanets with periods ranging from 0.2 to 5 days, for each photometric aperture. The colored points indicate the False Positive Rate (FPR) and True Positive Rate (TPR) corresponding to the adopted detection cut-off points (Table 3.3), while the dashed line represents the perfectly random classifier. PSF-fitting photometry: red; 1-pixel aperture (1 px.): green; 2-pixel aperture (2 px.): blue; 3-pixel aperture (3 px.): magenta; 4-pixel aperture (4 px.): cyan.

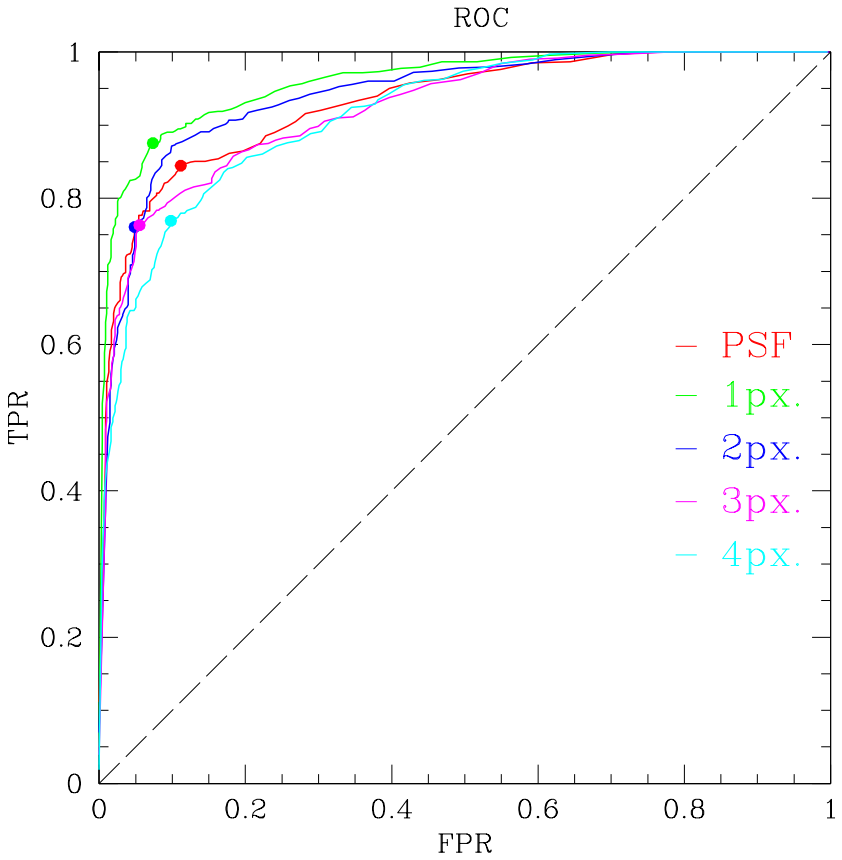

Figure 3.6: Same as Figure 3.5 but for candidates with long periods from 5 to 365 days using the logistic regression models of Table 3.2. The colored points indicate the False Positive Rate (FPR) and True Positive Rate (TPR) corresponding to the adopted detection cut-off points (Table 3.4), while the dashed line represents the perfectly random classifier. PSF-fitting photometry: red; 1-pixel aperture (1 px.): green; 2-pixel aperture (2 px.): blue; 3-pixel aperture (3 px.): magenta; 4-pixel aperture (4 px.): cyan.

3.3 Validation Tests

To validate the candidate exoplanets found by the classification in our sample we performed four different tests. First, in order to identify possible eclipsing binaries in our candidates list we analyzed the odd/even transits of each star and examined possible variations of their depths. In the second test, we investigated if a secondary eclipse is present in the candidate's light curve, which is usually an indication that the candidate is a false positive. As a third test, we ensured that the transit depth does not show variations between light curves obtained with different photometric methods. Last but not least, we calculated the in-transit and out-of-transit centroid difference to verify that the transits are occurred in the target star and not in a close by neighbor.

3.3.1 Odd/Even transits

To perform the first validation test, we categorized the transits of each candidate into odd/even, calculated the difference of their depths ($\Delta\delta_{\rm tr} = |\delta_{odd} - \delta_{even}|$) and the error associated to each depth ($e_{odd/even}$), as the standard deviation of the out-of-transit points (sd(out)) divided by the square root of the sum of the in-transit points (N_{in}) ($e_{odd/even} = sd(out)/\sqrt{N_{in}}$).

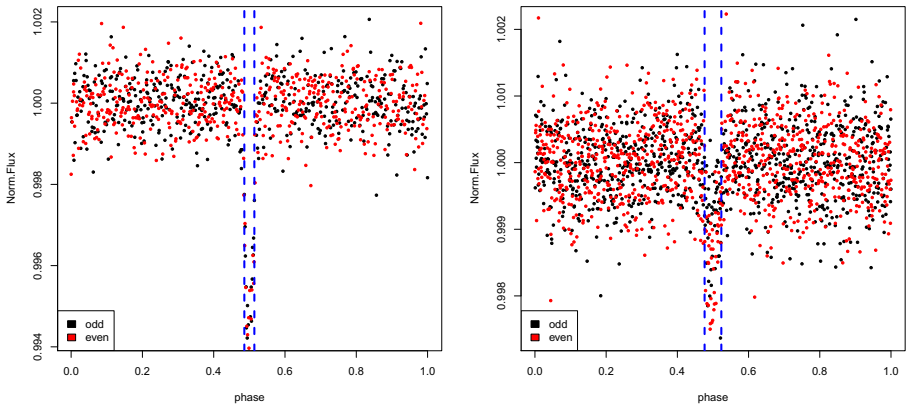

(a) (b)

Figure 3.7: Application of the first validation test of odd/even transits in two light curves. (a) TIC 0098161270 has passed the odd/even test; (b) TIC 0075817981 failed the test because $\Delta\delta_{\rm tr} > 3 \times \sigma$. Details on the application of the test can be found on the main text. In these plots, for representation reasons the primary transit is placed at phase 0.5 and its duration (as found by the BLS algorithm) is defined by the blue dashed line, the odd transits are plotted with black color whereas the even transits with red.

A candidate is excluded from our list if: $\Delta\delta_{\rm tr} > 3 \times \sigma$, where $\sigma = \sqrt{e_{odd}^2 + e_{even}^2}$. In Figure 3.7 the left panel shows a case where the odd and even transit depths are consistent ($\Delta\delta_{\rm tr} < 3 \times \sigma$) with each other and consequently this candidate passed the odd/even test. On the contrary, the light curve on the right panel shows different depths in the odd and even transits ($\Delta\delta_{\rm tr} > 3 \times \sigma$), so it failed the test and its discarded from our candidates list.

3.3.2 Secondary eclipse

For the second test, we identified possible secondary eclipses in the candidate's light curve, estimated the secondary depth and the respective error. We searched for secondary eclipses around phase 0.5, considering a circular orbit, and if the value of the secondary depth is consistent with zero within $3\times\sigma_{sec}$ then the candidate passed the second validation test. In this case, σ_{sec} is calculated as:

$$\sigma_{sec} = sd(out) \times \sqrt{\frac{1}{N_{in}} + \frac{1}{N_{out}}}, \tag{3.5}$$

where sd(out) is the standard deviation of the out-of-transit points, N_{in} and N_{out} the sum of the in-transit and out-of transit points, respectively.

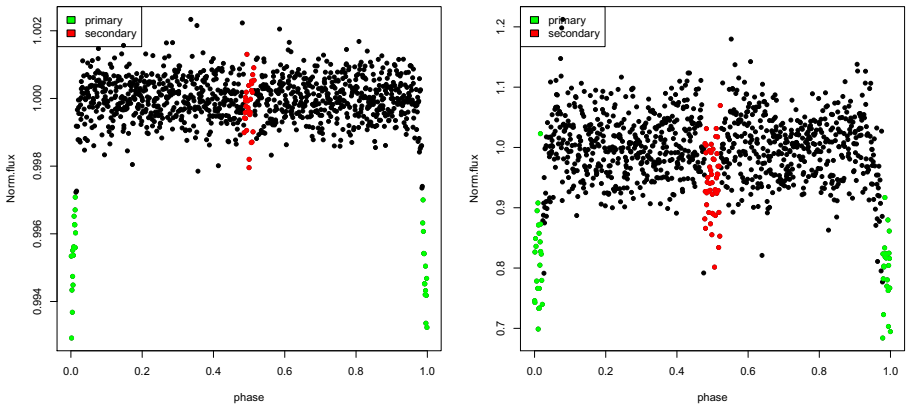

(a) (b)

Figure 3.8: Application of the second validation test in two light curves. Panel (a) shows the normalized phased light curve of TIC 0098161270, with no secondary eclipse ($\delta_{\rm tr,sec} < 3 \times \sigma_{sec}$), so this candidate succeeded this test. On the other hand, panel (b) shows the light curve of TIC 0111954404, for which a secondary eclipse is present ($\delta_{\rm tr,sec} > 3 \times \sigma_{sec}$) which means that this candidate is a false positive. In both panels, the primary transits (phase 0, 1) are plotted with green color and the secondary eclipses (phase 0.5) with red.

In Figure 3.8, the left panel shows a light curve with no secondary eclipse ($\delta_{\rm tr,sec} < 3 \times \sigma_{sec}$), so this candidate around TIC 0098161270 passed the second test. On the other hand, a secondary eclipse is present ($\delta_{\rm tr,sec} > 3 \times \sigma_{sec}$) in the light curve of the star (TIC 0111954404) in the right panel and consequently this candidate is a false positive.

3.3.3 Transit depth for different photometric methods

In the third validation test, we calculated the transit depth for each candidate in the light curve obtained using the optimal photometry based on the T magnitude of the host star (Section 2.4) and the next available bigger aperture. So, in the case of the 4-pixel aperture photometry and the PSF-fitting photometry the test was not performed. In the first case, there is not an available aperture bigger than 4-pixel to perform the comparison and for the PSF-fitting photometry the contamination by neighbor stars has been basically already taken into account during the extraction of the light curves.

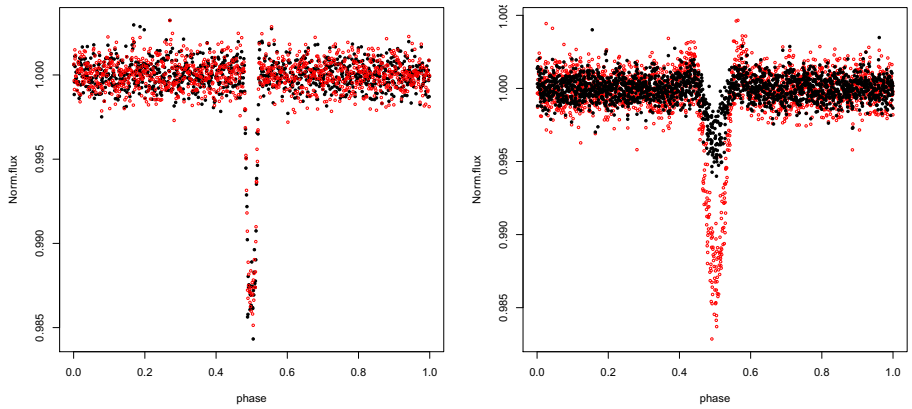

(a) (b)

Figure 3.9: Application of the third validation test in two light curves. Panel (a) shows a light curve of TIC 0097921547 that has passed the test since the transit depths in the compared photometries are consistent within $3\times\sigma$. This star had T ∼11 mag so the comparison is made between the 3-pixel aperture photometry (optimal) and 4-pixel. On the other hand, the transit depths in the light curve of TIC 0080808684 in the panel (b) are not consistent and the depth of the bigger aperture (red circles) is deeper than of the optimal photometry (black circles) for the star. The latter is identified as false positive and is excluded from our candidate list. The black filled circles represent the optimal photometry for the given star and the red open ones the next bigger aperture photometry.

The test is applied as described below. For instance, the star with TIC 0097921547 has a $TESS$ magnitude $T \sim 11$ mag, so we compared the depth of the transits obtained in 3-pixel aperture photometry, which is the optimal

photometry for this star, and 4-pixel aperture photometry (Fiqure 3.9(a)). If the transit depths in the compared photometries were consistent within $3 \times \sigma$ (σ calculated using Eq.3.5) and the transit of the bigger aperture was not deeper, then the star succeeded the third test.

3.3.4 Centroid motion

In the final validation test, we calculated the in-transit and out-of-transit centroid difference to investigate if the transit events are occurring on our target or on a close by star following the procedure described in Nardiello et al. (2020). For each candidate, we plotted a finding chart (100×100 arcsec^2) using the GAIA DR2 catalogue and placed the target star in the center (Figure 3.10). We calculated and plotted the centroid of each transit (colored crosses) and the corresponding mean and standard deviation value for each sector of TESS the star is observed. The finding charts of each candidate were visually inspected to discard cases were the mean centroids are not positioned in our targets but in neighbor stars, which means that the transits occuring in neighbor stars and not in our tested candidate (Figure 3.11). We would like to comment that the centroid test usually can not provide useful and accurate information about the transits of the candidates if the host star is faint. In these cases, if the candidate succeeded the first three validation tests and the mean centroids show big errors, we kept the candidate in our list and progress it for additional analysis (see Chapter 4).

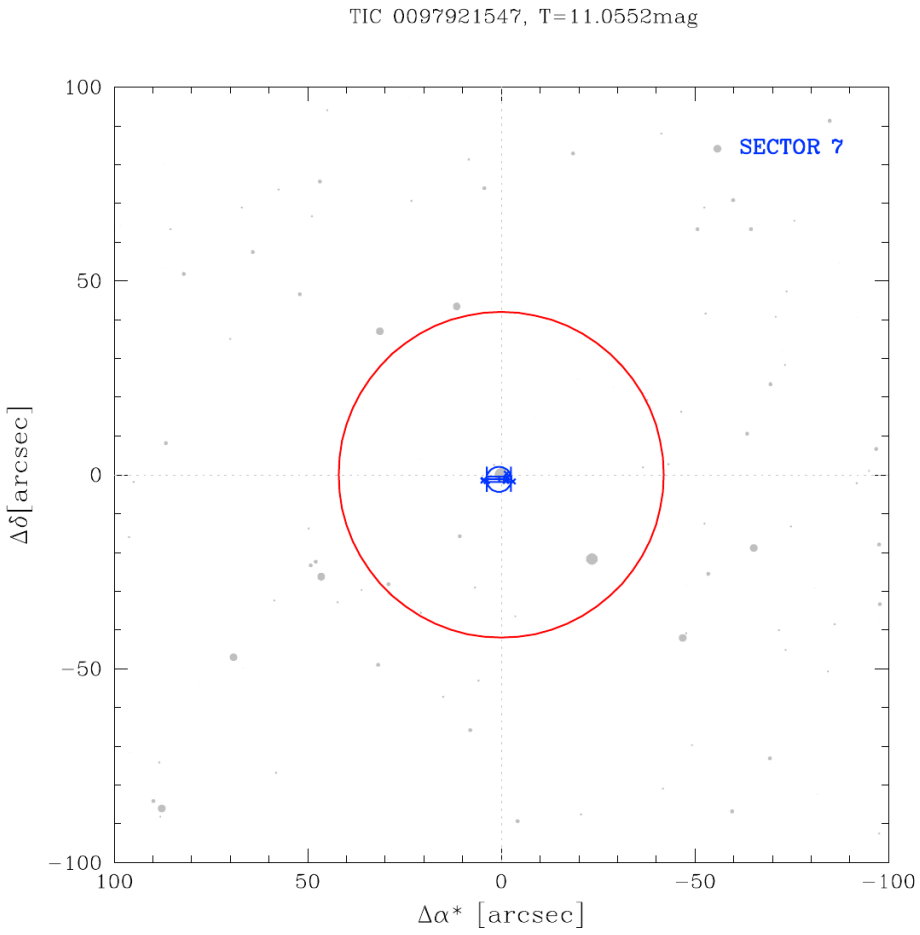

Figure 3.10: Finding chart for the candidate TIC 0097921547 using the Gaia DR2 catalogue. The crosses are the centroids associated to each transit, the blue circle is the mean centroid and its standard deviation for Sector 7. The red circle is an approximation of the photometric aperture used for the extraction of the candidates' light curve. In this case the transits are occurring in the star we are interested, so we kept this candidate in our list.

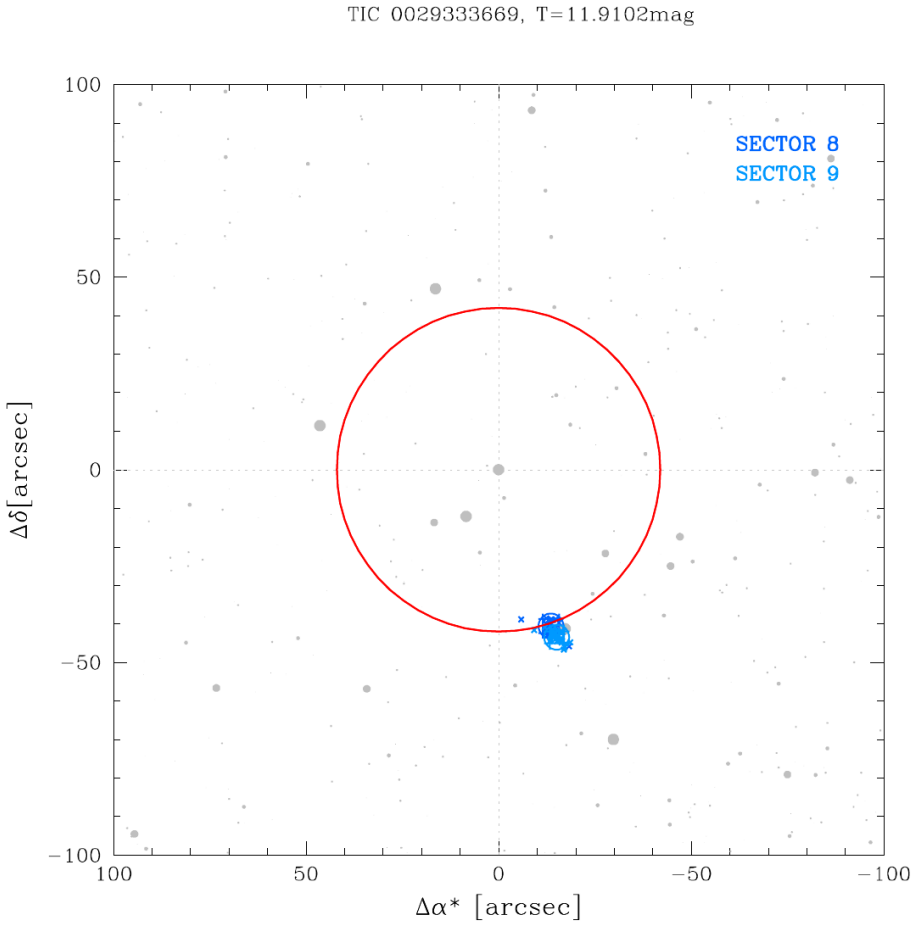

Figure 3.11: Similar with Figure 3.10 but for the star TIC 0029333669. In this case its evident by the position of the mean centroids that the transits are happening in a near by star and not in the target star which is placed in the center of the finding chart. Consequently, we excluded this candidate from our list.

Chapter 4

Candidate exoplanets

After the application of the validation tests described in Section 3.3, 27 exoplanet candidates survived our selection. These candidates are orbiting stars belonging in young associations and moving groups with ages ranging from 10 to 50 Myr. We have found candidate planets in 11 different associations and moving groups: (i) Upper Scorpius association; (ii) Tucana Horologium association; (iii) AB Doradus moving group; (iv) Octans association; (v) Vela Puppis - Population I; (vi) Vela Puppis - Population II; (vii) Vela Puppis - Population III; (viii) Vela Puppis - Population IV; (ix) Vela Puppis - Population V; (x) Vela Puppis - Population VI; (xi) Vela Puppis - Population VII. Information about the candidates detected in each association, their validation tests and light curves are presented in the next sections. We also report the dilution factor (*dil*) associated with each host star which is calculated by taking into consideration all the neighbor stars in the GAIA DR2 catalogue that fall inside the same pixel of the target. Moreover, we have transformed the Gaia magnitudes of the stars into TESS magnitudes using Eq.(2.1) by Stassun et al. (2019a).

4.1 Upper Scorpius association

The Upper Scorpius association (USCO) is observed by TESS in the Southern ecliptic hemisphere and has an age of 10^{+3}_{-3} Myr Pecaut & Mamajek (2016). We found one candidate exoplanet in USCO around the star TIC 0023846678.

4.1.1 TIC 0023846678

TIC 0023846678 is observed in Sector 12 of TESS and has a TESS magnitute $T = 13$ mag. The BLS search returned a period of $P \sim 0.453$ days for the candidate exoplanet. Also 43 transits are observed as seen in Figure 4.1 and the dilution factor (*dil*) associated with the star is zero. The host star is

isolated and the transits mean centroid of Sector 12 are concentrated on it as presented in Figure 4.2.

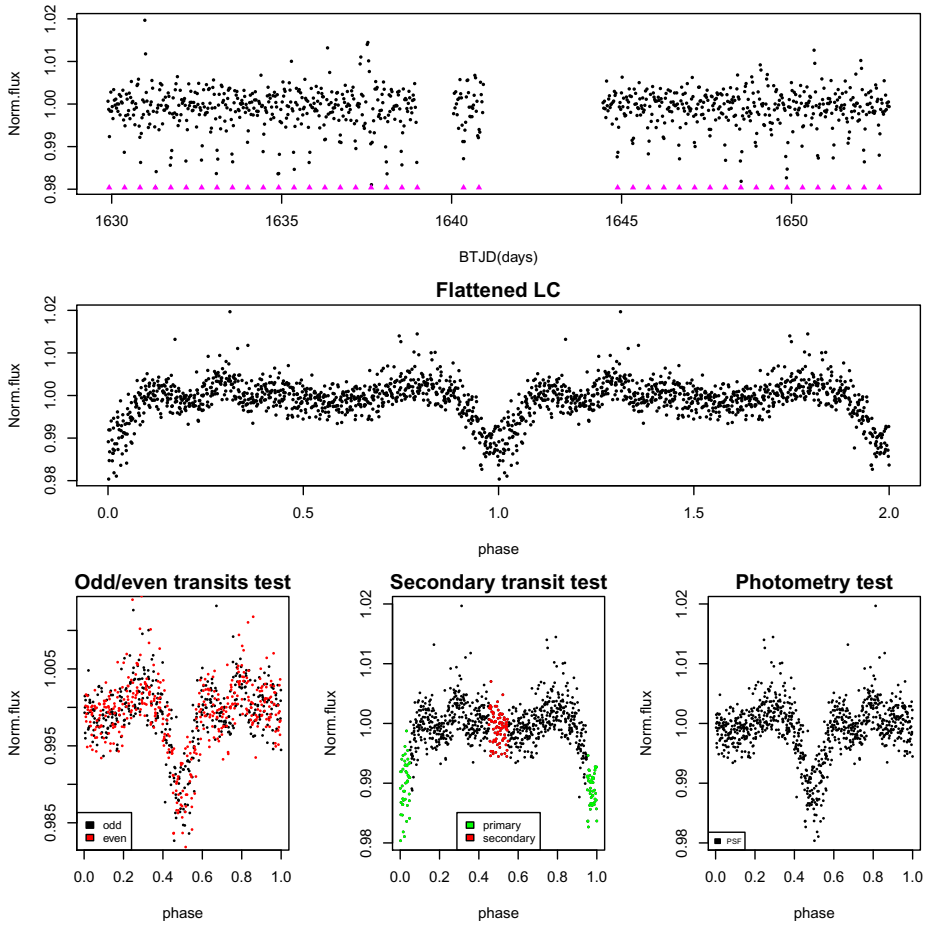

Figure 4.1: Validation tests for TIC 0023846678. Upper panel: normalized and flattened light curve in Barycentric TESS Julian Date (BTJD). The magenta triangles point the transits observed; Middle panel: normalized, flattened light curve (Flattened LC) in phase (primary transit in phase 0, 1 and 2); Lower panel: First three validation tests as described in Section 3.3.

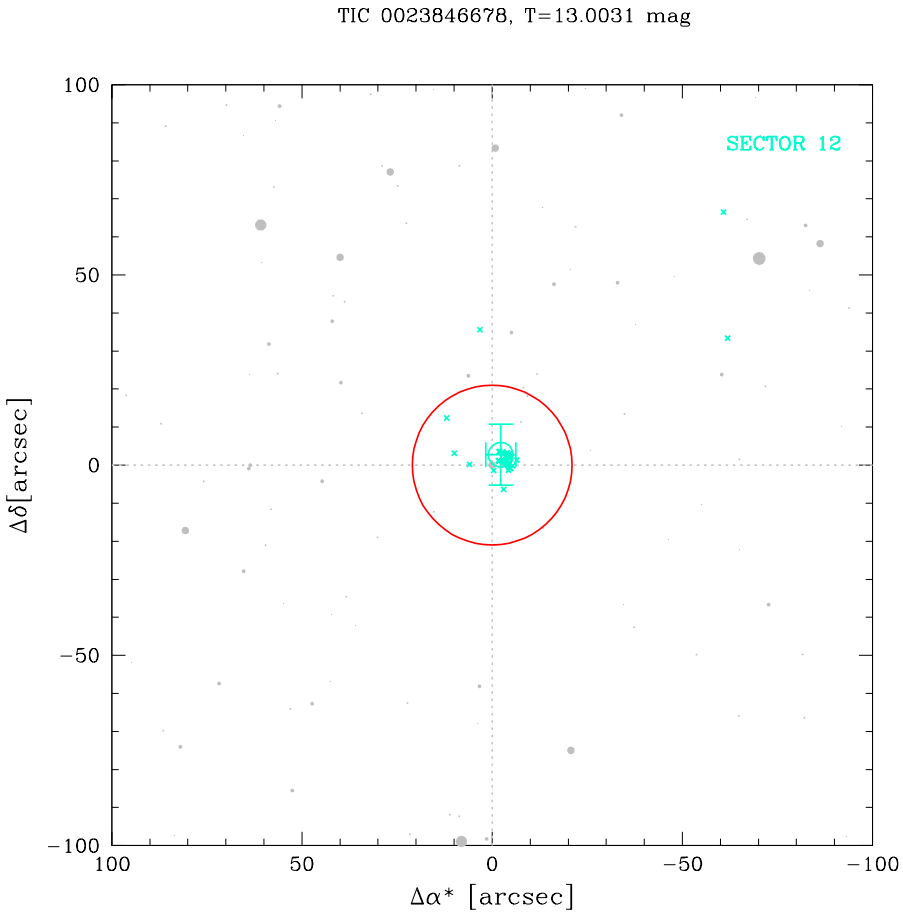

Figure 4.2: Finding chart for TIC 0023846678, used for the centroid test as described in Section 3.3.4

4.2 Tucana Horologium association

Tucana Horologium association (THA) is observed by TESS in the Southern ecliptic hemisphere and has an age of 45^{+4}_{-4} Myr (Bell et al., 2015). Two candidates have been recovered in THA.

4.2.1 TIC 0038820496

The host star, TIC 0038820496, is observed in two Sectors of TESS, Sector 1 and 2, and has a magnitude of $T = 13.23$ mag. Our transit search returned a period of $P \sim 0.65$ days and 80 transits are observed for the candidate exoplanet, as shown in Figure 4.3. Moreover, the dilution factor associated with TIC 0038820496 is zero and the centroid test show that the transits are concentrated on the host star (Figure 4.4).

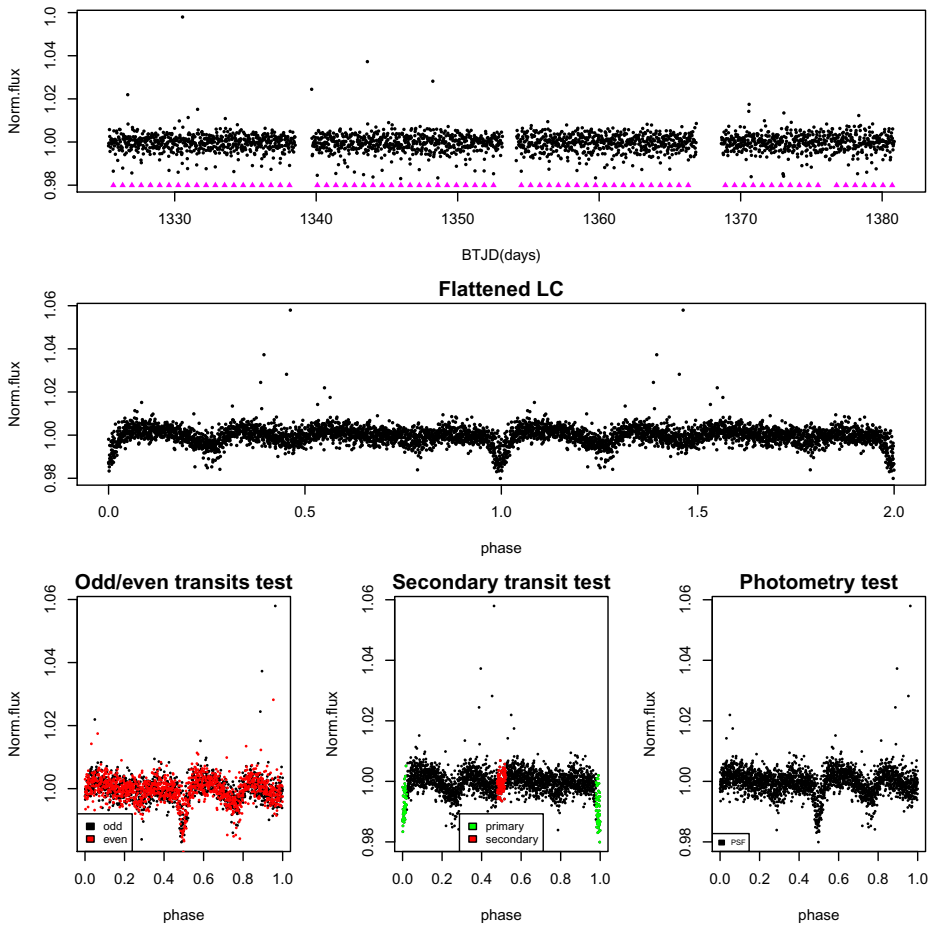

Figure 4.3: Validation tests for TIC 0038820496. Panels as in Figure 4.1.

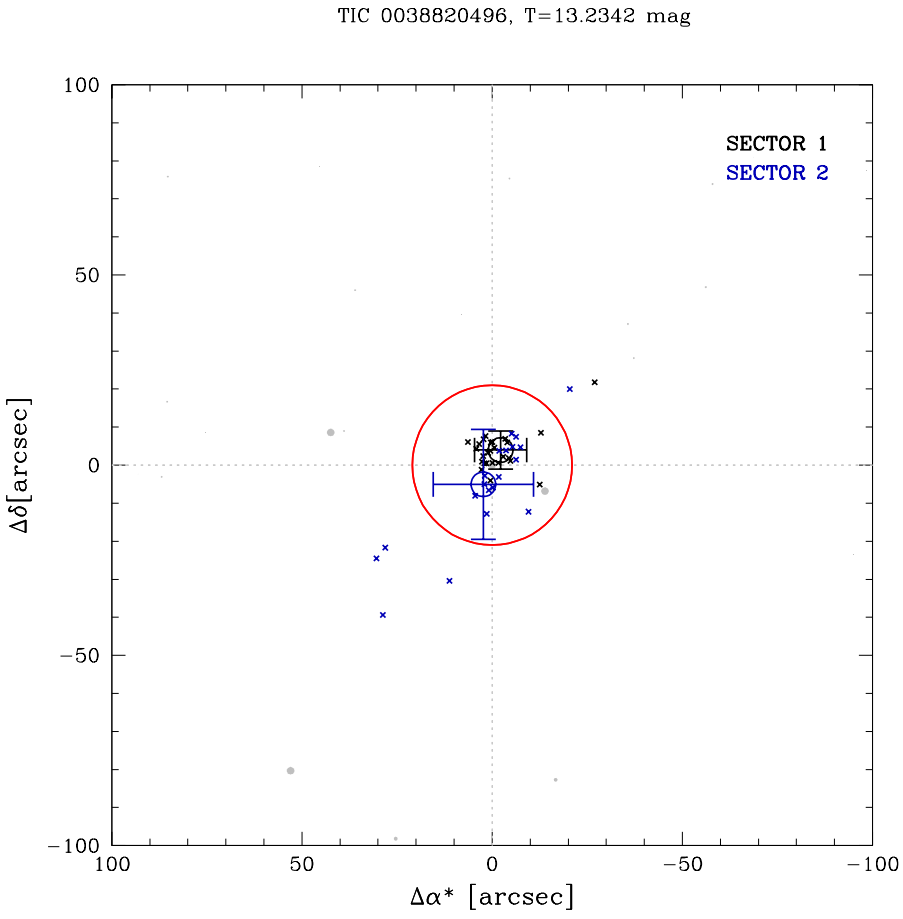

Figure 4.4: Finding chart for TIC 0038820496, used for the centroid test as described in Section 3.3.4.

4.2.2 TIC 0410214986

TIC 0410214986 is observed only in Sector 1 during the primary mission of TESS. It has a magnitude of $T = 7.85$ mag and we have recovered two transits of the candidate exoplanet with an orbital period $P \sim 8.14$ days. A third transit is observed in Sector 1 but it falls into a problematic photometric region of TESS in the range of BTJD=(1347-1350) days. The first three validation tests of the candidate are presented in Figure 4.5. There is indeed a known planet around TIC 0410214986 or DS Tuc A with a period of $P \sim 8.14$ days discovered by Benatti et al. (2019a); Newton et al. (2019). DS Tuc is a physical binary of a G6V star and a K3V companion at a projected separation of 240 AU (Figure 4.6).

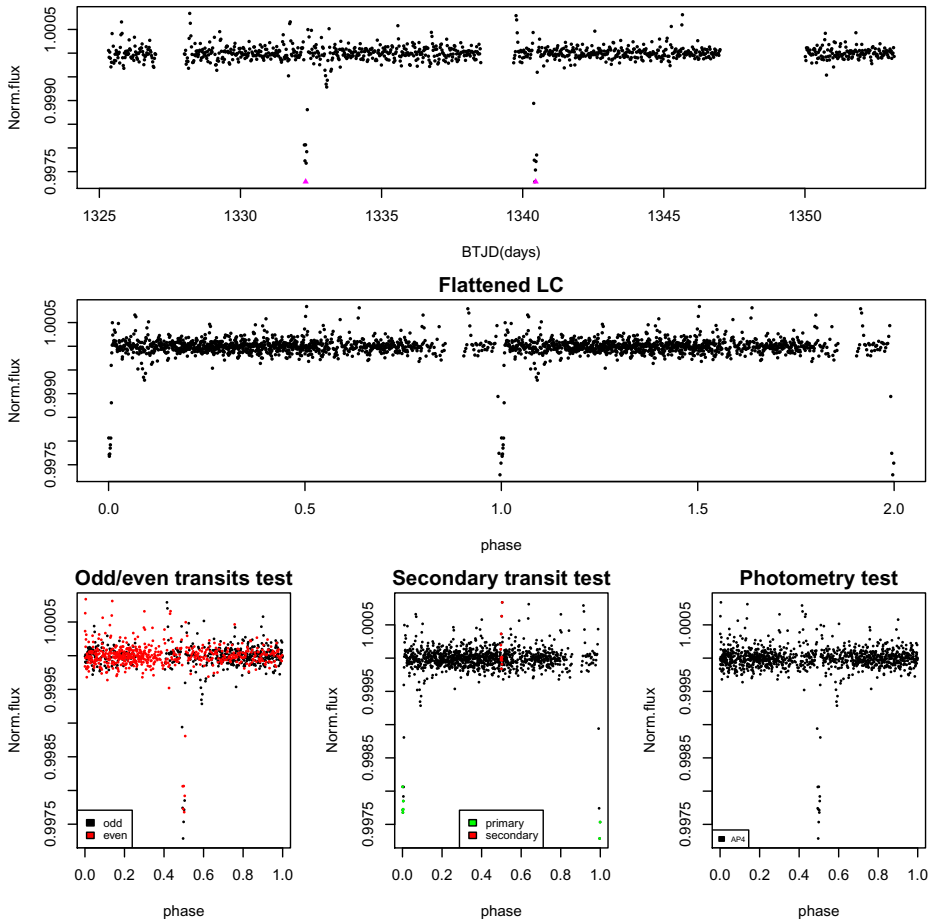

Figure 4.5: Validation tests for TIC 0410214986. Panels as in Figure 4.1.

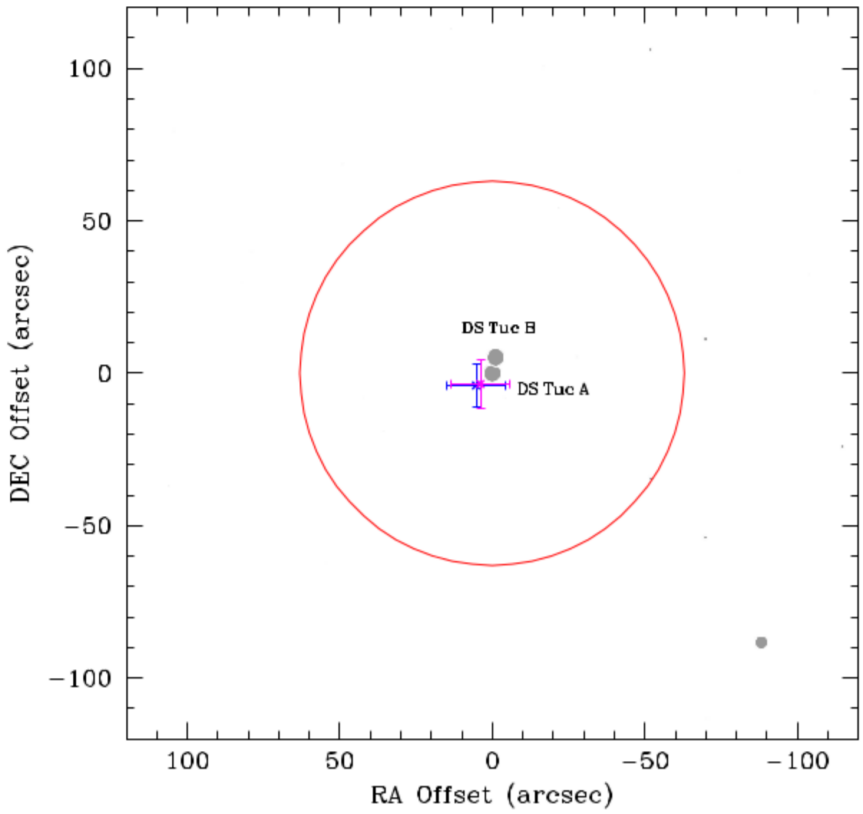

Figure 4.6: Finding chart for TIC 0038820496 illustrating the two components of the physical binary DS Tuc (grey dots). The red circle is a representation of the photometric aperture used for the extraction of the light curve and the magenta/blue crosses are the offsets with respect to the TESS out-of-transit images and the coordinates of the target from Gaia DR2. Details can be found in Benatti et al. (2019a). © Figure 3 in Benatti et al. (2019a) .

4.3 AB Doradus moving group

The AB Doradus moving group(ABDMG) has an age of 50^{+20}_{-5} Myr (Torres et al., 2008) and the members of the group are located both in the Southern and Northern ecliptic hemisphere. One candidate has been found in ABDMG around the star TIC 0067646988.

4.3.1 TIC 0067646988

TIC 0067646988 has TESS magnitude $T = 12.38$ mag and is observed by TESS in Sector 21, in the Northern ecliptic hemisphere. Based on the BLS search the candidate exoplanet around it has a period of $P \sim 1.88$ days and 13 transits have been recovered (Figure 4.7).

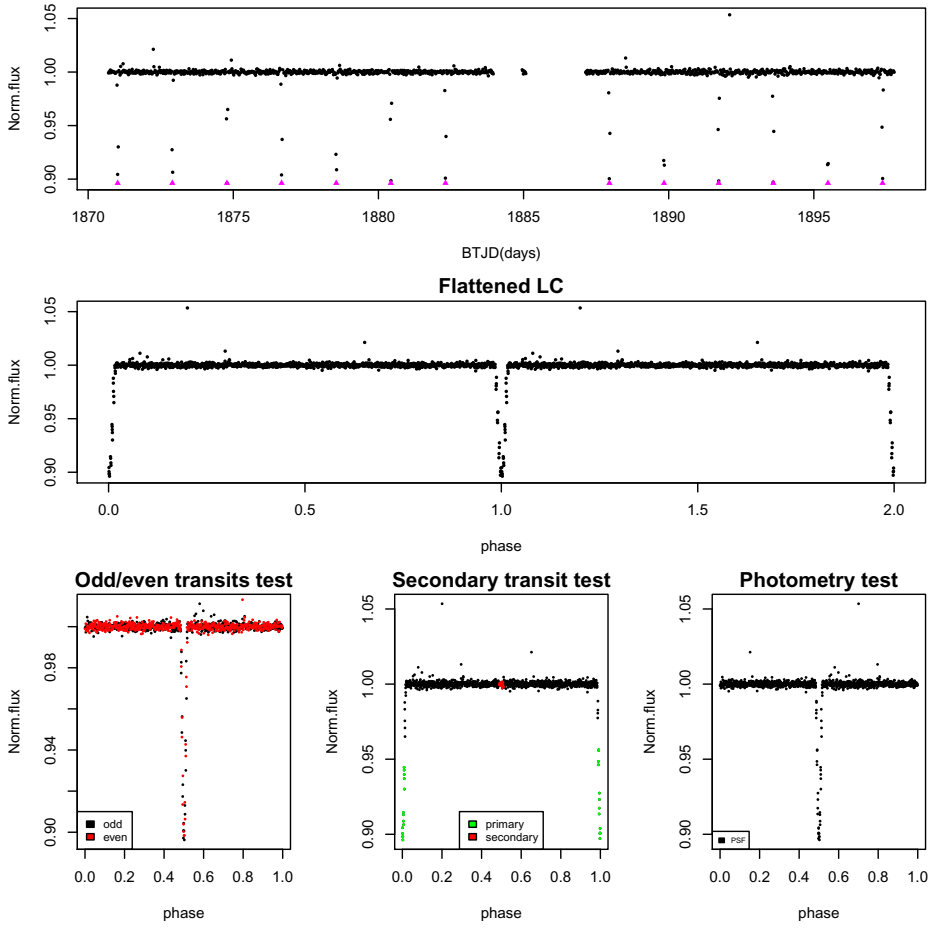

Figure 4.7: Validation tests for TIC 0067646988. Panels as in Figure 4.1.

The dilution factor associated with the host star is zero, since there are no neighbor sources in the same pixel based on GAIA DR2 catalogue.

Last but not least, in Figure 4.8 its evident that the transits observed as happening in the star we are interested in. Irwin et al. (2018) found that TIC 0067646988 (alternative name: LP 261-75) is a short-period ($P = 1.882$ days) single-lined system consisting of a mid M-dwarf eclipsed by a probable brown dwarf secondary, with another distant visual brown dwarf companion. So the recovered signals are not of a planetary origin.

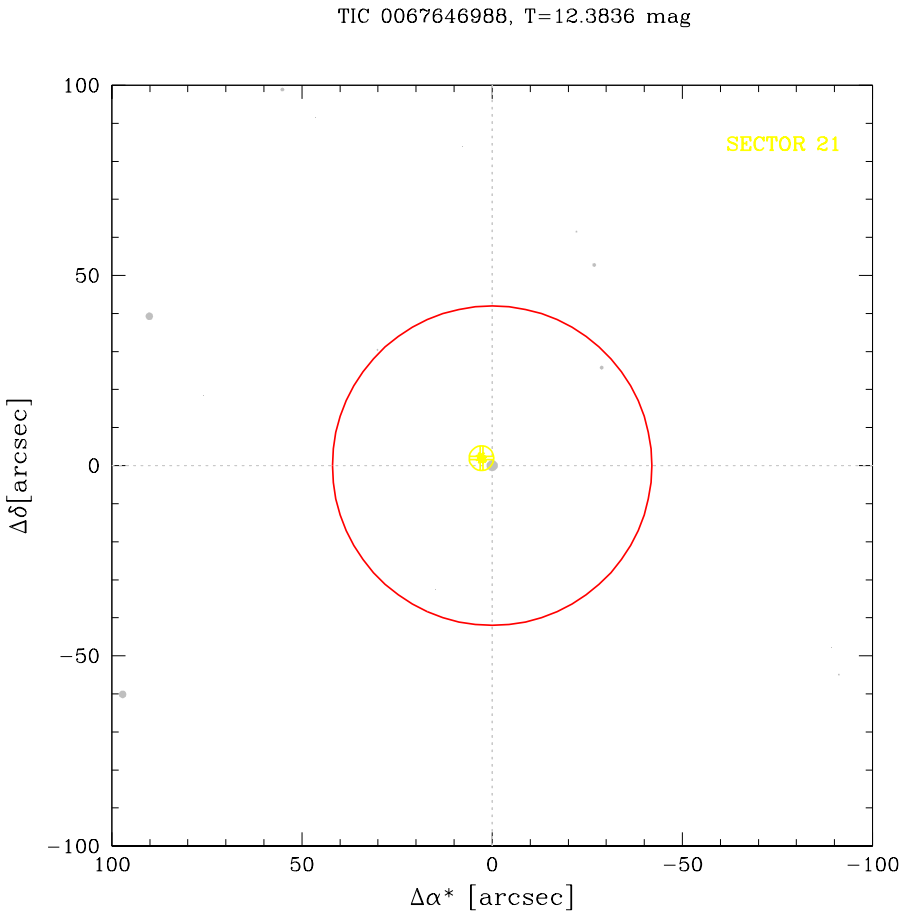

Figure 4.8: Finding chart for TIC 0067646988, used for the centroid test as described in Section 3.3.4.

4.4 Octans association

Octans association (OCT) is observed by TESS mostly in the Southern ecliptic hemisphere (only one member in the Northern hemisphere with TIC 0063790159) and has an age of 35^{+5}_{-5} Myr (Murphy & Lawson, 2015). We have discovered two candidate exoplanets in the OCT association.

4.4.1 TIC 0014091633

TIC 0014091633 is observed in two Sectors of TESS, Sector 5 and 6. The host star has a magnitude of $T = 8.83$ mag and the exoplanet around it is orbiting with a period of $P \sim 5.53$ days, based on the results of the BLS search, and 9 transits are observed by TESS (top panel of Figure 4.9).

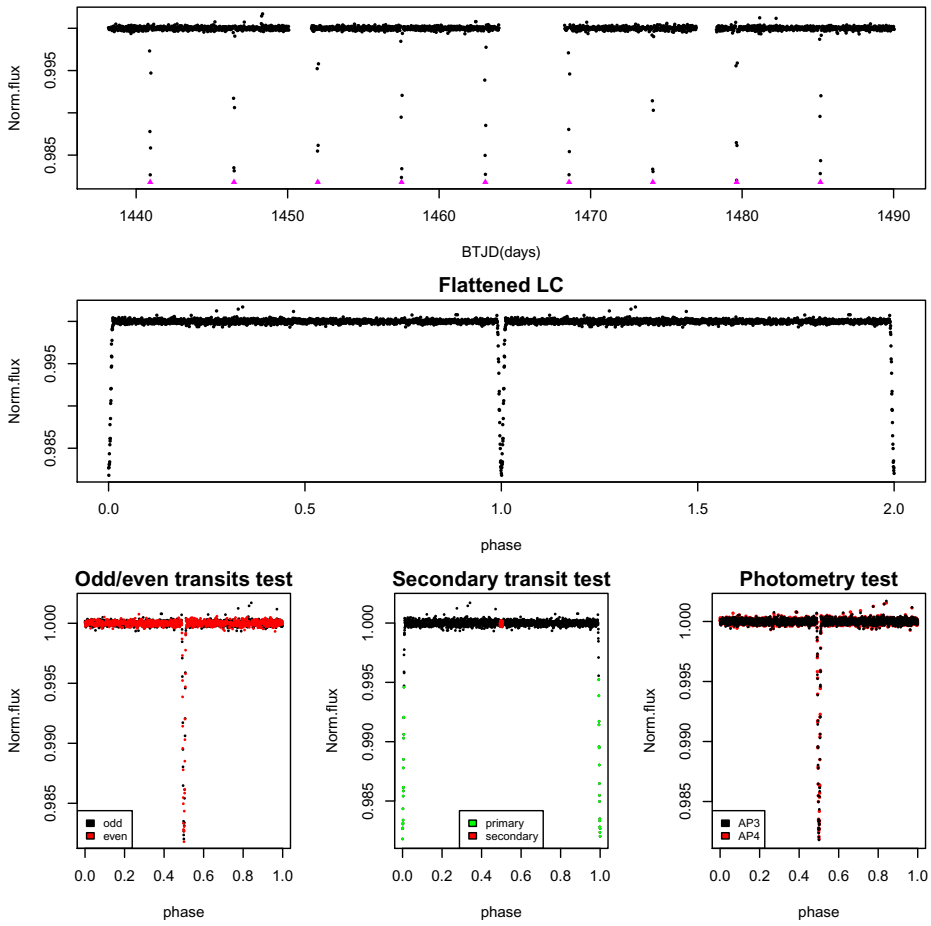

Figure 4.9: Validation tests for TIC 0014091633. Panels as in Figure 4.1.

The dilution factor associated with the host star is approximately equal to zero ($dil = 0.00002$). As shown in Figure 4.10, the mean centroids of Sector 5 and 6 are located on the host star in the center of the finding chart, which means that the observed transits are occurring on the star we are interested in.

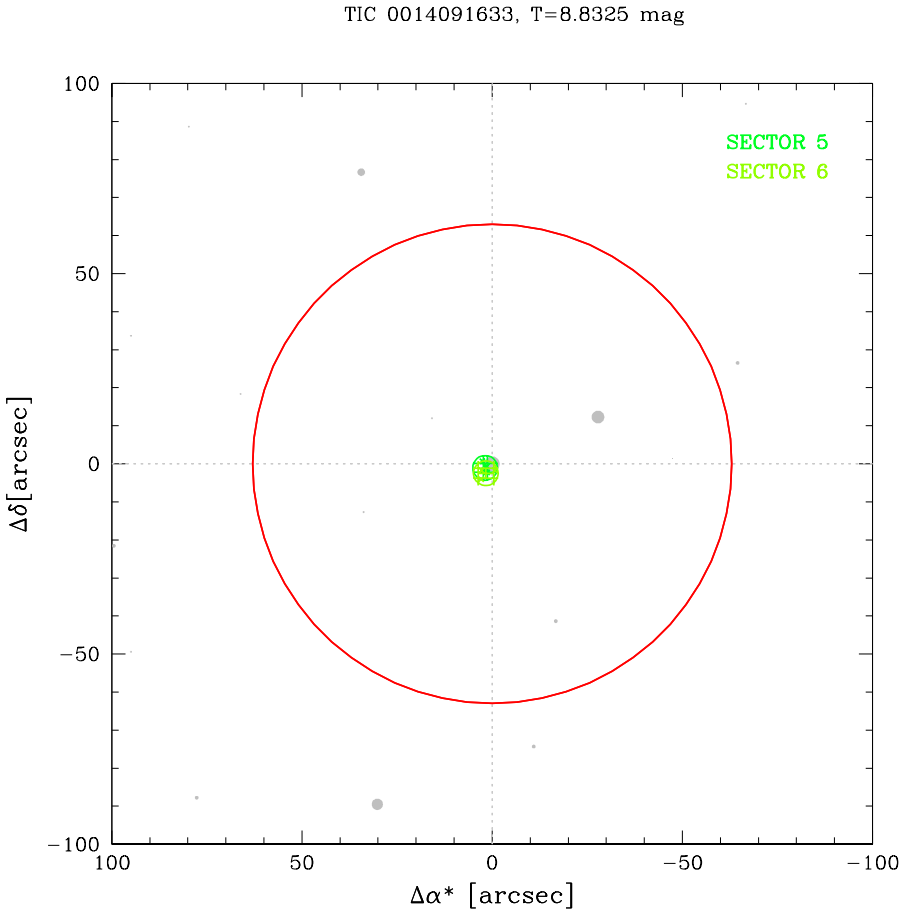

Figure 4.10: Finding chart for TIC 0014091633, used for the centroid test as described in Section 3.3.4.

4.4.2 TIC 0393126088

The second candidate exoplanet in OCT association is orbiting the star with TIC 03931126088. The host star has a magnitude $T = 13.44$ mag and is observed in two Sectors of TESS, Sector 6 and 7. The BLS transit search returned an orbital period of $P \sim 0.36$ days for the candidate and 120 transits have been observed in the FFIs of TESS, as presented in the top panel of Figure 4.11 along with the first three validation tests. The dilution factor associated with the host star is approximately equal to zero ($dil = 0.00664$). Figure 4.12 shows the mean centroids of Sector 6 and 7 which are concentrated on the host star TIC 0393126088, positioned in the center of the finding chart.

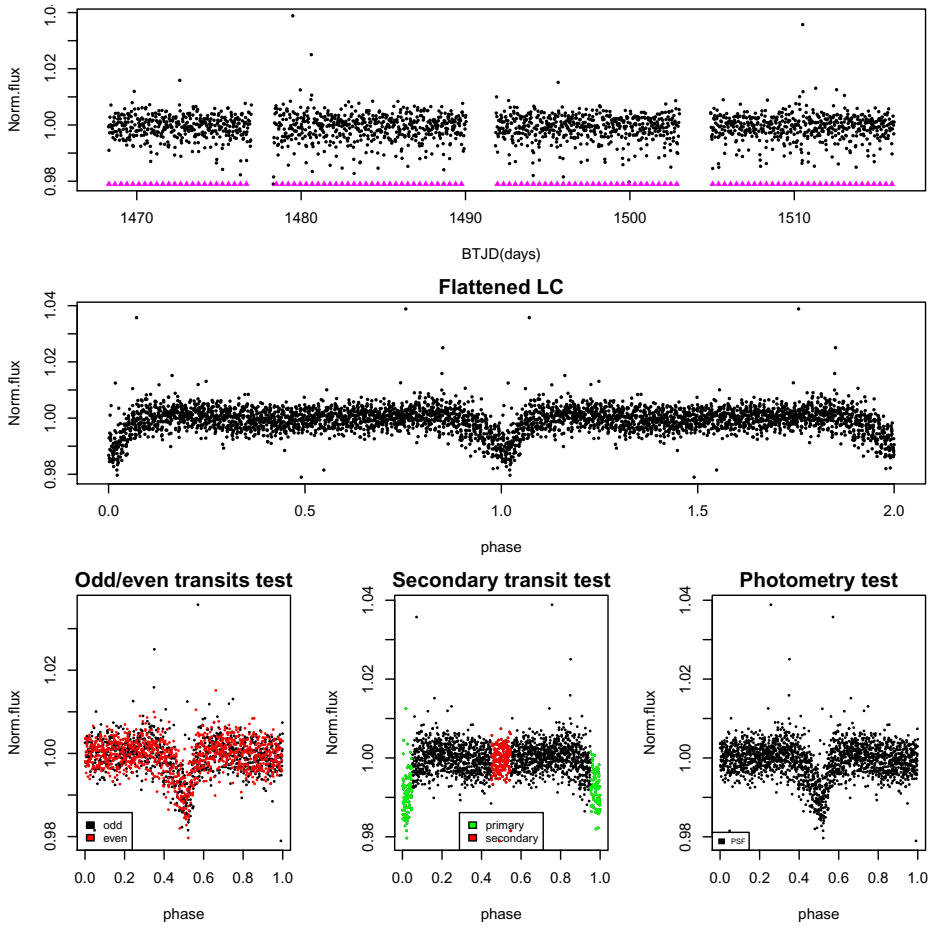

Figure 4.11: Validation tests for TIC 0393126088. Panels as in Figure 4.1.

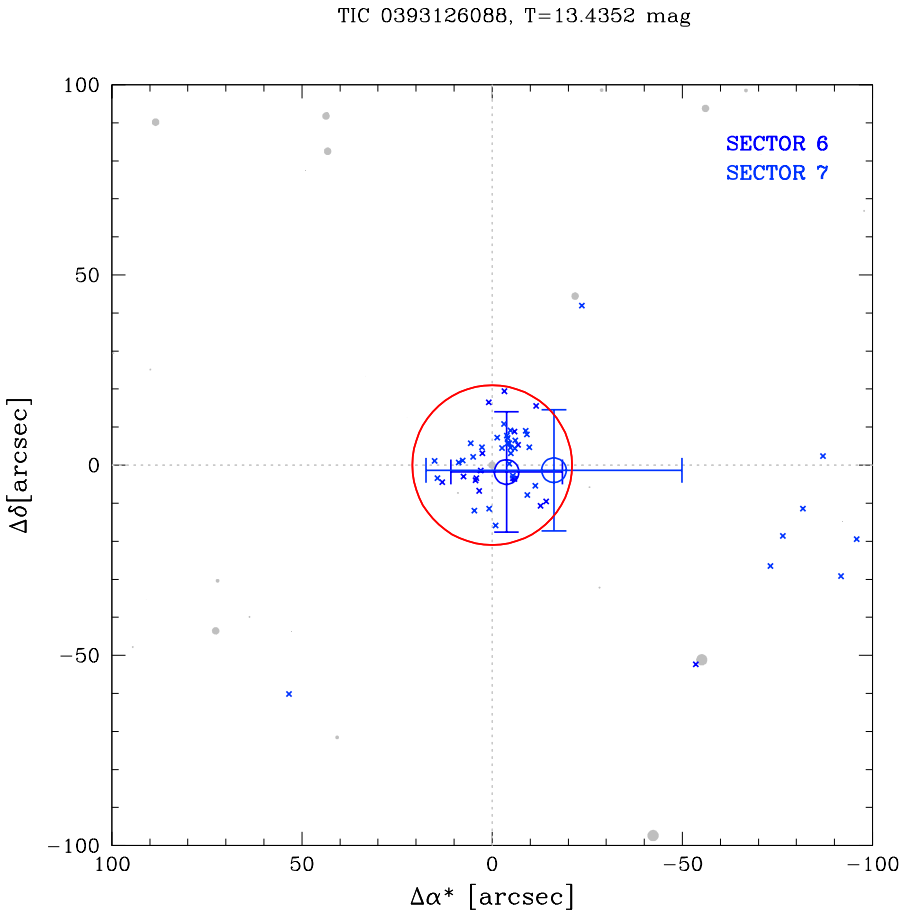

Figure 4.12: Finding chart for TIC 0393126088, used for the centroid test as described in Section 3.3.4.

4.5 Vela Puppis - Population I

As described in Section 2.1 the Vela Puppis region has been studied by Cantat-Gaudin et al. (2019) and they identified seven distinct young populations. The first of them is Population I (VLP1) which is the oldest one with an age of 45^{+5}_{-5} Myr. VLP1 is observed by TESS in the Southern ecliptic hemisphere and two candidates has been found around the star TIC 0075825581 and TIC 0140513181, respectively.

4.5.1 TIC 0075825581

TIC 0075825581 is observed in two Sectors of TESS, Sector 8 and 9. It has a magnitude of $T = 14.89$ mag and the exoplanet around it is orbiting with a period of $P \sim 0.38$ days, based on the results of the BLS search, and 116 transits are observed by TESS (Figure 4.13).

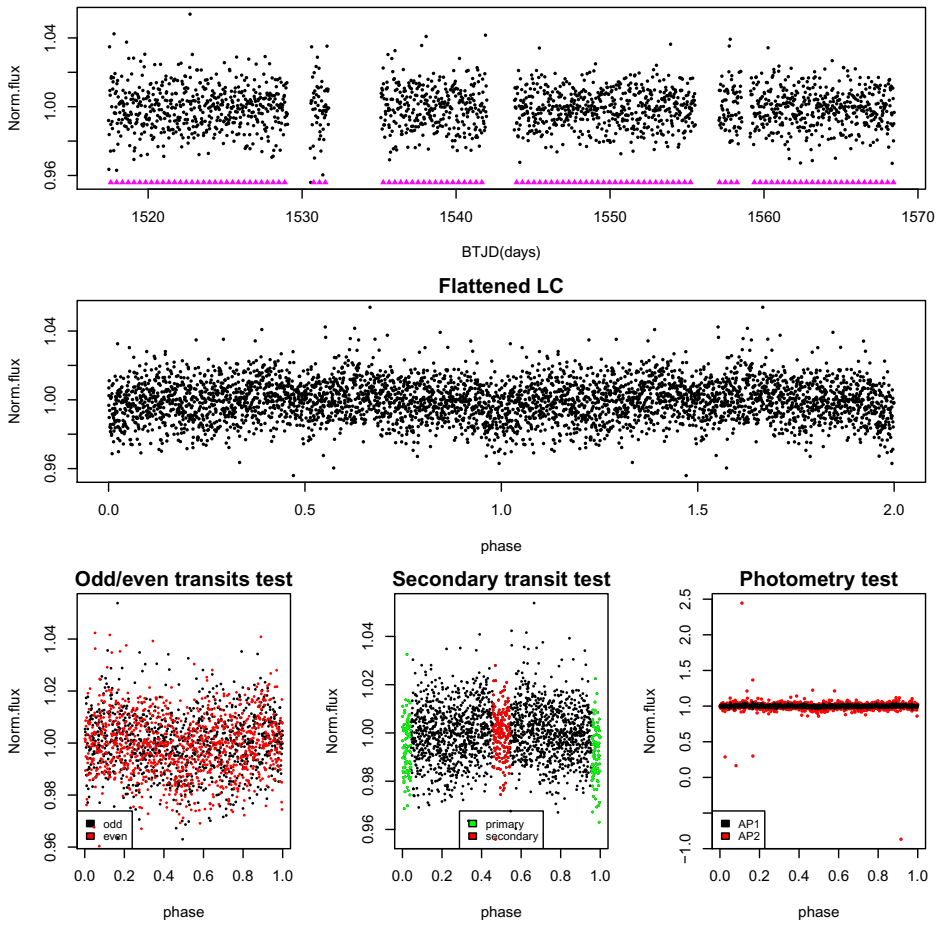

Figure 4.13: Validation tests for TIC 0075825581. Panels as in Figure 4.1.

The dilution factor associated with the host star is $dil \sim 0.25$. As shown in Figure 4.14, the error bars of the mean centroids for Sector 8 and 9 are big and no secure decision can be made about the centroids of the transits. Generally, the centroid test is not very accurate for faint stars as TIC 0075825581 and for these reasons we decided to keep the candidate in our list and analyze it further.

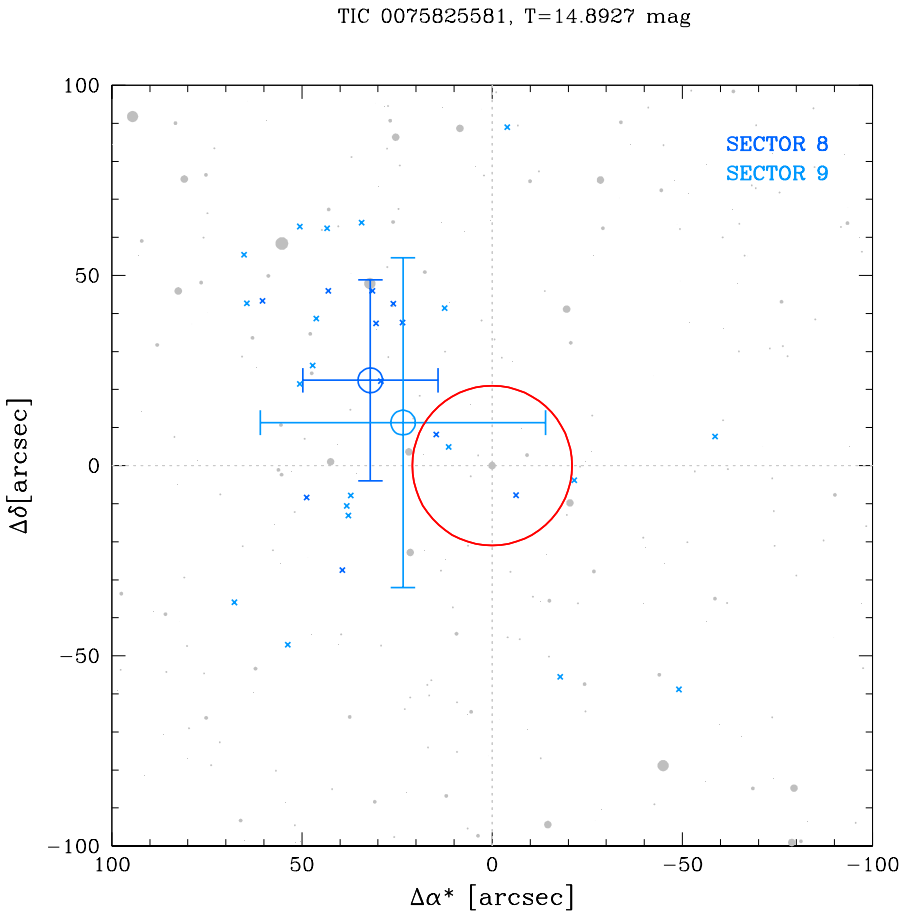

Figure 4.14: Finding chart for TIC 0075825581. In this case, the centroids are not very useful to understand more information and take a secure decision about the candidate, because the host star is faint with T= 14.89 mag. We decided to progress the candidate for further analysis.

4.5.2 TIC 0140513181

The host star with TIC 0140513181 is observed in Sector 8 and 9 of TESS during the first year of the mission and has a magnitude $T = 15.60$. The BLS transit search recovered a period $P \sim 0.91$ days for the candidate exoplanet and 50 of its transits have been observed by TESS, as shown in the top panel of Figure 4.15 along with the first three validation tests. The dilution factor associated with the host star is $dil \sim 0.21$. As mentioned before the centroid test (Figure 4.16) can not provide us secure information in the case of faint stars as TIC 0140513181. Since it passed the first three validation tests we proceeded for further analysis.

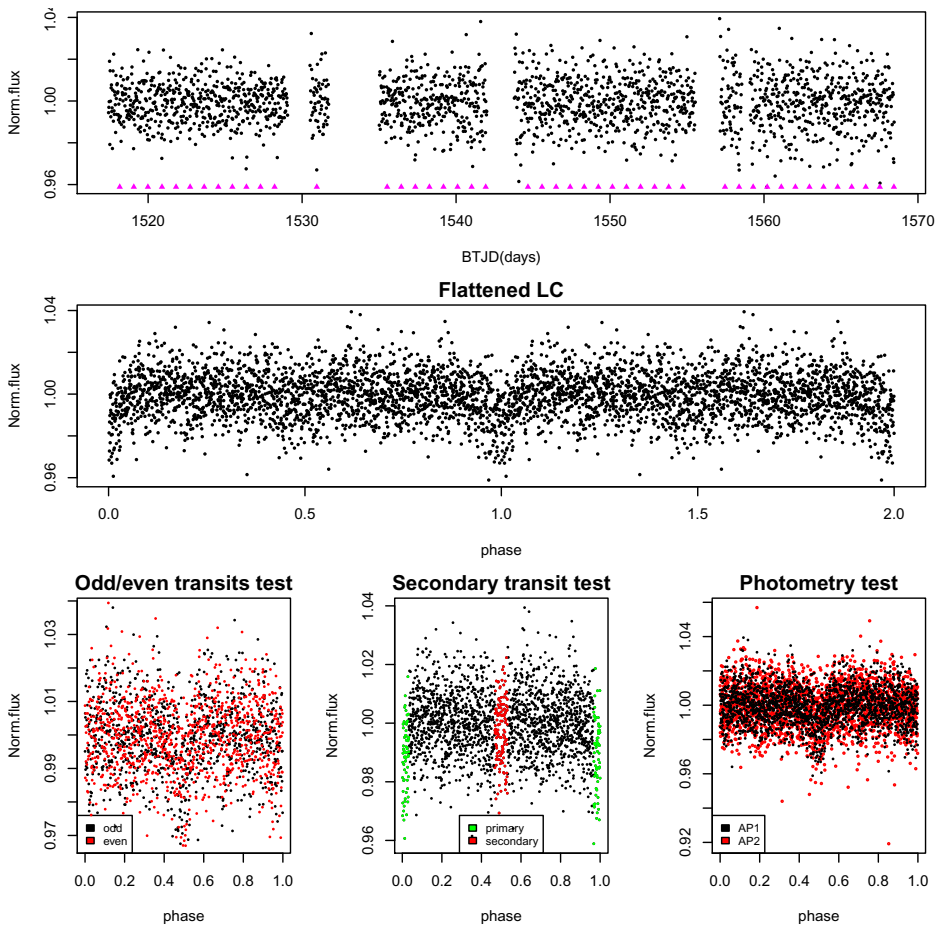

Figure 4.15: Validation tests for TIC 0140513181. Panels as in Figure 4.1.

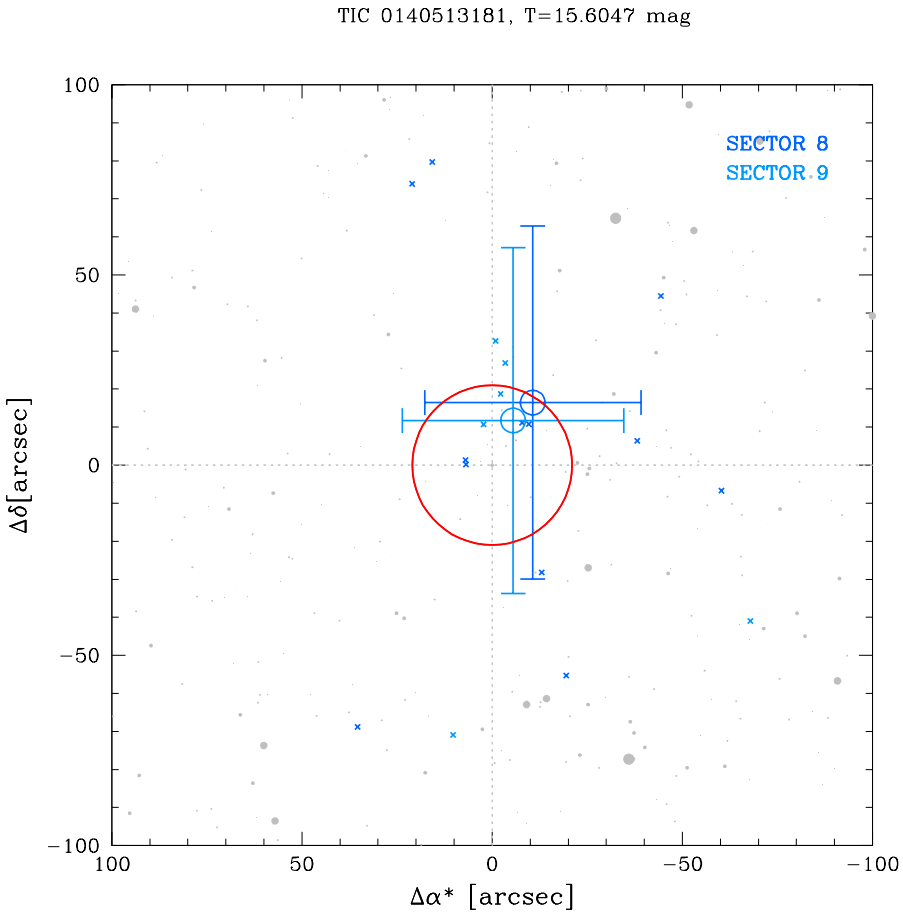

Figure 4.16: Finding chart for TIC 0140513181, used for the centroid test as described in Section 3.3.4.

4.6 Vela Puppis - Population II

The Vela Puppis - Population II (VLP2) is the second young population identified by Cantat-Gaudin et al. (2019) and has an age of 45^{+5}_{-5} Myr. It is located in the Southern ecliptic hemisphere and five candidates have been discovered orbiting stars belonging in VLP2.

4.6.1 TIC 0092896631

The first candidate exoplanet in VLP2 young population is orbiting TIC 0092896631 with $T = 10.88$ mag, which is observed by TESS in Sector 8 and 9. The BLS search returned a period of $P \sim 5.64$ days for the candidate planet and 9 transits are recovered from our analysis (Figure 4.17). The dilution factor related with TIC 0092896631 is almost zero ($dil = 0.00075$) and the mean centroid of Sector 8 and 9 are concentrated on the host star, TIC 0092896631, as shown in Figure 4.18.

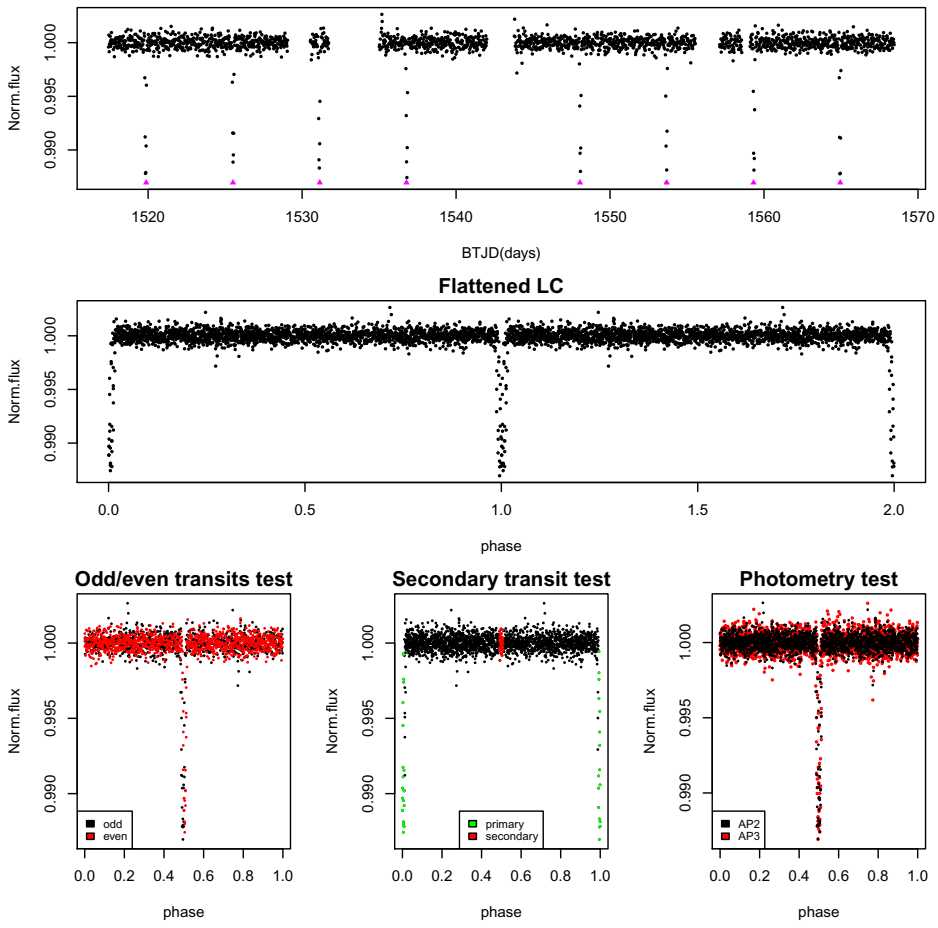

Figure 4.17: Validation tests for TIC 0092896631. Panels as in Figure 4.1.

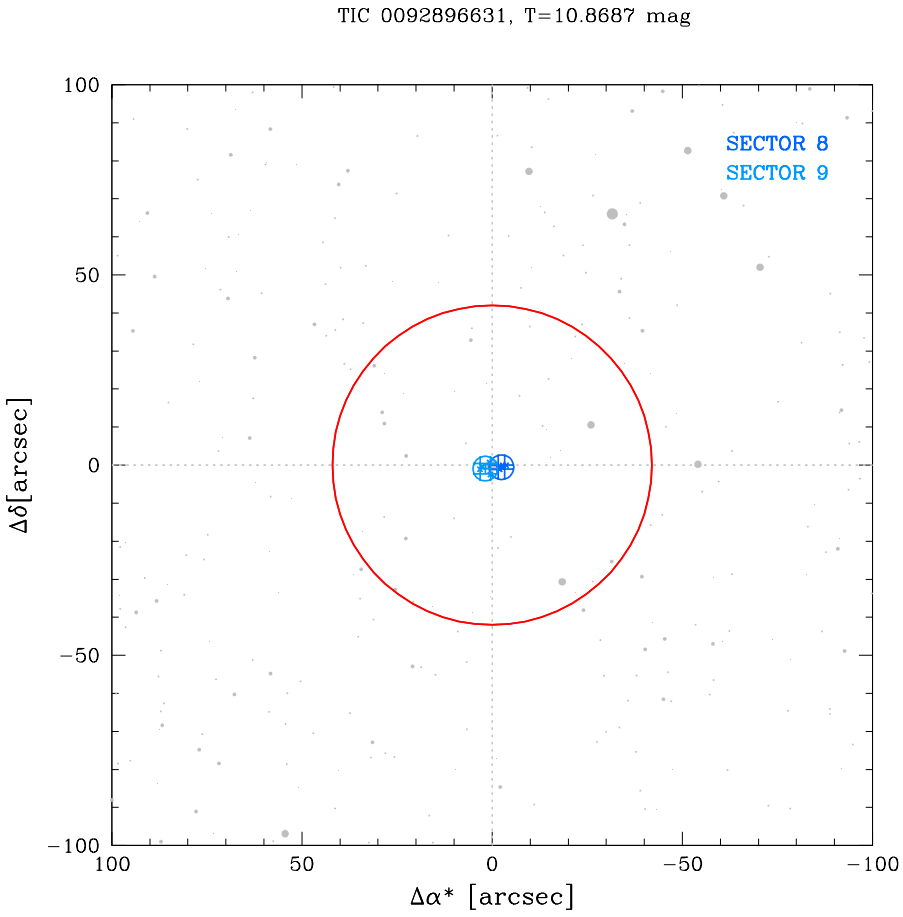

Figure 4.18: Finding chart for TIC 0092896631, used for the centroid test as described in Section 3.3.4.

4.6.2 TIC 0129877093

The second candidate in VLP2 young population is orbiting TIC 0129877093, which is observed by TESS in Sector 7 and 8 in the Southern ecliptic hemisphere and has a magnitude of $T = 12.54$ mag. The BLS search returned a period of $P \sim 1.56$ days for the candidate planet and 26 transits are observed as shown in the top panel of Figure 4.19, along with the first three validation tests. The dilution factor associated with TIC 0129877093 is $dil \sim 0.13$. Taking into account the error bars on the mean centroids of Sector 7 and 8 in Figure 4.20, we considered that this candidate passed our validation tests and progressed it for further analysis.

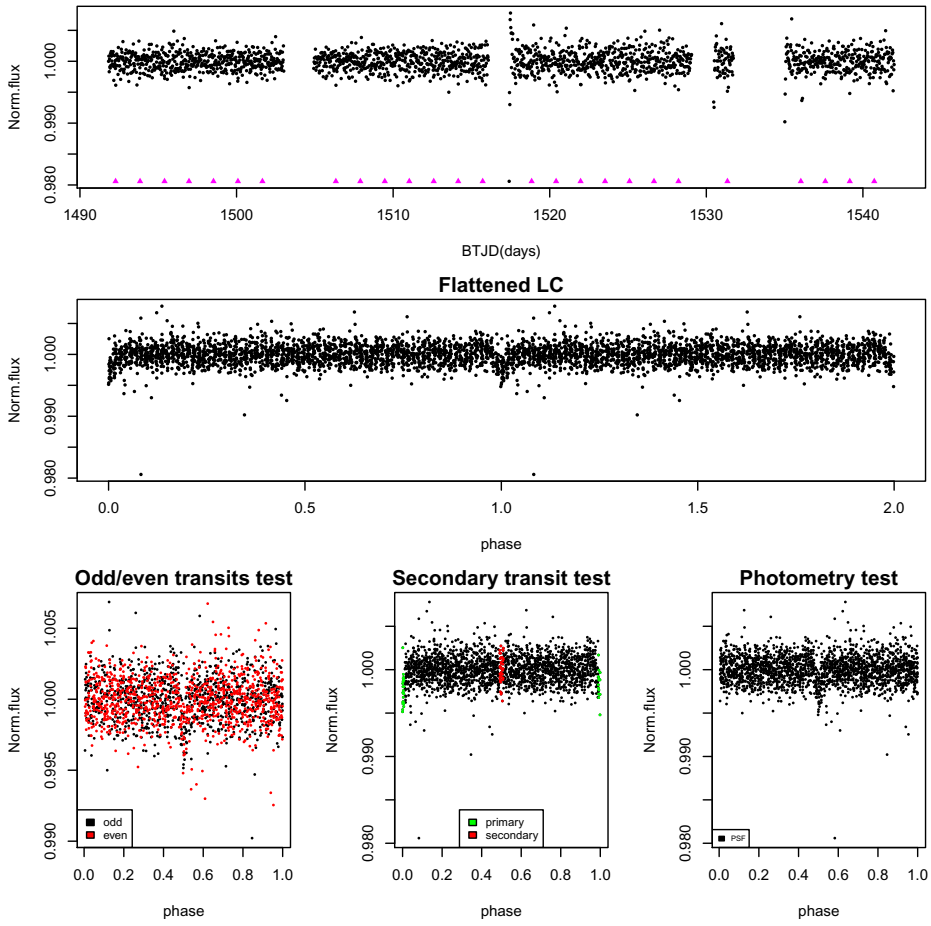

Figure 4.19: Validation tests for TIC 0129877093 . Panels as in Figure 4.1.

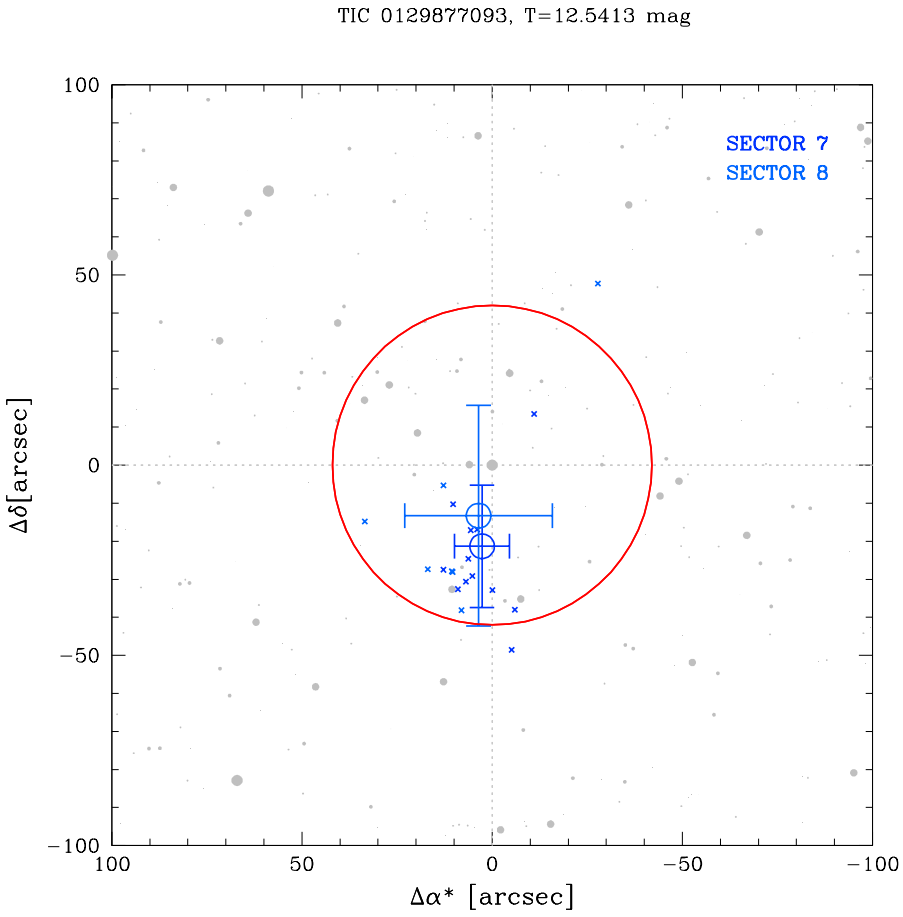

Figure 4.20: Finding chart for TIC 0129877093, used for the centroid test as described in Section 3.3.4.

4.6.3 TIC 0152084108

The third candidate in VLP2 young population is orbiting TIC 0152084108 which has a TESS magnitude of $T = 13.19$ mag and is observed by TESS in Sector 7 and 8 in the Southern ecliptic hemisphere. The BLS search recovered a period of $P \sim 0.46$ days for the candidate planet and 96 transits are observed as shown in the top panel of Figure 4.21, along with the first three validation tests. The dilution factor associated with TIC 0152084108 is $dil \sim 0.40$. Taking into account the error bars on the mean centroids of Sector 7 and 8 in Figure 4.22 and that the host star is faint, we decided to keep this candidate and progressed it for further analysis, also because it successfully passed the other validation tests.

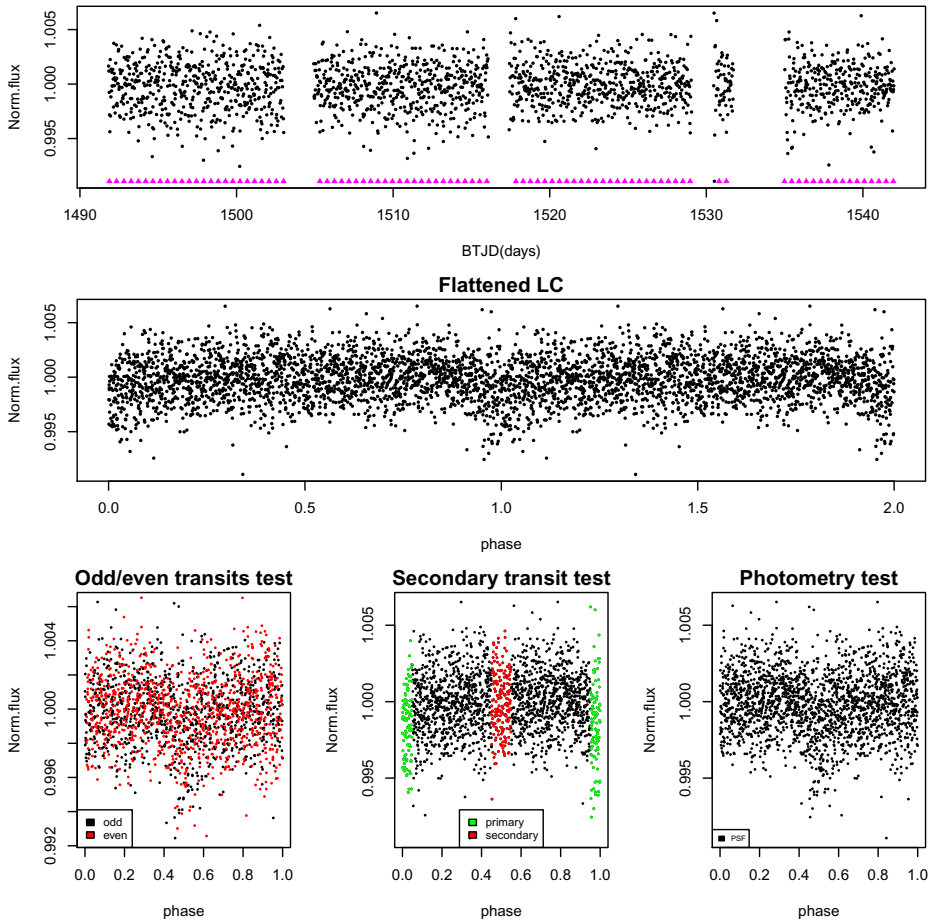

Figure 4.21: Validation tests for TIC 0152084108. Panels as in Figure 4.1.

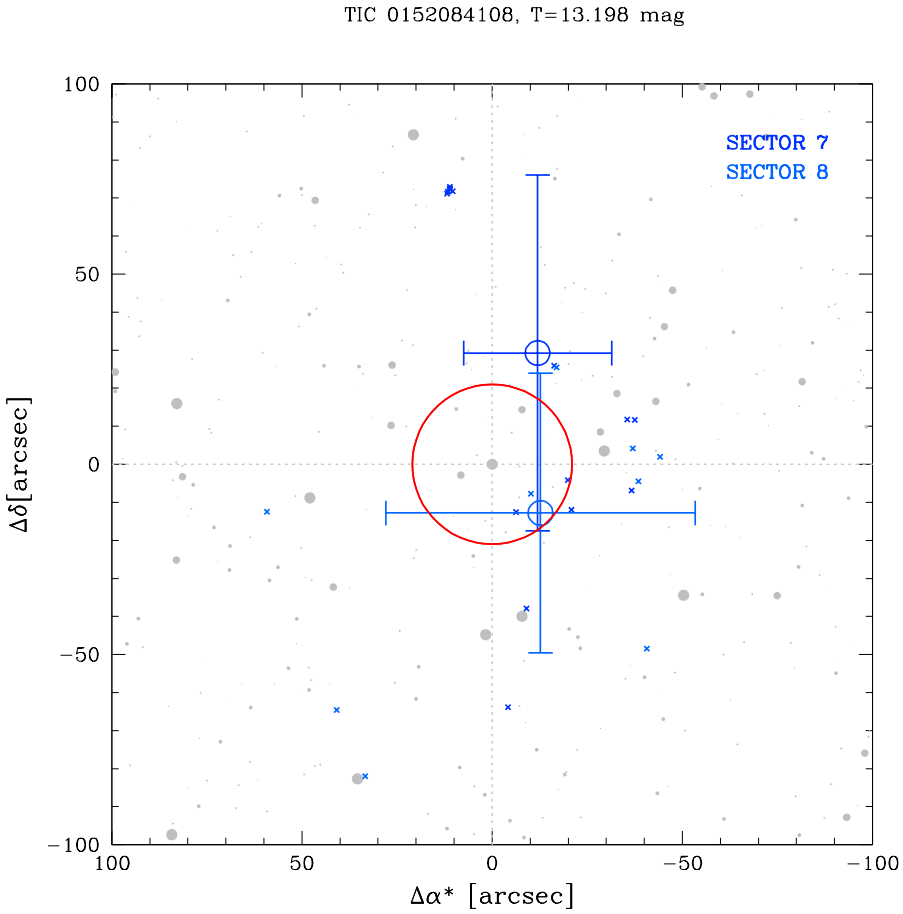

Figure 4.22: Finding chart for TIC 0152084108, used for the centroid test as described in Section 3.3.4. For this case, since the host star is faint we could not extract safe information from the centroid test, so we progressed the candidate into our next steps of our analysis since it successfully passed the other validation tests.

4.6.4 TIC 0032067057

The fourth candidate in VLP2 young population is orbiting the star with TIC 0032067057 and $T = 15.44$ mag, which is observed by TESS in the Southern ecliptic hemisphere in Sectors 8 and 9. The BLS search found a period of $P \sim 3.56$ days for the candidate planet and 12 transits are observed, as shown in the top panel of Figure 4.23 along with the first three validation tests. The dilution factor associated with TIC 0032067057 is $dil \sim 0.04$. Since the candidate is orbiting a faint star, we could not make secure decisions based on the centroid test (Figure 4.24) and taking into consideration that the candidate succeeded the first three validation tests we kept it in our list.

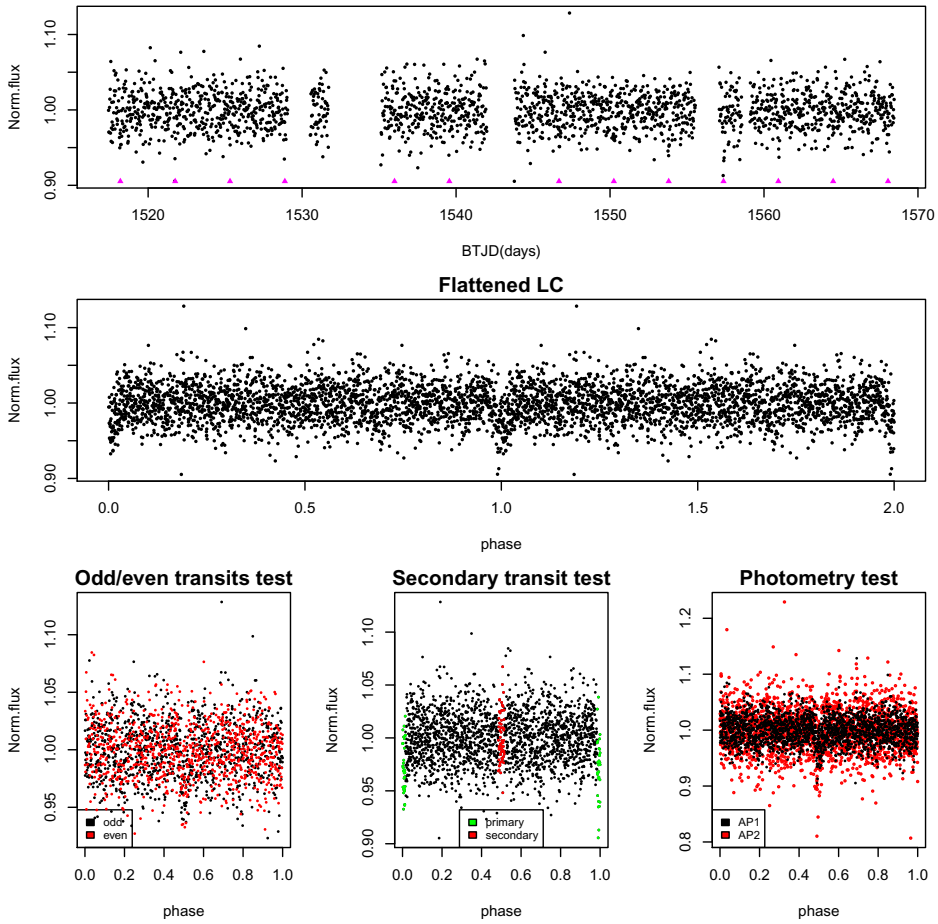

Figure 4.23: Validation tests for TIC 0032067057. Panels as in Figure 4.1.

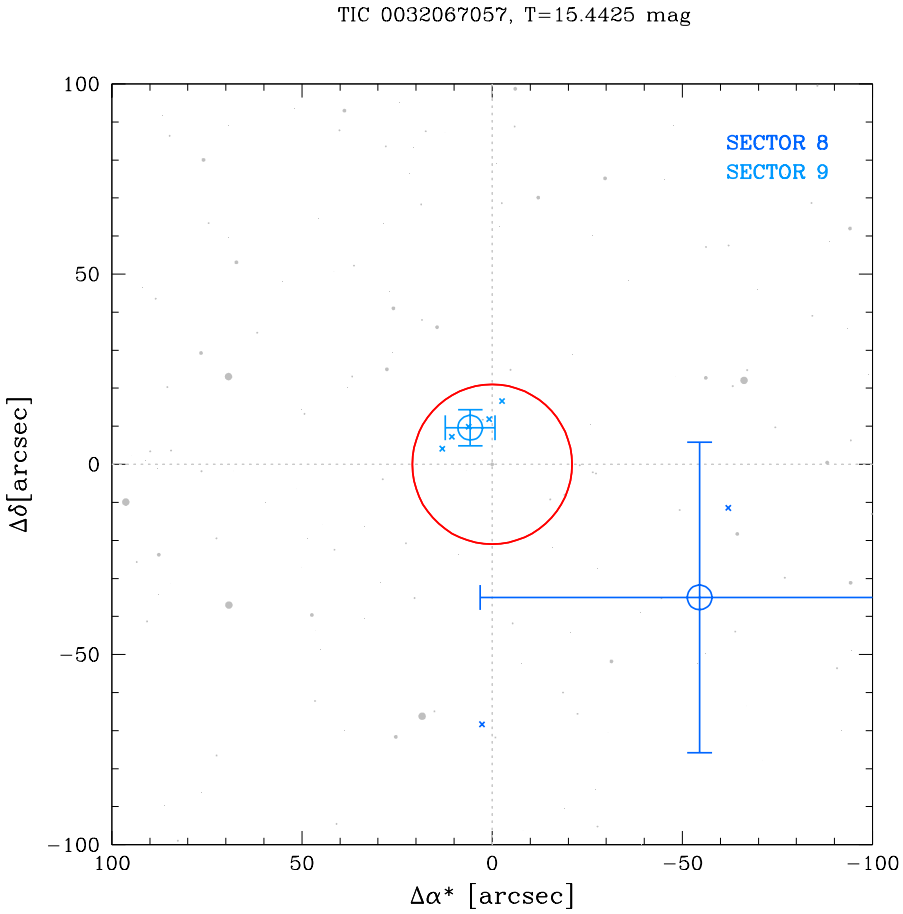

Figure 4.24: Finding chart for 0032067057, used for the centroid test as described in Section 3.3.4. For this candidate, because the host star is faint we could not extract safe information from the centroid test, so we progressed the candidate into our next steps of our analysis since it succeeded the other validation tests.

4.6.5 TIC 0133260600

The last and fifth candidate in VLP2 young population is orbiting the star with TIC 0133260600. The host star has a magnitude of $T = 13.77$ mag and is observed by TESS in the Southern ecliptic hemisphere in Sectors 7 and 8. The candidate orbits TIC 0133260600 with a period of $P \sim 1.42$ days, based on the results of the BLS search, and 30 transits are recovered as shown in the top panel of Figure 4.25, along with the first three validation tests. The dilution factor associated with TIC 0133260600 is $dil \sim 0.18$. As shown in Figure 4.26, the mean centroids of Sector 7 and 8 are concentrated in the host star so the transits are occurring in TIC 0133260600 and not in a nearby star.

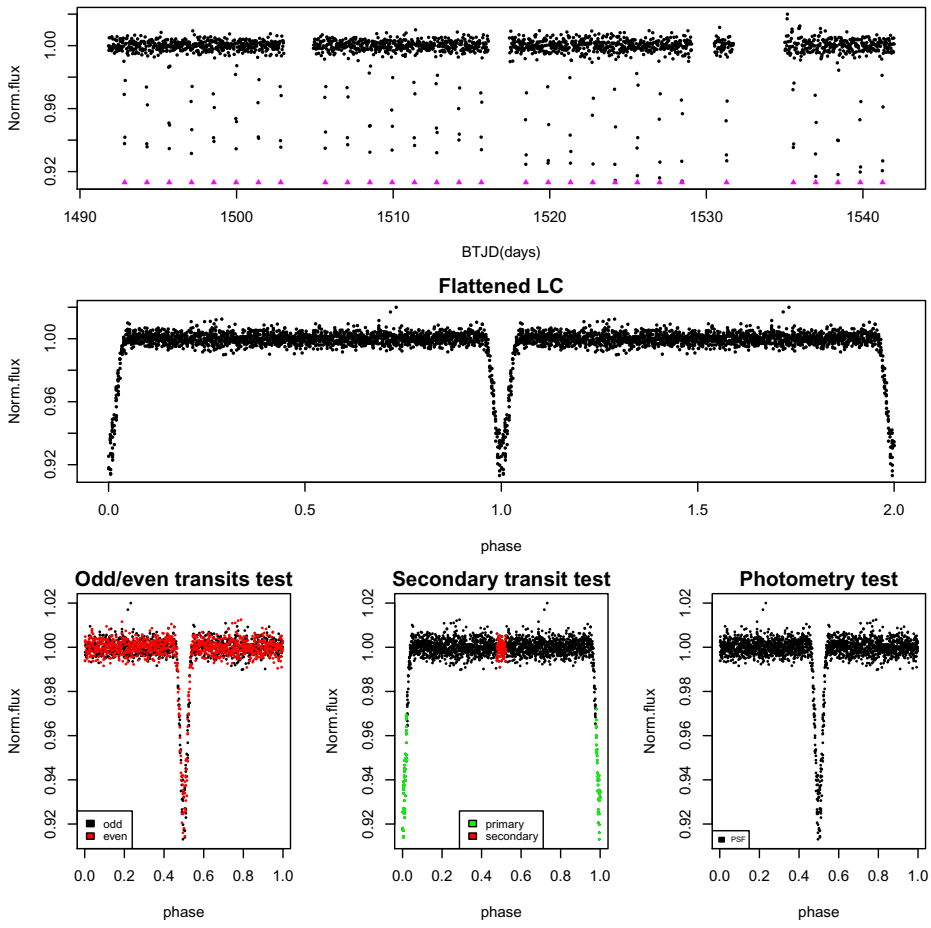

Figure 4.25: Validation tests for TIC 0133260600. Panels as in Figure 4.1.

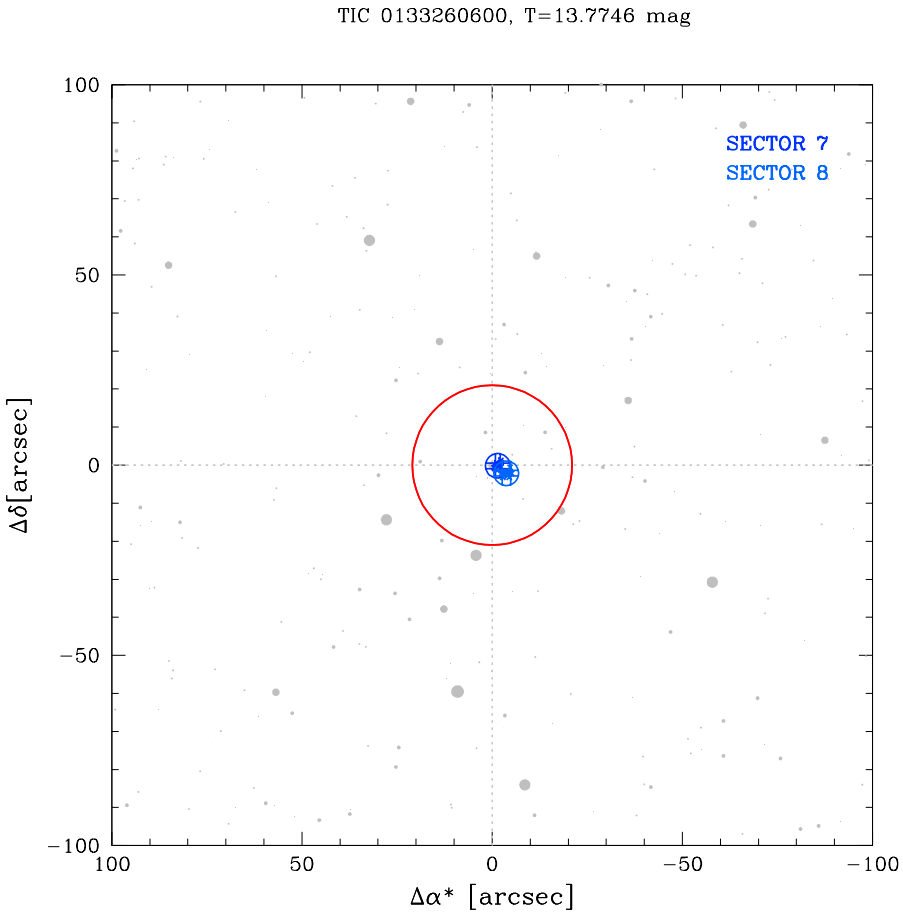

Figure 4.26: Finding chart for TIC 0133260600, used for the centroid test as described in Section 3.3.4.

4.7 Vela Puppis - Population III

The Vela Puppis - Population III (VLP3) is the third young population identified by Cantat-Gaudin et al. (2019) and has an age of 35^{+10}_{-5} Myr. It is also located in the Southern ecliptic hemisphere and we have identified one candidate orbiting the star TIC 0132620309.

4.7.1 TIC 0132620309

TIC 0132620309 is observed in two Sectors of TESS, Sector 7 and 8. It has a magnitude of $T = 15.44$ mag and the exoplanet around it has a period of $P \sim 1.07$ days and 40 transits are observed by TESS (Figure 4.27), based on the results of the BLS search.

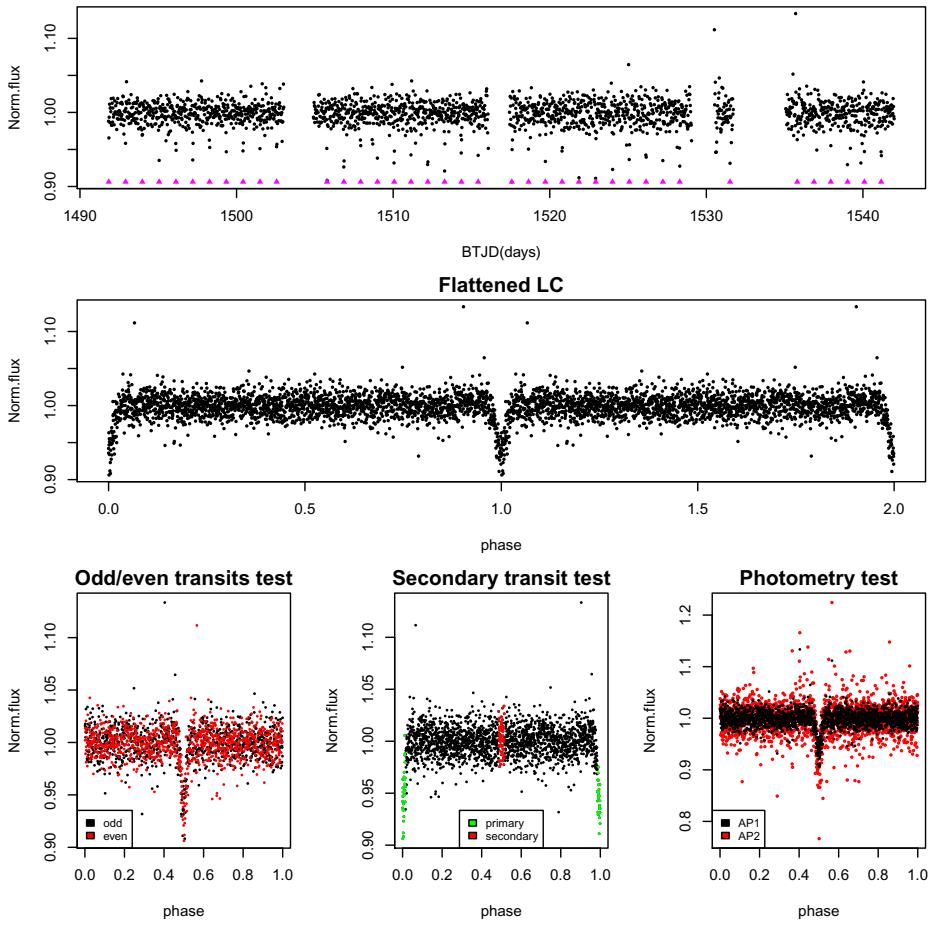

Figure 4.27: Validation tests for TIC 0132620309. Panels as in Figure 4.1.

The dilution factor associated with the host star is $dil \sim 0.20$. TIC 0132620309 is a faint star so we could not extract detailed information from the centroid test, but as shown in Figure 4.28 withing the errors the mean centroids of Sector 7 and 8 seem to be concentrated on the host star. So the star succeeded all the validation tests and is progressed for additional analysis.

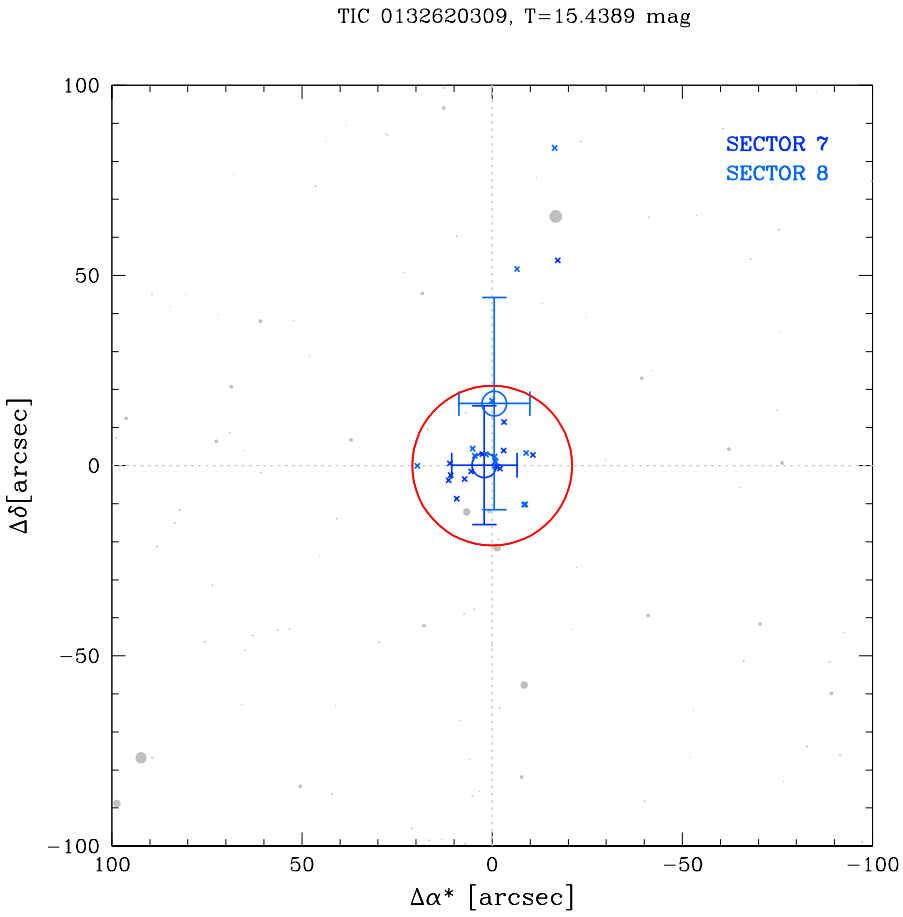

Figure 4.28: Finding chart for TIC 0132620309, used for the centroid test as described in Section 3.3.4. Even if the host star is faint, we can see that within the errors the mean centroids are concentrated on TIC 0132620309.

4.8 Vela Puppis - Population IV

The Vela Puppis - Population IV (VLP4) is the fourth young population identified by Cantat-Gaudin et al. (2019) and has an age of 35^{+10}_{-5} Myr. It is observed by TESS in the Southern ecliptic hemisphere and its the population with most candidate exoplanets discovered in our sample. Most specifically, we identified five candidates orbiting stars in VLP4.

4.8.1 TIC 0131743355

The first candidate we found in VLP4 is around the star with TIC 0131743355 and is observed in two sectors of TESS, Sector 7 and 8. The host star has a magnitude of $T = 9.33$ mag with a dilution factor approximately equal to zero ($dil = 0.00362$).

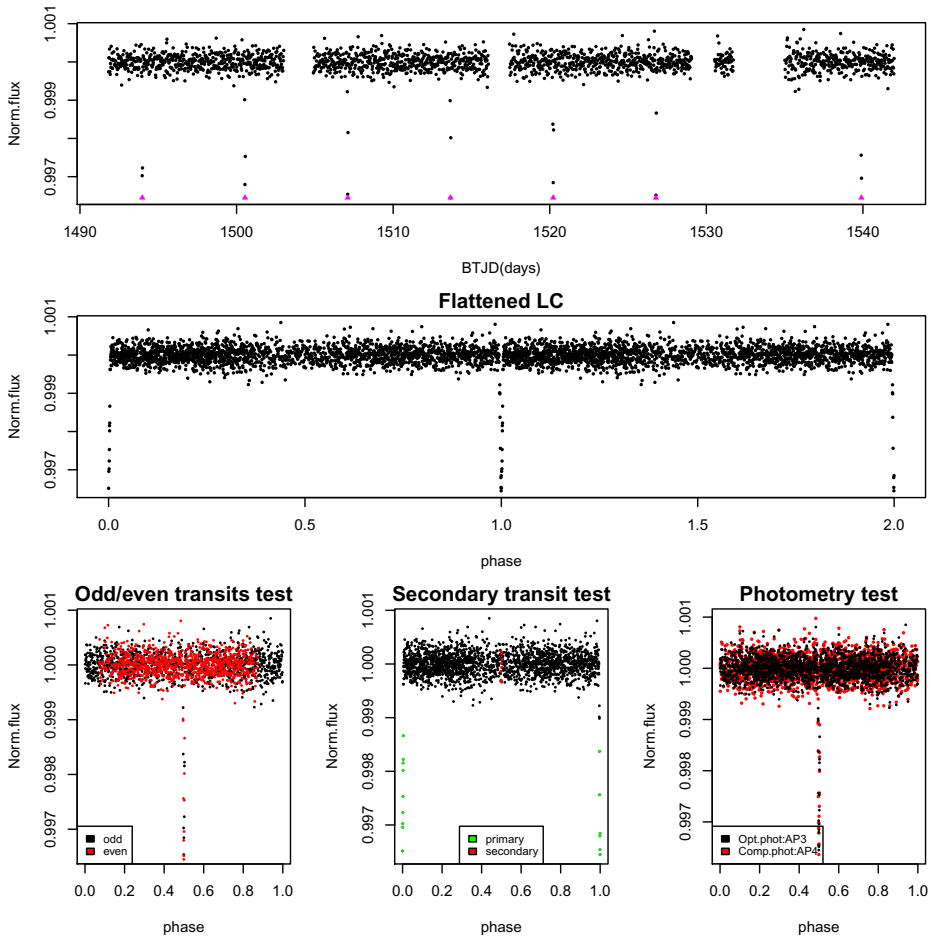

Figure 4.29: Validation tests for TIC 0131743355. Panels as in Figure 4.1.

The BLS search restituted a period of $P \sim 6.56$ days for the candidate exoplanet and 7 transits are observed, as shown in the top panel of Figure 4.29. The mean centroids of Sector 7 and 8 are positioned on the TIC 0131743355, so indeed the transits are occurring on it (Figure 4.32).

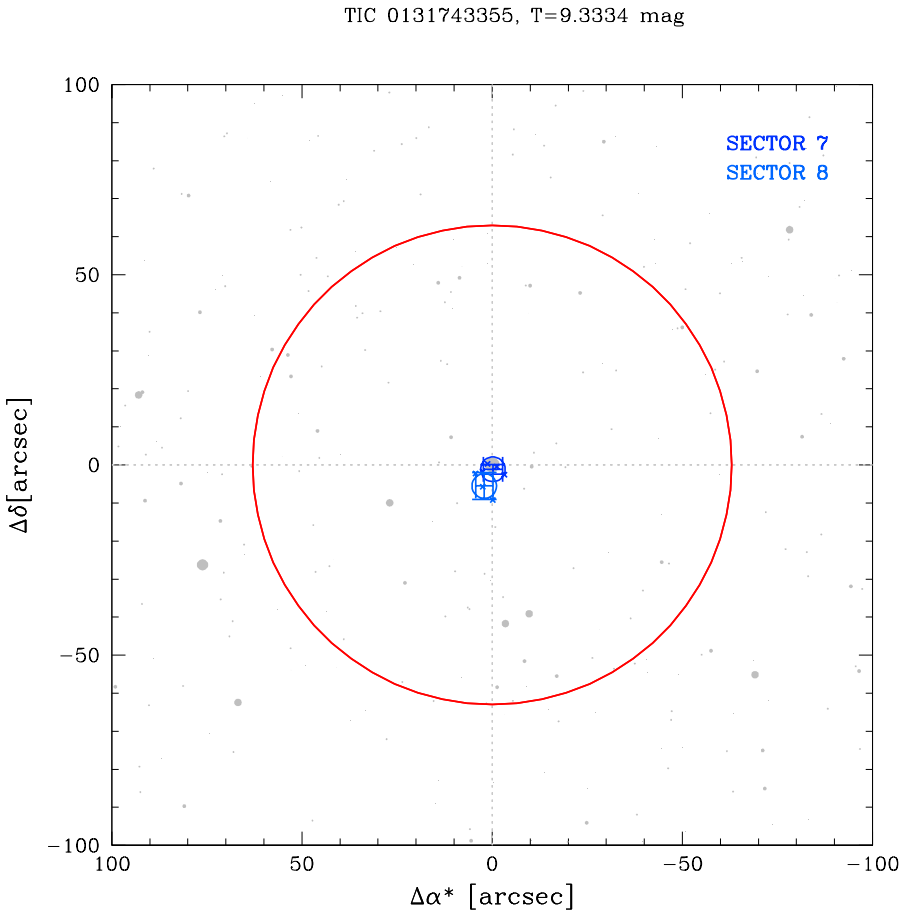

Figure 4.30: Finding chart for TIC 0131743355, used for the centroid test as described in Section 3.3.4.

4.8.2 TIC 0123378551

The second candidate we found in VLP4 is orbiting the star with TIC 0123378551 and is observed in two sectors of TESS, Sector 7 and 8. The host star has a magnitude of $T = 10.69$ mag with a dilution factor is almost zero ($dil = 0.00075$). The BLS search found a period of $P \sim 11.01$ days for the candidate exoplanet and 4 transits are observed as shown in the top panel of Figure 4.31. Last but not least, the mean centroids of Sector 7 and 8 are positioned on the TIC 0123378551 based on Figure 4.32.

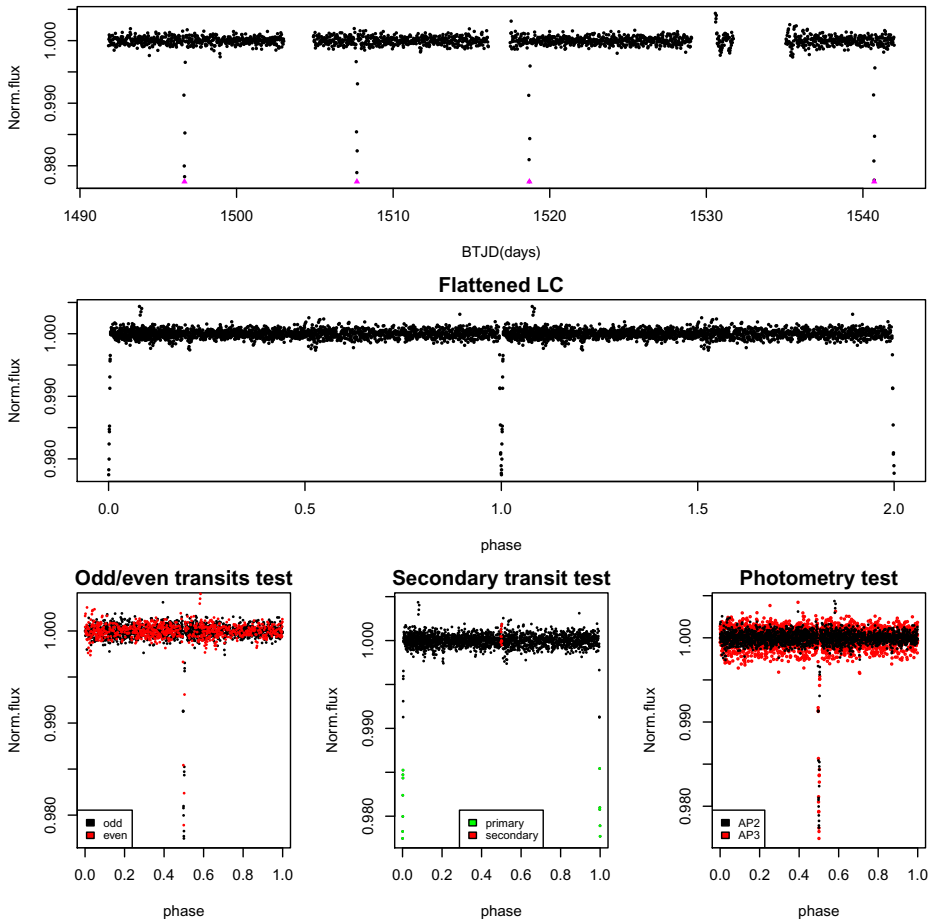

Figure 4.31: Validation tests for TIC 0123378551. Panels as in Figure 4.1.

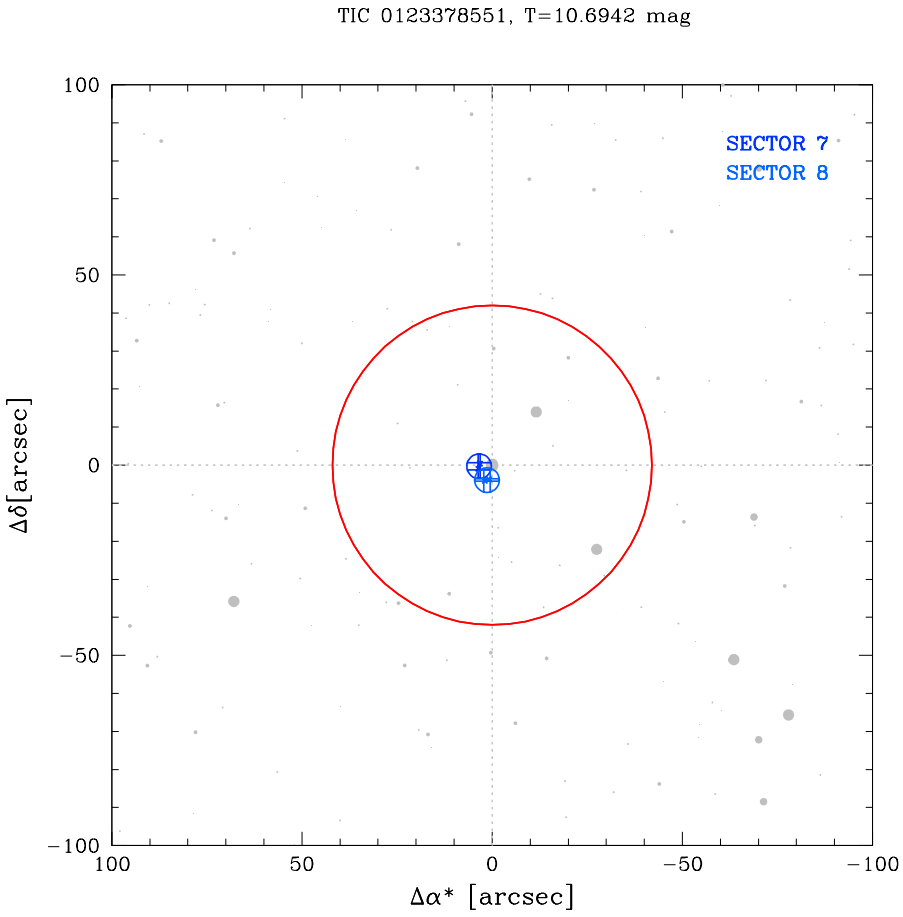

Figure 4.32: Finding chart for TIC 0123378551, used for the centroid test as described in Section 3.3.4.

4.8.3 TIC 0149608236

The third candidate we found in VLP4 is orbiting the star with TIC 0149608236 which is observed by TESS in Sector 7. The host star has a magnitude of $T = 13.79$ mag with a dilution factor equal to $dil \sim 0.14$. A period of $P \sim 1.68$ days has been found from the BLS search for the candidate and 13 transits are observed as shown in the top panel of Figure 4.33. Moreover, TIC 0149608236 is a faint star and for this reason the centroid test (Figure 4.34) is not accurate, so we progressed it for additional analysis since it succeeded the other validation tests.

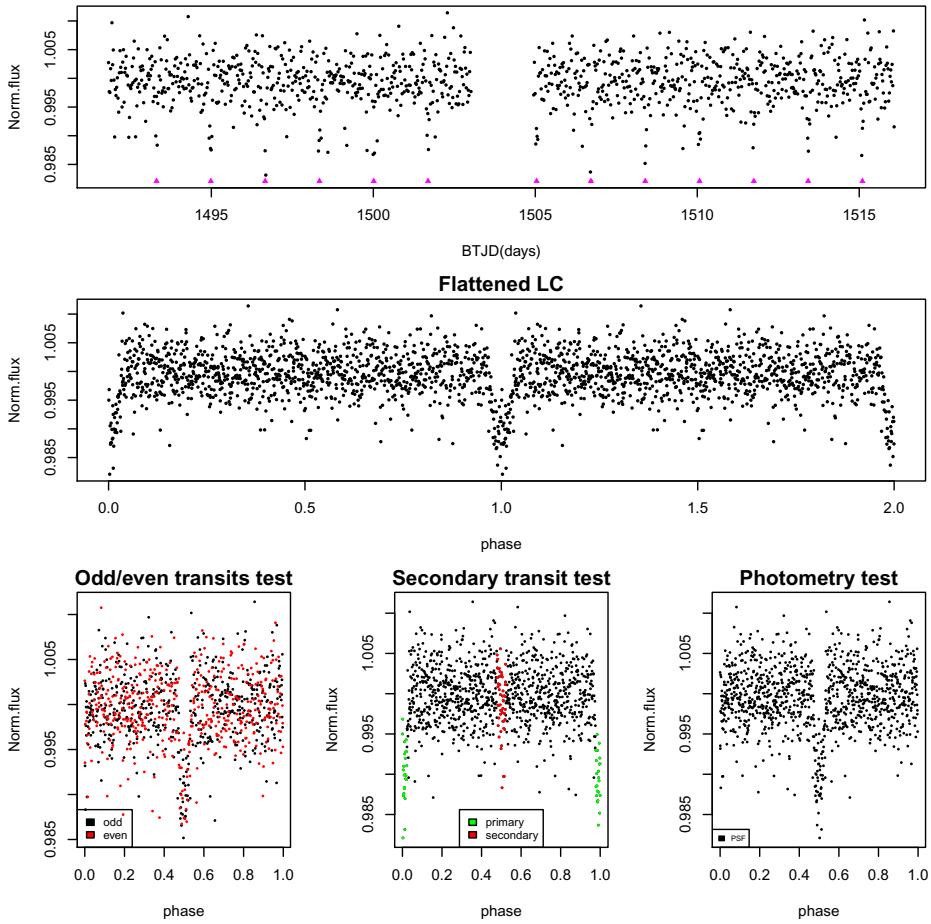

Figure 4.33: Validation tests for TIC 0149608236. Panels as in Figure 4.1.

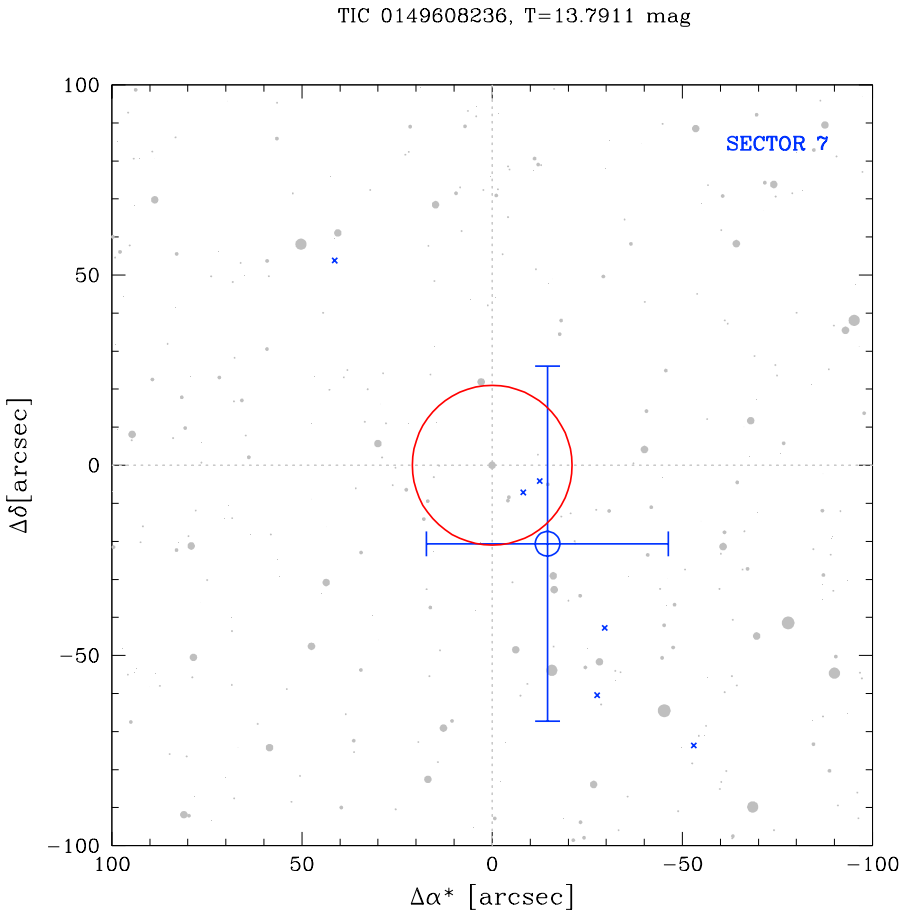

Figure 4.34: Finding chart for TIC 0149608236 which is a faint star and this is the reason why the centroids are not accurately calculated. Consequently, we could not use this chart to decide about the outcome of the candidate. Since it passed the first three validation tests, we kept it for further analysis.

4.8.4 TIC 0260119000

The fourth candidate exoplanet we found in VLP4 is orbiting the star with TIC 0260119000 which is observed by TESS in two sectors, Sector 8 and 9. The host star has a magnitude of $T = 13.45$ mag with a dilution factor equal to $dil \sim 0.37$. A period of $P \sim 2.94$ days has been recovered from the BLS search for the candidate and 17 transits are observed as shown in the top panel of Figure 4.35. As mentioned before, if the host star is faint, like TIC 0260119000, the centroid test can not provide us accurate information to help us decide for the fate of the candidate (Figure 4.36). Since the candidate around TIC 0260119000 succeeded the other validation tests we kept it in our list.

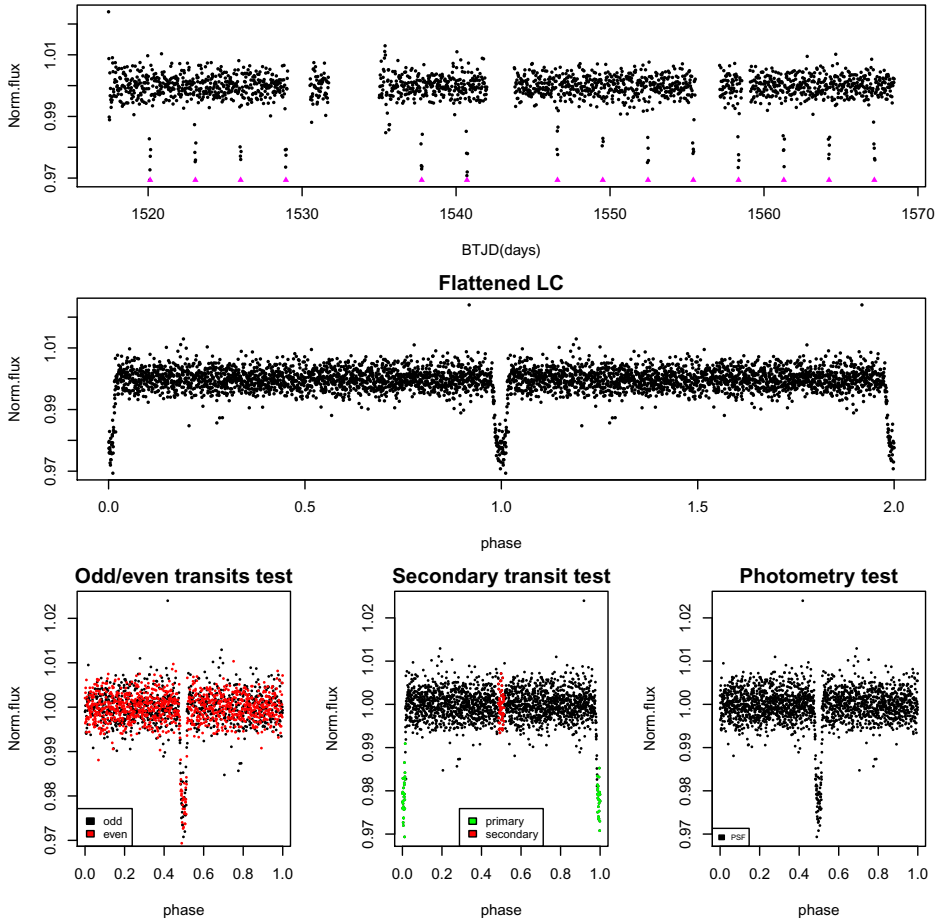

Figure 4.35: Validation tests for TIC 0260119000. Panels as in Figure 4.1.

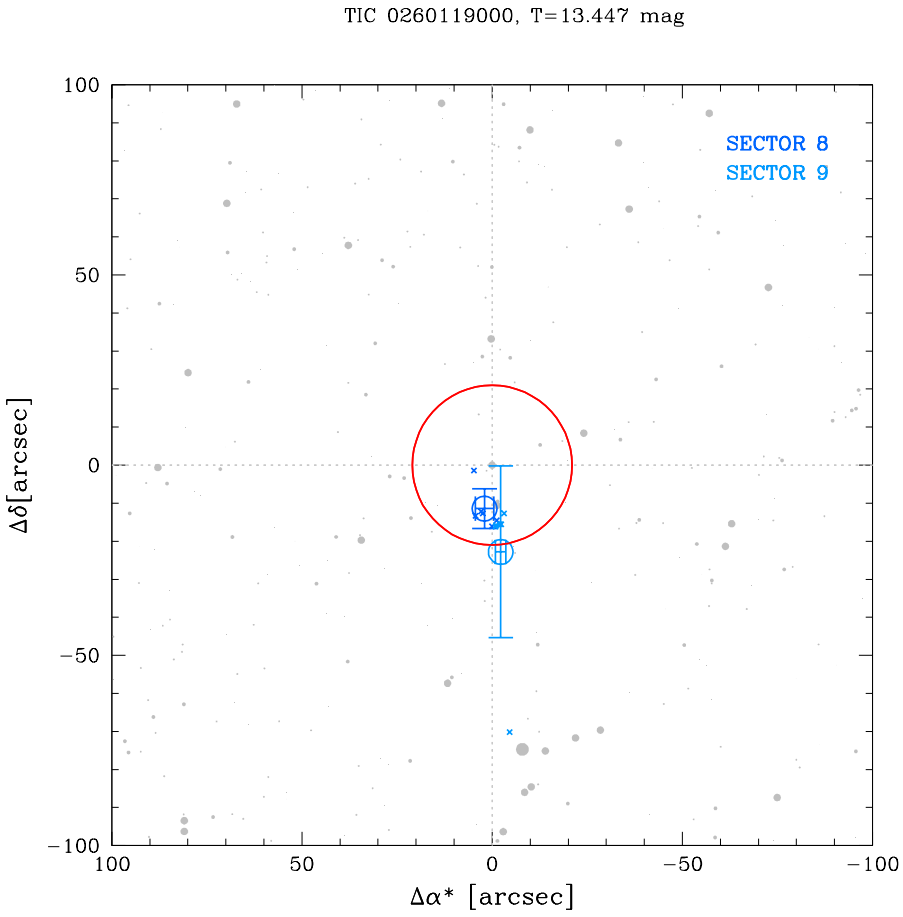

Figure 4.36: Finding chart for TIC 0260119000, used for the centroid test as described in Section 3.3.4.

4.8.5 TIC 0270846098

The last and fifth candidate exoplanet discovered in VLP4 is orbiting the star with TIC 0270846098 which is observed by TESS in two sectors, Sector 8 and 9. The host star has a magnitude of $T = 10.24$ mag with a dilution factor almost equal to zero, $dil \sim 0.007$. A period of $P \sim 2.12$ days has been recovered from the BLS search for the candidate and 23 transits are observed by TESS as shown in the top panel of Figure 4.37, along with the first three validation tests. The mean centroids, taking into account the error bars, seem to be concentrated on the host star as shown in Figure 4.38.

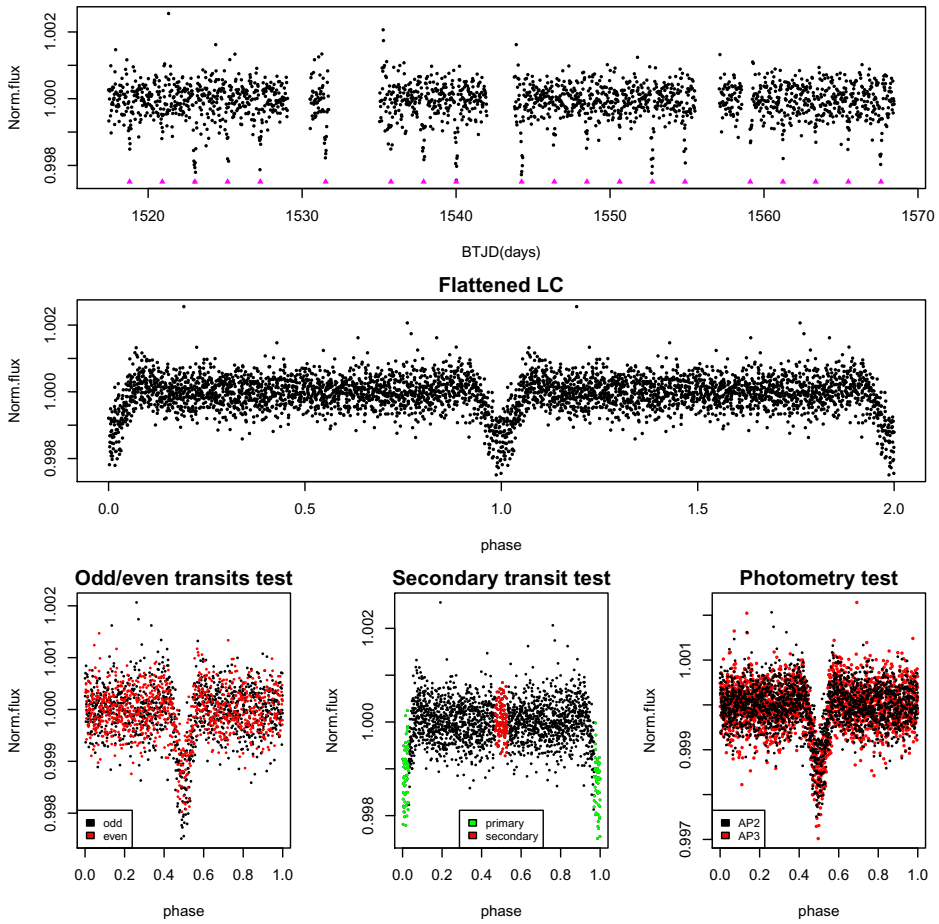

Figure 4.37: Validation tests for TIC 0270846098. Panels as in Figure 4.1.

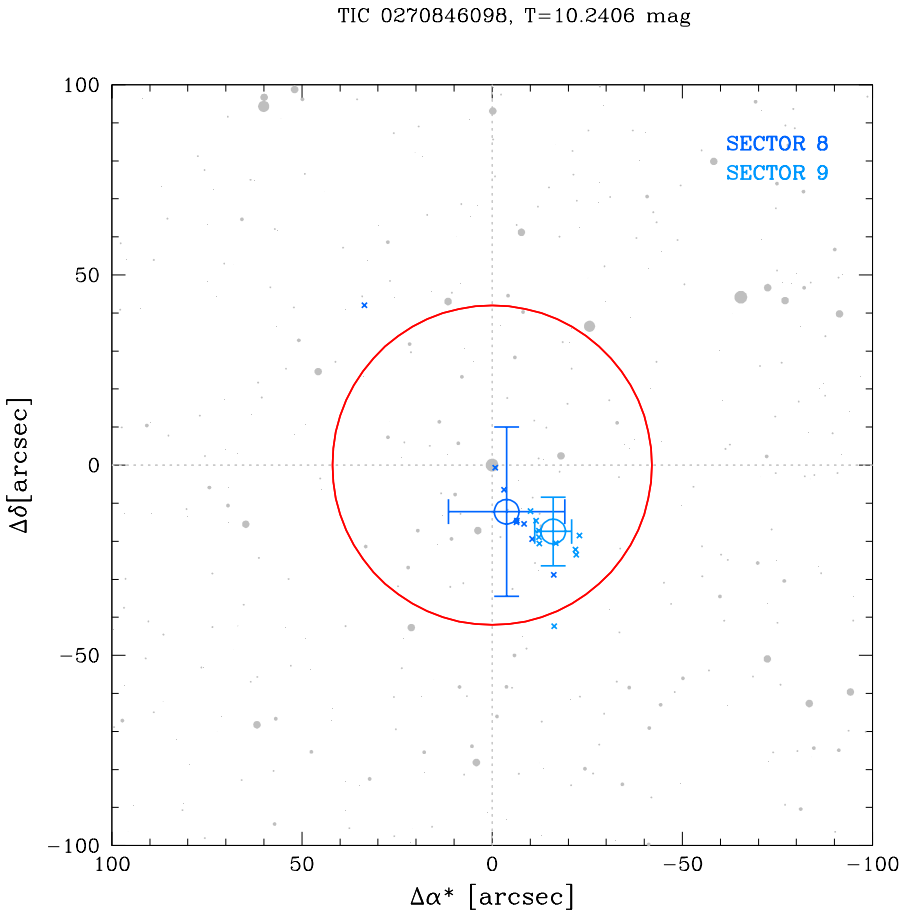

Figure 4.38: Finding chart for TIC 0270846098, used for the centroid test as described in Section 3.3.4.

4.9 Vela Puppis - Population V

The Vela Puppis - Population V (VLP5) is the fifth young population identified by Cantat-Gaudin et al. (2019) and has an age of 25^{+10}_{-5} Myr. It is observed by TESS in the Southern ecliptic hemisphere and we discovered two candidates orbiting stars in VLP5.

4.9.1 TIC 0097921547

The first candidate exoplanet we discovered in VLP5 is orbiting the star with TIC 0097921547 which is observed by TESS in Sector 7. The host star has a magnitude of $T = 11.05$ mag with a dilution factor almost equal to zero ($dil = 0.00055$).

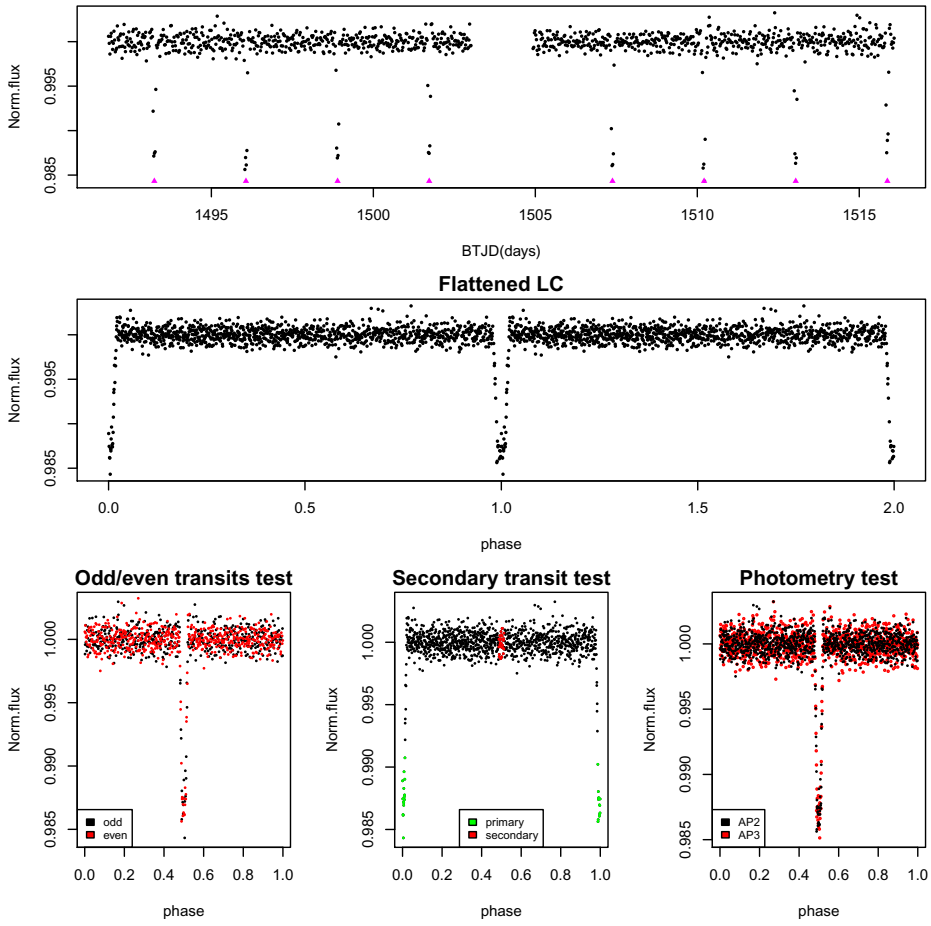

Figure 4.39: Validation tests for TIC 0097921547. Panels as in Figure 4.1.

A period of $P \sim 2.83$ days has been recovered from the BLS search for the candidate and 8 transits are observed by TESS as shown in the

top panel of Figure 4.39, along with the first three validation tests in the bottom panel. The mean centroid of Sector 7 are concentrated on the host star, which means that the transits are occurring on TIC 0097921547 and not in a nearby star, as shown in Figure 4.40.

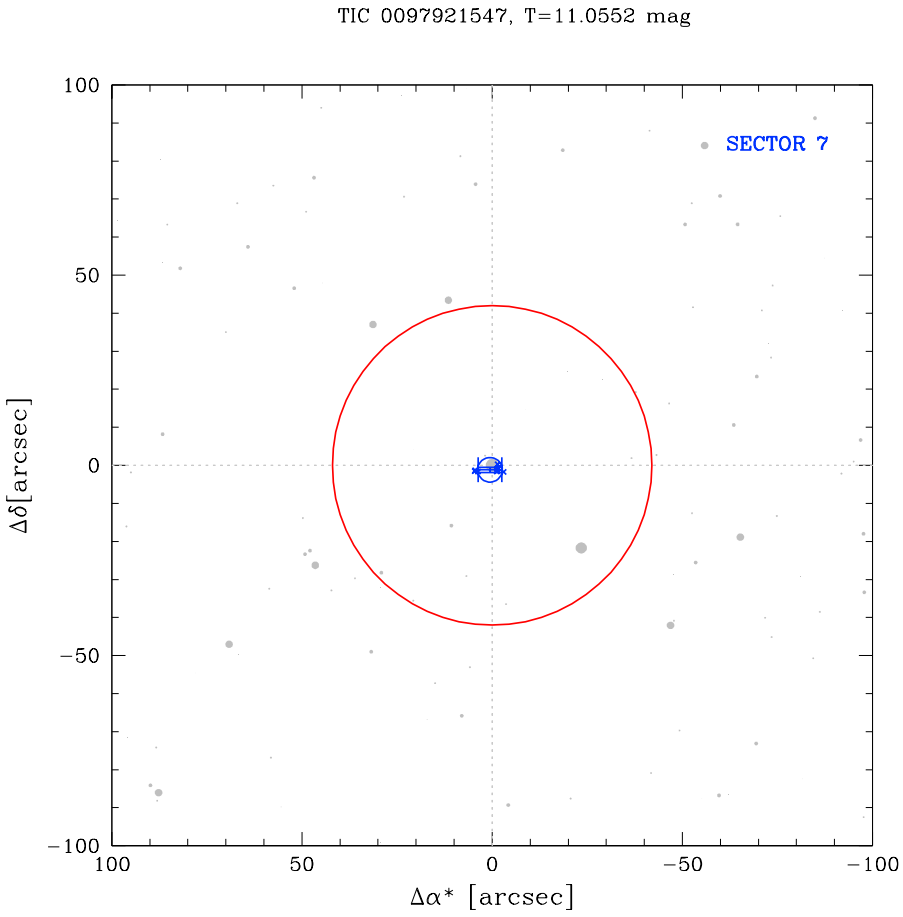

Figure 4.40: Finding chart for TIC 0097921547, used for the centroid test as described in Section 3.3.4.

4.9.2 TIC 0098161270

The second candidate exoplanet we discovered in VLP5 is orbiting the star with TIC 0098161270 which is observed by TESS in Sector 7. The host star has a magnitude of $T = 11.53$ mag with a dilution factor equal to $dil \sim 0.02$. A period of $P \sim 1.22$ days has been recovered from the BLS search for the candidate and 19 transits are observed by TESS as shown in the top panel of Figure 4.41, along with the first three validation tests in the bottom panel. The mean centroid of Sector 7 are concentrated on the host star, which means that the transits are occurring on TIC 0098161270 as shown in Figure 4.42.

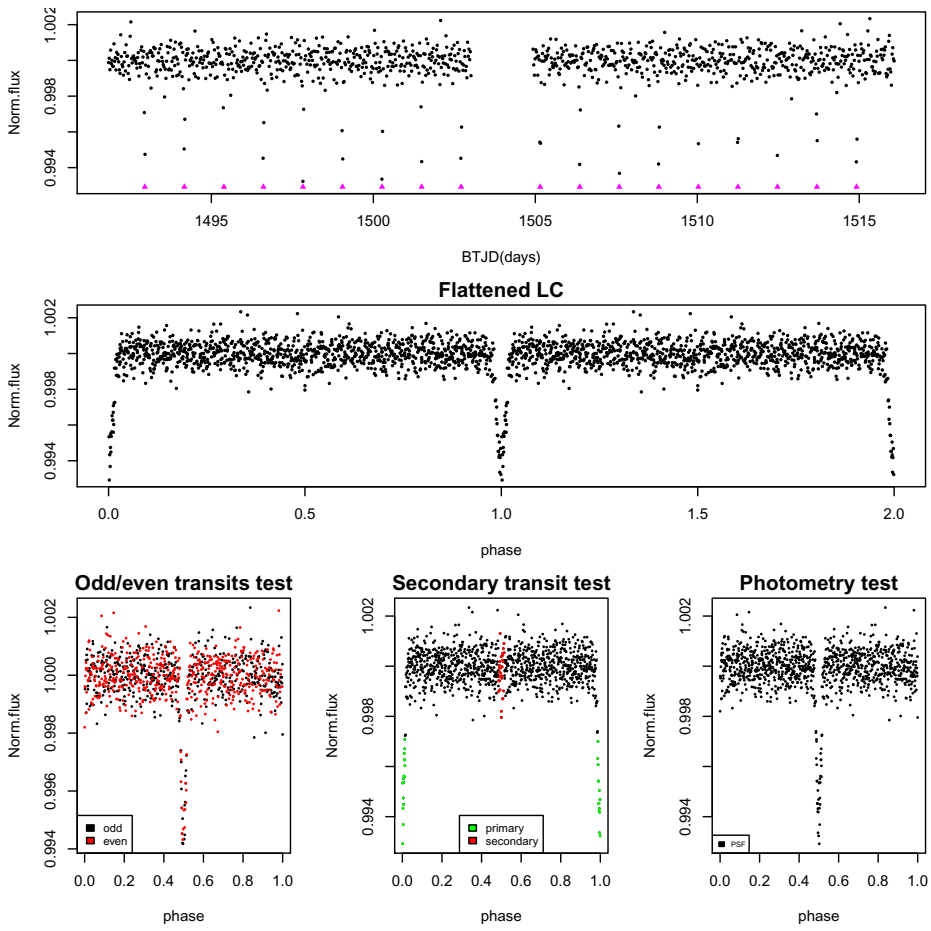

Figure 4.41: Validation tests for TIC 0098161270. Panels as in Figure 4.1.

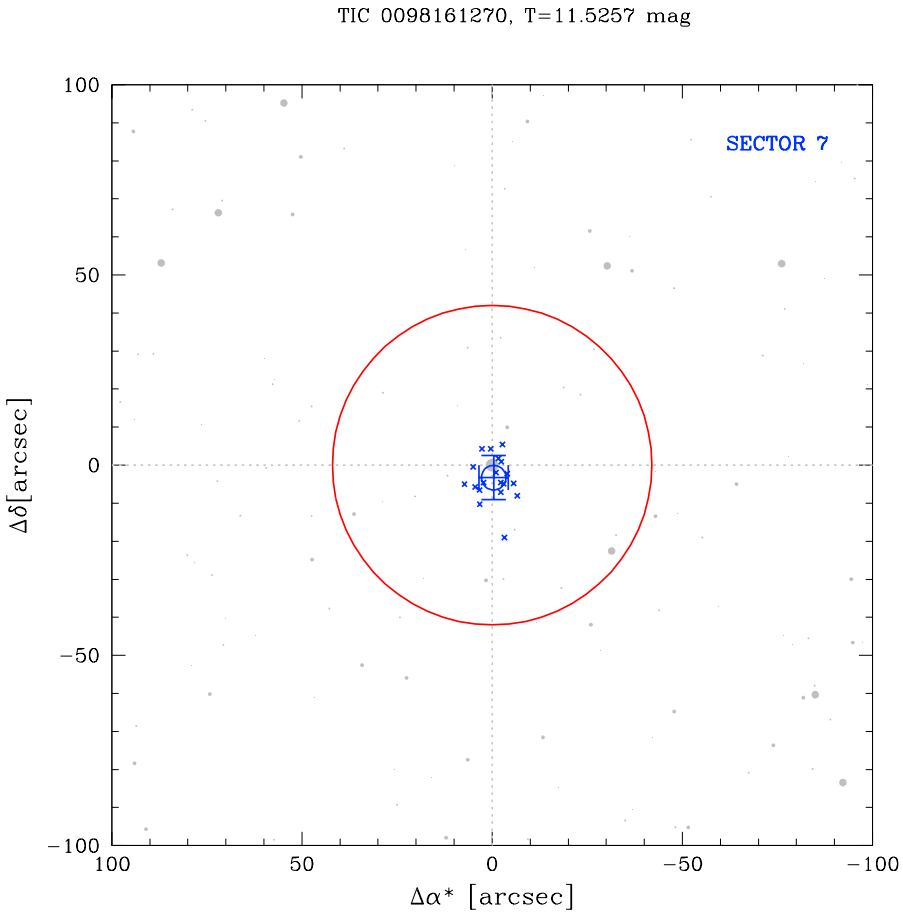

Figure 4.42: Finding chart for TIC 0098161270, used for the centroid test as described in Section 3.3.4.

4.10 Vela Puppis - Population VI

The Vela Puppis - Population VI (VLP6) is the sixth young population identified by Cantat-Gaudin et al. (2019) and has an age of 20^{+5}_{-5} Myr. It is observed by TESS in the Southern ecliptic hemisphere and we identified two candidates orbiting stars in VLP6.

4.10.1 TIC 0146129313

The first candidate exoplanet discovered in VLP6 is orbiting the star with TIC 0146129313 which is observed in two sectors of TESS, Sector 7 and 8. The host star has a magnitude of $T = 10.74$ mag with a dilution factor equal to $dil \sim 0.48$.

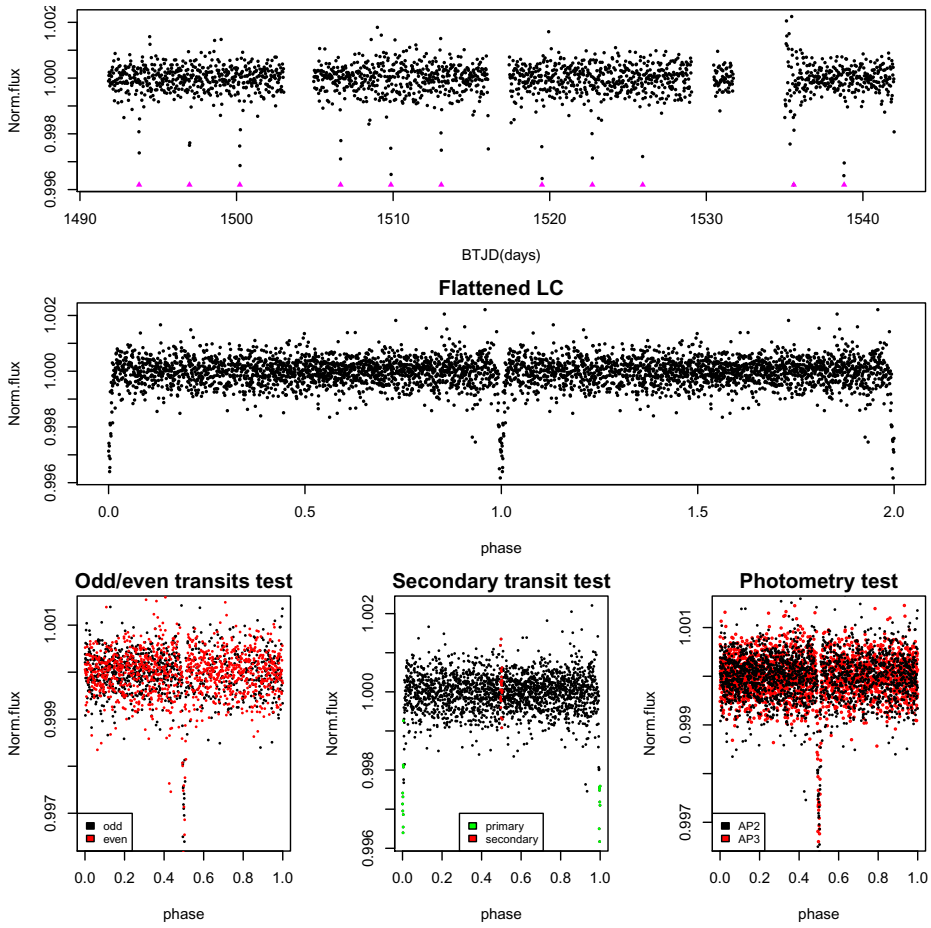

Figure 4.43: Validation tests for TIC 0146129313. Panels as in Figure 4.1.

A period of $P \sim 3.22$ days has been recovered from the BLS search for the candidate and 12 transits are observed by TESS as shown in the

top panel of Figure 4.43, along with the first three validation tests in the bottom panel. In Figure 4.44 its evident that there are two stars close to each other, the host star TIC 0146129313 positioned in the center of the finding chart and a neighbor star TIC 0146129309 on the right side (Section 4.11.1). The BLS search recovered a candidate with a similar period for both of them and from the centroid tests (Figure 4.44 and 4.48) its not clear in which star the transits are occurring. Both of the candidates have passed successfully the first three validation tests. The most probable scenario is that the candidate exoplanet is around TIC 0146129309, but we decided to progress both of them in our next steps of our analysis to acquire more information.

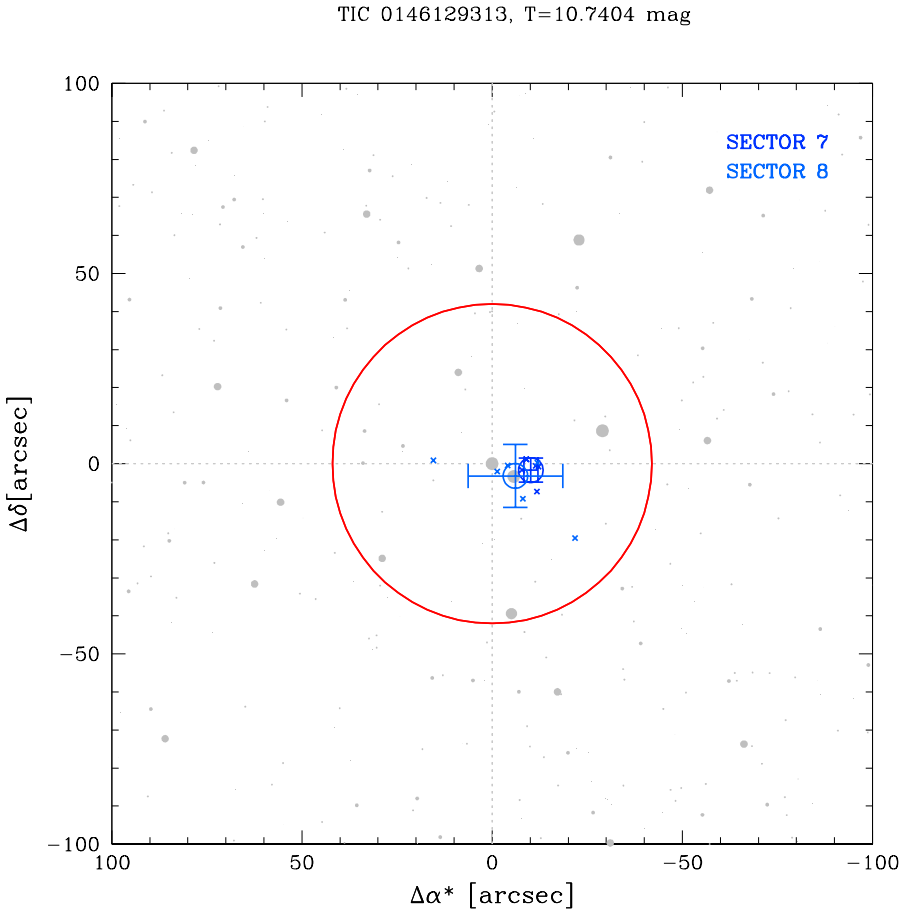

Figure 4.44: Finding chart for TIC 0146129313, used for the centroid test as described in Section 3.3.4.

4.10.2 TIC 0145582529

The second candidate discovered in VLP6 is orbiting the star with TIC 0145582529 which is observed in two sectors of TESS, Sector 7 and 8. The host star has a magnitude of $T = 15.46$ mag with a dilution factor equal to $dil \sim 0.095$. A period of $P \sim 2.22$ days has been recovered from the BLS search for the candidate and 21 transits are observed by TESS as shown in the top panel of Figure 4.45, along with the first three validation tests in the bottom panel. TIC 0145582529 is a faint star, so in this case we could not take a definite decision for the candidate by inspecting only Figure 4.46. Taking into consideration that the candidate passed all the other validation tests we kept it in our list for further analysis.

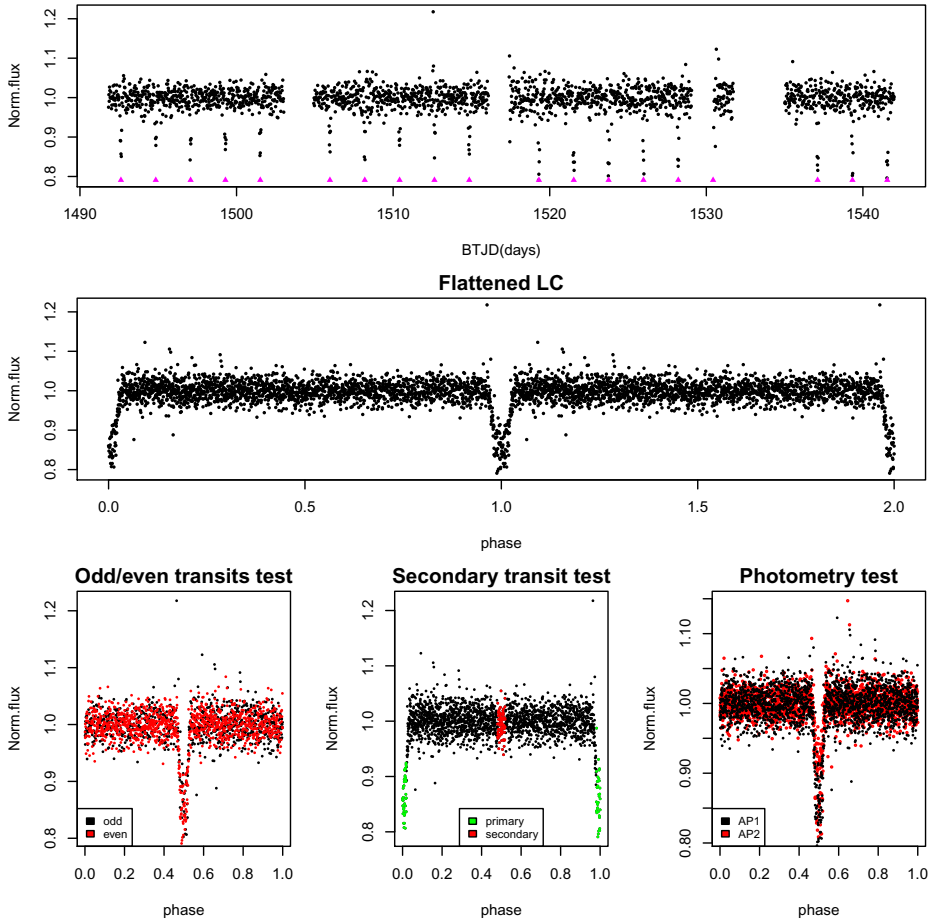

Figure 4.45: Validation tests for TIC 0145582529. Panels as in Figure 4.1.

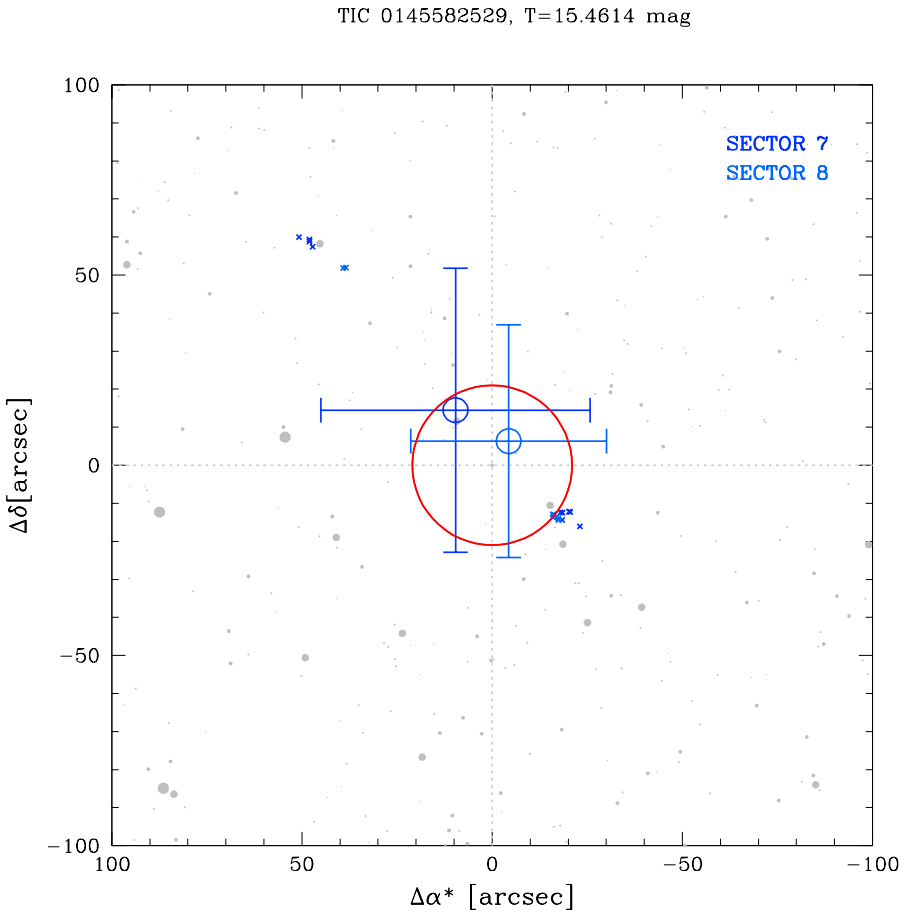

Figure 4.46: Finding chart for TIC 0145582529, used for the centroid test as described in Section 3.3.4. The host is a faint star so the centroids could not reliably estimated. Considering that the candidate passed the other validation tests we progressed it to the next steps of our analysis.

4.11 Vela Puppis - Population VII

The Vela Puppis - Population VII (VLP7) is the seventh and last young population identified by Cantat-Gaudin et al. (2019) in Vela region and is the youngest population with an age of 10^{+5}_{-3} Myr. It is observed by TESS in the Southern ecliptic hemisphere and we identified four candidates orbiting stars belonging to VLP7.

4.11.1 TIC 0146129309

The first candidate exoplanet discovered in VLP7 is around the star with TIC 0146129309 which is observed by TESS in Sectors 7 and 8. The host star has a magnitude of $T = 10.82$ mag with a dilution factor equal to $dil \sim 0.52$.

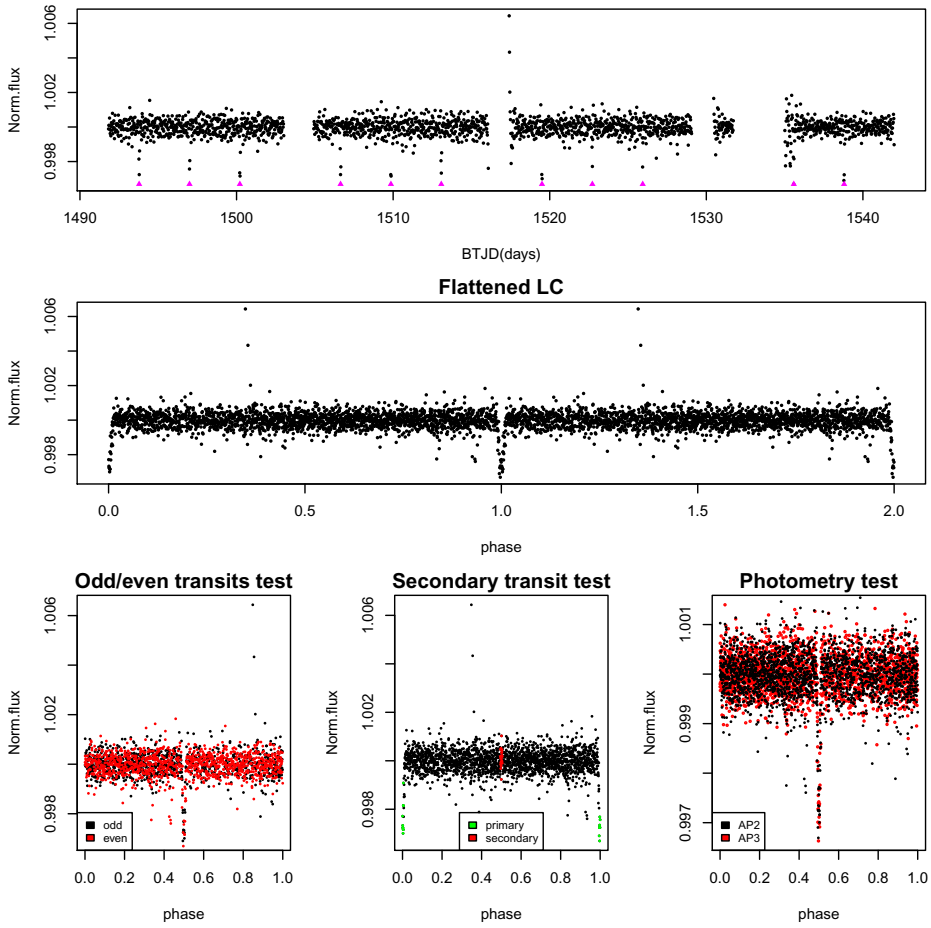

Figure 4.47: Validation tests for TIC 0146129309. Panels as in Figure 4.1.

A period of $P \sim 3.22$ days has been recovered from the BLS search for the candidate and 13 transits are observed by TESS as shown in the

top panel of Figure 4.47, along with the first three validation tests in the bottom panel. As mentioned in Section 4.10.1, TIC 0146129309 and TIC 0146129313 are in close proximity to each other and from the centroid tests (Figure 4.48 and 4.44) its not evident in which of the star the transits are occurring. Even though it seems that the candidate exoplanet with P$\sim$ 3.22 days is orbiting TIC 0146129309 we decided to progress both of them in the next steps of our analysis.

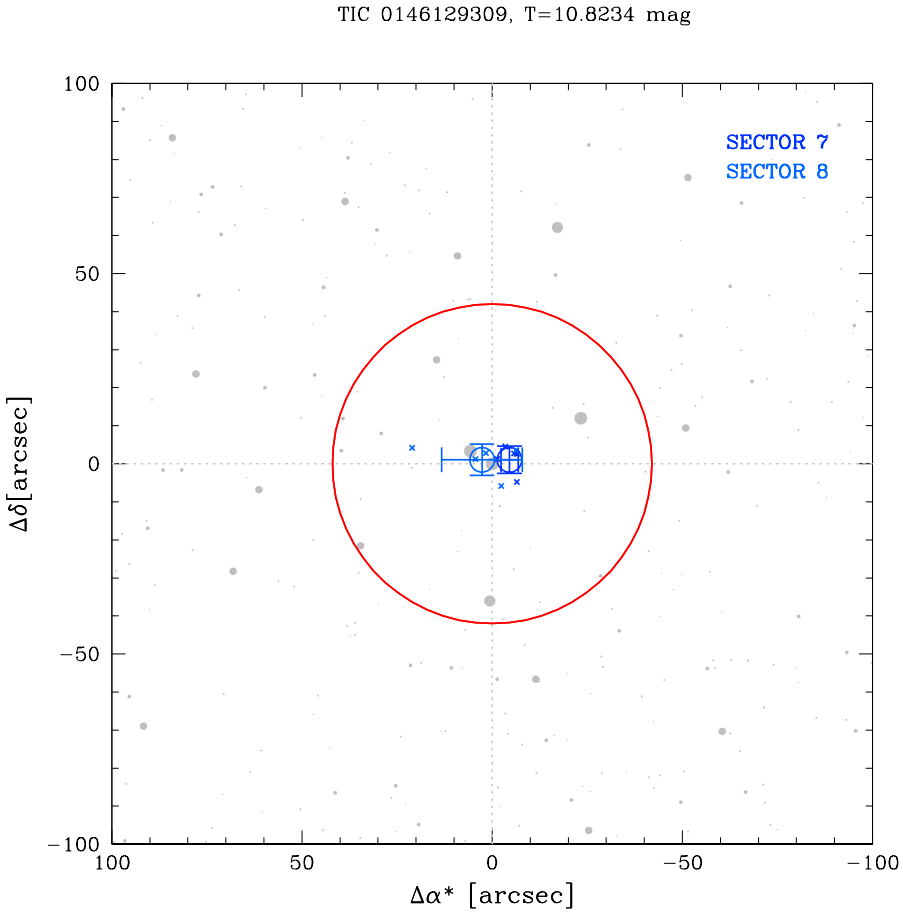

Figure 4.48: Finding chart for TIC 0146129309, used for the centroid test as described in Section 3.3.4.

4.11.2 TIC 0082369548

The second candidate we identified in VLP7 is orbiting the star with TIC 0082369548 which is observed in two sectors of TESS, Sector 8 and 9. The host star has a magnitude of $T = 13.38$ mag with a dilution factor equal to $dil \sim 0.14$. A period of $P \sim 0.58$ days has been recovered from the BLS search for the candidate and 76 transits are observed by TESS as shown in the top panel of Figure 4.49, along with the first three validation tests in the bottom panel. TIC 0082369548 is a faint star, so in this case we could not take a definite decision for the candidate by just inspecting only Figure 4.50. Taking into consideration that the candidate passed all the other validation tests we kept it in our list for further analysis.

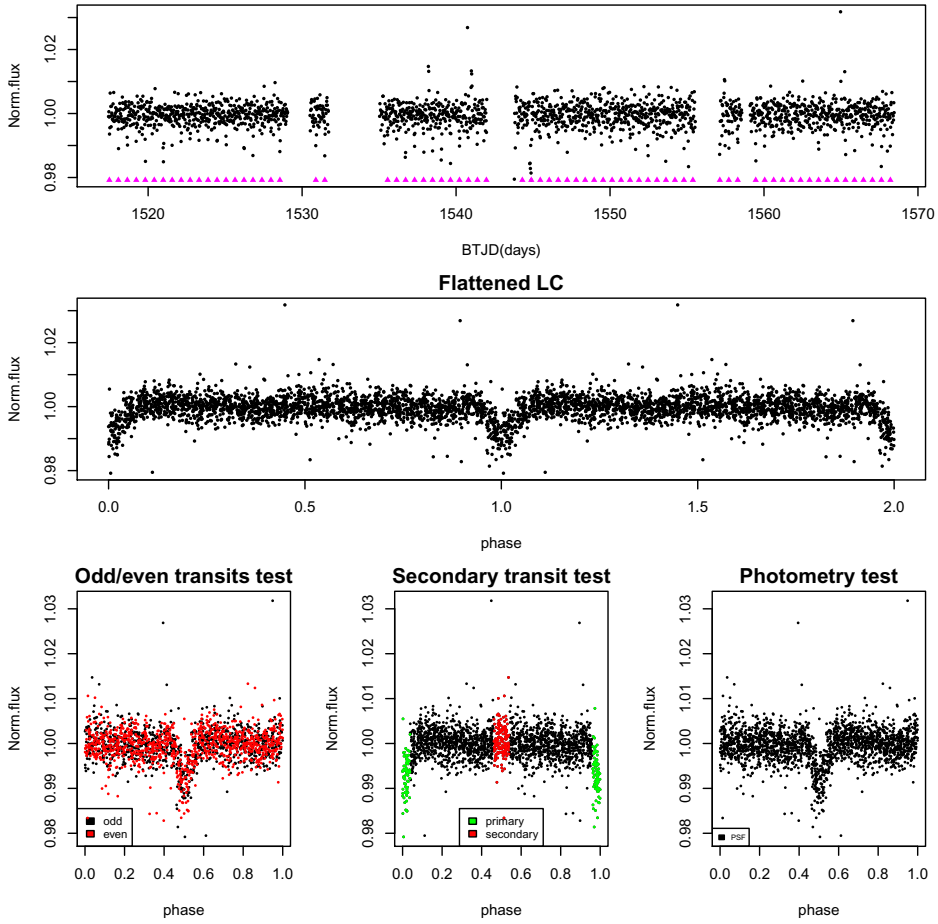

Figure 4.49: Validation tests for TIC 0082369548. Panels as in Figure 4.1.

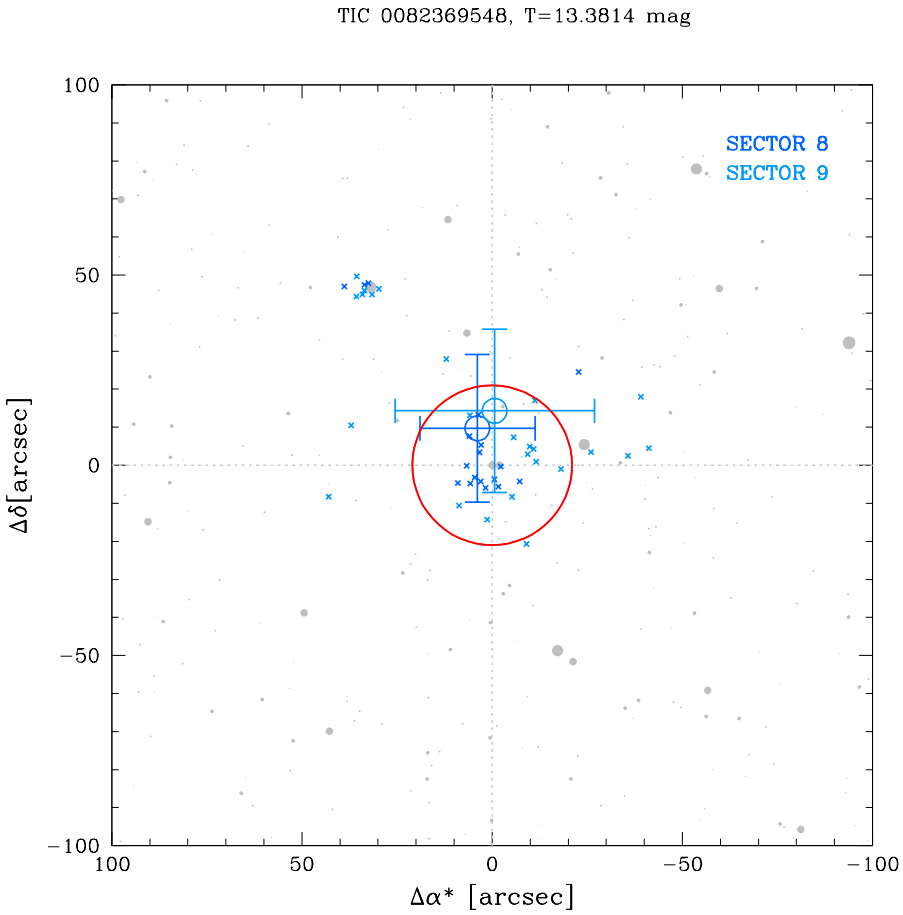

Figure 4.50: Finding chart for TIC 0082369548, used for the centroid test as described in Section 3.3.4. The host is a faint star so the centroids could not be reliably estimated. Considering that the candidate passed the other validation tests we progressed it to the next steps of our analysis.

4.11.3 TIC 0143497753

The third candidate recovered in VLP7 is orbiting around the star with TIC 0143497753 which is observed in two sectors of TESS, Sector 7 and 8. The host is a faint star with a magnitude of $T = 15.54$ mag and a dilution factor equal to $dil \sim 0.03$. A period of $P \sim 0.61$ days has been recovered from the BLS search for the candidate and 72 transits are observed by TESS as shown in the top panel of Figure 4.51, along with the first three validation tests in the bottom panel. As mentioned, TIC 0143497753 is a faint star and for this reason we could not take a definite decision for the candidate by just inspecting only Figure 4.52, because the centroids can not be reliably estimated for faint stars. Considering that the candidate succeeded all the other validation tests we progressed it for additional analysis.

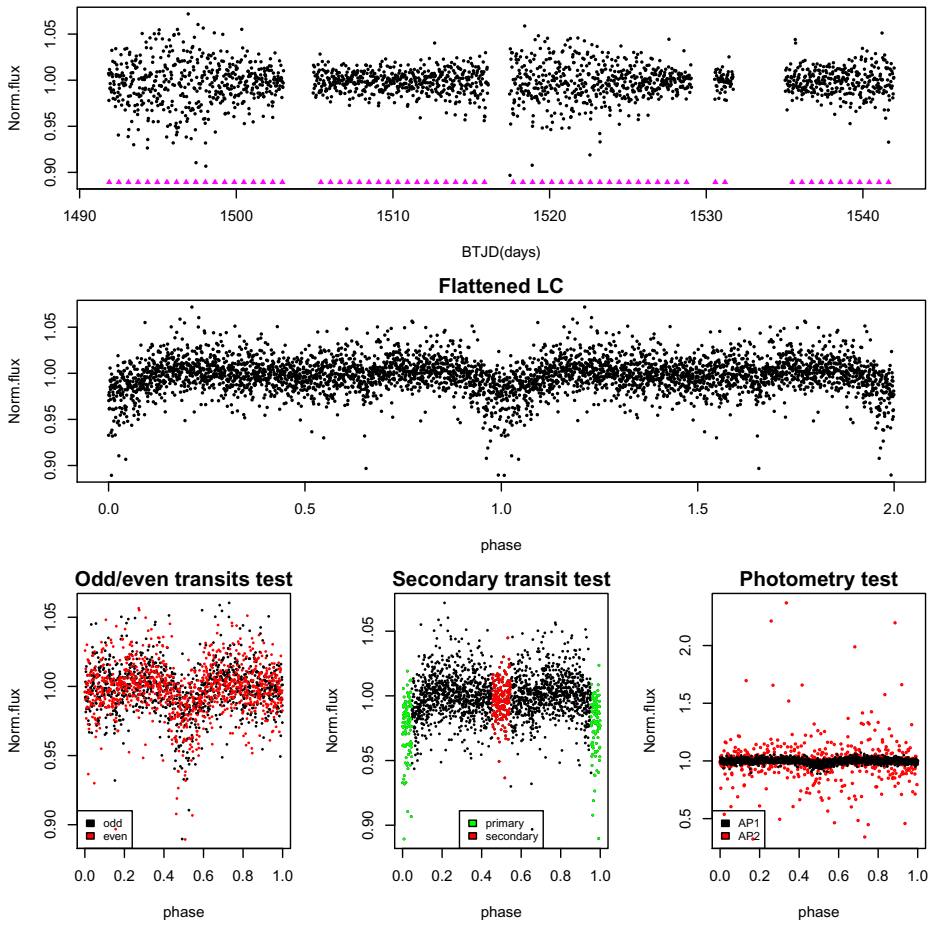

Figure 4.51: Validation tests for TIC 0143497753. Panels as in Figure 4.1.

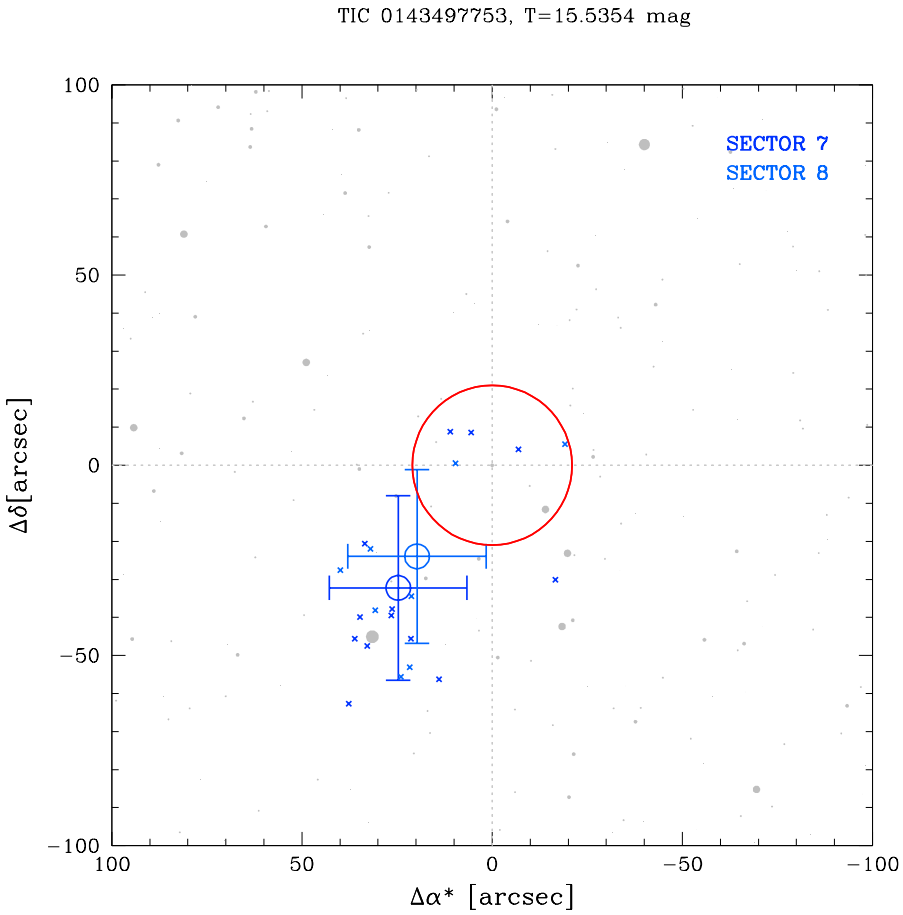

Figure 4.52: Finding chart for TIC 0082369548, used for the centroid test as described in Section 3.3.4. The host is a faint star so the centroids could not be reliably estimated. The candidate exoplanet passed all the other validation tests and we decided to keep it in our list for further analysis.

4.11.4 TIC 0184347065

The fourth and last candidate we discovered in VLP7 is orbiting around the star with TIC 0184347065 which is observed by TESS in Sector 8. The host is a faint star with a magnitude of $T = 15.68$ mag and a dilution factor equal to zero. A period of $P \sim 2.64$ days has been recovered from the BLS search for the candidate and 9 transits are observed by TESS as shown in the top panel of Figure 4.53, along with the first three validation tests in the bottom panel. Because TIC 0184347065 is a faint star we could not decide for the fate of the candidate by just inspecting Figure 4.54, because the centroids can not be reliably estimated for faint stars. The candidate passed all the other validation tests, so we progressed it for further analysis.

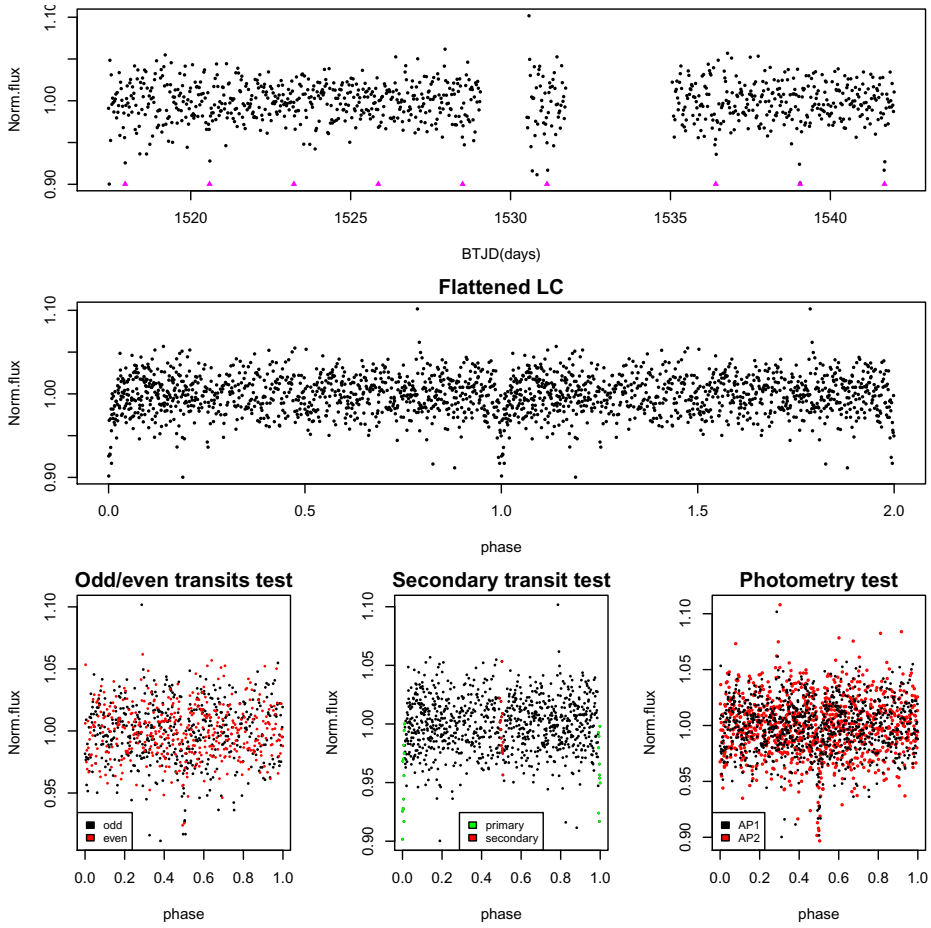

Figure 4.53: Validation tests for TIC 0184347065. Panels as in Figure 4.1.

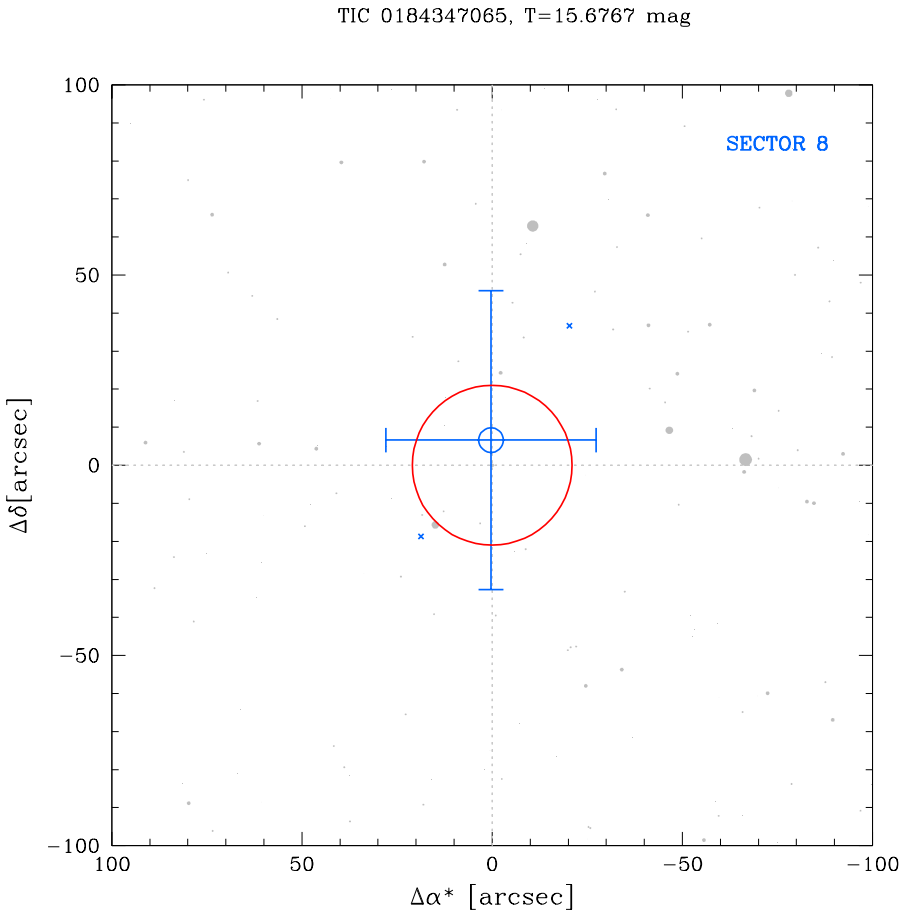

Figure 4.54: Finding chart for TIC 0082369548, used for the centroid test as described in Section 3.3.4. The host is a faint star so the centroids could not be reliably estimated. The candidate exoplanet passed all the other validation tests and we decided to keep it in our list and analyze it further.

Chapter 5

Transit modelling

5.1 Modeling of the transits

To model the transits of the candidate exoplanets mentioned in Chapter 4 we used `PyORBIT`[1](Malavolta 2016, Malavolta et al. 2018, see also Nardiello et al. 2021; Montalto et al. 2022) a python wrapper for the analysis of light curves, radial velocities, activity indexes and transit time variations. In our work we used it to model light curves showing transits. For the stars with TIC 0067646988 and TIC 0410214986, we found that are TESS Object of Interest (TOIs). As mentioned in Section 4.3.1 Irwin et al. (2018) published that TIC 0067646988 is actually a system consisting of a M-dwarf eclipsed by a brown dwarf secondary, with another distant visual brown dwarf companion. Regarding TIC 0410214986 or DS Tuc A (Section 4.2.2), it is confirmed that hosts an exoplanet with an orbital period of $\sim$ 8.14 days and a planetary radius of $\sim$0.5 R_J (Benatti et al. 2019a; Newton et al. 2019). Recently, Benatti et al. (2021) published an upper mass limit for the planet of 14.4 $M_\oplus$. Since the origin of the signals detected in TIC 0067646988 and TIC 0410214986 have already been defined and the objects around them are characterized, we did not model them with `PyORBIT` or calculated their False Positive Probability with `VESPA` in Section 5.2.

For each light curve of a candidate exoplanet we fitted the central time of transit (T_0), period (P), impact parameter (b), planetary-to-stellar-radius ratio ($R_P/R_\star$), stellar density ($\rho_\star$), and dilution factor (dil). The stellar parameters of the host stars, such as stellar radius ($R_\star$), mass ($M_\star$), effective temperature (T_{eff}), and gravity (logg) are determined from the all-sky PLATO Input Catalogue (PIC, Montalto et al. (2021b)) if available, from the TESS Input Catalogue (TIC, Stassun et al. (2019b)) and from the isochrone fitting we described in Section 2.2. More specifically, six of our host stars have stellar parameters determined from the PIC catalogue which we used for their modelling with PyORBIT. For the remaining host stars, we used

[1] `https://github.com/LucaMalavolta/PyORBIT`

the stellar parameters defined from the isochrones if they were main sequence stars otherwise from the TIC catalogue (Table 5.1). Moreover, we considered a quadratic limb-darkening law with Gaussian priors on the coefficients u_1, u_2, through a bilinear interpolation of the limb darkening grids published by Claret (2018) [2] and we adopted the parametrization by Kipping (2010). We have also included a jitter term (for transits observed in the same sector of TESS), to account possible TESS systematic errors and short term stellar activity noise. The local variability of the host star is also considered by the modelling routine by fitting a second degree polynomial to the out of transit points of the light curve. Each transit model is computed with the `batman` package (Kreidberg, 2015) considering a fixed circular orbital eccentricity ($e = 0$), with an exposure time of 1800 seconds, since we used the FFIs of TESS which have 30 min cadence, and an oversampling factor of 10 (Kipping, 2010).

The priors on stellar parameters used for the modelling are reported in Table 5.1. `PyORBIT` explored all the parameters in linear space and the global optimization of the parameters was made using the differential evolution code `PyDE`[3]. The parameters found from `PyDE` were then used as the starting point of the Bayesian analysis using the `emcee` package (Foreman-Mackey et al., 2013), which is a Markov chain Monte Carlo (MCMC) algorithm with an affine invariant ensemble sampler (Goodman & Weare, 2010). The number of walkers used to run the chains was set 10 times the number of free parameters and each model was executed for N number of steps, ranging from 100 000 to 300 000, adapted for each individual fit. We checked the convergence using the Gelman-Rubin statistics (Gelman & Rubin, 1992) which have a threshold value equal to $\hat{R} = 1.01$. Additionally, we performed an auto-correlation analysis of the chains by checking if they were longer than 100 times the estimated auto-correlation time and the latter changed by less than 1%. If these two conditions were satisfied then we considered the chains as converged. We also conservatively set the value of burn-in equal to a number bigger than the convergence point and a thinning factor equal to 100.

[2] `https://vizier.u-strasbg.fr/viz-bin/VizieR?-source=J/A+A/618/A20`
[3] `https://github.com/hpparvi/PyDE`

Table 5.1: Priors for the modelling of the 25 candidate exoplanets in our sample with PyORBIT

TIC	T_0 (BTJD)	P (days)	$M_\star$ ($M_\odot$)	$R_\star$ ($R_\odot$)	$\rho_\star$ ($\rho_\odot$)	LD_1	LD_2	*dil*	Ref.
0023846678	[1440, 1441]	[0.44, 0.48]	0.632±0.023	0.657±0.024	2.232±0.169	0.1665±0.10	0.4706±0.10	0.0	(3)
0038820496	[1325, 1326]	[0.64, 0.67]	0.253±0.020	0.279±0.008	11.617±0.116	0.1711±0.10	0.4952±0.10	0.0	(3)
0075825581	[1516.5, 1517.5]	[0.3, 1]	0.193±0.022	0.388±0.032	3.316±0.837	0.4052±0.10	0.2517±0.10	0.25±0.05	(1)
0082369548	[1516, 1517.5]	[0.57, 0.6]	0.771±0.049	1.010±0.114	0.750±0.259	0.4648±0.10	0.2022±0.10	0.14±0.05	(1)
0097921547	[1493, 1494]	[2.5, 3.5]	1.484±0.022	1.413±0.058	0.526±0.065	0.2655±0.10	0.2350±0.10	0.0005±0.001	(1)
0098161270	[1492, 1493.5]	[1, 1.5]	1.211±0.107	1.280±0.075	0.577±0.114	0.3090±0.10	0.2272±0.10	0.02±0.05	(2)
0129877093	[1491.5, 1493]	[1.5, 1.7]	1.100±0.022	0.997±0.022	1.111±0.078	0.3341±0.10	0.2257±0.10	0.13±0.05	(1)
0132620309	[1491.5, 1492.5]	[0.9, 1.2]	0.626±0.024	0.648±0.025	2.299±0.184	0.2012±0.10	0.4088±0.10	0.19±0.05	(3)
0143497753	[1492, 1493]	[0.60, 1.0]	0.611±0.024	0.629±0.024	2.457±0.192	0.1668±0.10	0.4649±0.10	0.03±0.05	(1)
0145582529	[1491.5, 1493]	[2.1, 2.4]	0.611±0.023	0.628±0.023	2.461±0.180	0.1895±0.10	0.4243±0.10	0.095±0.05	(3)
0146129309	[1492.5, 1494]	[3.1, 3.3]	1.406±0.124	1.770±0.116	0.255±0.055	0.2996±0.10	0.2294±0.10	0.52±0.05	(2)
0146129313	[1492.5, 1494]	[3.1, 3.3]	1.455±0.252	1.840±0.085	0.234±0.056	0.2949±0.10	0.2289±0.10	0.48±0.05	(3)
0149608236	[1493.5, 1495]	[1.5, 1.8]	0.802±0.037	0.812±0.060	1.499±0.337	0.4510±0.10	0.1872±0.10	0.14±0.05	(1)
0152084108	[1490.5, 1491.5]	[0.45, 0.90]	0.946±0.033	0.832±0.021	1.645±0.132	0.3911±0.10	0.2034±0.10	0.40±0.05	(1)
0184347065	[1516, 1518]	[2.5, 2.7]	0.523±0.023	0.526±0.019	3.598±0.231	0.1669±0.10	0.4621±0.10	0.0±0.0	(3)
0260119000	[1519.5, 1521]	[2.8, 3.1]	0.820±0.030	0.827±0.058	1.450±0.310	0.3732±0.10	0.2061±0.10	0.37±0.05	(1)
0131743355	[1493, 1495]	[6.3, 6.7]	2.840±0.392	1.725±0.047	0.553±0.095	0.1482±0.10	0.2417±0.10	0.0032±0.01	(3)
0032067057	[1517.5, 1518.5]	[3.4, 3,7]	0.566±0.023	0.574±0.022	2.995±0.219	0.2131±0.10	0.3952±0.10	0.045±0.05	(3)
0270846098	[1517.5, 1519]	[2.0, 2.2]	1.471±0.129	2.067±0.133	0.666±0.067	0.2937±0.10	0.2288±0.10	0.008±0.01	(2)
0092896631	[1519, 1520]	[5.5, 5.7]	1.340±0.119	1.855±0.149	0.210±0.054	0.2975±0.10	0.2294±0.10	0.00077±0.0001	(2)
0123378551	[1495.5, 1497]	[10.9, 11.2]	1.275±0.112	1.397±0.097	0.516±0.115	0.3065±0.10	0.2279±0.10	0.00075±0.0001	(2)
0133260600	[1492, 1494]	[1, 1.5]	0.750±0.026	1.061±0.050	0.628±0.091	0.4808±0.10	0.1692±0.10	0.18±0.05	(3)
0014091633	[1440, 1442]	[5.0, 6]	1.269±0.025	1.210±0.025	0.716±0.047	0.3069±0.10	0.2278±0.10	0.0	(1)
0140513181	[1517.8, 1518.4]	[0.85,1]	0.638±0.024	0.618±0.023	2.378±0.179	0.2312±0.10	0.3782±0.10	0.21±0.1	(3)
0393126088	[1468, 1469]	[0.3,0.4]	0.521±0.016	0.519±0.020	3.660±0.185	0.1668±0.10	0.4647±0.10	0.007±0.005	(3)

(1) This work, through isochrone fitting; (2) PIC (Montalto et al., 2021b); (3) TIC (Stassun et al., 2019b)

In Table 5.2 we report the results of the transit fitting for the candidate exoplanets detected in our sample. For six of our candidates (depicted with * in Table 5.2) `PyORBIT` resulted in a transit model that has an impact parameter (b) bigger than 1. In these cases we can only report a lower limit of their planetary radius as an approximation. Three of these candidates (with $b > 1$) and also TIC 0133260600 ($b \sim 1$) have a planet radius bigger than 28 $R_\oplus$ or 2.5 R_J, which is usually a limit a lot of studies are imposing on their candidate's radius due to the doubtful nature of the planet above it. Considering that these candidates are young and since there are no other indicators imposing that these candidates with $R_P > 2.5 R_J$ are false positives, we decided to keep them in our list for future investigation.

Three of our candidates TIC 0038820496, TIC 0075825581, and TIC 0152084108 are mini Neptune ($R_P \sim 3.5\ R_\oplus$), nine of them (TIC 0023846678, TIC 0082369548, TIC 0129877093, TIC 0143497753, TIC 0149608236, TIC 0270846098, TIC 92896631, TIC 140513181, and TIC 393126088) belong in the regime of Neptune to super Neptune planets ($3.9\ R_\oplus \leq R_P < 11.2\ R_\oplus$), and the remaining thirteen candidates are Giant planets ($R_P \geq 11.2\ R_\oplus$). Moreover, two of them TIC 0131743355 and TIC 0014091633 are TOIs with a suspected planet candidate around them but not confirmed yet. Three of our Giant planet candidates (TIC 0260119000, TIC 0033260600, and TIC 0146129309) and TIC 0092896631 belong to the Community TESS Objects of Interest (CTOIs) list and based on the information found on the Exoplanet Follow-up Observing Program (ExoFOP) website[4] are dispositioned as hosts of a possible planet candidate. Regarding TIC 0146129313 and TIC 0146129309, the transit modelling resulted in a similar period of $P \sim 3.21$ days and a planet candidate with $R_P \sim 5\ R_J$. This behavior was expected as we mentioned in Section 4.10.1 and 4.11.1, because the two stars are close to each other (Figure 4.44 and 4.48) and it is not clear which is the host star of the candidate. The most probable scenario is that the candidate exoplanet is around TIC 0146129309 and similar suggestions are found on the ExoFOP website. For the remaining objects there are no reports of a candidate exoplanet around them in the literature, so these are new detections awaiting for confirmation. The candidate exoplanets we discovered belong in 10 different young associations and moving groups with ages ranging from 10 Myr to 50 Myr.

[4] `https://exofop.ipac.caltech.edu/tess/`

Table 5.2: Results of transit modelling for the 25 candidate exoplanets in our sample with PyORBIT

TIC	P (days)	T_0 (BTJD)	$R_P/R_\star$	b	α (AU)	$\rho_\star$ ($\rho_\odot$)	i (deg)	R_P (R_J)	R_P ($R_\oplus$)
0023846678	$0.453085^{+0.000052}_{-0.000052}$	$1440.5398^{+0.0228}_{-0.0232}$	$0.104^{+0.002}_{-0.002}$	$0.06^{+0.07}_{-0.04}$	$0.0087^{+0.0004}_{-0.0004}$	$1.543^{+0.161}_{-0.151}$	$88.6^{+0.9}_{-1.4}$	$0.66^{+0.02}_{-0.02}$	$7.45^{+0.31}_{-0.31}$
0038820496	$0.655382^{+0.000029}_{-0.000029}$	$1325.6610^{+0.0011}_{-0.0011}$	$0.110^{+0.054}_{-0.008}$	$0.78^{+0.15}_{-0.07}$	$0.0070^{+0.0002}_{-0.0002}$	$4.998^{+0.001}_{-0.002}$	$81.6^{+0.8}_{-1.6}$	$0.30^{+0.14}_{-0.02}$	$3.38^{+1.64}_{-0.29}$
0075825581	$0.376471^{+0.000050}_{-0.000056}$	$1517.1999^{+0.0041}_{-0.0036}$	$0.087^{+0.008}_{-0.006}$	$0.30^{+0.27}_{-0.20}$	$0.0056^{+0.0007}_{-0.0007}$	$2.929^{+0.847}_{-0.906}$	$84.4^{+3.8}_{-5.5}$	$0.33^{+0.04}_{-0.03}$	$3.71^{+0.48}_{-0.43}$
0082369548	$0.583034^{+0.000034}_{-0.000034}$	$1516.9015^{+0.0018}_{-0.0018}$	$0.092^{+0.179}_{-0.006}$	$0.78^{+0.35}_{-0.12}$	$0.0116^{+0.0025}_{-0.0024}$	$0.654^{+0.337}_{-0.343}$	$72.2^{+4.7}_{-18.7}$	$0.93^{+1.69}_{-0.19}$	$10.56^{+18.98}_{-1.58}$
0097921547	$2.828052^{+0.000293}_{-0.000291}$	$1493.2395^{+0.0012}_{-0.0012}$	$0.118^{+0.002}_{-0.001}$	$0.73^{+0.03}_{-0.03}$	$0.0446^{+0.0025}_{-0.0025}$	$0.528^{+0.064}_{-0.062}$	$83.7^{+0.4}_{-0.5}$	$1.62^{+0.07}_{-0.07}$	$18.22^{+0.81}_{-0.80}$
0098161270*	$1.220576^{+0.000074}_{-0.000074}$	$1492.9449^{+0.0007}_{-0.0007}$	$0.283^{+0.137}_{-0.117}$	$1.17^{+0.15}_{-0.13}$	$0.0244^{+0.0017}_{-0.0016}$	$0.629^{+0.079}_{-0.071}$	$73.2^{+2.2}_{-2.0}$	> 1.80	> 20.25
0129877093	$1.563601^{+0.000643}_{-0.000724}$	$1492.2723^{+0.0073}_{-0.0068}$	$0.040^{+0.008}_{-0.003}$	$0.49^{+0.33}_{-0.37}$	$0.0271^{+0.0008}_{-0.0008}$	$1.106^{+0.078}_{-0.078}$	$85.1^{+3.6}_{-3.2}$	$0.39^{+0.08}_{-0.03}$	$4.40^{+0.94}_{-0.42}$
0132620309	$1.072297^{+0.000049}_{-0.000050}$	$1491.8395^{+0.0012}_{-0.0012}$	$0.371^{+0.080}_{-0.071}$	$0.95^{+0.11}_{-0.11}$	$0.0177^{+0.0008}_{-0.0007}$	$2.400^{+0.168}_{-0.168}$	$80.6^{+1.1}_{-1.0}$	$2.34^{+0.51}_{-0.45}$	$26.24^{+5.73}_{-5.12}$
0143497753	$0.614278^{+0.000070}_{-0.000071}$	$1492.4987^{+0.0031}_{-0.0029}$	$0.161^{+0.004}_{-0.004}$	$0.07^{+0.08}_{-0.05}$	$0.0111^{+0.0006}_{-0.0006}$	$1.963^{+0.219}_{-0.228}$	$88.8^{+0.8}_{-1.2}$	$0.98^{+0.04}_{-0.04}$	$11.07^{+0.54}_{-0.53}$
0145582529	$2.224800^{+0.000121}_{-0.000122}$	$1492.6125^{+0.0016}_{-0.0016}$	$0.374^{+0.005}_{-0.005}$	$0.05^{+0.06}_{-0.04}$	$0.0205^{+0.0009}_{-0.0008}$	$0.948^{+0.067}_{-0.063}$	$89.5^{+0.3}_{-0.5}$	$2.28^{+0.09}_{-0.09}$	$25.64^{+1.03}_{-1.01}$
0146129309*	$3.215134^{+0.000181}_{-0.000182}$	$1493.7843^{+0.0014}_{-0.0014}$	$0.279^{+0.141}_{-0.126}$	$1.21^{+0.15}_{-0.13}$	$0.0494^{+0.0040}_{-0.0039}$	$0.282^{+0.041}_{-0.037}$	$78.2^{+1.5}_{-1.4}$	> 2.34	> 26.21
0146129313*	$3.214869^{+0.000177}_{-0.000178}$	$1493.7863^{+0.0015}_{-0.0015}$	$0.296^{+0.126}_{-0.114}$	$1.23^{+0.13}_{-0.12}$	$0.0524^{+0.0033}_{-0.0032}$	$0.299^{+0.040}_{-0.037}$	$78.3^{+1.3}_{-1.2}$	> 3.04	> 34.09
0149608236	$1.676043^{+0.000474}_{-0.000495}$	$1494.9868^{+0.0036}_{-0.0035}$	$0.095^{+0.003}_{-0.003}$	$0.16^{+0.17}_{-0.11}$	$0.0217^{+0.0020}_{-0.0020}$	$0.923^{+0.160}_{-0.151}$	$88.4^{+1.1}_{-1.7}$	$0.75^{+0.06}_{-0.06}$	$8.48^{+0.69}_{-0.68}$
0152084108	$0.463628^{+0.000111}_{-0.000118}$	$1490.9484^{+0.0058}_{-0.0057}$	$0.038^{+0.002}_{-0.001}$	$0.17^{+0.18}_{-0.12}$	$0.0113^{+0.0004}_{-0.0004}$	$1.596^{+0.131}_{-0.133}$	$86.4^{+2.4}_{-3.5}$	$0.31^{+0.01}_{-0.01}$	$3.48^{+0.21}_{-0.20}$
0184347065	$2.637791^{+0.001001}_{-0.001010}$	$1517.9521^{+0.0068}_{-0.0062}$	$0.214^{+0.050}_{-0.016}$	$0.46^{+0.31}_{-0.29}$	$0.0300^{+0.0012}_{-0.0012}$	$3.585^{+0.230}_{-0.230}$	$87.8^{+1.3}_{-1.4}$	$1.10^{+0.26}_{-0.09}$	$12.37^{+2.95}_{-1.09}$
0260119000	$2.940341^{+0.000129}_{-0.000127}$	$1520.1191^{+0.0012}_{-0.0012}$	$0.143^{+0.002}_{-0.002}$	$0.17^{+0.17}_{-0.12}$	$0.0353^{+0.0028}_{-0.0028}$	$1.221^{+0.110}_{-0.143}$	$88.9^{+0.7}_{-1.1}$	$1.15^{+0.08}_{-0.08}$	$12.94^{+0.95}_{-0.94}$
0131743355*	$6.560228^{+0.000197}_{-0.000194}$	$1493.9811^{+0.0007}_{-0.0007}$	$0.320^{+0.111}_{-0.104}$	$1.25^{+0.12}_{-0.11}$	$0.1043^{+0.0042}_{-0.0041}$	$0.687^{+0.062}_{-0.058}$	$84.4^{+0.5}_{-0.5}$	> 3.38	> 39.04
0032067057	$3.566567^{+0.001311}_{-0.002338}$	$1518.1681^{+0.0104}_{-0.0088}$	$0.179^{+0.010}_{-0.010}$	$0.17^{+0.20}_{-0.12}$	$0.0374^{+0.0017}_{-0.0017}$	$2.914^{+0.223}_{-0.226}$	$89.2^{+0.5}_{-0.7}$	$1.00^{+0.07}_{-0.06}$	$11.24^{+0.82}_{-0.78}$
0270846098	$2.122121^{+0.000309}_{-0.000330}$	$1518.7903^{+0.0044}_{-0.0039}$	$0.032^{+0.001}_{-0.001}$	$0.09^{+0.09}_{-0.06}$	$0.0379^{+0.0029}_{-0.0028}$	$0.185^{+0.022}_{-0.023}$	$88.7^{+0.9}_{-1.4}$	$0.66^{+0.04}_{-0.04}$	$7.42^{+0.51}_{-0.50}$
0092896631*	$5.640889^{+0.000732}_{-0.000729}$	$1519.8553^{+0.0029}_{-0.0029}$	$0.217^{+0.196}_{-0.096}$	$1.07^{+0.22}_{-0.13}$	$0.0547^{+0.0062}_{-0.0054}$	$0.106^{+0.028}_{-0.017}$	$80.0^{+2.0}_{-2.0}$	> 0.42	> 4.67
0123378551*	$11.010741^{+0.000238}_{-0.000237}$	$1496.6749^{+0.0006}_{-0.0006}$	$0.356^{+0.064}_{-0.054}$	$1.15^{+0.07}_{-0.06}$	$0.1409^{+0.0099}_{-0.0100}$	$1.129^{+0.050}_{-0.050}$	$86.9^{+0.2}_{-0.2}$	> 3.90	> 43.66
0133260600	$1.423656^{+0.000023}_{-0.000023}$	$1492.8532^{+0.0004}_{-0.0004}$	$0.418^{+0.056}_{-0.071}$	$0.97^{+0.07}_{-0.10}$	$0.0214^{+0.0010}_{-0.0010}$	$0.547^{+0.022}_{-0.021}$	$77.0^{+1.3}_{-0.8}$	$4.31^{+0.61}_{-0.74}$	$48.32^{+6.87}_{-8.33}$
0014091633	$5.529282^{+0.000043}_{-0.000043}$	$1440.9335^{+0.0002}_{-0.0002}$	$0.184^{+0.026}_{-0.014}$	$0.95^{+0.04}_{-0.02}$	$0.0656^{+0.0018}_{-0.0018}$	$0.699^{+0.040}_{-0.043}$	$85.3^{+0.2}_{-0.3}$	$2.17^{+0.31}_{-0.17}$	$24.36^{+3.57}_{-1.97}$
0140513181	$0.914267^{+0.000161}_{-0.000147}$	$1518.1515^{+0.0048}_{-0.0049}$	$0.109^{+0.005}_{-0.005}$	$0.14^{+0.14}_{-0.09}$	$0.0154^{+0.0007}_{-0.0007}$	$2.269^{+0.183}_{-0.182}$	$88.5^{+1.1}_{-1.6}$	$0.67^{+0.04}_{-0.04}$	$7.58^{+0.45}_{-0.44}$
0393126088	$0.363589^{+0.000016}_{-0.000016}$	$1468.6748^{+0.0013}_{-0.0013}$	$0.095^{+0.002}_{-0.002}$	$0.13^{+0.13}_{-0.09}$	$0.0079^{+0.0003}_{-0.0003}$	$3.575^{+0.184}_{-0.182}$	$87.7^{+1.62}_{-2.33}$	$0.48^{+0.02}_{-0.02}$	$5.42^{+0.21}_{-0.21}$

5.1.1 Candidate exoplanets with a TOI, not validated by our pipeline

We performed a cross-match of our catalogue and the TOI list[5] to understand if we have missed any reported candidate exoplanet or confirmed exoplanets. The following three objects were detected but not validated by our pipeline.

TIC 0441420236

Recently was found that TIC 0441420236 or AU Microscopii (AU Mic) hosts two transiting planets (Plavchan et al. 2020a; Klein et al. 2021; Martioli et al. 2021). During the primary mission of TESS, AU Mic was observed only in Sector 1 in the 2-min cadence data and in the FFIs. Plavchan et al. (2020a) initially used the 2-min cadence data to discover the candidate and after they visually identified the transits in the 2-min cadence light curve they independently validated the candidate also in the FFI data. They reported a planet (AU Mic b) with a period of 8.46 days in an orbital distance of 0.07 AU, a radius of 0.4 R_J and upper limit on the mass of 0.18 M_J. Moreover, they reported the detection of an isolated transit event possibly associated with a second candidate planet around the star AU Mic. Using infrared observations, Klein et al. (2021) measured a planetary mass of $17^{+4.7}_{-4.5}$ $M_\oplus$ for AU Mic b. Martioli et al. (2021) used also TESS data from the extended mission during July 2020 (Sector 27, 20s cadence[6]) and detected two additional transit events for the second planet (AU Mic c). After analysing the three available transit signals for AU Mic c, one from the primary mission and two from the extended, they reported a period of 18.859019± 0.000016 days, a planet radius of 3.24 ± 0.16 $R_\oplus$ and a mass in the range of 2.2 $M_\oplus < M_P <$ 25.0 $M_\oplus$. The star AU Mic is a magnetically active star with strong flaring activity (Robinson et al., 2001) and its surface is filled by starspots which are producing a BY Draconis-type light curve with a quasi-periodic rotational modulation and a period of 4.863 ∼ 0.010 days as reported by Plavchan et al. (2020a). Both Plavchan et al. (2020a) and Martioli et al. (2021) modeled the starspots and flares of AU Mic to improve the detection of the transit events in TESS light curves. The fact that we did not specifically account for these effects in the light curve of AU Mic and that we only used the FFI data from Sector 1, can explain why we did not recovered the reported candidate exoplanets. In general, for active stars with strong flaring and magnetic activity, like AU Mic, it is not easy to detect transiting planets from photometric data. Actually, we recovered a signal in the light curve of AU Mic with a period of $P \sim 8.46$ days, which

[5] In 29/12/2021 5 038 TOIS were reported in `https://exofop.ipac.caltech.edu/tess/view_toi.php`.

[6] Part of the TESS Guest Investigator Programs G03263 (PI: P. Plavchan), G03141 (PI: E. Newton), and G03273 (PI: L. Vega).

is in agreement with the period of AU Mic b, but with low S/N and SDE so it did not passed our validation tests.

TIC 0268914377

TIC 0268914377 is also a TOI (TOI 2610.01) with a suspected planet candidate and is a member of the Vela Puppis IV population. It was observed in the southern ecliptic hemisphere in three Sectors of TESS (7, 8, and 9) during the primary mission and in Sector 34 and 35 in the extended mission. Only after the observations of the extended mission were concluded the star was identified as a TOI on the 12/4/2021. A period of 2.15 days have been reported on the ExoFOP website by the TESS team[7]. We have used observations only from the primary mission of TESS and we have recovered a signal with a period $P = 2.15377$ days, in agreement with the one reported on ExoFOP, but the candidate fails our first validation test which checks if the odd/even transit depths are consistent (see Section 3.3.1).

Figure 5.1 illustrates the odd/even test we performed where the odd and even transits of TIC 268914377 are plotted with black and red colors, respectively. We have calculated that the difference of odd/even transit depths is equal to diff= 0.0049 which is higher than 3 $\times\sigma$ =0.0039[8]. Details on the definition of σ and odd/even test can be found in Section 3.3.1.

TIC 0159873822

TIC 0159873822 belongs in GROUP X and is a TOI (2048.01) hosting a possible planet candidate[9]. The star was observed in 3 sectors of TESS in Northern hemisphere (Sector 16, 13, and 24) during the primary mission. Our pipeline has recovered a period of $\sim$ 13.84 days similar with the value reported in ExoFOP website ($P = 13.79$ days), when we use the light curve only from Sector 24, but the candidate fails our classification test due to the low SDE and S/N recovered from the BLS search.

[7] `https://exofop.ipac.caltech.edu/tess/target.php?toi=2610.01`

[8] As mentioned in Section 3.3.1 candidates with diff $>3 \times \sigma$ are excluded from our list.

[9] The notes on the ExoFOP website mention that maybe its a variable star (odd/even differences)

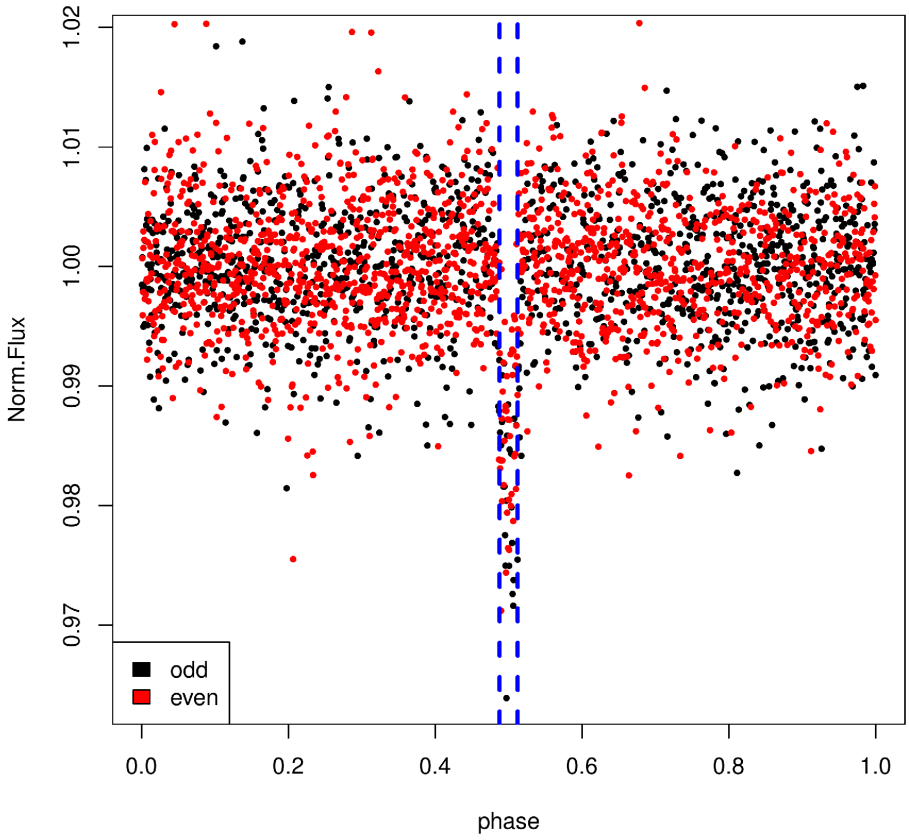

Figure 5.1: Odd/even validation test as described in Section 3.3.1 for TIC 0268914377. The candidate failed the test because the odd/even transit depths are not consistent with each other, so the difference of their depths diff $>3 \times \sigma$, where for TIC 0268914377 diff $= 0.0049$ and $3 \times \sigma = 0.0039$. Odd transits: black color; even transits: red color; transit duration: blue dashed line.

5.1.2 Candidate exoplanets with a TOI, identified as false positives

The following objects have been initially included in the TOI list of TESS but later on were identified as false positives. Our pipeline detected them and classified them also as false positives.

TIC 0077228304

TIC 0077228304 (TOI 456.01) was observed in two sectors of TESS, Sector 4 and 5, during the first scientific year of the mission. It was included on the TOI list and a signal with a period of $P \sim 0.33$ days was recovered, but after further investigation was excluded as a false positive. The same period was retrieved from our pipeline and the suspected "candidate" failed

our third validation test (Section 3.3.3), which checks if the transit depths of the light curves extracted with different photometric methods are consistent with each other and no differences are shown. So our pipeline identified it also as a false positive.

TIC 0146244533

The object TIC 0146244533 was monitored by TESS in four sectors in total, two during the primary mission (sector 8 and 9) and two in the extended mission (sector 35 and 36). Originally was identified as a potential host of an exoplanet with a period of $P \sim 8.8$ days, but later was identified as false positive (eclipsing binary). Our pipeline has also dispositioned it as a false positive from our classification step (see Section 3.2).

TIC 0459952217

TIC 0459952217 was observed in sector 5 during the primary mission of TESS and in sector 32 during the extended mission. Initially, was included in the TOI list with a suspected planet candidate but was later classified as a false alarm due to low S/N and potential stellar variability as mentioned in the Notes of the ExoFOP website [10]. Our pipeline recovered the signal but the potential candidate failed our classification step (see Section 3.2), due to the low S/N and SDE retrieved from the BLS algorithm using the TESS light curve only from sector 5.

5.2 False Positive Probability

Estimating the False Positive Probability (FPP) of each candidate exoplanet in our sample can provide us with additional information about the nature of the transit signal. For this purpose, we used the publicly available tool Validation of Exoplanet Signals using a Probabilistic Algorithm (`VESPA`) v.0.6[11] (Morton (2012); Morton (2015); Montet et al. (2015)) to calculate false positive probabilities and statistically validate the candidate exoplanets we discovered (see Chapter 4) in a Bayesian framework. More specifically, `VESPA` estimates the probability that the transits observed in the light curves are of planetary origin or if a different source masquerades as transiting exoplanet. The FPP of a candidate is calculated using the following equations:

$$\mathrm{FPP} = 1 - \Pr(\mathrm{planet}|\mathrm{signal}), \tag{5.1}$$

where Pr(planet|signal) is the probability that a certain planet exists given its observed signal and it is defined by:

[10] `https://exofop.ipac.caltech.edu/tess/target.php?id=459952217`
[11] `https://github.com/timothydmorton/VESPA`

$$\Pr(\text{planet}|\text{signal}) = \frac{\mathcal{L}_{\rm TP}\pi_{\rm TP}}{\mathcal{L}_{\rm TP}\pi_{\rm TP} + \mathcal{L}_{\rm FP}\pi_{\rm FP}} \tag{5.2}$$

In equation 5.2, $\mathcal{L}$ refers to the Bayesian likelihood factors. These factors provide information about the similarities between the observed and modeled transit signals. Furthermore, π represents the priors (the a priori probabilities that each scenario exists), the TP corresponds to "true positive" whereas FP to all "false positive" scenarios. `VESPA` models light curves that show transits (or eclipses in the case of variables) using a simple trapezoid and creates simulations of realistic populations of astrophysical false positives. The software takes into consideration the following scenarios for its modeling:

1. a simple eclipsing binary (EB, single/double period)
2. a hierarchical triple system where two components eclipse (HEB, single/double period)
3. a blended eclipsing binary inside the photometric aperture of the target (BEB, single/double period)
4. a real transiting planet on the target star (PL)

The possibility of a double period (specified with suffix $_{DP}$ in Table 5.3) version of each scenario is considered to avoid the cases of EB that show eclipses of the same depth (i.e W Uma type EB) and with a double orbital period of the one detected for the examined candidate.
In summary, `VESPA` is performing the following steps for the calculation of the FPP for a given candidate:

- simulates a representative population for every possible scenario (i.e EB, BEB etc) and sets the period equal to the period of the recovered candidate's signal;
- calculates the priors (π) for each scenario based on the simulated populations;
- calculates the likelihood ($\mathcal{L}$) of each transit signal under the hypothesis of each scenario, using the simulated populations of the first step;
- considers both the priors and likelihood probabilities to estimate the FPP for each transit (Eq. 5.1). Lower the FFP, the higher is the probability that the detected signal is due to a transiting exoplanet and not a false positive.

We report the FPP and the most probable scenario `VESPA` calculated for each of our candidate exoplanets (Chapter 4) in Table 5.3. Three candidates have

a probability $\gtrsim 50$ to be real exoplanets: TIC 0038820496, TIC 0097921547 and TIC 0014091633. `VESPA` could not calculate a FPP for three of our candidates (TIC 0023846678, TIC 0075825581 and TIC 0393126088) because all the scenarios it simulated were within the Roche lobe of the star. We also report the value of the Renormalzed Unit Weight Error (RUWE) diagnostic from the Gaia Early Data Release 3 (EDR3, Gaia Collaboration (2020)).

We would like to comment here that due to the low angular resolution of TESS camera's there is a strong bias on the priors used from `VESPA` for our candidates towards the BEB scenario (single or double period). There are some cases like TIC 0038820496 or TIC 0260119000 for which if we rule out the BEB scenario, through an analysis of their neighbor stars, then they are probably transiting planets with a much higher probability than the one reported in Table 5.3 (Figure 5.2 and 5.3). Moreover, `VESPA` does not take into consideration for the calculation of the FPP the dilution factor associated with the host star. Last but not least, `VESPA` re-calculates the stellar parameters of the imported star using the python package `isochrones`[12] which includes only the MIST models (Dotter (2016); Choi et al. (2016)). In the current version of `VESPA` there is no possibility for the user to import the stellar parameters of the star and force the software to use these values for the computation of the FPP. This can cause some inconsistencies if the values calculated from VESPA are not in agreement with the literature, which means that the resulted FPP is not very reliable. For example, for TIC 0038820496 `VESPA` calculates a stellar mass of $M_{\texttt{VESPA}} = 0.343 \pm 0.002$ $M_{\odot}$ and radius of $R_{\texttt{VESPA}} = 0.351 \pm 0.002$ $R_{\odot}$, whereas the stellar parameters reported in the TIC (Stassun et al., 2019b) are $M_{TIC} = 0.253 \pm 0.020$ $M_{\odot}$ and $R_{TIC} = 0.279 \pm 0.008$ $R_{\odot}$, respectively. It is clear that the stellar parameters from `VESPA` and TIC are not in agreement and, as shown in Figures 5.4 and 5.5, `VESPA` simulated a population (step 1) with much different stellar properties than the ones reported in the literature, so the resulted FPP is not very accurate in this case. For the above reasons, we took into consideration the resulted FPPs from `VESPA` with caution and used them as an additional indicator towards the validation of our candidate exoplanets and not as the definite solution of their origin.

[12] `https://isochrones.readthedocs.io/en/latest/`

Table 5.3: Results from VESPA: False Positive Probability

TIC	FPP	Scenario(prob.)	RUWE
0023846678	-	-	4.369
0038820496	0.52	PL(0.48)	1.078
0075825581	-	-	1.012
0082369548	0.98	BEB(0.84)	1.034
0097921547	0.00	PL(1.00)	0.856
0098161270	0.99	$\text{BEB}_{DP}(0.78)$	0.767
0129877093	1.00	BEB(0.70)	0.955
0132620309	0.99	$\text{BEB}_{DP}(0.64)$	2.183
0143497753	0.99	BEB(0.53)	1.045
0145582529	1.00	BEB(0.99)	1.001
0146129309	0.99	BEB(0.98)	1.801
0146129313	1.00	$\text{BEB}_{DP}(0.71)$	1.867
0149608236	0.97	BEB(0.93)	0.966
0152084108	0.96	$\text{BEB}_{DP}(0.51)$	0.908
0184347065	1.00	BEB(0.60)	1.069
0260119000	0.71	$\text{BEB}_{DP}(0.70)$	1.040
0131743355	0.57	EB(0.49)	0.963
0032067057	0.98	BEB(0.82)	1.027
0270846098	1.00	BEB(0.67)	3.376
0092896631	1.00	$\text{BEB}_{DP}(0.98)$	0.753
0123378551	0.93	EB(0.50)	1.952
0133260600	0.99	$\text{BEB}_{DP}(0.97)$	1.186
0014091633	0.50	PL(0.504)	0.988
0140513181	0.99	BEB(0.67)	1.220
0393126088	-	-	1.281

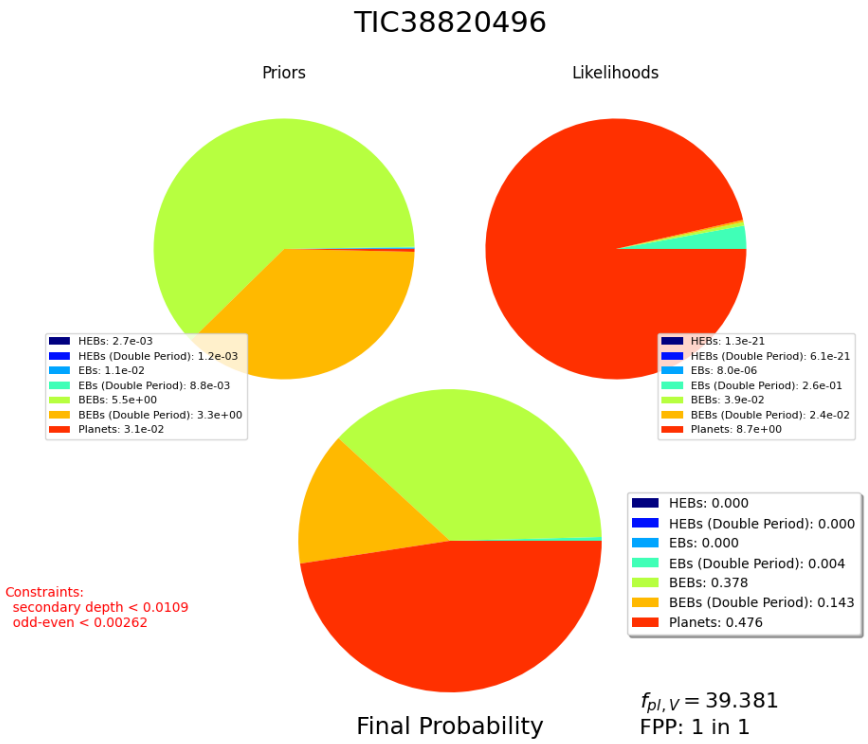

Figure 5.2: Pie chart from `VESPA` for TIC 0038820496. Top left: priors used for the modeling, showing strong bias towards the BEB scenario; Top right: the likelihood probabilities; Bottom center: the most probable scenarios with their respective probabilities for TIC 0038820496. If the BEB scenario is excluded for the host star then the probability of being a real planet will be $\sim 100\%$.

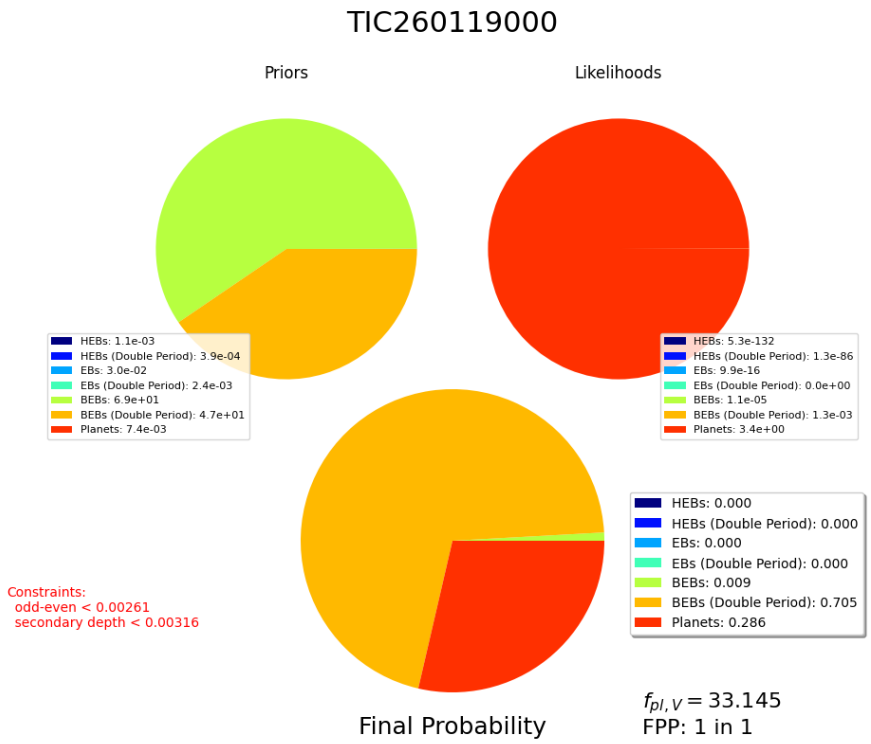

Figure 5.3: Pie chart from `VESPA` for TIC 0260119000. Top left: priors used for the modeling, showing strong bias towards the BEB scenario; Top right: the likelihood probabilities; Bottom center: the most probable scenarios with their respective probabilities for TIC 0260119000. If the BEB scenario is excluded for the host star then the probability of being a real planet will be $\sim 100\%$.

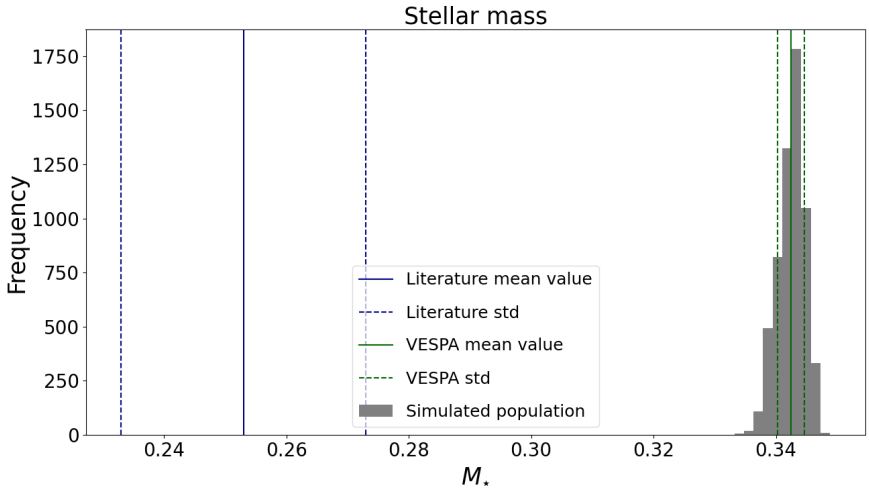

Figure 5.4: Comparison of stellar mass from `VESPA` and TIC for the star with TIC 0038820496. The values are not in agreement with each other and the simulated population from `VESPA` does not include the mass range provided by the TIC. Blue line: stellar radius from TIC; blue dotted lines: standard deviation of the radius from TIC; green line: mean radius from `VESPA`; green dotted lines: standard deviation of the radius from `VESPA`.

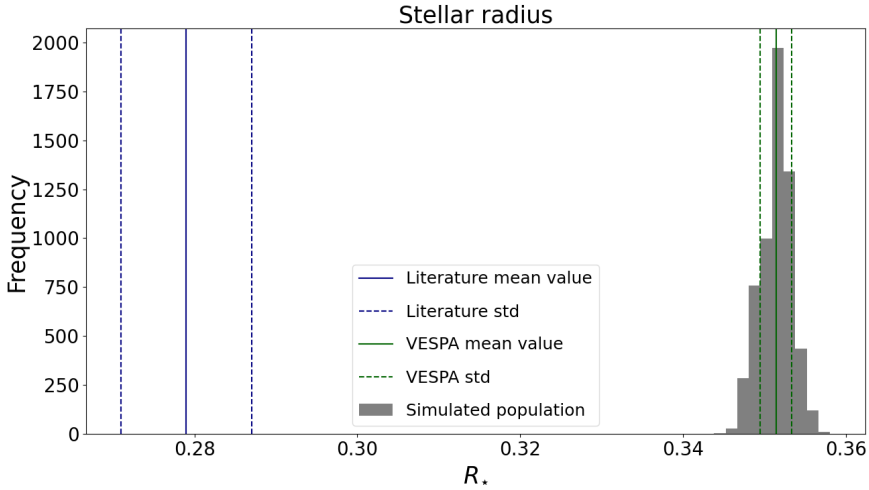

Figure 5.5: Comparison of stellar radius from `VESPA` and TIC for the star with TIC 0038820496. The values are not in agreement with each other and the simulated population from `VESPA` does not include the radius range provided by the TIC. Description of lines as in Figure 5.4.

Chapter 6

Frequency of exoplanets

6.1 Detection efficiency

We calculated the detection efficiency of our technique to discover different types of transiting exoplanets by performing transit simulations following a similar technique as the one described in Section 3.2.1. More specifically, we injected Mandel-Agol transit models (Mandel & Agol, 2002), in the constant light curves identified in Section 3.2.1, of planets with radii uniformly distributed in three radius grids: i) $R_P < 3.9R_\oplus$; ii) $3.9\mathrm{R}_\oplus \leq \mathrm{R}_P < 11.2\ \mathrm{R}_\oplus$; and iii) $R_P \geq 11.2R_\oplus$. Additionally, in each radius bin the injected transits have periods (P_{inj}), uniformly distributed in the following grids: a) 0.2 days$\leq \mathrm{P}_{inj} \leq$5 days; b) 5 days$< \mathrm{P}_{inj} \leq$50 days; and c) 50 days $< \mathrm{P}_{inj} \leq$365 days. In each planetary radius and period grid we have injected $\sim$ 1500 transits. Afterwards, we used the BLS algorithm (Kovács et al., 2002) to recover the injected transits in each grid and registered the S/N and SDE that it restituted. We considered that a transit was recovered if it satisfied the following conditions:

- its detection probability (P_r, Eq. 3.3) is bigger than the cut-off point we have defined for each photometric method and period bin (Table 3.1 and 3.2).
- its period has been recovered (P_{rec}) with high accuracy by imposing $\frac{|(P_{inj}-P_{rec})|}{P_{inj}} < 1\%$.

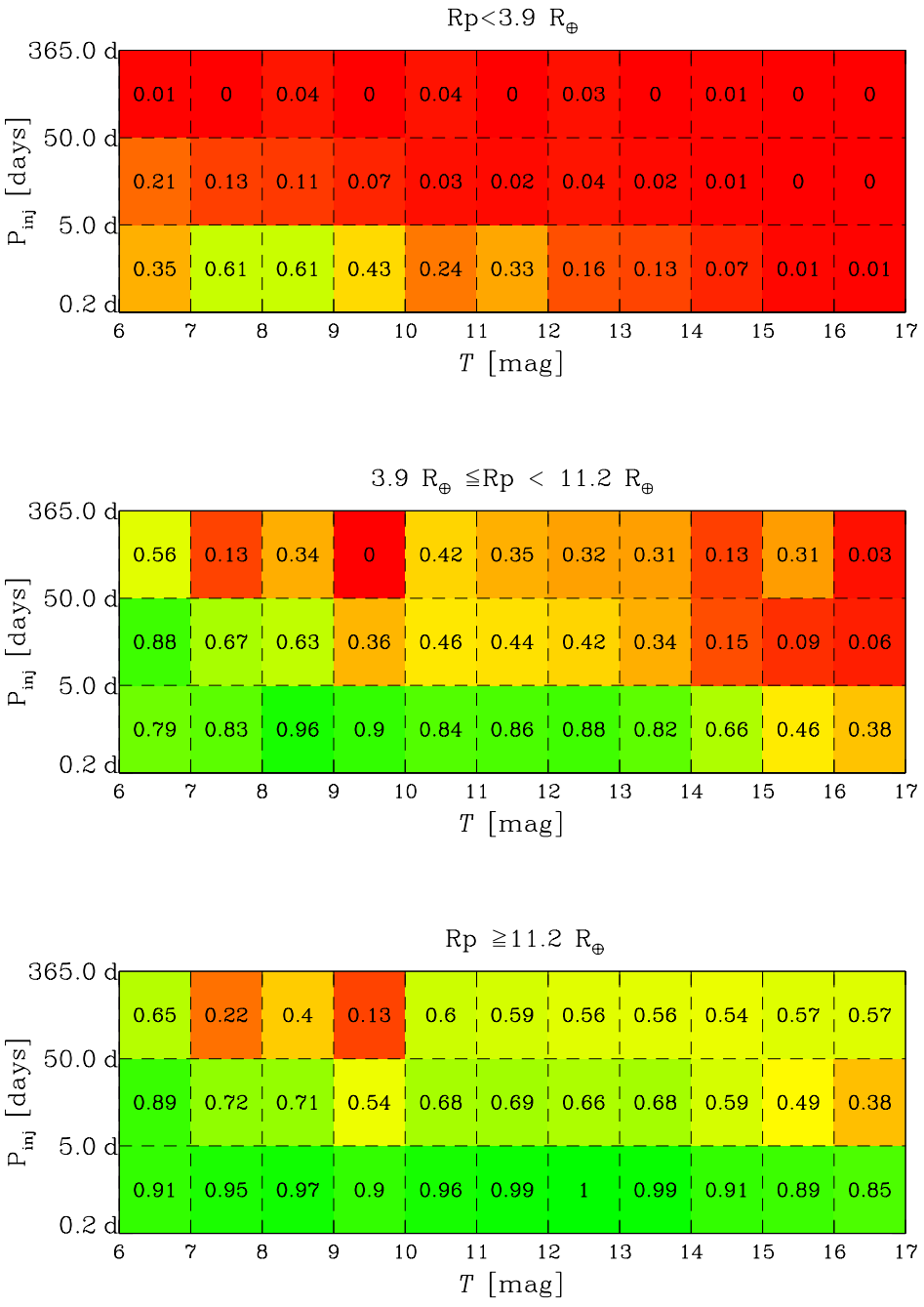

Figure 6.1: Detection efficiency of our technique normalized to 1 and color-coded (bright red: 0; bright green: 1) in function of *TESS* magnitude in three different period grids (P_{inj}). Top panel: Earth/super-Earth and mini-Neptune planets; middle panel: Neptune and super-Neptune planets; bottom panel: Giant planets.

Table 6.1: Detection efficiency of our technique

Detection efficiency (%)			
	$P = 0.2 - 5$ days		
T (mag)	$R_P < 3.9R_\oplus$	$3.9R_\oplus \leq R_P < 11.2R_\oplus$	$R_P \geq 11.2R_\oplus$
6-7	35^{+6}_{-6}	79^{+11}_{-11}	91^{+9}_{-12}
7-8	61^{+9}_{-9}	83^{+11}_{-11}	95^{+5}_{-12}
8-9	61^{+6}_{-6}	96^{+4}_{-9}	97^{+3}_{-9}
9-10	43^{+17}_{-17}	90^{+10}_{-29}	90^{+10}_{-19}
10-11	24^{+7}_{-7}	84^{+16}_{-17}	96^{+4}_{-19}
11-12	33^{+8}_{-8}	86^{+14}_{-15}	99^{+1}_{-17}
12-13	16^{+5}_{-5}	88^{+12}_{-14}	100^{+0}_{-16}
13-14	13^{+4}_{-4}	82^{+12}_{-12}	99^{+1}_{-13}
14-15	7^{+2}_{-2}	66^{+9}_{-9}	91^{+9}_{-12}
15-16	$1.3^{+0.7}_{-0.7}$	46^{+5}_{-5}	89^{+7}_{-7}
16-17	$0.6^{+0.4}_{-0.4}$	38^{+4}_{-4}	85^{+7}_{-7}
	$P = 5 - 50$ days		
6-7	21^{+5}_{-5}	88^{+12}_{-13}	89^{+11}_{-13}
7-8	13^{+4}_{-4}	67^{+10}_{-10}	72^{+11}_{-11}
8-9	11^{+2}_{-2}	63^{+5}_{-5}	71^{+5}_{-5}
9-10	7^{+5}_{-5}	36^{+13}_{-13}	54^{+17}_{-17}
10-11	3^{+2}_{-2}	46^{+10}_{-10}	68^{+13}_{-13}
11-12	2^{+1}_{-1}	44^{+8}_{-8}	69^{+11}_{-11}
12-13	4^{+2}_{-2}	42^{+7}_{-7}	66^{+10}_{-10}
13-14	2^{+1}_{1}	34^{+5}_{-5}	68^{+9}_{-9}
14-15	$0.7^{+0.7}_{-0.7}$	15^{+3}_{-3}	59^{+8}_{-8}
15-16	0^{+0}_{-0}	9^{+2}_{-2}	49^{+5}_{-5}
16-17	0^{+0}_{-0}	6^{+1}_{-1}	38^{+3}_{-3}
	$P = 50 - 365$ days		
6-7	$0.7^{+0.7}_{-0.7}$	56^{+8}_{-8}	65^{+8}_{-8}
7-8	0^{+0}_{-0}	13^{+4}_{-4}	22^{+5}_{-5}
8-9	4^{+2}_{-2}	34^{+6}_{-6}	40^{+7}_{-7}
9-10	0^{+0}_{-0}	0^{+0}_{-0}	13^{+7}_{-7}
10-11	4^{+1}_{-1}	42^{+5}_{-5}	60^{+6}_{-6}
11-12	0^{+0}_{-0}	35^{+6}_{-6}	59^{+8}_{-8}
12-13	3^{+1}_{-1}	32^{+5}_{-5}	56^{+7}_{-7}
13-14	0^{+0}_{-0}	31^{+4}_{-4}	56^{+6}_{-6}
14-15	$0.8^{+0.8}_{-0.8}$	13^{+3}_{-3}	54^{+8}_{-8}
15-16	0^{+0}_{-0}	31^{+6}_{-6}	57^{+9}_{-9}
16-17	0^{+0}_{-0}	3^{+3}_{-3}	57^{+17}_{-17}

In Table 6.1 and Figure 6.1 we present the detection efficiency of our technique as a function of the $TESS$ magnitude (T= 6–17 mag) in three period grids. For small planets with $R_P < 3.9R_\oplus$, the detection efficiency is between 24 – 60 % for short period exoplanets around stars with $T < 12$ mag and its very small ($\leq$ 21%) in longer period grids. For Neptune and super-Neptune planets ($3.9R_\oplus \leq R_P < 11.2R_\oplus$) the detection efficiency ranges from 38–90 % for short periods; from 34–88 % for stars with T=(6–14) mag and $\leq$ 15% for the fainter ones with for periods from 5 to 50 days; and it is $\leq$ 56 for transiting exoplanets with long periods. For Giant planets the detection efficiency is always $\geq$ 85% for short periods; it ranges from 38% to 89% for $P = (5 - 50)$ days; and $\leq$ 65% for longer periods. For the simulations of long period transits we have used light curves of stars observed in 13 Sectors of TESS. The fact that we had few ($\sim$ 40) stars with T= (7–10) mag observed in 13 Sectors of TESS ($\sim 365 days$) affected the statistics of our simulations and consequently the detection efficiency of our technique on the bright regime and for long periods. That is the reason why the detection efficiency of bright stars with T= (7–10) mag and long periods, both in the Neptune/super-Neptune and Giant planet regime, is low.

6.2 Frequency of exoplanets

Using the planetary properties (R_P, P) of the candidate exoplanets we discovered in young associations and moving groups (Section 5.1), the FPP calculated by `VESPA` (Section 5.2) for each candidate and considering the detection efficiency of our technique to recover different types of planets, we calculated the frequency of exoplanets as a function of the planet radius and period (R_P, P). To accomplish that we used an approach similar to Nardiello et al. (2021) and calculated the frequency using the equation:

$$f_\star(R_P, P) = \frac{\sum_{n=1}^{N_{cand}} [1 - FPP^n(R_P, P)]}{\sum_{j=1}^{N_{stars}} [de^j(R_P, P) \times P^j_{tr}(P)]} \tag{6.1}$$

where N_{cand} and N_{stars} correspond to the number of candidate exoplanets found in this work and number of stars in our catalogue, respectively. Moreover, the detection efficiency (de^j) that is associated with the j-th star in our catalogue having a $TESS$ magnitude T_j is calculated by interpolating the values of Figure 6.1 for each pair of (R_P, P). The parameter P^j_{tr} is the transit probability calculated as $P^j_{tr}(P) = R_\star/a(P)$, where $R_\star$ is the stellar radius of the j-th star, and a is the semi-major axis calculated using the Third Kepler law and considering three different periods: i) P_{min}; ii) $P_{mid} = 0.5(P_{min} + P_{max})$; and iii) P_{max}, for each period grid. If the numerator of Equation 6.1 is less than 1 (i.e no candidates in this (R_P, P)

range or (1-FPP)< 1) then we could only calculate an upper limit of the frequency. The resulted frequencies are reported in Table 6.2 for three planet radii grids: i) $R_P < 3.9R_\oplus$; ii) 3.9R$_\oplus \leq$ R$_P$ <11.2 R$_\oplus$; and iii) $R_P \geq 11.2R_\oplus$ with periods in ranges: a) 0.2 days$\leq$ P$\leq$ 5 days; b) 5 days< P$\leq$ 50 days; and c) 50 days < P$\leq$ 365 days. Consequently, in each (R$_P$, P) pair we have calculated three frequencies : $f_\star^{min}$, $f_\star^{mid}$, and $f_\star^{max}$. For short period Earth/super-Earth and mini-Neptune planets ($R_P < 3.9R_\oplus$) we found an upper limit of $f_{\star,E} < 0.65$ %; for Neptune and super-Neptune $f_{\star,N} < 0.18$ %; and for Giant planets $f_{\star,G} \sim 0.32$ %. The frequencies in the middle range periods are higher for all the planet types with upper values $f_{\star,E} <$ 18.20 % and $f_{\star,N} < 1.90$ % for small and medium sized planets and $f_{\star,J} \sim$ 1.00 % for Giants. For transiting planets with longer periods (P> 50 days) we calculated only an upper limit on the frequencies of all the planet types since we did not discovered a candidate belonging in this periods range. The frequencies from smaller to bigger planets are $f_{\star,E} < 55.28$ %, $f_{\star,N} < 2.49$ % and $f_{\star,J} < 1.22$ %, respectively.

As discussed in Section 5.2 there are some uncertainties introduced in the calculation of the FPP of our candidates with `VESPA`. For this reason we decided to calculate the frequencies also without considering the FPP, so imposing FPP=0 in Equation 6.1 (Table 6.3). The main differences of Table 6.2 and Table 6.3 are concentrated in the (R$_P$, P) pairs where we have detected candidate exoplanets, so in short periods for all type of planets and medium periods for Giant planets. As expected, the frequencies calculated without taking into consideration of the FPP are higher. For short periods less than 5 days we calculated $f_{\star,E}^{max} \sim 1.97$ %, $f_{\star,N}^{max} \sim 1.28$ % and $f_{\star,J}^{max} \sim$ 1.72 % for small, medium and giant size planets, respectively. For giant planets with periods in the range of 5 days < $P \leq$ 50 days we found $f_{\star,J}^{max} \sim$ 4.12 %.

Table 6.2: Frequency of candidate exoplanets, considering the FPP from VESPA.

	R$_p < 3.9R_\oplus$			3.9 R$_\oplus \leq R_p <$ 11.2$R_\oplus$			R$_p \geq$ 11.2$R_\oplus$		
Period (d)	$f_\star^{min}$ (%)	$f_\star^{mid}$ (%)	$f_\star^{max}$ (%)	$f_\star^{min}$ (%)	$f_\star^{mid}$ (%)	$f_\star^{max}$ (%)	$f_\star^{min}$ (%)	$f_\star^{mid}$ (%)	$f_\star^{max}$ (%)
0.2 - 5.0	< 0.08	< 0.43	< 0.66	< 0.02	< 0.12	< 0.18	0.04 ± 0.03	0.21 ± 0.14	0.32 ± 0.22
5.0 - 50.0	< 3.94	< 12.27	< 18.27	< 0.41	< 1.28	< 1.90	0.22 ± 0.22	0.69 ± 0.69	1.04 ± 1.04
50.0 - 365.0	< 11.91	< 37.11	< 55.28	< 0.54	< 1.67	< 2.49	< 0.26	< 0.82	< 1.22

Table 6.3: Frequency of candidate exoplanets, considering FPP=0

	R$_p < 3.9R_\oplus$			3.9 R$_\oplus \leq R_p <$ 11.2$R_\oplus$			R$_p \geq$ 11.2$R_\oplus$		
Period (d)	$f_\star^{min}$ (%)	$f_\star^{mid}$ (%)	$f_\star^{max}$ (%)	$f_\star^{min}$ (%)	$f_\star^{mid}$ (%)	$f_\star^{max}$ (%)	$f_\star^{min}$ (%)	$f_\star^{mid}$ (%)	$f_\star^{max}$ (%)
0.2 - 5.0	0.2 ± 0.1	1.3 ± 0.7	1.9 ± 1.2	0.15 ± 0.06	0.8 ± 0.3	1.3 ± 0.5	0.20 ± 0.06	1.1 ± 0.3	1.7 ± 0.5
5.0 - 50.0	< 3.94	< 12.27	< 18.27	< 0.41	< 1.28	< 1.90	0.9 ± 0.4	2.7 ± 1.4	4.1 ± 2.1
50.0 - 365.0	< 11.91	< 37.11	< 55.28	< 0.54	< 1.67	< 2.49	< 0.26	< 0.82	< 1.22

We compared the frequency of exoplanets we calculated for stars in stellar associations with the ones reported by Fressin et al. (2013) for field stars using data from the *Kepler mission*. The authors calculated the frequencies in five different planet radius grids: i) Earths with 0.8-1.25 $R_\oplus$; ii) super-Earths with (1.25-2) $R_\oplus$; iii) small Neptunes with (2-4) $R_\oplus$; iv) large Neptunes with (4-6) $R_\oplus$; and v) Giants with (6-22) $R_\oplus$. Since we are using slightly different grids for the planetary radius we can do an approximate comparison with Fressin et al. (2013) (hereafter F13) but still informative. For the comparison we used the frequencies calculated taking into consideration the FPP of our candidates(Table 6.2), unless it is stated otherwise.

For the Neptune/super-Neptune planets ($3.9\ R_\oplus \leq R_p < 11.2\ R_\oplus$) we compared our frequencies ($f_{\star,M}$) with the results of the large Neptunes, which is the closest planetary radius grid reported from F13 ($f_{\star,F}$). For the short periods, the authors reported a frequency of planets $f_{\star,F} = (0.12 \pm 0.03)\%$, which is in agreement with the value we have estimated $f_{\star,M} < 0.18$ %. For periods in the grid from 5 to 50 days, we have calculated a frequency $f_{\star,M} < 1.90$ %, which can be considered consistent with the one F13 reported with a value of $f_{\star,F} = (1.11 \pm 0.17)\%$. For the longer periods (P =50-365 days) the most similar range published from F13 is for periods from 50 to 418 days. Also in this case, our frequency ($f_{\star,M} < 2.49$ %) is consistent with $f_{\star,F} = (1.76 \pm 0.43)\%$ found by F13.

We have defined the Giant planets in our sample as the ones with radii $R_P \geq 11.2 R_\oplus$, whereas F13 used $R_P = $(6-22)$R_\oplus$. This difference adds some inconsistences in the comparison of the frequencies. For short period planets F13 reported a frequency of $f_{\star,F} = (0.25 \pm 0.04)\%$ which is in agreement with our frequency $f_{\star,M} = 0.32 \pm 0.22\%$), within the errors. For periods from 5 to 50 days our frequencies are suffering from high errors due to the poorly statistics of our sample in this period and planet range. We have calculated a frequency of $f_{\star,M} = 1.04 \pm 1.04\%$ and F13 reports $f_{\star,F} = (1.04 \pm 0.15)\%$. In the longer period grid we have calculated a lower upper limit on the frequency of Giant planets ($f_{\star,M} < 1.22\%$) than F13 with $f_{\star,F} = (3.83 \pm 0.57)\%$, probably because we do not have detected a candidate exoplanet in this period range and we are using different period and planetary radii grids.

For the frequencies of smaller planets with $R_p < 3.9\ R_\oplus$ is not easy to perform a direct comparison with the results from F13, because they have split this radius grid in three subsets: Earths, super-Earths and small Neptunes as we have already mentioned. In this case, for each period grid we will use a frequency range defined from the smaller to the maximum reported frequency by F13 to perform a comparison. For instance, in the short period grid they report a frequency of $f^1_{\star,F} = (2.39 \pm 0.44)\%$ for Earths; $f^2_{\star,F} = (2.20 \pm 0.23)\%$ for super-Earths; and $f^3_{\star,F} = (0.89 \pm 0.09)\%$ for small Neptunes, so the frequency of planets with $R_p < 3.9\ R_\oplus$ is in the range of

(0.89 ±0.09)% to (2.39 ±0.44)%. We have calculated a frequency of $f_{\star,M} <$ 0.66 when considering the FPP of our candidates from VESPA (Table 6.2), which is lower than the frequency range found by F13. If we consider that FPP=0 (Table 6.3) then $f_{\star,M} = 1.9 \pm 1.2\%$ which is inside the frequency range ∼(0.89-2.39)%. For the intermediate periods from 5 to 50 days, F13 published a frequency range ∼(11.10-14.59)% and we have calculated an upper limit of $f_{\star,M} < 18.27$ %. Finally, F13 have calculated a frequency for Earth-like planets up to 85 days and for Super-Earth and mini-Neptunes up to 145 and 245 days, respectively. For these period ranges, which are smaller than the long period range we consider (P=50-365 days) they found $f_{\star,F}$ ∼(3.06-10.52)% which is smaller than the value we calculated $f_{\star,M} <$ 55.28%.

6.3 Hints of exoplanet evolution

In Figure 6.2 we present the stellar age versus planetary radius distribution for the candidate exoplanets identified in this work (magenta circles), the candidate exoplanets in stellar clusters and associations found in the PATHOS project (light blue circles, Nardiello et al. 2020; Nardiello 2020; Nardiello et al. 2021), and finally confirmed and candidate exoplanets in stellar clusters and young associations found in the literature (grey circles, Table 6.4). All the objects shown in Figure 6.2 have transit periods less than 100 days.

Small planets like Earth/super-Earth and mini-Neptune planets ($R_P <$ 3.9 $R_\oplus$) seem to be concentrated at ages bigger than 100-200 Myr. As can been seen in Figure 6.2, there is a lack of small exoplanets around younger stars which probably is an observational bias, since it is challenging and difficult to detect small planets around young active stars. On the other hand, Giant planets with $R_P > 11.2$ $R_\oplus \sim 1$ R_J display a random distribution in various ages ranging from ∼ 10 Myr to ∼ 1000 Myr. Medium size planets in the radius regime $4R_\oplus \leq R_P < 10R_\oplus$ are clustering at ages less than 100 Myr. It is not clear yet why there are no detections of medium size planets around stars older than 100 Myr, maybe it is due to observational biases or there are some mechanisms behind this behavior. Owen (2019) proposed that this behavior can be a result of atmospheric escape. More specifically, the author mentions that atmospheric escape is the dominant mechanism that drives and controls the evolution of low-mass close-in exoplanets at their early life. Observations in few nearby exoplanet systems have shown detections of atmospheric escape resulting to mass loss over a duration of time. These exoplanets throughout their formation acquired large amount of H/He into their atmospheres resulting in an expansion of their radius to 5-13 $R_\oplus$ in a time scale of few Myr. If these planets are irradiated strongly they can experience significant loss of their atmosphere and end up in the

Table 6.4: Confirmed and candidate exoplanets in stellar clusters and associations from the literature.

Object	Cluster/Association	Age (Myr)	Period (days)	$R_P(R_\oplus)$	Reference
K-66b	NGC 6811	863^{+30}_{-30}	$17.815815^{+0.000075}_{-0.000075}$	$2.80^{+0.16}_{-0.16}$	Meibom et al. (2013)
K2-33b	Upp-Sco	$9.3^{+1.1}_{-1.1}$	$5.424865^{+0.000035}_{-0.000031}$	$5.04^{+0.34}_{-0.37}$	Mann et al. (2016a)
K-67b	NGC 6811	863^{+30}_{-30}	$15.72590^{+0.00011}_{-0.00011}$	$2.94^{+0.16}_{-0.16}$	Meibom et al. (2013)
TOI-200b	Tuc-Hor	40^{+5}_{-5}	$8.1387^{+0.0005}_{-0.0005}$	$5.63^{+0.22}_{-0.21}$	Benatti et al. (2019b)
HD 283869b	Hyades	728^{+71}_{-71}	$106^{+74.0}_{-25.0}$	$1.96^{+0.13}_{-0.16}$	Vanderburg et al. (2018)
TOI-451b	Psc-Eri	$134^{+6.5}_{-6.5}$	$1.858703^{+0.000025}_{-0.000035}$	$1.91^{+0.12}_{-0.12}$	Newton et al. (2021)
K2-25b	Hyades	728^{+71}_{-71}	$3.484552^{+0.000031}_{-0.000037}$	$3.43^{+0.95}_{-0.31}$	Mann et al. (2016b)
TOI-451c	Psc-Eri	$134^{+6.5}_{-6.5}$	$9.192522^{+0.00006}_{-0.00010}$	$3.10^{+0.13}_{-0.13}$	Newton et al. (2021)
K2-136Ab	Hyades	728^{+71}_{-71}	$7.975292^{+0.000833}_{-0.000770}$	$0.99^{+0.06}_{-0.04}$	Mann et al. (2018)
TOI-451d	Psc-Eri	$134^{+6.5}_{-6.5}$	$16.364988^{+0.00044}_{-0.000044}$	$4.07^{+0.15}_{-0.15}$	Newton et al. (2021)
K2-136Ac	Hyades	728^{+71}_{-71}	$17.307137^{+0.000252}_{-0.000284}$	$2.91^{+0.11}_{-0.10}$	Mann et al. (2018)
TOI-1098b	Melange-1	250^{+50}_{-70}	$10.18271^{+0.0004}_{-0.00004}$	$3.2^{+0.1}_{-0.1}$	Tofflemire et al. (2021)
K2-136Ad	Hyades	728^{+71}_{-71}	$25.575065^{+0.002418}_{-0.002357}$	$1.45^{+0.11}_{-0.08}$	Mann et al. (2018)
HD 63433b	UMa	414^{+23}_{-23}	$7.10801^{+0.00046}_{-0.00034}$	$2.15^{+0.10}_{-0.10}$	Mann et al. (2020b)
K2-95b	Praesepe	670^{+67}_{-67}	$10.135091^{+0.000495}_{-0.000488}$	$3.7^{+0.2}_{-0.2}$	Mann et al. (2017)
HD 63433c	UMa	414^{+23}_{-23}	$20.5455^{+0.0011}_{-0.0011}$	$2.64^{+0.12}_{-0.12}$	Mann et al. (2020b)
K2-100b	Praesepe	670^{+67}_{-67}	$1.673915^{+0.000011}_{-0.000011}$	$3.5^{+0.2}_{-0.2}$	Mann et al. (2017)
HIP 67522b	Sco-Cen	17^{+2}_{-2}	$6.959503^{+0.000016}_{-0.000015}$	$10.07^{+0.47}_{-0.47}$	Rizzuto et al. (2020)
K2-101b	Praesepe	670^{+67}_{-67}	$14.677303^{+0.000824}_{-0.000809}$	$3.0^{+0.1}_{-0.1}$	Mann et al. (2017)
HIP 67522c	Sco-Cen	17^{+2}_{-2}	$54.0^{+70.0}_{-24.0}$	$8.01^{+0.75}_{-0.71}$	Rizzuto et al. (2020)
K2-102b	Praesepe	670^{+67}_{-67}	$9.915651^{+0.001194}_{-0.001175}$	$1.3^{+0.1}_{-0.1}$	Mann et al. (2017)
AU Mic b	AU Mic	22^{+3}_{-3}	$8.46321^{+0.00004}_{-0.00004}$	$4.20^{+0.20}_{-0.20}$	Plavchan et al. (2020b)
K2-103b	Praesepe	670^{+67}_{-67}	$21.169687^{+0.001636}_{-0.001655}$	$2.2^{+0.2}_{-0.1}$	Mann et al. (2017)
AU Mic c	AU Mic	22^{+3}_{-3}	$30.0^{+6.0}_{-6.0}$	$2.35^{+0.67}_{-0.67}$	Plavchan et al. (2020b)
K2-104b	Praesepe	670^{+67}_{-67}	$1.974189^{+0.000110}_{-0.000109}$	$1.9^{+0.2}_{-0.1}$	Mann et al. (2017)
V 1298c	Tau	23^{+4}_{-4}	$8.24958^{+0.00072}_{-0.00072}$	$5.59^{+0.36}_{-0.32}$	David et al. (2019)
K2-264b	Praesepe	670^{+67}_{-67}	$5.839770^{+0.000063}_{-0.000063}$	$2.27^{+0.20}_{-0.16}$	Rizzuto et al. (2018)
V 1298d	Tau	23^{+4}_{-4}	$12.4032^{+0.0015}_{-0.0015}$	$6.41^{+0.45}_{-0.40}$	David et al. (2019)
K2-264c	Praesepe	670^{+67}_{-67}	$19.663650^{+0.000303}_{-0.000306}$	$2.77^{+0.20}_{-0.18}$	Rizzuto et al. (2018)
V 1298b	Tau	23^{+4}_{-4}	$24.1396^{+0.0018}_{-0.0018}$	$10.27^{+0.58}_{-0.53}$	David et al. (2019)
K2-231b	Ruprecht 147	3000^{+250}_{-250}	$13.841901^{+0.001352}_{-0.001352}$	$2.5^{+0.2}_{-0.2}$	Curtis et al. (2019)
V 1298e	Tau	23^{+4}_{-4}	60^{+60}_{-18}	$8.74^{+0.84}_{-0.72}$	David et al. (2019)
K2-284b	Cas-Tau	120^{+640}_{-20}	$4.79507^{+0.00012}_{-0.00012}$	$2.77^{+0.12}_{-0.12}$	David et al. (2018)

Earth/super-Earth to mini-Neptune regime as proposed in Owen (2020). Consequently, transiting planets with radii between $4R_\oplus \leq R_P < 10R_\oplus$ are probably the progenitors of the super-Earth/min-Neptune planets we observe today. Accurate measurements of the exoplanet masses (with errors $< 20\%$) in Figure 6.2 are also required, together with the planetary radius and stellar age, to contribute towards our understanding of the mechanisms and compute the time scales of planetary atmospheric evolution (Owen, 2020). An alternative explanation for the observed valley on the radius distribution of medium size exoplanets is related with core-powered mass loss. Ginzburg et al. (2018) proposed that atmosphere mass loss, driven by the cooling luminosity of the rocky core, is possible to result in a bimodal population. More specifically, if the heat capacity of the gas envelope is larger than that of the rocky core it can lead up to significantly increased planet radius. On the other hand, if the rocky core prevails the heat capacity, then the atmosphere of the planet can be entirely blown off from the cooling luminosity of the core in a runaway process. As a result the planetary size is minimized to its bare core. The authors tested this theory on realistic planet populations (without accounting for atmospheric escape/photoevapotation as Owen (2020) proposed) and found that the planets are modified due to core-powered mass loss into a bimodal population that can resemble the observations of exoplanets. A third explanation for the absence of exoplanets with radii $4R_\oplus \leq R_P < 10R_\oplus$ is related with the dynamical evolution these planets undergo after their formation, like migration due to interaction with the protoplanetary disc or planet-planet scattering (Fabrycky & Tremaine 2007; Chatterjee et al. 2008). Usually these phenomena occur on time scales of few Myr (or less) and if present they affect the orbital properties (i.e eccentricity, semi-major axis, and inclination) of the exoplanets making the discovery of close-in planets more challenging.

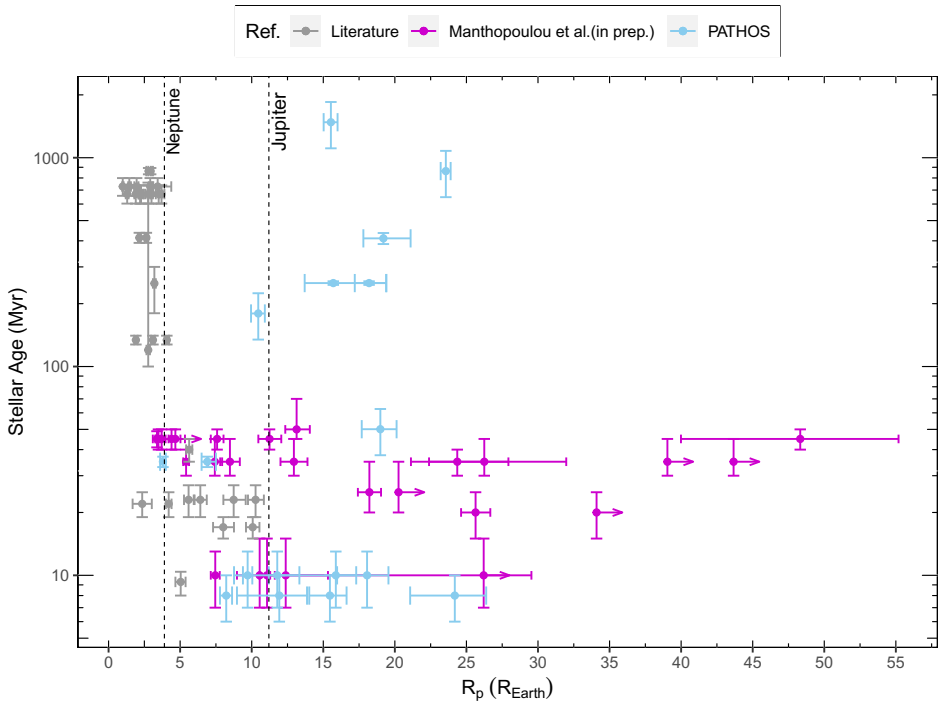

Figure 6.2: Stellar age versus planetary radius for the candidate exoplanets identified in this work with magenta color; candidate exoplanets in stellar clusters and associations from PATHOS project with light blue color; confirmed and candidate exoplanets in stellar clusters and young associations found in the literature with grey color. The transit periods of these objects are less than 100 days.

Chapter 7

Summary and Conclusions

The objective and main goal of this PhD project is the discovery and characterization of transiting exoplanets orbiting stars in young associations and moving groups observed by TESS. The members of young associations and moving groups provide us a sample of targets for which we can precisely define their stellar parameters (i.e radius, mass, effective temperature) but also their age, which is generally not well constrained for the majority of known exoplanet hosts until today. Consequently, we can investigate the planetary properties as a function of the host's star parameters and explore planet demographics and occurrence rates as a function of time.

In order to achieve this goal we have created a sample of young stars monitored by TESS belonging in 40 young associations and moving groups with ages spanning from 1 to 680 Myr. Using the PATHOS pipeline (Nardiello et al. 2019; Nardiello et al. 2020) we have extracted 11 598 light curves of stars observed in FFIs of TESS in Sectors 1-26 during the first two scientific years of the mission. In the first year (July 2018 - July 2019), 10 593 stars were monitored in the southern hemisphere which represent the 91% of our targets. During the second year (July 2019 - July 2020) the remaining 1 005 stars were observed in the northern hemisphere. TESS light curves are affected by systematic errors related with the spacescraft, detector and environment. Stars observed in the same sector of TESS share the same systematic errors which we have modeled using cotrending basis vectors (PATHOS pipeline). Except of the systematic errors we have also accounted for the variability of the stars in our sample. We have interpolated each light curve by using a cubic smoothing splines defined in three different grid of knots: (i) one knot every 4-hours, (ii) one knot every 8-hours and (iii) one knot every 13-hours; in order to exclude short and long period variables, but also ensure that transits with a duration longer than 4 or 8 hours are not flattened out from the light curves. Then, we searched for transiting planets in the corrected TESS light curves using the BLS algorithm and implemented a machine learning algorithm named logistic regression, which

is used for binary classification, to identify the most promising candidate exoplanets in our sample. We validated the candidate planets by applying four different tests: i)the odd/even transit depths are consistent with each other; ii) there is no secondary transit present in the candidates light curve; iii) the transit depth is not changing in light curves extracted with different photometric methods; iv) we calculated the in-transit and out-of-transit centroid difference to verify that the transits are occurred in the target star and not in a close by neighbor. After the application of the validation tests 27 candidate exoplanets have survived our selection process and the origin of two them around TIC 0067646988 (brown dwarf) and TIC 0410214986 (confirmed exoplanet) has been already found so we did not proceed with their characterization. Using the `VESPA` (Morton 2012; Montet et al. 2015; Morton 2015) software we have estimated the False Positive Probability for each of our candidates. Due to the biases introduced in the pipeline related with the priors (strong bias towards the blended eclipsing binary scenario) and the stellar parameters used for the modeling, we have decided to use the results from `VESPA` as an additional indication towards the validation of our candidate exoplanets and not as their definite solution of their origin.

We modelled the light curves of the remaining 25 candidate exoplanets in our sample using the python package PyORBIT (Malavolta, 2016) and extracted their planetary properties. Our candidates belong in 10 different associations and moving groups: (i) Upper Scorpius association; (ii) Tucana Horologium association; (iii) Octans association; (iv) Vela Puppis - Population I; (v) Vela Puppis - Population II; (vi) Vela Puppis - Population III; (vii) Vela Puppis - Population IV; (viii) Vela Puppis - Population V; (ix) Vela Puppis - Population VI; (x) Vela Puppis - Population VII with ages ranging from 10 to 50 Myr. Three of our candidates are mini Neptunes ($R_P \sim 3.5$ $R_\oplus$), nine of them belong in the regime of Neptune to super Neptune planets ($3.9\ R_\oplus \leq R_P < 11.2\ R_\oplus$), and the remaining thirteen candidates are Giant planets ($R_P \geq 11.2\ R_\oplus$). TIC 0131743355 and TIC 0014091633 are TESS Object of Interest (TOIs); whereas TIC 0260119000, TIC 0033260600, TIC 0146129309 and TIC 0092896631 belong to the Community TESS Objects of Interest (CTOIs) list with a suspected planet candidate around them but not confirmed yet. For the remaining 19 candidates there are no information in the literature, so they are novel discoveries.

Using the detection efficiency of our technique and the rate of false positives in our sample, we calculated the frequencies ($f_\star$) of candidate exoplanets in stellar associations for three different sizes of planets with radii: i) $R_P < 3.9 R_\oplus$; ii) $3.9 R_\oplus \leq R_P < 11.2\ R_\oplus$; and iii) $R_P \geq 11.2 R_\oplus$ and with periods: a) 0.2 days$\leq$ P$\leq$ 5 days; b) 5 days$<$ P$\leq$ 50 days; and c) 50 days $<$ P$\leq$ 365 days. For short period Earth/super-Earth and mini-Neptune planets ($R_P < 3.9 R_\oplus$) we calculated an upper limit on the frequency of $f_{\star,E} <$ 0.65 %; for Neptune and super-Neptune $f_{\star,N} < 0.18$ %; and for Giant planets $f_{\star,G} \sim 0.32$ %. The frequencies in the intermediate range periods are

higher for all the planet types with upper values $f_{\star,E} < 18.20$ % and $f_{\star,N} < 1.90$ % for small and medium sized planets and $f_{\star,J} \sim 1.00$ % for Giants. For transiting planets with longer periods (P> 50 days) the frequencies from smaller to bigger planets are $f_{\star,E} < 55.28¡$ %, $f_{\star,N}$ 2.49 % and $f_{\star,J} < 1.22$ %, respectively. We performed a comparison of our frequencies with the values reported by Fressin et al. (2013). The majority of the frequencies we calculated (measured or upper limits) are in agreement or slightly higher than Fressin et al. (2013) have published for field stars using data from the Kepler mission. The only case where we have calculated lower frequencies is for Giant planets with long periods from 50 to 365 days with a value of $f_{\star,M} < 1.22\%$ whereas Fressin et al. (2013) reported $f_{\star,F} = (3.83 \pm 0.57)\%$. This is probably caused because we have not detected a candidate exoplanet in this period range and we are using different period and planetary radii grids. The latter is a problem also for the frequencies of small planets in our sample ($R_P < 3.9 R_\oplus$) because Fressin et al. (2013) has split this radius range in three smaller subsets, so it is not easy to perform a direct comparison.

We explored the stellar age versus planetary radius distribution (Figure 6.2) of candidate and confirmed planets orbiting stars in stellar clusters, young associations and moving groups with periods less than 100 days. Except of the candidates we found in our sample, we took into consideration the candidate exoplanets reported in the PATHOS project (Nardiello et al. 2020; Nardiello 2020; Nardiello et al. 2021) and also the confirmed and candidate exoplanets reported in the literature for stars with well constrained ages. Small planets with radii $R_P < 3.9$ $R_\oplus$ seem to be concentrated at ages bigger than 100-200 Myr and there is a lack of small exoplanets around younger stars. This is probably an observational bias, due to the difficulty to recover small planets from light curves of active young stars. Giant planets with $R_P > 11.2$ $R_\oplus \sim 1$ R_J show a random distribution in various ages ranging from $\sim$ 10 Myr to $\sim$ 1000 Myr. Exoplanets in the radius regime $4R_\oplus \leq R_P < 10R_\oplus$ are clustering at ages less than 100 Myr. It is still under investigation why there are no detections of this size of planets around stars older than 100 Myr, maybe it is due to observational biases or there are some mechanisms behind this behavior. Owen (2019) proposed that atmospheric escape is the mechanism that prevails during the early life of exoplanets, causing them to loose a large part of their atmospheres in time scales of $\sim$ 100-200 Myr and end up with radii in the regime of $4R_\oplus \leq R_P < 10R_\oplus$. On the other hand, Ginzburg et al. (2018) proposed that the radius distribution of medium size exoplanets is a product of core-powered mass loss mechanism. If the heat capacity of the gas envelope is larger than that of the rocky core it can lead up to significantly increased planet radius in agreement with the observed planet radius distribution. Additional explanations have been proposed which are related with the dynamical evolution of these type of planets such as migration due to interaction with the protoplanetary

disc or planet-planet scattering. The candidate exoplanets we discovered in our sample are in agreement with the radius distribution of young planets observed until today. By increasing the candidate and eventually confirmed exoplanets around young stars we can take significant steps towards the understanding of the evolution and formation mechanisms that prevail in the early stages of an exoplanet's life which are still into debate among the exoplanet community.

To achieve that in the future we will need to continue monitoring the candidate exoplanets in our sample. As already mentioned, due to the low angular resolution of the TESS cameras ($\sim$ 21 arcsec/pixel), a detected transiting signal in the light curve of a star belonging in a stellar association might not be due to the presence of a planet and might caused by nearby stars (e.g, close eclipsing binaries). Additional observations with higher resolution ground-based facilities will be crucial to disentangle the real nature of the transiting signals detected from the TESS FFIs, by applying supplementary validation tests to the obtained light curves and exclude any possible false positives from our candidates's list. Then, we can move on with the follow-up of the candidates using spectroscopic facilities to measure also their planetary mass, without wasting important observing time and funds on the follow-up of a false positive.

Even though detecting planets orbiting active, young stars is undoubtedly challenging in comparison with older stars, a lot of techniques, including the one presented in this thesis, have been developed and have succeeded their purpose. However, if a more generic pipeline is developed which can more effectively account for the activity of the host stars, the number of known young planets can be quickly increased. Moreover, an other barrier that holds back young exoplanet discoveries is the relatively small number of bona-fide members of young associations and moving groups. Having a larger pool of young stars to search for planets can increase the probability of discovering one. So a lot of work is required in these two aspects, before the search and detection of young exoplanets can come into fruition in the same rhythm as older planets.

References

Backer D. C., Foster R. S., Sallmen S., 1993, Nature, 365, 817

Bailer-Jones C. A. L., Rybizki J., Fouesneau M., Demleitner M., Andrae R., 2021, AJ, 161, 147

Baron F., et al., 2018, AJ, 156, 137

Baron F., Lafrenière D., Artigau É., Gagné J., Rameau J., Delorme P., Naud M.-E., 2019, AJ, 158, 187

Barrado y Navascués D., Stauffer J. R., Jayawardhana R., 2004, ApJ, 614, 386

Bell C. P. M., Mamajek E. E., Naylor T., 2015, MNRAS, 454, 593

Benatti S., et al., 2019a, A&A, 630, A81

Benatti S., et al., 2019b, A&A, 630, A81

Benatti S., et al., 2021, A&A, 650, A66

Billot N., Noriega-Crespo A., Carey S., Guieu S., Shenoy S., Paladini R., Latter W., 2010a, ApJ, 712, 797

Billot N., Noriega-Crespo A., Carey S., Guieu S., Shenoy S., Paladini R., Latter W., 2010b, ApJ, 712, 797

Bressan A., Marigo P., Girardi L., Salasnich B., Dal Cero C., Rubele S., Nanni A., 2012, MNRAS, 427, 127

Cantat-Gaudin T., et al., 2019, A&A, 626, A17

Chatterjee S., Ford E. B., Matsumura S., Rasio F. A., 2008, The Astrophysical Journal, 686, 580

Choi J., Dotter A., Conroy C., Cantiello M., Paxton B., Johnson B. D., 2016, ApJ, 823, 102

Claret A., 2018, A&A, 618, A20

Curtis J. L., Agüeros M. A., Mamajek E. E., Wright J. T., Cummings J. D., 2019, AJ, 158, 77

Dahm S. E., 2015, ApJ, 813, 108

David T. J., et al., 2018, AJ, 156, 302

David T. J., Petigura E. A., Luger R., Foreman-Mackey D., Livingston J. H., Mamajek E. E., Hillenbrand L. A., 2019, ApJL, 885, L12

Deeg H. J., Alonso R., 2018, Transit Photometry as an Exoplanet Discovery Method. p. 117, doi:10.1007/978-3-319-55333-7_117

Dobbie P. D., Lodieu N., Sharp R. G., 2010, MNRAS, 409, 1002

Dotter A., 2016, ApJS, 222, 8

Eggen O. J., 1958, MNRAS, 118, 154

Elliott P., Bayo A., Melo C. H. F., Torres C. A. O., Sterzik M. F., Quast G. R., Montes D., Brahm R., 2016, A&A, 590, A13

Fabrycky D., Tremaine S., 2007, The Astrophysical Journal, 669, 1298

Feinstein A. D., David T. J., Montet B. T., Foreman-Mackey D., Livingston J. H., Mann A. W., 2021, arXiv e-prints, p. arXiv:2111.08660

Fernández D., Figueras F., Torra J., 2008, A&A, 480, 735

Foreman-Mackey D., Hogg D. W., Lang D., Goodman J., 2013, Publications of the Astronomical Society of the Pacific, 125, 306

Fressin F., et al., 2013, ApJ, 766, 81

Gagné J., Faherty J. K., 2018, ApJ, 862, 138

Gagné J., Lafrenière D., Doyon R., Malo L., Artigau É., 2014, ApJ, 783, 121

Gagné J., et al., 2015a, ApJS, 219, 33

Gagné J., Lafrenière D., Doyon R., Malo L., Artigau É., 2015b, ApJ, 798, 73

Gagné J., et al., 2018a, ApJ, 856, 23

Gagné J., Roy-Loubier O., Faherty J. K., Doyon R., Malo L., 2018b, ApJ, 860, 43

Gagné J., Faherty J. K., Mamajek E. E., 2018c, ApJ, 865, 136

Gagné J., David T. J., Mamajek E. E., Mann A. W., Faherty J. K., Bédard A., 2020, ApJ, 903, 96

Gaia Collaboration 2020, VizieR Online Data Catalog, p. I/350

Gaia Collaboration et al., 2018, A&A, 616, A1

Gelman A., Rubin D. B., 1992, Statistical Science, 7, 457

Gennaro M., Prada Moroni P. G., Tognelli E., 2012, MNRAS, 420, 986

Ginzburg S., Schlichting H. E., Sari R., 2018, Monthly Notices of the Royal Astronomical Society, 476, 759

Goodman J., Weare J., 2010, Communications in Applied Mathematics and Computational Science, 5, 65

Gossage S., Conroy C., Dotter A., Choi J., Rosenfield P., Cargile P., Dolphin A., 2018, ApJ, 863, 67

Ida S., Lin D. N. C., Nagasawa M., 2013, The Astrophysical Journal, 775, 42

Irwin J. M., et al., 2018, AJ, 156, 140

Jones J., et al., 2015, ApJ, 813, 58

Kenyon S. J., Hartmann L., 1995, ApJS, 101, 117

Kipping D. M., 2010, MNRAS, 408, 1758

Klein B., et al., 2021, MNRAS, 502, 188

Klutsch A., Frasca A., Guillout P., Montes D., Pineau F. X., Grosso N., Stelzer B., 2020, A&A, 637, A43

Kovács G., Zucker S., Mazeh T., 2002, A&A, 391, 369

Kreidberg L., 2015, PASP, 127, 1161

Luhman K. L., Steeghs D., 2004, ApJ, 609, 917

Luhman K. L., Herrmann K. A., Mamajek E. E., Esplin T. L., Pecaut M. J., 2018, AJ, 156, 76

Malavolta L., 2016, PyORBIT: Exoplanet orbital parameters and stellar activity (ascl:1612.008)

Malavolta L., et al., 2018, AJ, 155, 107

Manara C. F., Mordasini C., Testi L., Williams J. P., Miotello A., Lodato G., Emsenhuber A., 2019, A&A, 631, L2

Mandel K., Agol E., 2002, ApJL, 580, L171

Mann A. W., et al., 2016a, AJ, 152, 61

Mann A. W., et al., 2016b, ApJ, 818, 46

Mann A. W., et al., 2017, AJ, 153, 64

Mann A. W., et al., 2018, AJ, 155, 4

Mann A. W., et al., 2020a, AJ, 160, 179

Mann A. W., et al., 2020b, AJ, 160, 179

Martín E. L., Lodieu N., Pavlenko Y., Béjar V. J. S., 2018, ApJ, 856, 40

Martioli E., Hébrard G., Correia A. C. M., Laskar J., Lecavelier des Etangs A., 2021, A&A, 649, A177

Mayor M., Queloz D., 1995, Nature, 378, 355

Meibom S., et al., 2013, Nature, 499, 55

Messina S., Nardiello D., Desidera S., Baratella M., Benatti S., Biazzo K., D'Orazi V., 2021, arXiv e-prints, p. arXiv:2112.08061

Montalto M., et al., 2020, MNRAS, 498, 1726

Montalto M., et al., 2021a,] 10.1051 / 0004-6361 / 202140717

Montalto M., et al., 2021b, Astronomy & Astrophysics

Montalto M., et al., 2022, MNRAS, 509, 2908

Montet B. T., et al., 2015, ApJ, 809, 25

Morton T. D., 2012, ApJ, 761, 6

Morton T. D., 2015, VESPA: False positive probabilities calculator (ascl:1503.011)

Murphy S. J., Lawson W. A., 2015, MNRAS, 447, 1267

Murphy S. J., Lawson W. A., Bessell M. S., 2013, MNRAS, 435, 1325

Nardiello D., 2020, MNRAS, 498, 5972

Nardiello D., et al., 2019, MNRAS, 490, 3806

Nardiello D., et al., 2020, MNRAS, 495, 4924

Nardiello D., et al., 2021, MNRAS, 505, 3767

Naud M.-E., Artigau É., Doyon R., Malo L., Gagné J., Lafrenière D., Wolf C., Magnier E. A., 2017, AJ, 154, 129

Newton E. R., et al., 2019, The Astrophysical Journal, 880, L17

Newton E. R., et al., 2021, AJ, 161, 65

Oh S., Price-Whelan A. M., Hogg D. W., Morton T. D., Spergel D. N., 2017, The Astronomical Journal, 153, 257

Owen J. E., 2019, Annual Review of Earth and Planetary Sciences, 47, 67

Owen J. E., 2020, MNRAS, 498, 5030

Pecaut M. J., Mamajek E. E., 2016, MNRAS, 461, 794

Platais I., Kozhurina-Platais V., van Leeuwen F., 1998, AJ, 116, 2423

Plavchan P., et al., 2020a, Nature, 582, 497

Plavchan P., et al., 2020b, Nature, 582, 497

Pöhnl H., Paunzen E., 2010, A&A, 514, A81

Ricker G. R., et al., 2014, Journal of Astronomical Telescopes, Instruments, and Systems, 1, 1

Rizzuto A. C., Vanderburg A., Mann A. W., Kraus A. L., Dressing C. D., Agüeros M. A., Douglas S. T., Krolikowski D. M., 2018, AJ, 156, 195

Rizzuto A. C., et al., 2020, AJ, 160, 33

Robinson R. D., Linsky J. L., Woodgate B. E., Timothy J. G., 2001, ApJ, 554, 368

Schlichting H. E., Sari R., Yalinewich A., 2015, Icarus, 247, 81

Silaj J., Landstreet J. D., 2014, A&A, 566, A132

Spiegel D. S., Burrows A., 2012, The Astrophysical Journal, 745, 174

Stassun K. G., et al., 2019a, AJ, 158, 138

Stassun K. G., et al., 2019b, AJ, 158, 138

Tang S.-Y., Chen W. P., Chiang P. S., Jose J., Herczeg G. J., Goldman B., 2018, ApJ, 862, 106

Tang S.-Y., et al., 2019, ApJ, 877, 12

Tofflemire B. M., et al., 2021, arXiv e-prints, p. arXiv:2102.06066

Torres C. A. O., Quast G. R., da Silva L., de La Reza R., Melo C. H. F., Sterzik M., 2006, A&A, 460, 695

Torres C. A. O., Quast G. R., Melo C. H. F., Sterzik M. F., 2008, Young Nearby Loose Associations. p. 757

Ujjwal K., Kartha S. S., Mathew B., Manoj P., Narang M., 2020, AJ, 159, 166

Vanderburg A., et al., 2018, AJ, 156, 46

Wenger M., et al., 2000, A&AS, 143, 9

Winn J. N., 2010, arXiv e-prints, p. arXiv:1001.2010

Wolszczan A., Frail D. A., 1992, Nature, 355, 145

Zari E., Brown A. G. A., de Zeeuw P. T., 2019, A&A, 628, A123

Zechmeister M., Kürster M., 2009, A&A, 496, 577

Zuckerman B., Bessell M. S., Song I., Kim S., 2006, ApJL, 649, L115

Appendix A

A.0.1 Color magnitude diagrams & isochrones

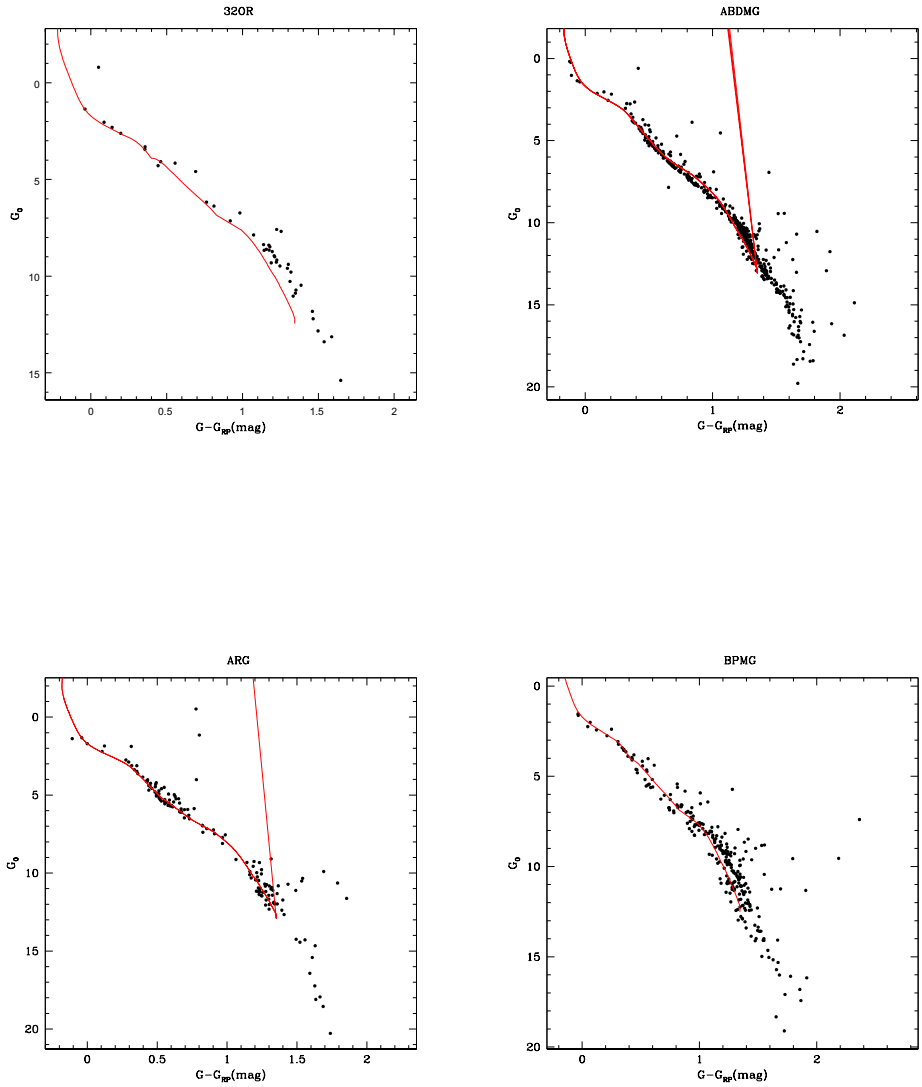

Figure A.1: G_0 versus $G-G_{RP}$ CMD of the associations: 32OR, ABDMG, ARG, and MPMG and the corresponding isochrone (red line) fitted with the parameters listed in Tables 2.1 and 2.2

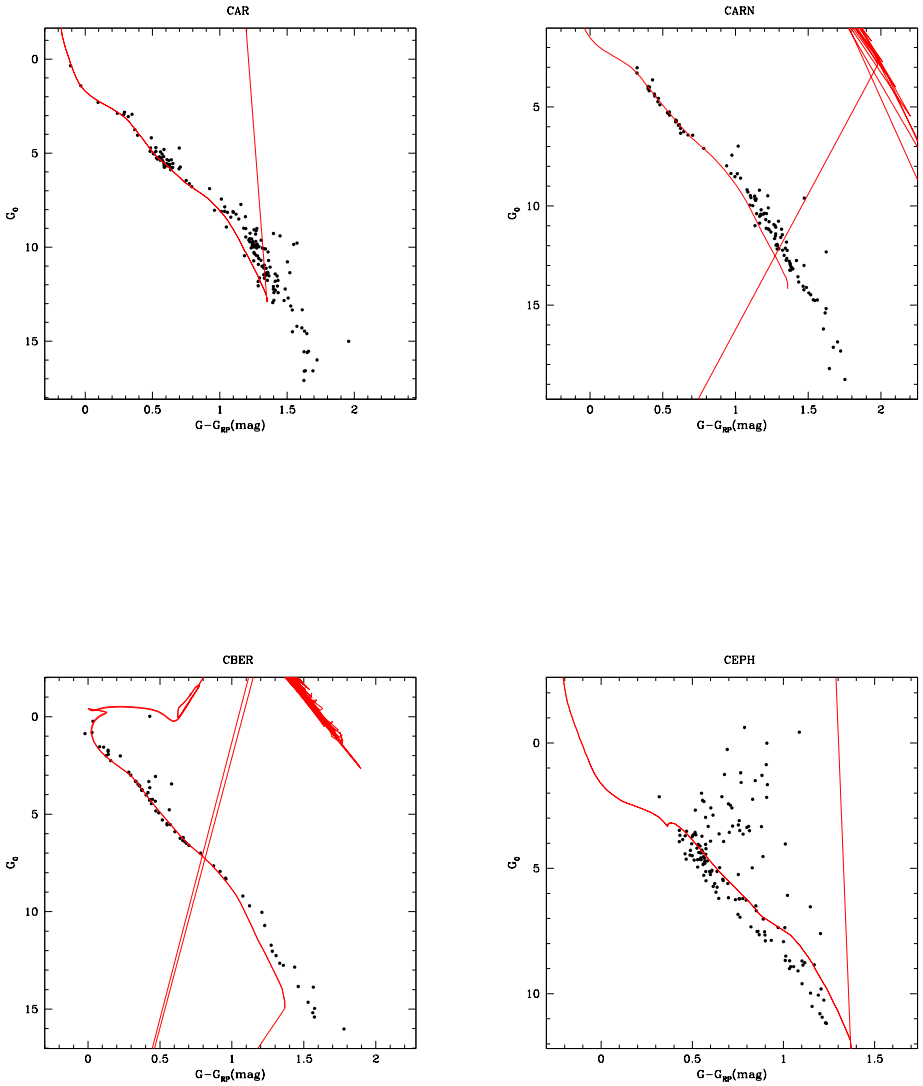

Figure A.2: Same as in Figure A.1 but for the associations: CAR, CANR, CBER, and CEPH.

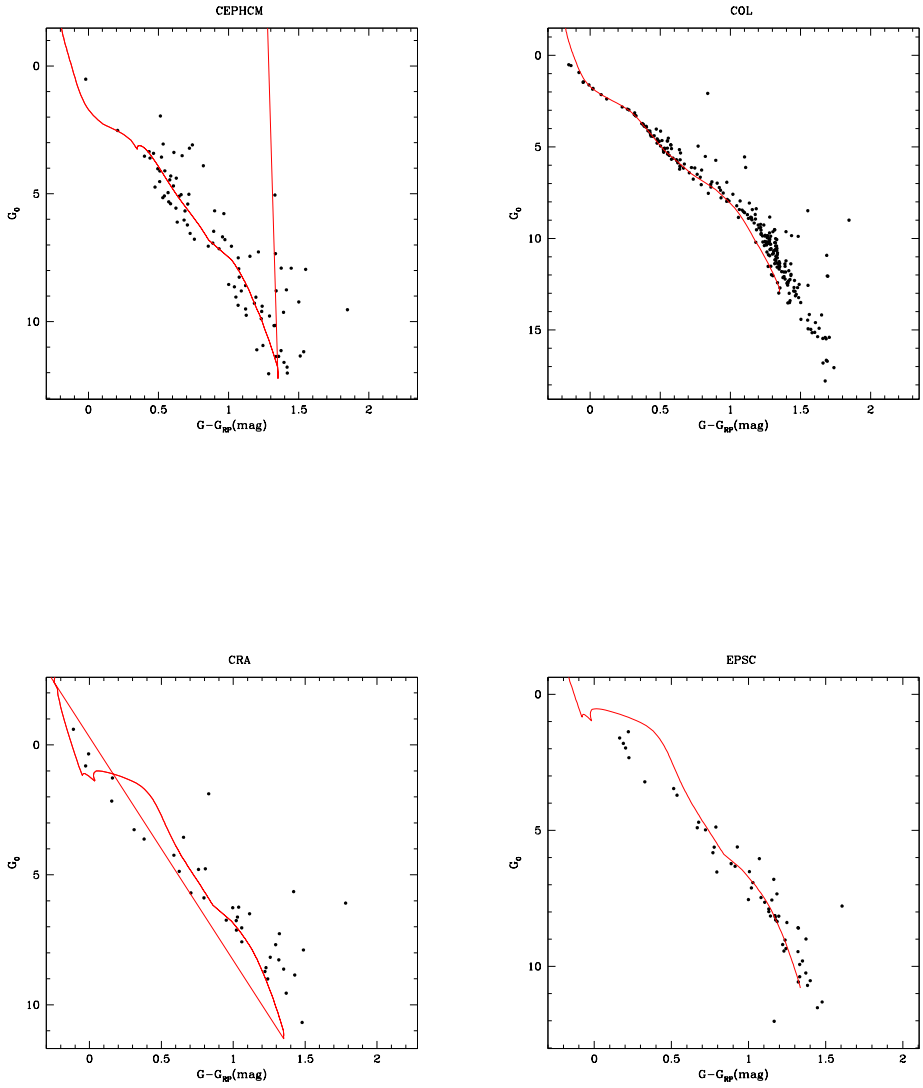

Figure A.3: Same as in Figure A.1 but for the associations: CEPHCM, COL, CRA, and EPSC.

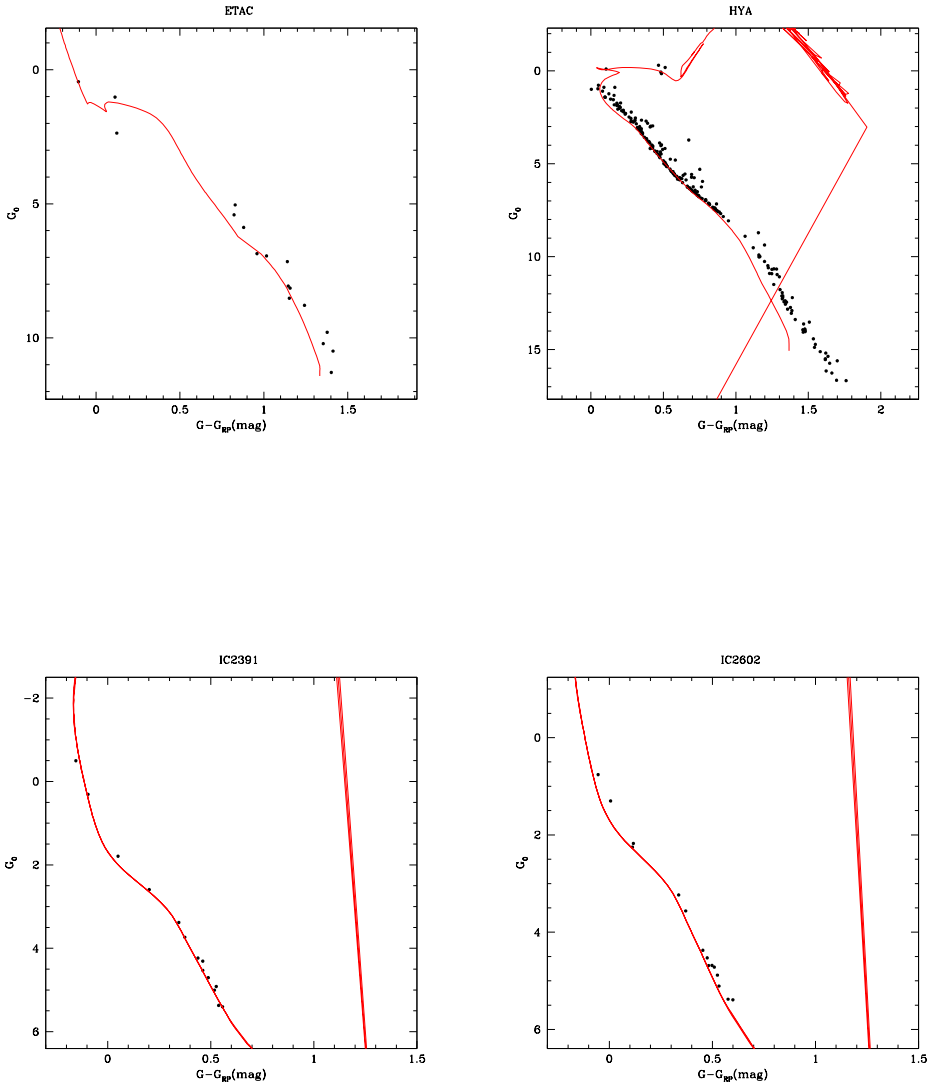

Figure A.4: Same as in Figure A.1 but for: ETAC, IC2391, IC2602

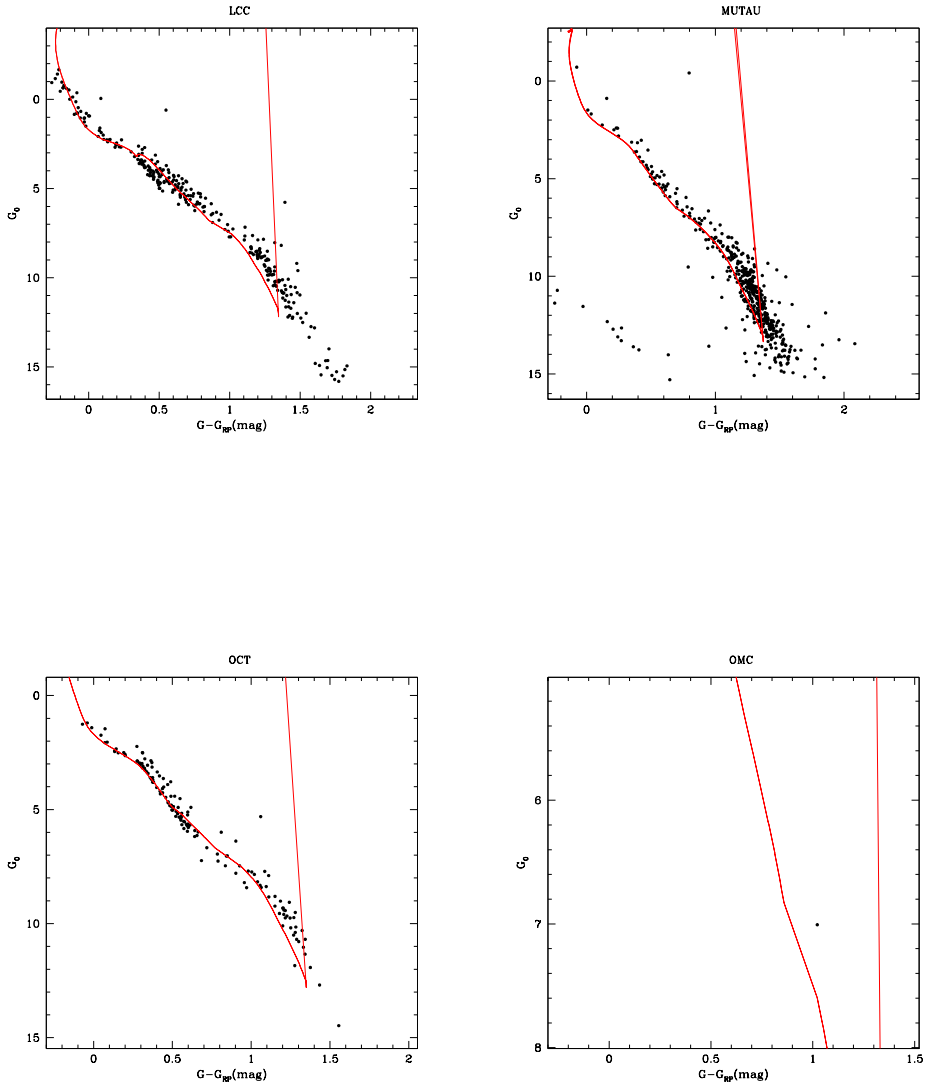

Figure A.5: Same as in Figure A.1 but for LCC, MUTAU, OCT, and OMC.

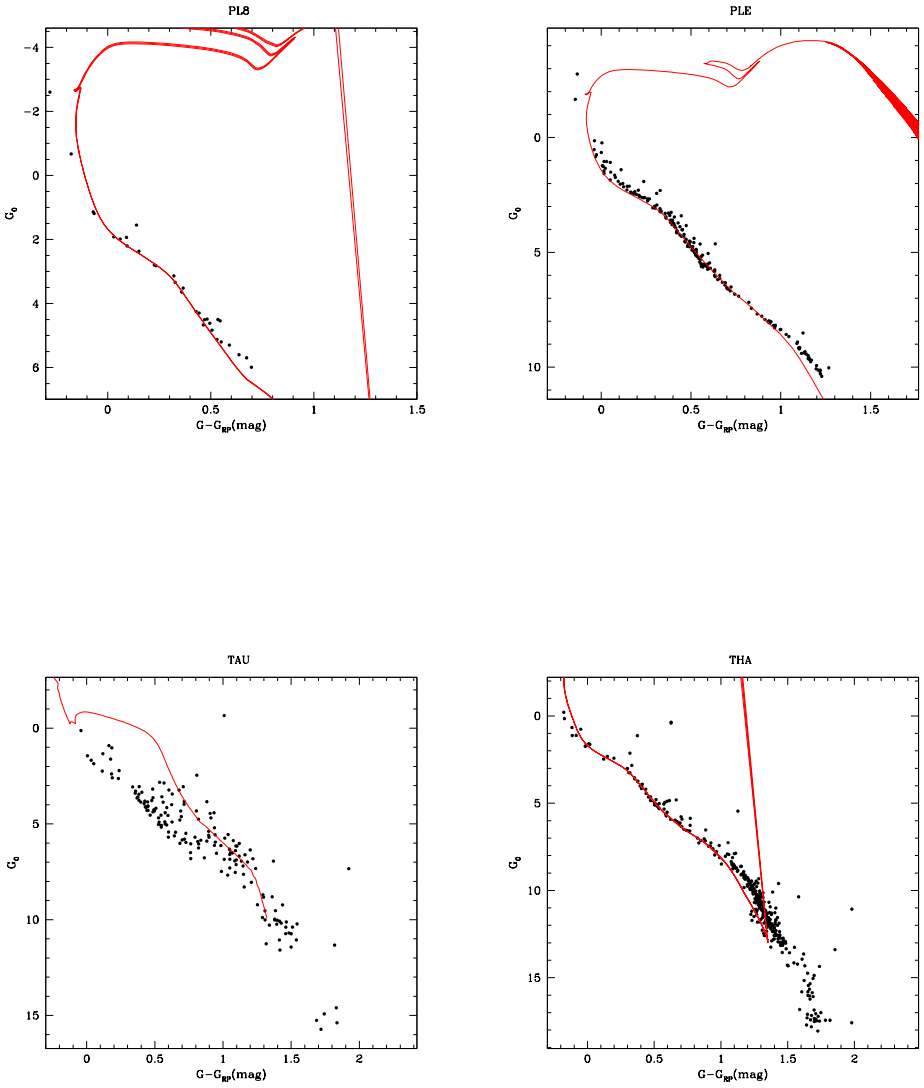

Figure A.6: Same as in Figure A.1 but for PL8, PLE, TAU, and THA.

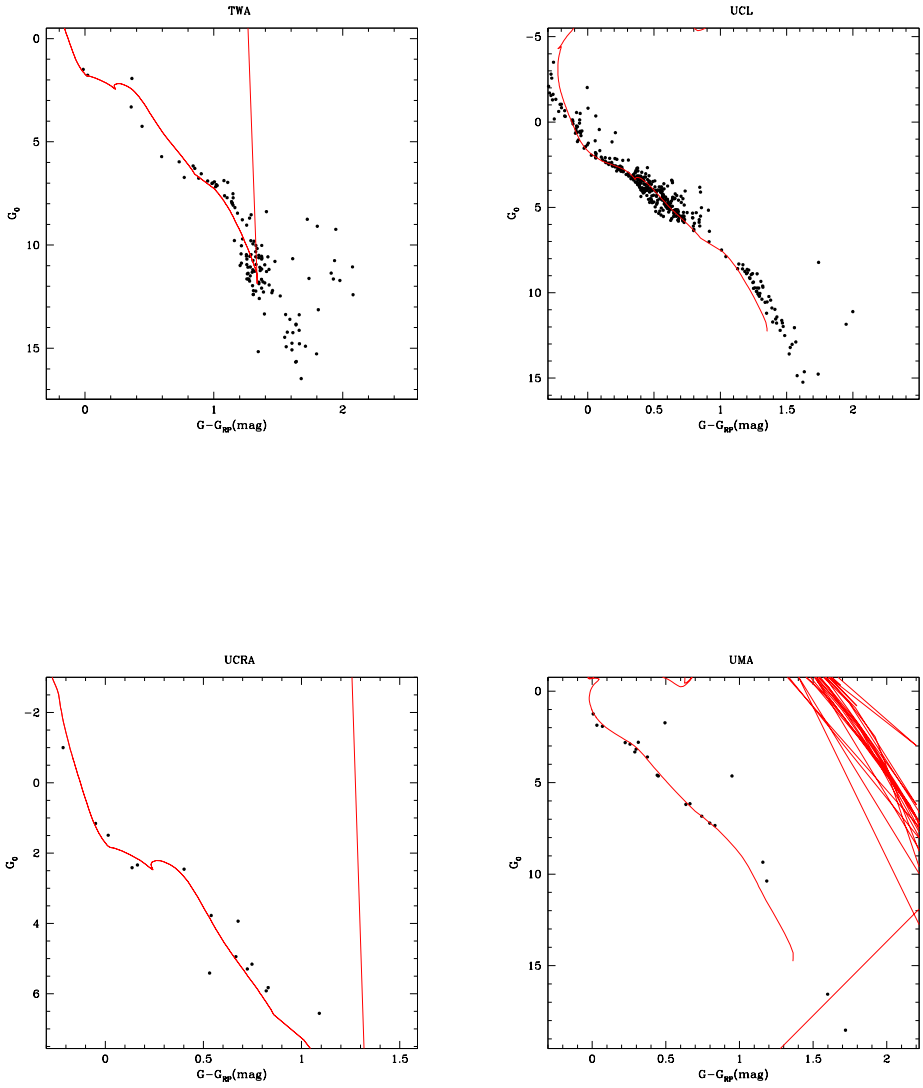

Figure A.7: Same as in Figure A.1 but for TWA, UCL, UCRA, and UMA.

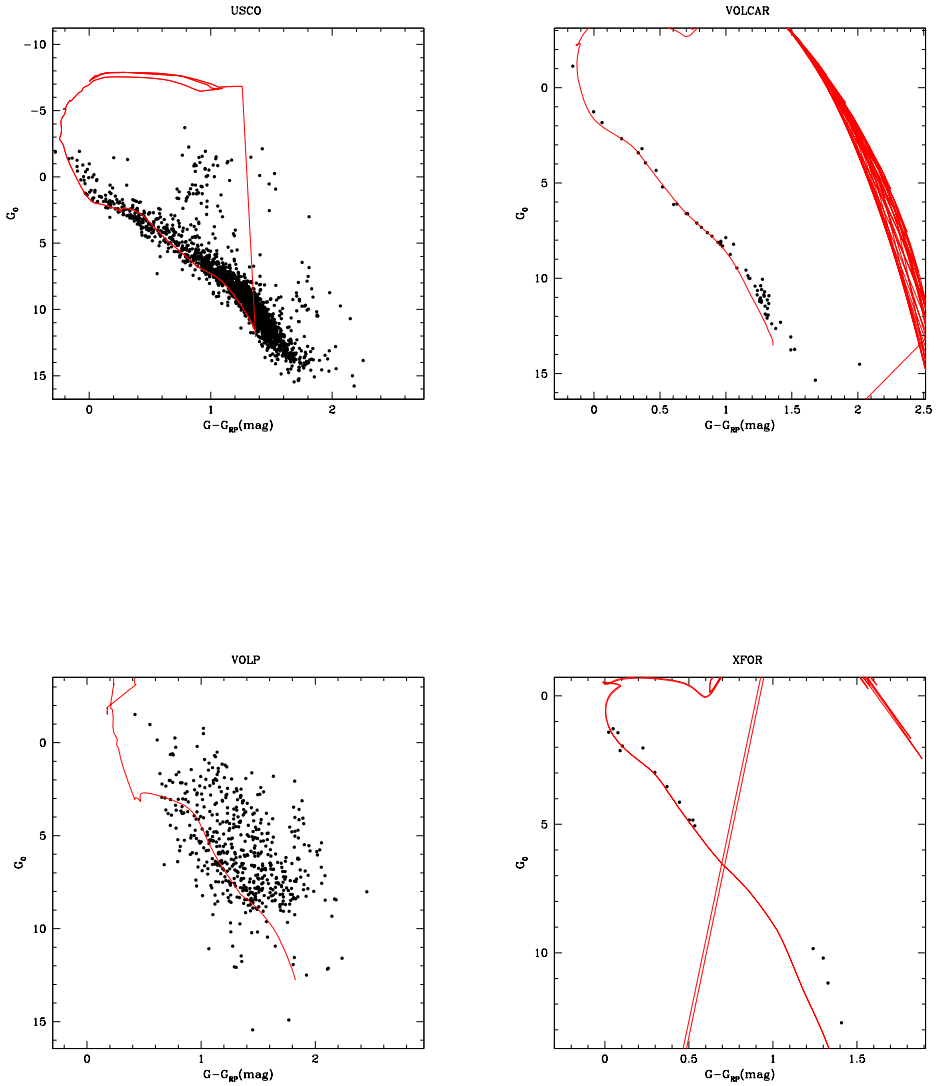

Figure A.8: Same as in Figure A.1 but for USCO, VOLCAR, VOLP, and XFOR.

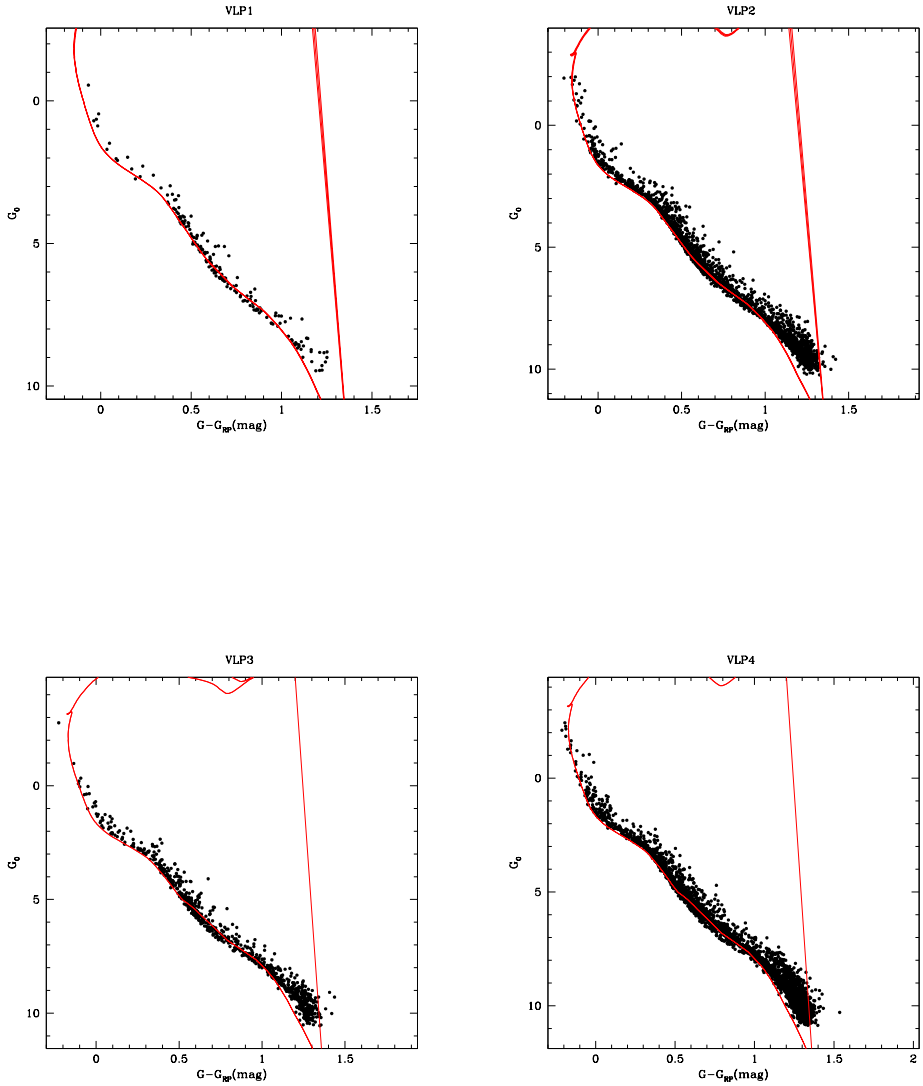

Figure A.9: Same as in Figure A.1 but for VLP1, VLP2, VLP3, and VLP4.

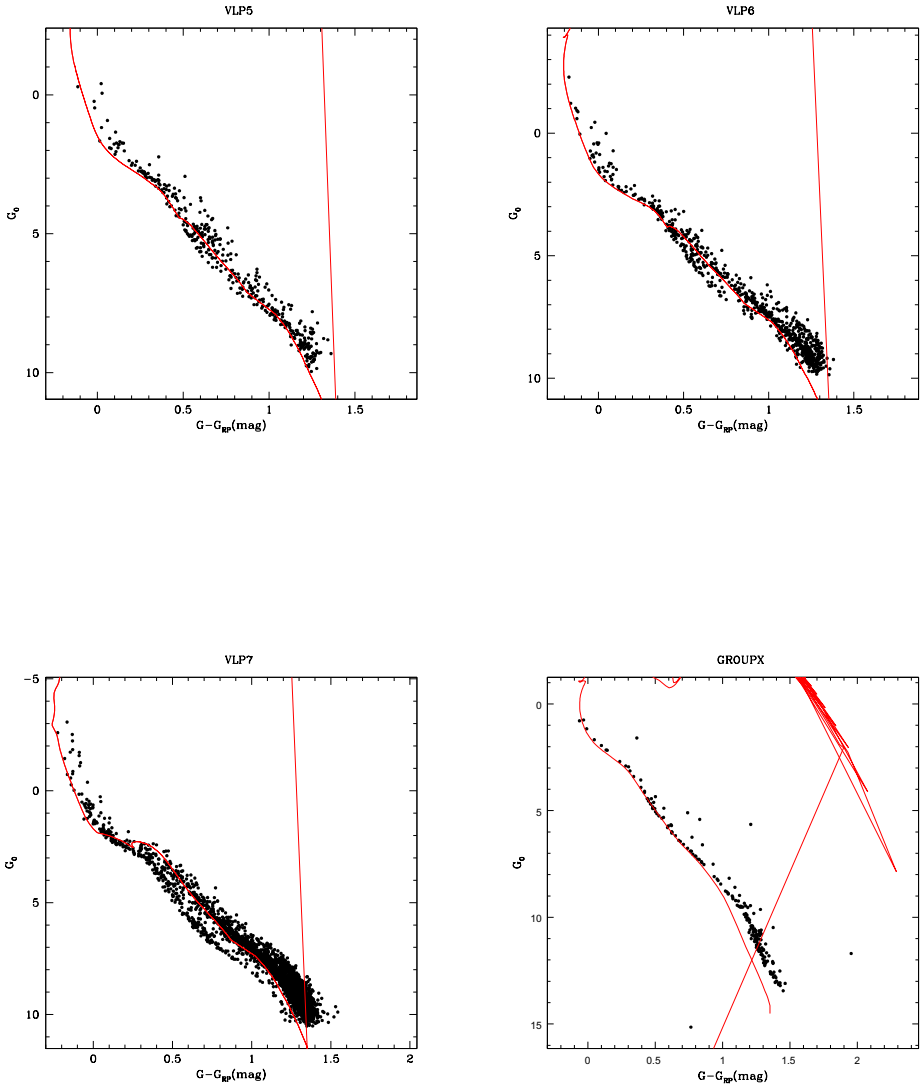

Figure A.10: Same as in Figure A.1 but for VLP5, VLP6, VLP7, and GROUPX

A.0.2 Transit modeling

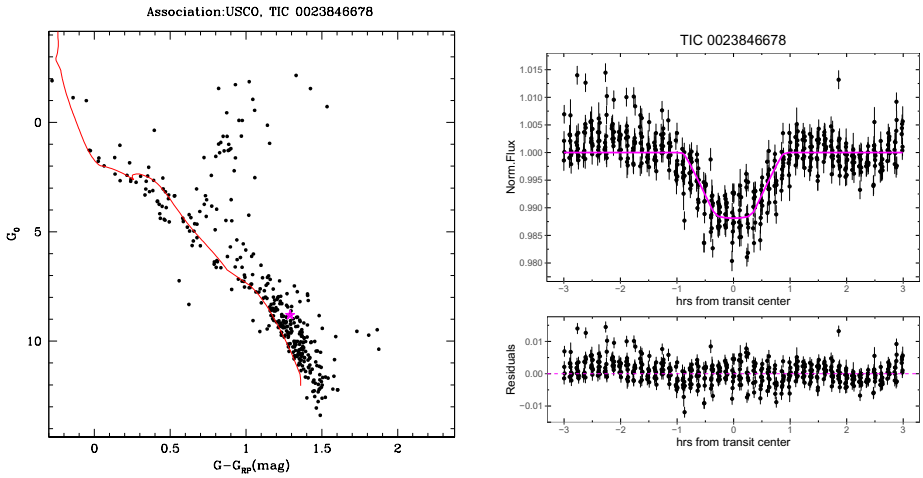

(a) (b)

Figure A.11: Overview of the candidate around TIC 0023846678. (a): G_0 versus $G - G_{RP}$ CMD of USCO association where the host star TIC 0023846678 belongs (magenta star) and the isochrone (red line) fitted with the parameters listed in Tables 2.1 and 2.2; (b) Top panel: folded light curve of the candidate exoplanet (in black) and transit modeling using PyORBIT (in magenta); Bottom panel: residuals of the transit modeling.

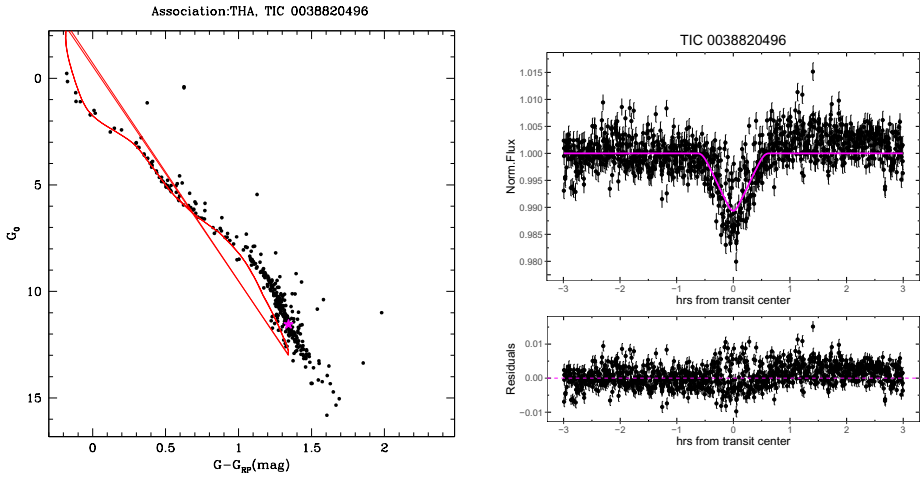

(a) (b)

Figure A.12: Overview of the candidate around TIC 0038820496 in THA association. Panels as in Figure A.11.

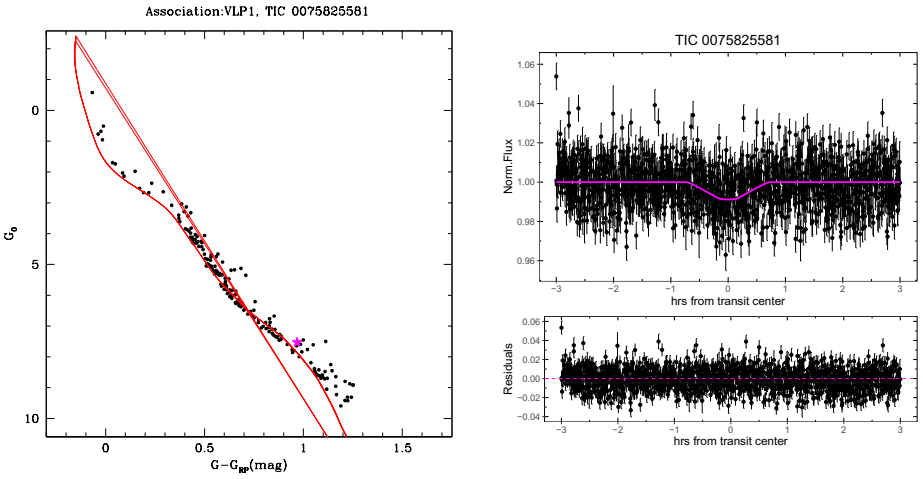

(a) (b)

Figure A.13: Overview of the candidate around TIC 0075825581 in the VLP1 population. Panels as in Figure A.11.

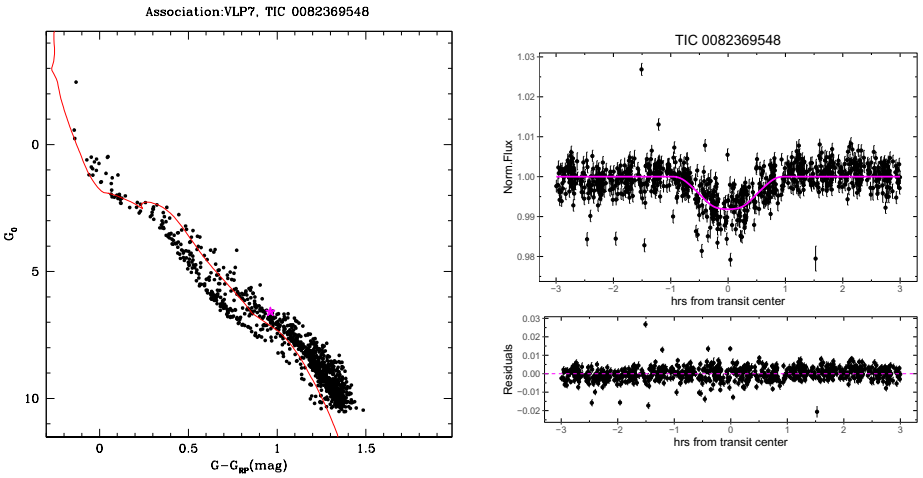

(a) (b)

Figure A.14: Overview of the candidate around TIC 0082369548 in the VLP7 population. Panels as in Figure A.11.

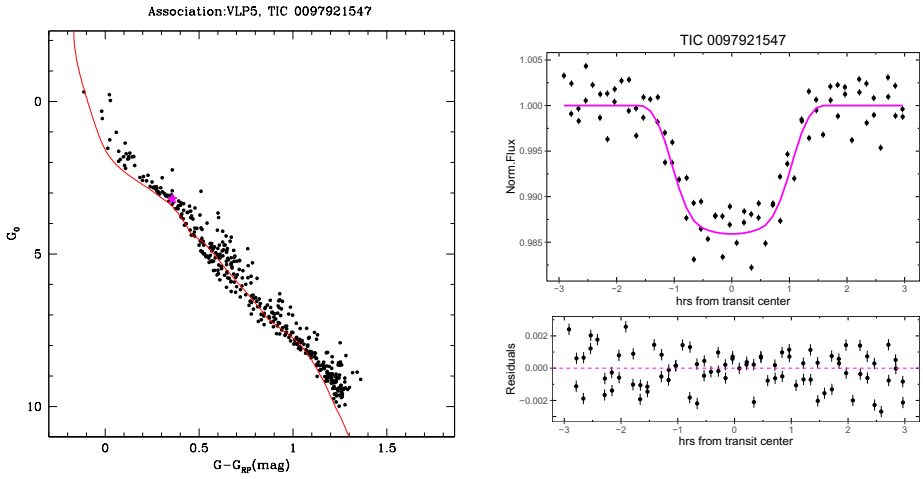

(a) (b)

Figure A.15: Overview of the candidate around TIC 0097921547 in the VLP5 population. Panels as in Figure A.11.

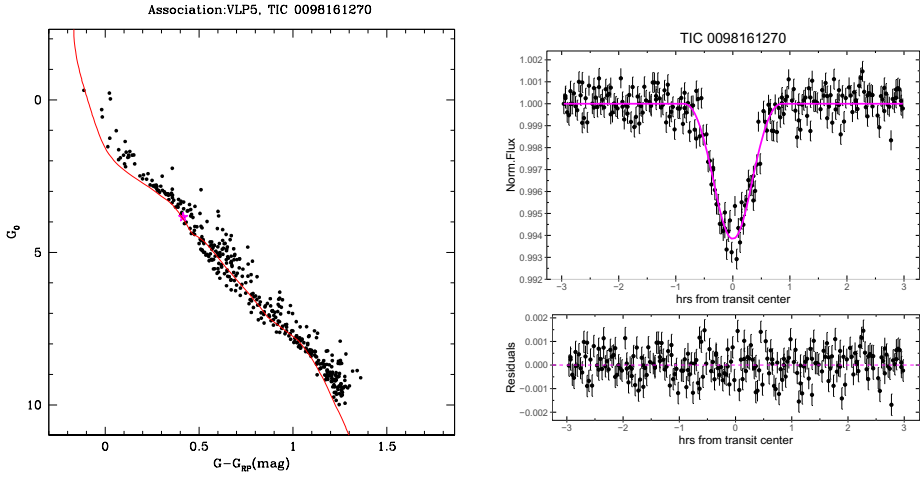

(a) (b)

Figure A.16: Overview of the candidate around TIC 0098161270 in the VLP5 population. Panels as in Figure A.11.

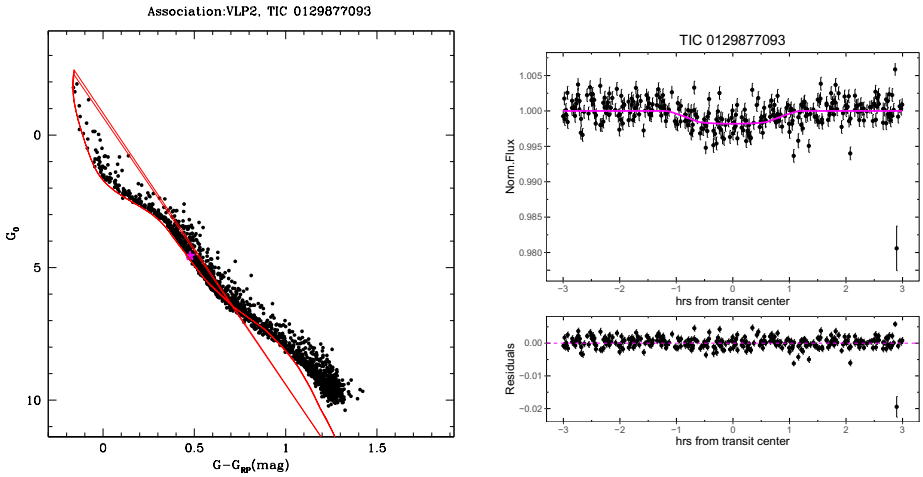

(a) (b)

Figure A.17: Overview of the candidate around TIC 0129877093 in the VLP2 population. Panels as in Figure A.11.

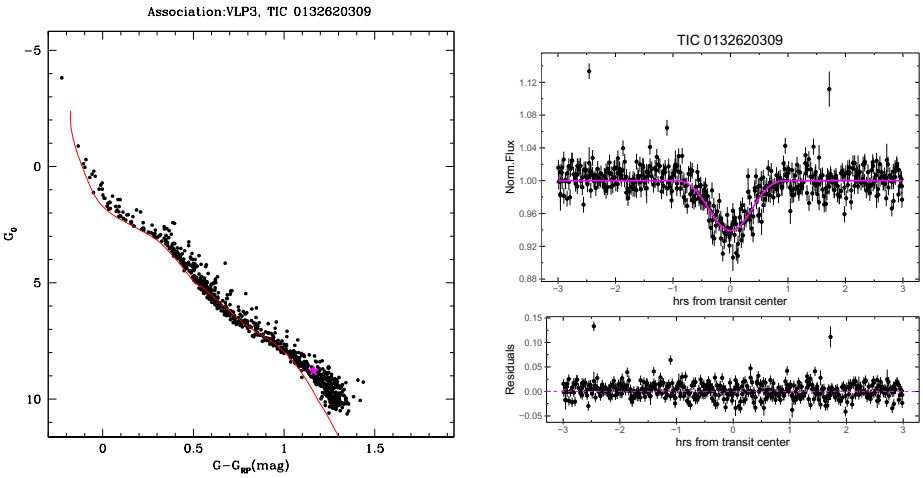

(a) (b)

Figure A.18: Overview of the candidate around TIC 0132620309 in the VLP3 population. Panels as in Figure A.11.

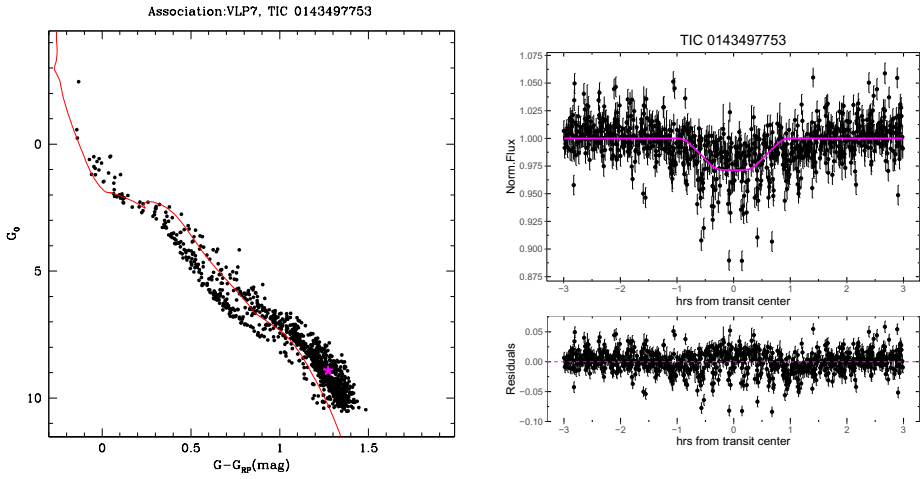

(a) (b)

Figure A.19: Overview of the candidate around TIC 0143497753 in the VLP7 population. Panels as in Figure A.11.

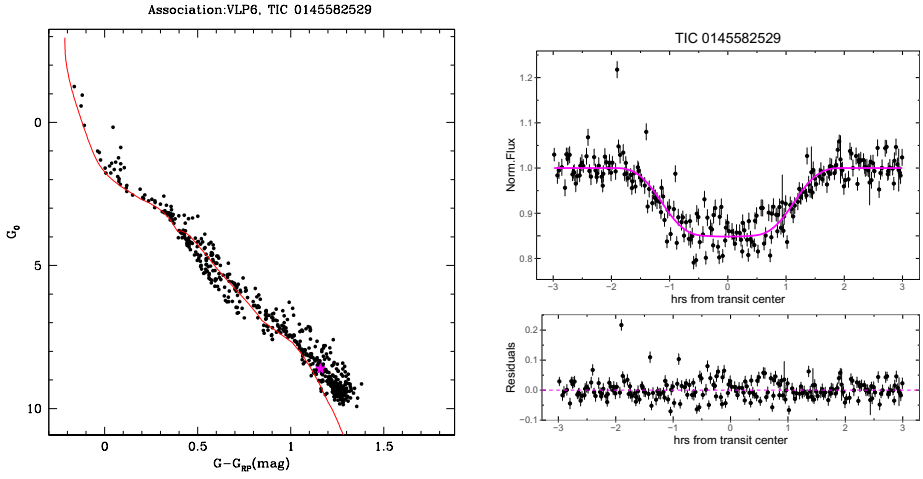

(a) (b)

Figure A.20: Overview of the candidate around TIC 0145582529 in the VLP6 population. Panels as in Figure A.11.

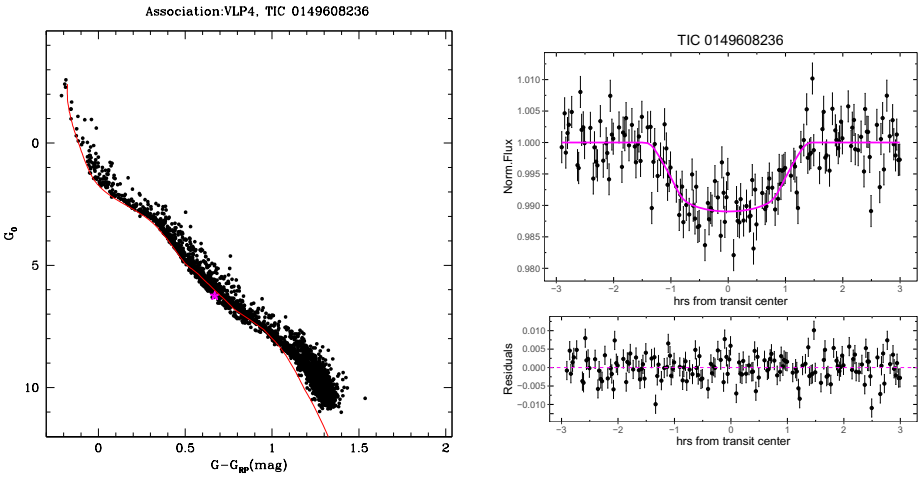

(a) (b)

Figure A.21: Overview of the candidate around TIC 0149608236 in the VLP4 population. Panels as in Figure A.11.

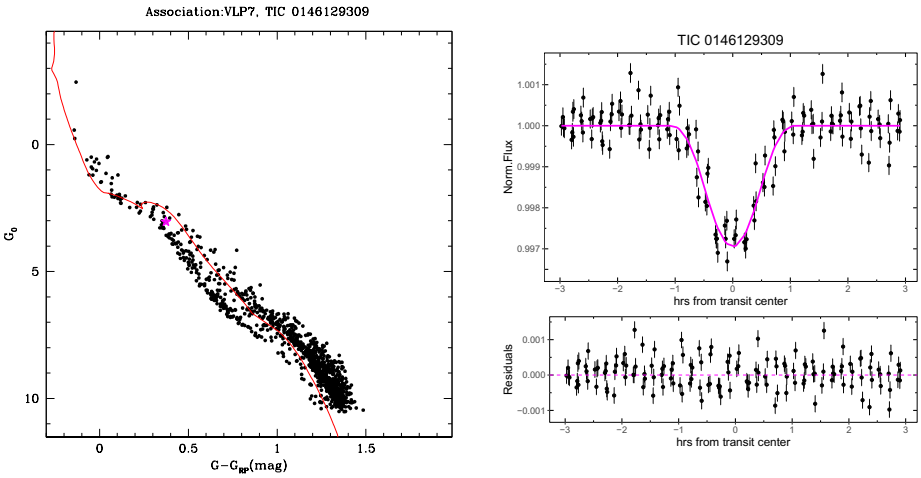

(a) (b)

Figure A.22: Overview of the candidate around TIC 0146129309 in the VLP7 population. Panels as in Figure A.11.

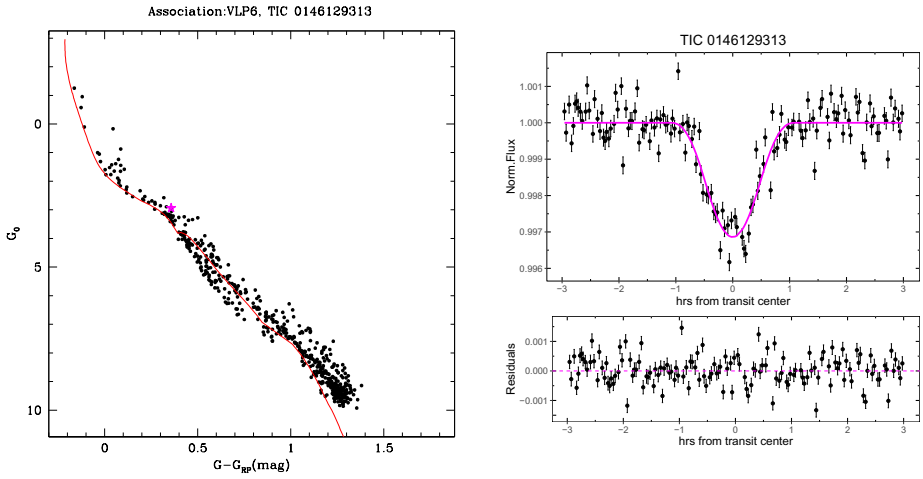

(a) (b)

Figure A.23: Overview of the candidate around TIC 0146129313 in the VLP6 population. Panels as in Figure A.11.

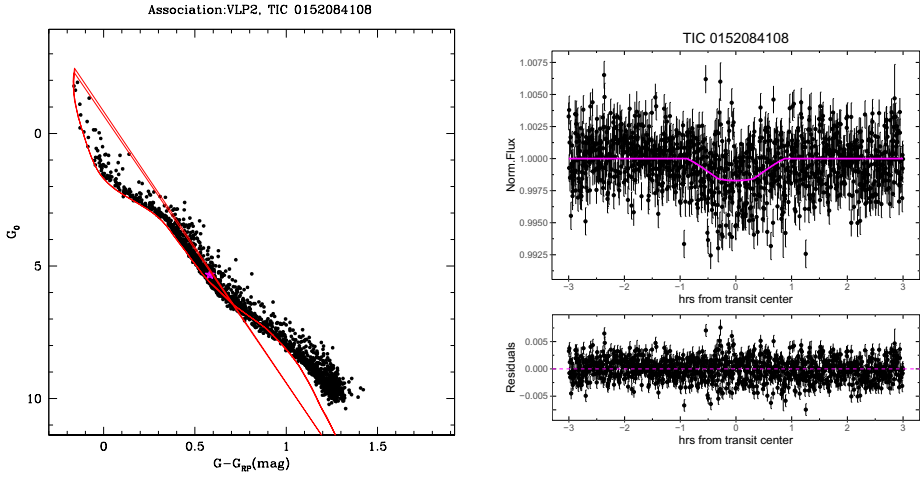

(a) (b)

Figure A.24: Overview of the candidate around TIC 0152084108 in the VLP2 population. Panels as in Figure A.11.

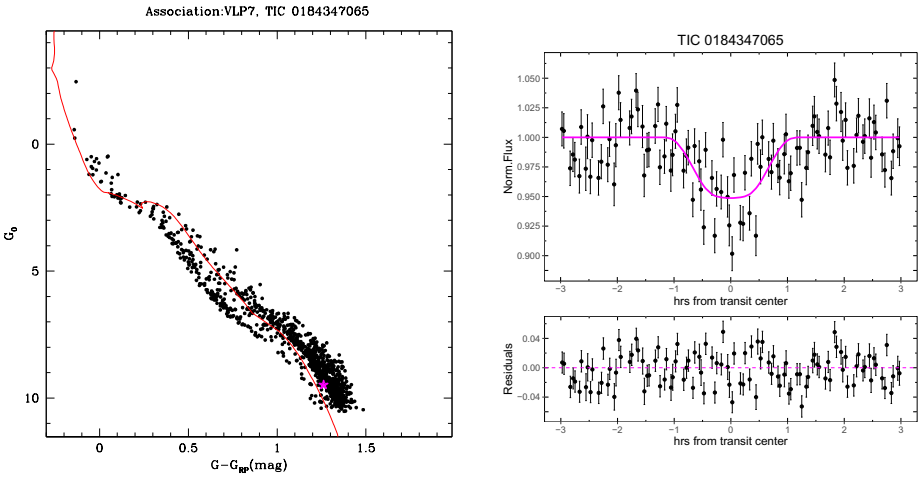

(a) (b)

Figure A.25: Overview of the candidate around TIC 0184347065 in the VLP7 population. Panels as in Figure A.11.

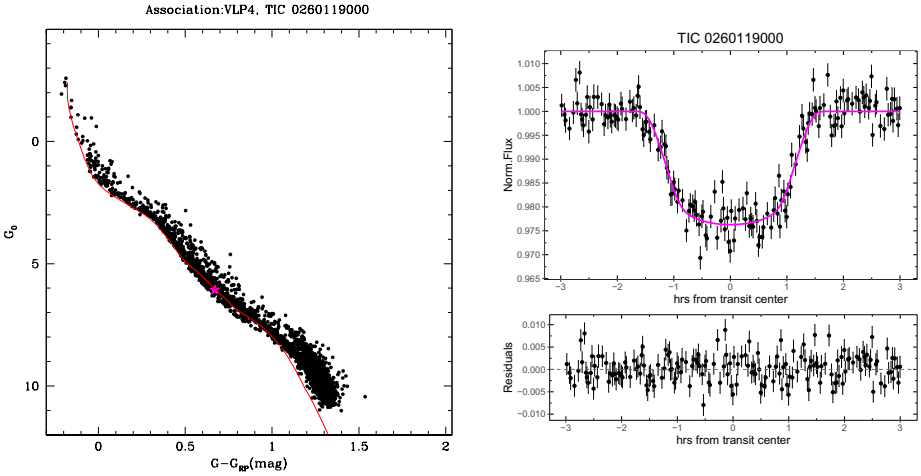

(a) (b)

Figure A.26: Overview of the candidate around TIC 0260119000 in the VLP4 population. Panels as in Figure A.11.

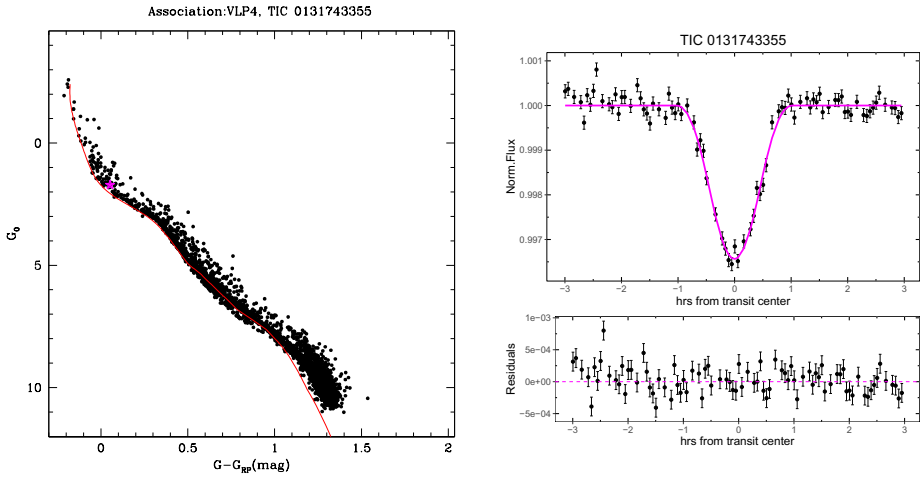

(a) (b)

Figure A.27: Overview of the candidate around TIC 0131743355 in the VLP4 population. Panels as in Figure A.11.

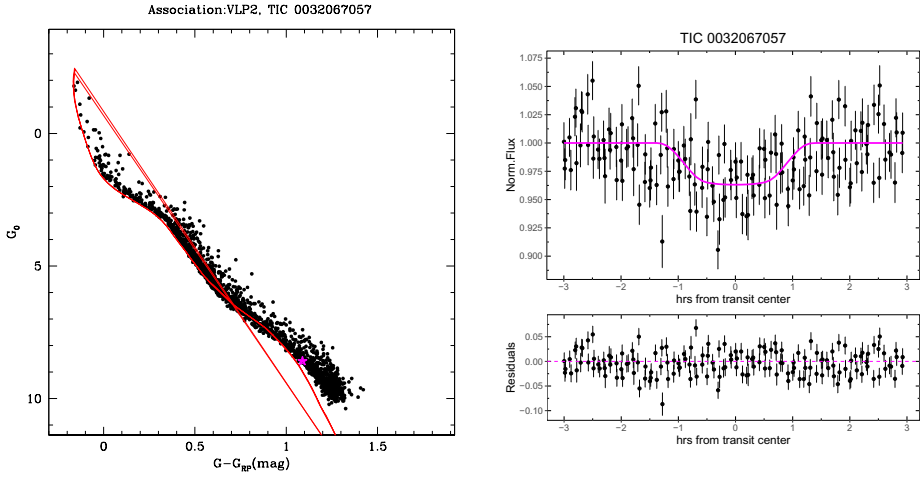

(a) (b)

Figure A.28: Overview of the candidate around TIC 0032067057 in the VLP2 population. Panels as in Figure A.11.

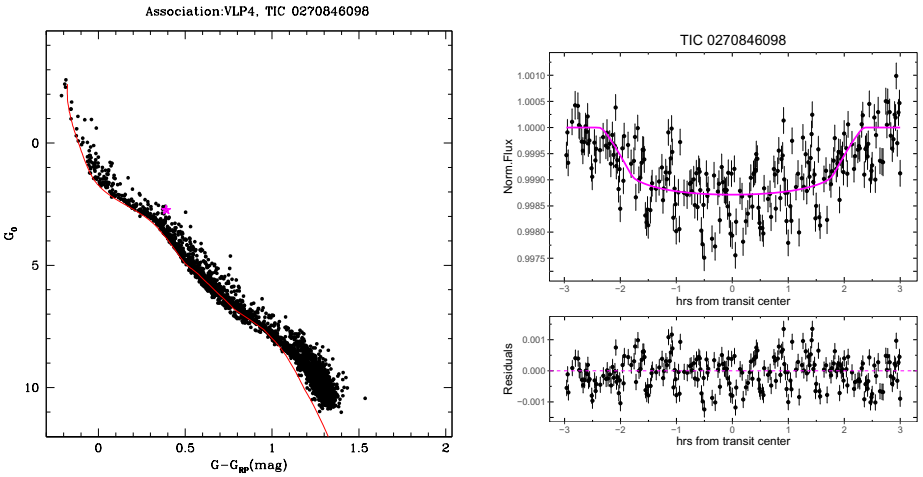

(a) (b)

Figure A.29: Overview of the candidate around TIC 0270846098 in the VLP4 population. Panels as in Figure A.11.

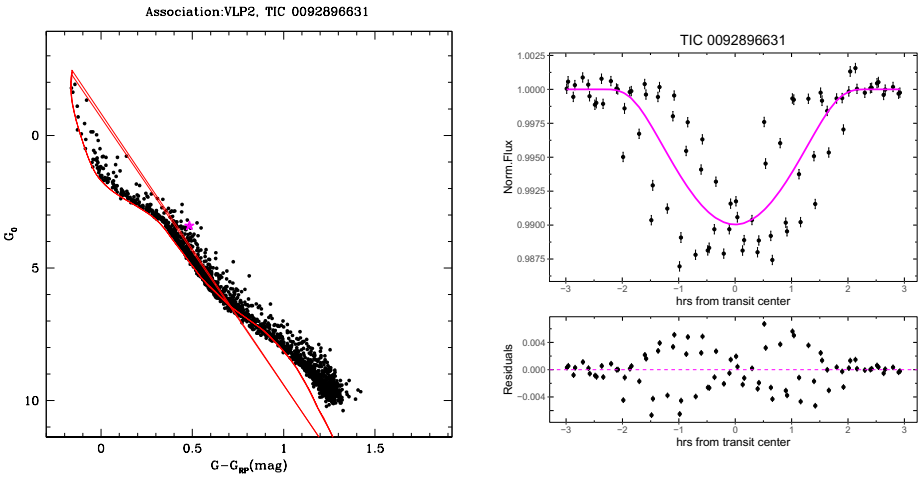

(a) (b)

Figure A.30: Overview of the candidate around TIC 0092896631 in the VLP2 population. Panels as in Figure A.11.

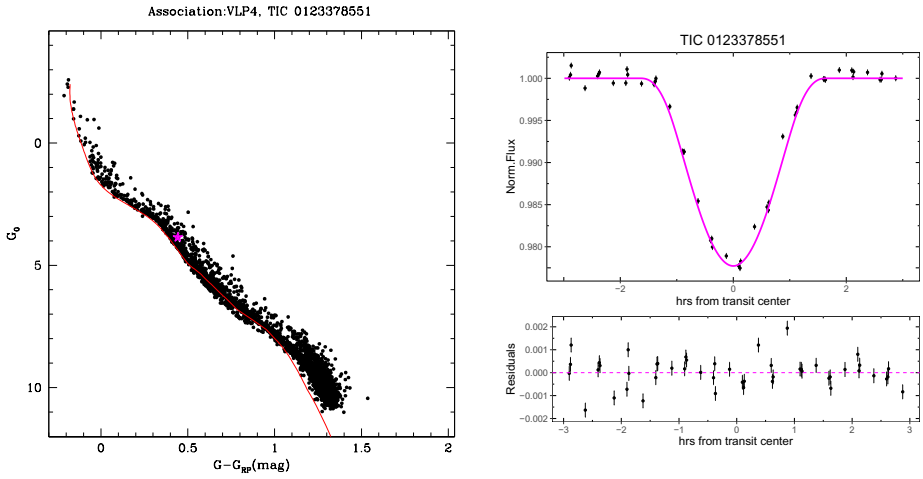

(a) (b)

Figure A.31: Overview of the candidate around TIC 0123378551 in the VLP4 population. Panels as in Figure A.11.

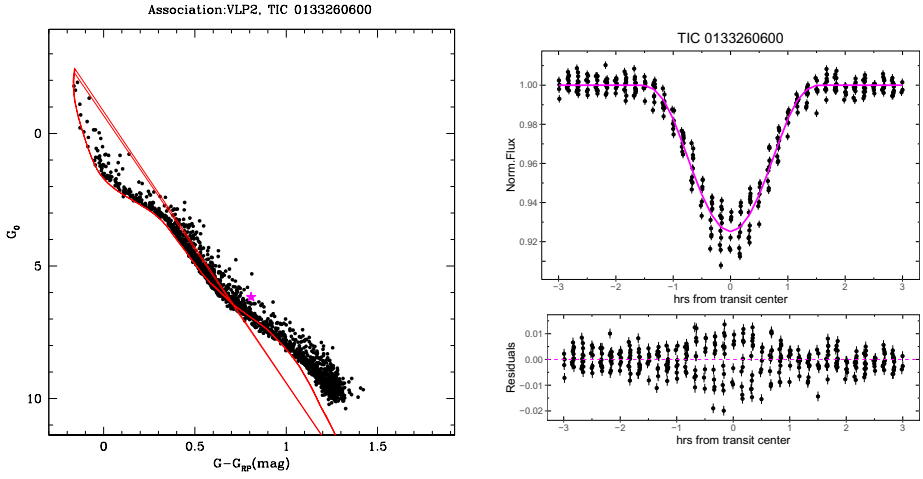

(a) (b)

Figure A.32: Overview of the candidate around TIC 0133260600 in the VLP2 population. Panels as in Figure A.11.

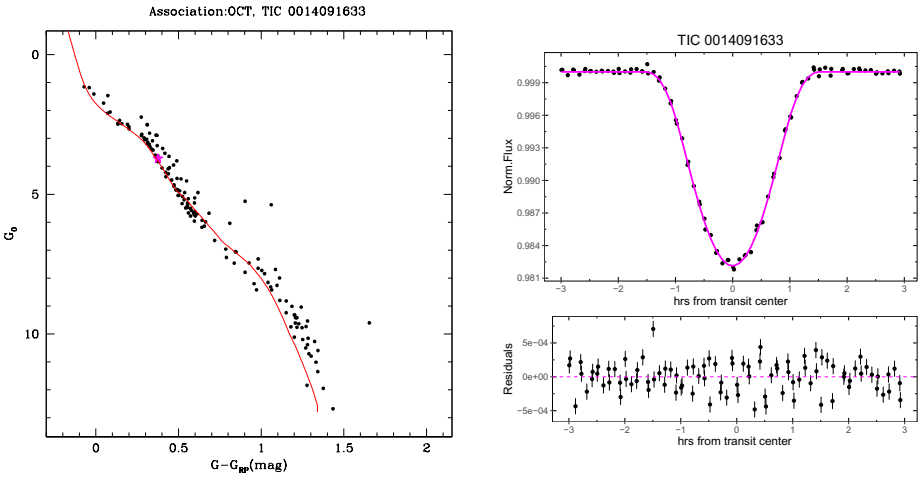

(a) (b)

Figure A.33: Overview of the candidate around TIC 0014091633 in the OCT association. Panels as in Figure A.11.

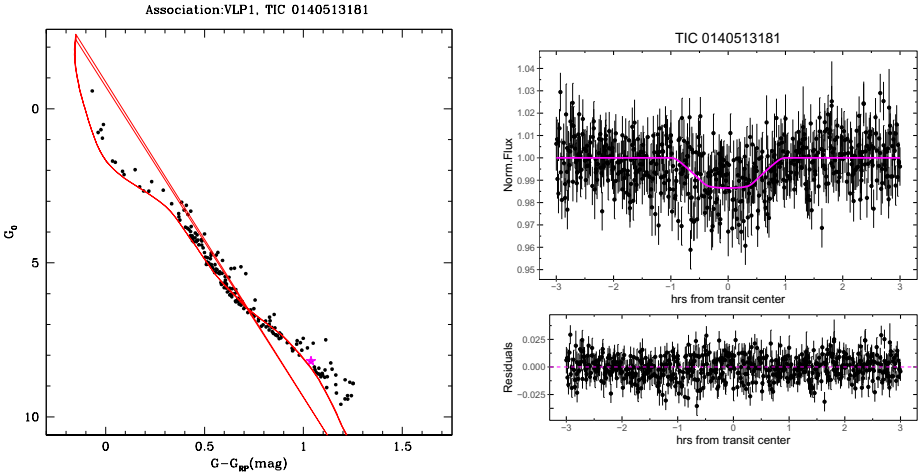

(a) (b)

Figure A.34: Overview of the candidate around TIC 0140513181 in the VLP1 population . Panels as in Figure A.11.

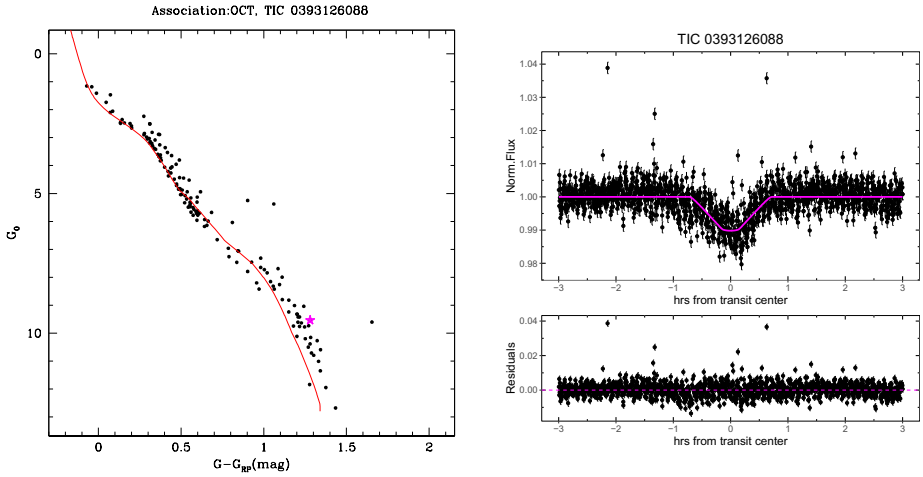

(a) (b)

Figure A.35: Overview of the candidate around TIC 0393126088 in the OCT association. Panels as in Figure A.11.